

# Self-organization in multifaceted active matter systems

Impact of microscopic diversity on pattern formation,  
emergent order, and phase transitions

Lorenz Andreas Horst Huber



München 2019



# Self-organization in multifaceted active matter systems

Impact of microscopic diversity on pattern formation,  
emergent order, and phase transitions

Lorenz Andreas Horst Huber

A dissertation submitted  
to the Faculty of Physics at the  
Ludwig–Maximilians–Universität München  
for the degree of  
DOCTOR RERUM NATURALIUM



München, 7th February 2019

First referee: Prof. Dr. Erwin Frey

Second referee: Prof. Dr. Andreas Bausch

Day of the oral examination: 21st March 2019

# Zusammenfassung

(Summary in German)

Meine Doktorarbeit behandelt die Mechanismen der Selbst-Organisation in Systemen der aktiven Materie. Dieses Prinzip ist allgegenwärtig in lebenden Systemen und dessen Erforschung gehören zu einem wichtigen Teilgebiet der Nichtgleichgewichts-Physik. Aktive Systeme weisen kollektive Phänomene auf, wie sie in der Gleichgewichtsphysik nicht möglich wären und welche im Allgemeinen von den Eigenschaften ihrer einzelnen Bestandteile und den Wechselwirkungen zwischen diesen abhängen. Dabei untersuchte ich, in welchem Umfang diese mikroskopischen Eigenschaften die globale Selbst-Organisation beeinflussen. Dies lässt sich in zwei Aspekte aufteilen, nämlich den Einfluss von (I) Teilchensymmetrien auf die emergente Ordnung und die dazugehörigen Muster, sowie die Auswirkung der (II) Teilchenkinetik auf die Dynamik auf großen Längenskalen und von Phasenübergänge.

## I Emergenz von Symmetrien, kollektiver Ordnung und Musterbildung

mit *J. Denk, E. Reithmann, R. Suzuki, T. Krüger, A. Bausch und E. Frey*.

In diesem Teil der Arbeit untersuchten wir aktive Systeme mit einer variablen Symmetrie ihrer mikroskopischen Bestandteile. Im ersten Projekt (Abschnitt 1 von Kapitel II) befassten wir uns mit Musterbildung im Kontext chiraler Teilchenbewegung, welche durch aktuelle Experimente mit Ring-bildenden FtsZ-Filamenten motiviert ist. Mit einem theoretischen Ansatz zeigten wir, dass die aktive Bewegung, intrinsische Teilchenkrümmung und sterische Abstoßung ausreichen, um eine Phase dynamischer Wirbel zu erzeugen, die allein durch die Filamentdichte kontrolliert wird. Die dazugehörige Veröffentlichung (*Phys. Rev. Lett.* **116**(17), 178301 (2016)), ist in Abschnitt 1.6, Kapitel II abgedruckt (ebenso in den Dissertationen von J. Denk und E. Reithmann). Im zweiten Projekt (Abschnitt 2, Kapitel II) studierten wir, wie emergente Ordnung und Muster von den Symmetrien der mikroskopischen Ausrichtungswechselwirkungen abhängen. Hierzu führten wir sowohl Experimente als auch agentenbasierte Simulationen durch und zeigten, dass die Symmetrie der Ordnung selbst eine emergente Eigenschaft ist. Hierbei tritt ein neuer, zuvor unbekannter Zustand einer Drei-Phasen-Koexistenz auf. Die entsprechende Publikation (*Science* 361.6399 (2018)) ist in Abschnitt 2.5, Kapitel II abgedruckt. In beiden Arbeiten wirkte ich als Ko-Erstautor mit.

## II Dynamische Prozesse, Phasenübergänge und Kritikalität

mit *T. Krüger, J. Denk, P. Baumgartner, O. Dauchot und E. Frey*

Im zweiten Teil dieser Arbeit untersuchten wir den Einfluss einer komplexen Mikro-Struktur auf die Dynamik der Ordnungsbildung und auf die dazugehörigen Phaseübergänge von aktiven Systemen. Durch die Verwendung agentenbasierter Simulationen und eines kinetischen Modells (Abschnitt 1, Kapitel III) deckten wir auf, dass globale Ordnung erst durch kollektive Prozesse von emergenten Teilchen-Clustern ermöglicht wird. Das Manuskript dieses Projekts, zu welchem ich als Estautor beigetragen habe und welches sich aktuell vor der Einreichung zum Peer-Review-Prozess befindet, ist in Abschnitt 1.7, Kapitel III abgedruckt. In einem weiteren Projekt (Abschnitt 2, Kapitel III) analysierten wir die Bifurkationsstruktur und Stabilität des polaren Ordnungsübergangs mit theoretischen Methoden und konnten zeigen, dass polare aktive Materie eine enorme Breite an verschiedenen Übergangs-Szenarien aufweist, welche empfindlich von den Details allgemeiner Ausrichtungsmodelle abhängen.



# Overview of the thesis

My thesis is devoted to the principles of self-organization in active matter systems, which are ubiquitous in nature and prominent examples of nonequilibrium physics. Active systems exhibit collective and emergent phenomena that outreach by far those of equilibrium physics, depending on the properties of the individual, constituent particles and the interaction between them. During my doctoral studies I investigated to which extent these microscopic details affect self-organization on the global scale. This can be subdivided into two parts, namely (I) the influence of particle symmetries on the emerging order and the accompanied patterns, and (II) the effect of particle kinetics on large-scale dynamics and phase transitions.

## I Emergence of symmetries, collective order and pattern formation

with *J. Denk, E. Reithmann, R. Suzuki, T. Krüger, A. Bausch, and E. Frey*

In this part of the thesis, we examined active systems where the symmetries of the microscopic constituents are, to some degree, varying. In section 1 of chapter II, we addressed pattern formation in the context of chiral particle motion, motivated by recent experiments with ring-forming FtsZ filaments. Using a theoretical approach, we showed that active motion, intrinsic particle curvature, and steric repulsion suffice to produce a dynamic vortex phase, solely controlled by the filament density. A corresponding publication (*Phys. Rev. Lett.* **116**(17), 178301 (2016)) is reprinted in section 1.6 of chapter II (also reprinted in the dissertations of J. Denk and E. Reithmann). In another project (section 2 of chapter II), we studied how emergent order and patterns depend on the symmetries of alignment interactions. By performing both experiments and agent-based simulations, we showed that the symmetry of order is itself an emergent property and found a previously unseen state of three-phase coexistence. The corresponding publication (*Science* 361.6399 (2018)) is reprinted in section 2.5 of chapter II. For both projects, I contributed as co-first author.

## II Dynamical processes, phase transitions and criticality

with *T. Krüger, J. Denk, P. Baumgartner, O. Dauchot, and E. Frey*

In the second part of this thesis, we studied the influence of a complex micro-structure on the dynamics of order formation and the corresponding phase transitions of active systems. By employing agent-based simulations and a kinetic toy model in section 1 of chapter III, we revealed that global order is facilitated by collective processes of emerging particle aggregates. At present, a corresponding manuscript to which I contributed as first author is to be submitted for peer review (also reprinted in section 1.7, chapter III). In a second project, we theoretically analyzed the bifurcation structure and stability of the polar ordering transition (see section 2, chapter III). Our results show that polar active matter exhibits a vast spectrum of transition scenarios, which depend sensitively on specific details of generic alignment models.



# Projects and contributions

The physics of many-body systems bear features that deviate substantially from the properties of its constituent entities, or to quote Nobel laureate Philip W. Anderson [1], “*the behavior of large and complex aggregates of elementary particles, as it turns out, is not to be understood in terms of a simple extrapolation of the properties of a few particles*”. While these so-called collective or emergent phenomena are already crucial for the statistical physics at thermal equilibrium, they are indispensable for biological and living systems which rely on self-organization into hierarchical, functional structures. Exploring the underlying principles and mechanisms of those systems is a central goal in the field of *active matter*.

During my doctoral studies, I worked on several aspects of self-organization and emergence in systems of interacting, actively propelled particles. I focussed in particular on a bottom-up description of collective phenomena such as order and pattern formation, to assess in which way versatile, multifaceted properties of microscopic agents affect the large-scale features of such systems. This research can broadly be subdivided into two parts: in the first one (presented in chapter II), we investigate how emerging order and patterns depend on the local symmetries of the constituents, which inhere in the particle shape or the type of directed motion (section 1), or in the details of local alignment interactions between objects (section 2). In the second part (presented in chapter III), we examined the impact of a diverse micro-structure on the ordering transitions of active systems. Specifically, we addressed in which way local dynamics generate a self-organized, ordered state by coupling kinetic processes on all length scales (section 1), and how subtle details of these dynamics lead to a range of different, unexpected bifurcation scenarios and corresponding phase transitions (section 2). Furthermore, chapter I of this work includes a brief introduction to the field of active matter and the related questions on which we concentrate. At the end, in chapter IV, the main results of my dissertation are summarized and critically discussed in the context of the prevailing literature and future developments in the field. In the following, I enclose a compact description of the separate projects which arose from my research.

## I Active Curved Polymers Form Vortex Patterns on Membranes

with Jonas Denk, Emanuel Reithmann, and Erwin Frey.

### Background information

An important part of cell division in bacteria is the mid-cell formation of the so-called Z-ring, which is an assembly of many membrane-anchored FtsZ filaments

that is vital for the constriction of the dividing cell. Yet, how these FtsZ filaments self-organize into a contractile, ring-like structure is poorly understood, especially due to the apparent absence of any FtsZ-related motor proteins [2] or significant lateral cohesion [3]. Furthermore it was shown that FtsZ filaments are intrinsically curved structures [4], which perform treadmilling dynamics when anchored on a membrane [5, 6]. Our curiosity was sparked by recent experiments with a reconstituted system on a flat surface [6]: depending on their density, FtsZ filaments either assemble into rotating, ring-like structures that closely resemble the bacterial Z-ring or into dense and jammed filament bundles.

### Research question

How can this pattern formation be understood, in particular, since there are no cohesive forces that would facilitate spatial structures? What is the influence of the treadmilling property of FtsZ polymers and their intrinsic curvature on the global evolution? How are the collective phenomena controlled?

### Summary and contribution

We used Brownian dynamics simulations of self-propelled, semiflexible polymers with an intrinsic curvature to investigate pattern formation on microscopic length scales. To complement this method, we employed a kinetic Boltzmann approach to assess collective effects of active chiral particles on mesoscopic scales. Both methods revealed a parameter region of intermediate particle density and noise strength that favors the formation of a phase of dense vortex states; for extended filaments, these vortices appear as dynamic ring-like structures. Our work shows that active motion, intrinsic curvature and steric repulsion suffice to generate ring patterns, which are fully controlled by the FtsZ density. This could serve as a robust and rudimentary mechanism of pattern formation in bacterial cells. On more general grounds, we found that these patterns are governed by a generalized complex Ginzburg-Landau equation that couples synchronization of rotating motion with the hydrodynamic fields of the active fluid, promising a variety of novel nonlinear states. Our study was published in “[Active Curved Polymers Form Vortex Patterns on Membranes](#)” (*Phys. Rev. Lett.* **116**(17), 178301 (2016)). The theoretical research was performed to equal parts by Jonas Denk and me, supported by critical assessment of Emanuel Reithmann. Jonas Denk and I contributed as co-first authors.

### Significance and outlook

Our work is the first theoretical study that highlights the role of active particle dynamics on the self-organization of FtsZ pattern formation. A recent *in vitro* study has confirmed that active motion and curvature are essential for ring formation, which is controlled by filament density [7]. Recently, it was found that active treadmilling is also vital for the bacterial cell division by dragging functional cargo along the cell equator [8–10]. Furthermore, a variety of studies have examined further details of chiral active systems [11–17].

## II Emergence of coexisting ordered states in active matter systems

with Ryo Suzuki, Timo Krüger, Andreas Bausch, and Erwin Frey.

### Background information

The rich variety of emergent phenomena observed in active systems exceeds the phenomenology of conventional equilibrium physics by far. In particular, collective motion and globally ordered states with either a polar or a nematic symmetry have been predicted by theoretical studies of two-dimensional active systems [18, 19], and have subsequently been observed in experiments with self-propelled colloids or cytoskeletal filaments: all these systems spontaneously form spatial patterns and phase-separate into a dilute, disordered phase that uniquely coexists with dense, ordered structures which are either polar flocks [20–23], nematic trails [24], or swirling vortices [6, 25]. Hence, emergent order in active matter appears to be robust. While in theory, the corresponding ordering transitions rely on simplified collision rules between the constituents that exhibit either polar or nematic alignment, recent experiments [26, 27] have indicated that realistic microscopic interactions are, in fact, extremely faint and lack a clear alignment symmetry.

### Research question

How robust is the global order that emerges in active systems? To which extent is its symmetry predestined by local alignment interactions? How can this be reconciled with the malleability of self-organized structures in living systems?

### Summary and contribution

We combined theory and experiment to show that active matter systems can produce steady states that have no equilibrium analogue: a generic three-phase coexistence of patterns with fluctuating polar and nematic symmetry, embedded in a disordered background. By carefully manipulating the particle interaction of an actomyosin gliding assay and analyzing a multi-scale agent-based model, we identify that sufficiently weak alignment interactions, which lack a distinct symmetry, are a prerequisite of this novel state. This work was recently published as “[Emergence of coexisting ordered states in active matter systems](#)” (*Science* 361.6399 (2018): 255-258). Together with Ryo Suzuki and Timo Krüger with whom I contributed as co-first author, I conducted experiments in the lab of Andreas Bausch. Timo Krüger and I developed, implemented, and analyzed the theoretical model.

### Significance and outlook

From a physical perspective, our results demonstrate that nonequilibrium systems do not obey the Gibbs phase rule [28] or the universality principle [29, 30]. For biological systems, our findings show that emergent order is unchained from underlying constituent symmetries and able to express different types of order from identical building blocks. This is highly relevant for ‘multi-tasking’ in living systems such as the cellular actin network, which forms stress fibres and filopodia simultaneously [31, 32], or the variable structures of migrating cell layers [33, 34].

### III Cluster assembly kinetics drive polar nucleation of active polymers with *Timo Krüger and Erwin Frey*.

#### Background information

Polar flocking in two dimensions is one of the most well-studied active phenomena, and was observed in a range of experiments [20–23, 26, 35–39]. On the basis of simplified interaction rules, various theoretical models predicted that the transition to polar order is in general discontinuous [40–42]. Here, flocking is accompanied by a phase separation into dense, ordered structures within a dilute background, which bears similarities to a liquid-gas phase transition of passive systems [43, 44]. However in contrast to equilibrium, experiments and agent-based simulations suggest that polar patterns only form micro-phases and coarsening arrests at a non-macroscopic length scale [21, 22, 45, 46]. The mechanisms that underlie this pattern selection are, despite several efforts [43, 44, 46, 47], not fully understood. In this context, a clear picture of the corresponding self-organization dynamics on different length scales is also elusive.

#### Research question

How exactly does polar order emerge from disorder in an experimentally relevant system? Which microscopic processes generate this transition and the corresponding stationary state and how is this manifested on different length scales? Can we find a simple description of this ordering transition on a level of kinetic processes?

#### Summary and contribution

Employing the agent-based simulations that we have developed in the previous project, we closely analyzed the formation of polar order using a new representation of local structures in terms of heterogeneously ordered particle clusters. We found that polar order already emerges at the level of small, nucleating clusters. The stationary polar state is characterized by a cyclic competition between two cluster populations – an ordered one and a disordered one – and depends on cluster processes on all length scales. By identifying the essential mechanisms of self-organization, we developed a kinetic model of cluster aggregation on heuristic reasoning, which reproduces the emergent properties of flocking remarkably well, despite lacking any information of spatial patterns. The preprint of this research, to which I contributed as first author, is to be submitted to peer review.

#### Significance and outlook

Our analysis demonstrates that collective behavior already arises at the level of local particle aggregates, and that polar nucleation requires not only sufficiently large, but also structured clusters in contrast to equilibrium systems [48]. As a consequence, polar nucleation should be easily excitable in experiments, by inserting small but ordered nuclei. On more general grounds, our work sheds new light on the dynamics of micro-phase separation and provides an interesting correspondence of active systems with the physics of self-assembly and population dynamics.

## IV Robustness of the Vicsek ordering paradigm

with *Timo Krüger, Peter Baumgartner, Jonas Denk, Olivier Dauchot, Erwin Frey.*

### Background information

In the theory of active systems, it has been tacitly assumed that the emergence of polar order is – for the majority of experiments and theoretical models – at least qualitatively described by the Vicsek model [40, 45, 49]. This model entails an ordering paradigm that includes a universal phase transition with a critical exponent of  $1/2$  towards a locally stable ordered state, as it was shown by mean-field theories [42, 50–52]: in the vicinity of this transition, this state is laterally unstable and polar patterns arise; further away, beyond a second transition point, the uniform ordered state is also laterally stable [19, 45, 50, 53–55]. Recent studies demonstrated that, depending on the details of local alignment interactions, a discontinuous, subcritical transition towards the uniformly ordered state is in principle possible for active polar systems [38, 56].

### Research question

Is the phase transition from disorder to polar order universal in active systems? How generic is the Vicsek ordering paradigm in the context of models with realistic alignment interactions? What are generic criteria to classify ordering transitions?

### Summary and contribution

Using a kinetic Boltzmann approach [42, 52], we studied the effect of different binary collision rules on the bifurcation structure of the system and the corresponding stationary states. We focussed in particular on collision rules that successively depart from the original Vicsek case [42, 49], towards more realistic microscopic alignment. Our results show that the continuous, Vicsek-type transition to polar order is generically replaced by a discontinuous ordering transition. We identified a functional criterion for this bifurcation, which corresponds to particle interactions that favor alignment for acute scattering angles and disalignment for obtuse angles, in opposition to the Vicsek rule. Furthermore, we found that the second transition towards stable uniform order exhibits a power-law dependence on the strength of collision noise. Upon engineering alignment interactions, a whole plethora of new bifurcations and ordering transitions can be constructed. Preliminary results show that this non-universal behavior is also recovered in agent-based simulations.

### Significance and outlook

The analytical results obtained from the kinetic Boltzmann approach affect the perception of ordering transitions and emergent states in many experiments and theoretical models of polar active systems, and demonstrate that these systems are – analogous to the results of project II – not necessarily constrained to a universal ordering paradigm but may exhibit a variety of interesting, coexisting states. These predictions can be readily tested in experiment and agent-based models that allow for a direct manipulation of the microscopic alignment interactions.



# Contents

Zusammenfassung (Summary in German)	v
Overview of the thesis	vii
Projects and contributions	ix
<b>I Introduction to active systems</b>	<b>1</b>
1 Experimental motivation . . . . .	1
2 Theoretical picture . . . . .	2
3 Open questions . . . . .	5
<b>II Emergence of symmetries, collective order and pattern formation</b>	<b>9</b>
1 Chiral particle motion . . . . .	12
1.1 Ring formation of curved FtsZ filaments <i>in vitro</i> as a precursor to bacterial cell division . . . . .	12
1.2 Agent-based simulation of self-propelled, curved polymers . . . .	13
1.2.1 Model definitions . . . . .	13
1.2.2 Implementation . . . . .	14
1.2.3 Emergence of rotating rings . . . . .	17
1.3 Kinetic Boltzmann ansatz with curved particles . . . . .	19
1.3.1 Model definitions . . . . .	19
1.3.2 Spectral analysis . . . . .	22
1.3.3 Weakly nonlinear analysis . . . . .	22
1.3.4 Numerical integration using SNAKE . . . . .	25
1.4 Generalized complex Ginzburg-Landau equations . . . . .	26
1.4.1 Derivation . . . . .	26
1.4.2 Homogeneous solutions and stability . . . . .	28
1.4.3 Inhomogeneous solutions . . . . .	29
1.5 Particle density and chirality control localized vortices . . . . .	30
1.6 Publication in <i>Physical Review Letters</i> (2016): Active Curved Polymers Form Vortex Patterns on Membranes by J. Denk, L. Huber, E. Reithmann, E. Frey . . . . .	33
2 Mixed symmetry of alignment interactions . . . . .	47
2.1 The actomyosin gliding assay . . . . .	47
2.1.1 Background . . . . .	47
2.1.2 Controlling collective motion . . . . .	49

2.2	Multi-scale simulations of the gliding assay . . . . .	51
2.2.1	Modelling weakly-aligning self-propelled polymers (WASP)	51
2.2.2	Implementation of WASP simulations . . . . .	57
2.2.3	Single filament properties . . . . .	58
2.2.4	Emergence of collective order and patterns . . . . .	62
2.2.5	Hysteresis analysis . . . . .	67
2.2.6	Three-phase coexistence, breakdown of universality, and emergent symmetry of order . . . . .	68
2.3	Experimental verification . . . . .	74
2.3.1	Setup of the gliding assay . . . . .	74
2.3.2	Analysis of single particle and collective properties . . . .	75
2.3.3	Three-phase coexistence . . . . .	80
2.4	Summary and Outlook . . . . .	83
2.5	Publication in <i>Science</i> (2018): Emergence of coexisting ordered states in active matter systems by L. Huber, R. Suzuki, T. Krüger, E. Frey, A. R. Bausch . . . . .	85
<b>III</b>	<b>Dynamical processes, phase transitions and criticality</b>	<b>121</b>
1	Cluster assembly and nucleation kinetics of WASP systems . . . . .	126
1.1	Background . . . . .	126
1.2	The cluster size-order decomposition . . . . .	127
1.3	Mesoscopic processes of the disordered gas . . . . .	129
1.4	Mesoscopic processes at the flocking onset . . . . .	134
1.4.1	Emerging clusters drive the nucleation of polar order . . .	134
1.4.2	Effective kinetic model of flocking . . . . .	141
1.5	Mesoscopic processes at the nematic onset . . . . .	149
1.6	Summary and outlook . . . . .	152
1.7	Prepared manuscript (2019): Cluster assembly kinetics and fluc- tuations drive polar nucleation of active polymers by L. Huber, T. Krüger, E. Frey . . . . .	155
2	Robustness of the Vicsek ordering paradigm . . . . .	171
2.1	Background . . . . .	171
2.2	Revisiting the kinetic approach for the Vicsek model . . . . .	171
2.3	Kinetic Boltzmann ansatz for generic alignment models . . . .	176
2.3.1	Restricted Vicsek alignment . . . . .	179
2.3.2	Refined Vicsek collision noise . . . . .	183
2.3.3	Variable alignment rules . . . . .	184
2.4	Criticality of collective order . . . . .	186
2.5	Lateral stability of collective order . . . . .	188
2.5.1	Homogeneous polar order revisited . . . . .	188
2.5.2	Onset of polar patterns . . . . .	191

<i>Contents</i>	xvii
2.6 Agent-based simulations . . . . .	195
2.7 Summary and outlook . . . . .	198
<b>IV Conclusion</b>	<b>201</b>
1 Discussion . . . . .	201
2 Outlook . . . . .	204
3 Future perspectives . . . . .	205
<b>Bibliography</b>	<b>209</b>
<b>Acknowledgements</b>	<b>227</b>



*He said, in effect, that everything should be as simple as it can be, but not simpler.*

— Roger Sessions on Albert Einstein, NEW YORK TIMES

# I Introduction to active systems

One of the most exciting and challenging fields of biological physics is the study of *living matter*. It attempts to tackle a central question of science - *What is life?* or rather *What distinguishes life from inanimate matter?* - using physical concepts and methods. While it is certainly true that life relies on the ability to create order and patterns out of disorder, little is known about generic principles how this self-organization is achieved. Matter at thermal equilibrium, in particular large ensembles of interacting constituents, may already form ordered systems and can be fully described by a few ingredients like conservation of energy and symmetries in the statistical limit. As a result, such systems can be macroscopically described by phases such as, for instance, liquids, solids, or ferromagnets which are separated by corresponding phase transitions between them. Individual units of living systems, on the other hand, are inherently out of equilibrium and not bound by global energy conservation: their key feature is the ability to generate forces or stresses on their environment, for instance by locally converting (ambient) energy into mechanical work. In general, remarkable features of interacting ensembles of such *active* subunits is the ability to self-organize, and to produce emergent properties on large scales. Describing such systems is commonly referred to as *active matter physics*, which is still a relatively young research field. A central example is that of active motion or self-propelled particles: objects which move with an intrinsic velocity, and, depending on their type of interaction, give rise to collective phenomena. However, only few of these aspects have been studied and a clear picture of the mechanisms of self-organization in these systems is largely elusive. In the following we will present some important examples of active matter from natural systems and experiments, as well as seminal theoretical studies that attempt to explain the observed phenomena. From this, we formulate a set of research questions, which we will address subsequently in this thesis.

## 1 Experimental motivation

Active matter is omnipresent in nature and biological systems. On macroscopic scales, a variety of ecological setups and phenomena can be viewed as active systems, such as animal swarming and migration [18, 19, 57]. These examples are particularly fascinating because it is hard to grasp how such large communities, like flocks of birds, insect swarms or fish schools, are coordinated to such precision

that they behave as a uniform collective, which exhibits very different, *emergent* properties as compared to a single individual. There are countless examples of collective behavior in the animal kingdom, and also several man-made ones, like traffic congestion [58] or human crowds [59]. Also on microscopical scales, active systems are ubiquitous in biology and range from the active, intracellular mechanics of the actomyosin cytoskeleton [32] or the mitotic spindle [60], to the collective motion of bacteria or cells, and the emergence of order in tissues and cell communities (see also Ref. [18] for a list of research examples). This shows that emergent phenomena of active systems are an essential motif in biology to create complex structures out of simpler constituents. Apart from these naturally occurring examples, there is a growing range of artificial systems or experiments that exhibit similar phenomena. These include reconstituted biological systems such as actin and microtubule gliding assays [21, 22, 25, 61, 62], which yield the formation of large-scale dynamic patterns due to active motion generated by nucleoside-triphosphate-consuming motor proteins. Similar phenomena of self-organization due to intrinsic propulsion can be found in colloidal particle systems which are fueled by chemical gradients [63] or electromagnetic interactions [23], or even mechanically-driven discs [20, 64] or robotic agents [65]. With this vast range of different active agents and emergent phenomena, much research is devoted to identify a basic set of principles and mechanisms that describe many of these systems. This aim gave rise to a large collection of theoretical work of active matter, which successfully reproduce collective phenomena using simplified model assumptions and which we will briefly discuss below. However given the sometimes daunting complexity of agents and their 'micro-structure' in active systems (e.g. for animals), this reductionist approach, which is very successful in equilibrium, non-living systems, has to be treated with caution in nonequilibrium systems as there is no insuring physical law that justifies that this method works. In this thesis we will therefore address a basic question here: *Do details matter, and if so, to which extent?*

## 2 Theoretical picture

*How does order emerge in active systems?* - Within the last decades, much research, especially from theoreticians, was devoted to approach the basic mechanisms of collective motion and self-organization in active matter. In his seminal study, Vicsek and coworkers suggested a paradigmatic model of aligning particles in two dimensions to understand the onset of flocking [49] using a simple update rule, according to which particles increase order locally by aligning their direction of motion (collision), and decrease order locally by angular diffusional noise (see introduction of chapter II, Fig. II.2, and Eqs. (II.2) for details). It was observed that such

systems experience a continuous transition from random, isotropic gas, to a phase of collective motion and global order by increasing the particle density (Fig. I.1), or by decreasing noise [49, 66, 67]. In many subsequent and detailed studies of large systems [41, 45], it was shown that this transition is, at onset, accompanied with a phase separation into disordered regions and dense, ordered regions, rendering the transition to be in fact discontinuous. These dense regions, with particles being oriented in the same 'polar' direction, take the shape of large density waves or polar flocks. By further increasing the particle density or decreasing noise, a homogeneously polar state is recovered. Furthermore, Chaté and co-workers showed that the Vicsek model admits true long-range polar order in a two-dimensional setup [45], proving that the famous Mermin-Wagner theorem [68] is violated for active, nonequilibrium systems. Subsequently, we will refer to this phase space behavior as *Vicsek Ordering Paradigm* (VOP) and elaborate more subtle details in chapter III. Using a different, top-down approach lending symmetry arguments from liquid crystals, Toner and Tu postulated a set of hydrodynamic equations to describe the onset of polar order for active 'liquids' [50, 69]. As in the Vicsek model, the corresponding solutions experience a transition to collective motion at the homogeneous level which is unstable close to the onset, but with subtle differences concerning the inhomogeneous structure owing to missing microscopic details. To fill this gap between a microscopic and a macroscopic description, Bertin

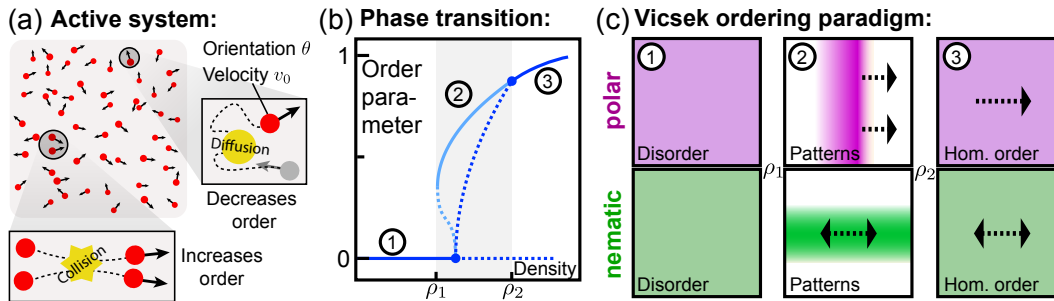


**Figure I.1** (a) System of actively propelled particles subject to diffusion and alignment interactions. (b) Generic phase diagram of the Vicsek ordering paradigm (VOP) and onset of collective order: at density  $\rho_1$ , the order parameter of the system bifurcates continuously towards a homogeneous ordered state at  $\rho_1$  (dark blue), and discontinuously towards spatial patterns (light blue). Beyond  $\rho_2$ , patterns vanish again. Solid lines: stable solutions; dashed lines; unstable ones. (c) Illustration of the density fields corresponding to different states in (b) (numbered by 1,2,3), for a polar collision rule (purple) and a nematic collision rule (green), respectively.

and Marchetti independently developed analytical frameworks to circumvent the stochastic and discrete nature of the agent-based Vicsek model, and introduced mesoscopic approximations based on a kinetic Boltzmann ansatz [42, 52, 54] and

Fokker-Planck equations [51, 70–72], respectively; recently, it was also proven that both approaches are equivalent [73]. While these theories are formally based on single-particle properties, they come at the cost of neglecting all local correlations, fluctuations, or multi-particle interactions. For dilute systems, these theories describe the evolution of the (mean-field) particle density in space and orientation, which is subject to advection, diffusion, and local, binary particle interactions. Including the latter marks the crucial step in the approximation, translating the Vicsek collision rule - local polar alignment with noise - to a field of particles. Upon increasing the particle density or decreasing noise in these mesoscopic models, one observes both the formation of polar density waves at the onset of collective motion, as well as a homogeneous polar state further away from the onset [51, 54, 55]. At the onset of order, a set of hydrodynamic equations can be derived, which reconciles the microscopic features of the Vicsek model with the macroscopic behavior of the Toner-Tu equations [50, 69], with deviations on the level of spatial gradients. Remarkably, the polar wave patterns that emerge in these field theories closely resemble the patterns from experiments in actin gliding assays [21] or colloidal suspensions [23], at least on a phenomenological level.

In addition to active matter with a polar alignment symmetry, many experimental systems experience a *nematic* interaction symmetry, that is, the constituent particles align along a common axis instead of the mean particle orientation, for instance by steric repulsion. Very analogously to the polar case, the above procedures can be repeated using a nematic alignment rule, in agent-based simulations [74–77] as well as in mean-field theories [52, 72, 78]: again, a continuous transition from disorder towards a – now nematically-ordered – homogeneous phase is found, while at the onset of order, inhomogeneous patterns emerge [76]. Here, the systems phase-separate into dilute, disordered regions, and dense ‘trails’ of nematic order, with particles streaming along both directions of a trail. As in the polar case, similar nematic patterns have been observed in experiments [24, 25]. On large scales, these trails are subject to chaotic dynamics due to orientational instabilities [78, 79].

For these both modes of alignment, a whole plethora of agent-based models have been developed recently [36, 44, 80–85], all sharing an ordering paradigm similar to Vicsek case (VOP) and spatial patterns, despite their different footing: upon changing the balance between local ordering and local decorrelation, large-scale order emerges from a disordered gas, with inhomogeneous patterns emerging at the onset.

It is hence very tempting to subdivide all these active systems into 1) a polar universality class, and 2) a nematic universality class. In equilibrium physics, universality provides a powerful framework to classify phase transitions *ad hoc* [29, 30]. In this picture, the underlying mechanisms are universal and depend only on symmetry, with all other microscopic specificities becoming effectively negligible. Or in simple words, to take up on the question from the previous section, *details*

*don't matter*. While it was suggested that this universality principle may also hold for nonequilibrium systems like active matter [18, 19, 53, 57, 86], a proof is lacking.

Apart from these model systems and questions on which we will focus throughout this thesis, it should be mentioned that these topics represent only a small part in the zoo of active matter research. Other systems include:

- additional constraints on the dynamics, like the conservation of particle momentum and the coupling to a hydrodynamic field. This is then commonly referred to as *wet* active systems [19].
- particle densities close to full packing or incompressible fluids, where density fluctuations become negligible and topological defects appear, accompanied with a *active turbulence* at low Reynolds numbers [19, 86].
- particle interactions without alignment, but with repulsive forces, leading to macroscopic clusters and *motility-induced phase separation* [87, 88].

### 3 Open questions

While universality would provide an elegant formalism to simplify theories of active matter systems, several doubts should be raised whether this principle is really applicable. Reflecting living active systems, which are much more complicated than simplified experimental systems and theoretical models, insensitive ordering (polar or nematic) may not necessarily be desirable - in fact, some biological systems require to be malleable and inherently adaptive, that is, to rearrange their intrinsic order with respect to minuscule stimuli, or even to be flexible enough to produce different types of order simultaneously. Phenomenological examples would be, for instance, the switching from uni- to bidirectional collective motion in ant colonies [89, 90], or the multiple orderings and functionalities of cytoskeletal actin [31, 32] or epithelial cells [33, 34]. In this context, drastic and physiologically costly control mechanisms on the microscopic scale would be required to overcome the robustness of universal ordering.

On more general grounds, while the theories presented above have produced large-scale statistical properties and spatial patterns similar to experiments and agent-based approaches, the concern arises whether this result came at the cost of potentially over-simplifying assumptions on the particle level. This aspect includes for example, the specific details of Vicsek-like alignment rules and the negligence of correlations in mean-field theories. Furthermore, a rigorous picture of the relevant microscopic processes that lead to global order or specific patterns, is lacking. Without previous knowledge, the following properties on the level of constituent particles may, in general, affect the collective effects and self-organization:

- **Particle motion:** this includes the type of motion, that is, if this is a continuous [36] or a discrete process [40], its symmetry [78], memory effects [25, 91], and the degree and type of noise or stochasticity [45, 66, 67].
- **Particle shape:** point- or disc-like objects move and interact in a different fashion [36, 56] than elongated or deformable objects like polymers [21]; asymmetric particles may also break chirality of motion [92, 93].
- **Particle interaction:** this aspect is the essential ingredient for collective effects, but it depends very specifically on model details; it may be point-like [42] or over a predefined 'neighborhood' [49], comprise a discrete update rule or a process continuous in time and space. Alignment or anti-alignment may be gradual or complete [36, 56], randomness may play a role or not. All of which depends, in general, on the particles shape, position, and orientation.
- **Correlations between particles:** due to collisions, particles become correlated in position and orientation, with increasing entanglement between successive collisions. In many field theories, these correlations are neglected at the lowest levels [42, 70].
- **Environment:** boundaries of active systems or dislocations may constrain collective effects or even trigger them [64, 94], leading to complicated phenomena at the interfaces [95].

Despite some case studies, the way how these microscopic diversities affect the global properties and dynamics of an active system is, in general, widely unexplored. In this thesis, we want to assess a few of these aspects and their impact on the emergence of order and pattern formation, by refining some particle properties with respect to observations from real experimental systems.

In chapter II, we investigate the effect of different particle symmetries: motivated by *in vitro* experiments with the bacterial cell division protein FtsZ [6], we show that asymmetric active particles perform a chiral motion which self-organize into a new mode of chiral patterns on the collective scale (section 1). For pattern formation in the paradigmatic actomyosin gliding assay [21], we study the effect of continuously varying the interaction symmetry of aligning particle collisions in experiment and theory. To this end, we introduce a computational model that faithfully resolves the dynamics of **Weakly-Aligned, Self-propelled Polymers (WASP)** from microscopic up to macroscopic scales. We find the emergence of a new active matter state - the three-phase coexistence of polar, nematic, and disordered regions - which is not compatible with simple universality arguments (section 2).

In chapter III, we examine how the transition towards order depends on the microscopic dynamics and local correlations of the active objects. In particular, we will heavily focus on a specific ordering transition, the formation of polar order from a disordered isotropic system. Section 1 elaborates how kinetic processes on the particle level generate the ordering transition and shows that the dynamics of intermediate size clusters is essential to understand the nonlinear properties of polar phase separation, using the WASP simulation paradigm and a phenomenological kinetic model. In section 2, we address the robustness of Vicsek-type phase transitions and the associated ordering paradigm (VOP) for generic alignment models, by using the analytical framework of the kinetic Boltzmann ansatz at mesoscopic scales [52]. We find that the key feature of the proclaimed polar universality class - the continuous transition from disorder to polar order - breaks down over a wide range of realistic alignment assumptions, giving rise to a variety of new bifurcation scenarios including a discontinuous transition between disorder and a stable, uniformly polar state. Subsequently, we detail how some of these features affect self-organization in agent-based simulations.



*Symétrie, en ce qu'on voit d'une vue, fondée sur ce qu'il n'y a pas de raison de faire autrement.*  
— Blaise Pascal

## II Emergence of symmetries, collective order and pattern formation

The physical properties of a self-propelled particle are inherently anisotropic. Regardless of shape and surrounding, such an object possesses an orientation, which is typically the direction in which it moves. For two-dimensional systems, on which we focus in this thesis, the orientation is described by an angle  $\theta(t)$  or equivalently by a vector  $\mathbf{u}(t) = (\cos \theta(t), \sin \theta(t))^T$  (Fig. II.1(a)). In general, this orientation may be subject to stochastic fluctuations from a surrounding thermal bath, internal variations, or scattering from heterogeneities or dislocations of the environment. Such a random process may be continuous or discrete, with vectorial noise  $\delta\boldsymbol{\eta}(t)$  on the level of  $\mathbf{u}(t)$  or with scalar noise  $\delta\xi(t)$  on the direction  $\theta(t)$ , effectively resulting in a diffusion process for the orientation. This describes a persistent

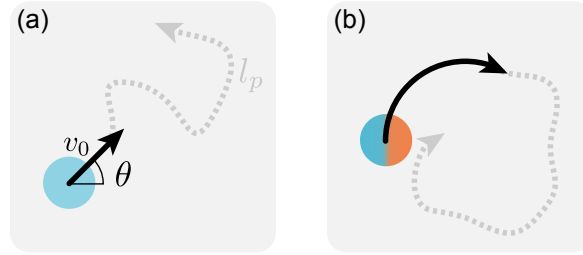


**Figure II.1** Schematic of active particles with preferentially straight motion (a) and simultaneous motion and rotation (b), resulting in a curved trajectory.  $v_0$  is the velocity amplitude and  $\theta$  the direction. The rotational part of propulsion may for example be driven by particle asymmetries (double coloring in (b)). Furthermore, fluctuations alter the deterministic motion, resulting in a persistent random walk with some finite persistence length  $l_p$  (gray trajectories).

random walk of the individual active particles (so-called *active Brownian particles*), in contrast to a simple random walk of passive particles. Its properties are set by the random fluctuations: for instance, consider a white noise  $\delta\xi(t)$  with  $\langle \delta\xi(t) \rangle = 0$  and  $\langle \delta\xi(t)\delta\xi(t') \rangle = 2/\alpha\delta(t-t')$  with some constant  $\alpha$ , and the particle dynamics given by

$$\begin{aligned}\dot{\mathbf{r}}(t) &= v_0(\cos \theta(t), \sin \theta(t))^T, \\ \dot{\theta}(t) &= \delta\xi(t).\end{aligned}\tag{II.1}$$

Then the mean squared displacement of the particle position is given by  $\langle (\mathbf{r}(t) - \mathbf{r}(0))^2 \rangle = 2v_0^2 \alpha t (1 - \frac{\alpha}{t} (1 - \exp(-t/\alpha)))$ . For  $t \ll \alpha$  the particle moves ballistically with  $\langle (\mathbf{r}(t) - \mathbf{r}(0))^2 \rangle \approx v_0^2 t^2$ , and for  $t \gg \alpha$  it behaves diffusive like  $\langle (\mathbf{r}(t) - \mathbf{r}(0))^2 \rangle \approx 2v_0^2 \alpha t$ . Importantly, this defines the persistence of the active motion and describes the decorrelation of single particles with  $\langle \mathbf{u}(t) \mathbf{u}(t') \rangle = \exp(-|t - t'|/\alpha)$  with the persistence time  $\alpha$  and the persistence length  $l_p = \alpha v_0$ . This analysis is equivalent to other random processes due to the central limit theorem, and requires only finite fluctuations (i.e. no diverging moments of the corresponding distribution). For a system of interacting particles, collective effects will only appear when the time between successive interactions is smaller or comparable with correlation time; otherwise, the system will effectively behave like a thermal gas. Note that so far we have assumed that the particles move, if not perturbed by noise, straight-ahead. This is plausible for simple objects which are symmetric with respect to their orientational axis, like isotropic discs or elongated rods. If this is not the case, then the evolution of the orientation may be subject to additional stresses like persistent rotation (Fig. II.1(b)). In section 1, we will investigate the effects of a broken particle symmetry.

The second important ingredient for the emergence of order in active systems are alignment interactions. They 'propagate' the orientation of a particle to its environment, and subsequently, allow for collective order to emerge. While these interactions may be arbitrarily complicated in general, symmetry arguments suggest that only a few distinct directions are important. When only the orientations or the motion of particles are considered, these are their average direction (the polar direction) and their average nematic axis (composed of equal amounts of the polar and the anti-polar direction), which represent the two lowest modes of spherical harmonics. In this context, the alignment interaction, or collision, is a process that tries to locally project the orientations of individuals onto these common directors (Fig. II.2). This is quite analogous to equilibrium systems of interacting spins, like the XY model [96]. This conjecture may be more complicated when additional cues like spatial arrangements, different collision impact parameters, or a variable amount of collision partners are relevant. A very simple example of alignment along these two modes are at the core of the Vicsek update rules [49, 77]:

$$\theta_i^{t+1} = \arg \left[ \sum_{j \in \mathcal{N}} g(\theta_j^t, \theta_i^t) \right] + \delta \xi_i^t$$

$$g(\theta_j^t, \theta_i^t) = \begin{cases} \exp(i\theta_j^t) & \text{for polar alignment} \\ \text{sign}[\cos(\theta_j^t - \theta_i^t)] \exp(i\theta_j^t) & \text{for nematic alignment} \end{cases} \quad (\text{II.2})$$

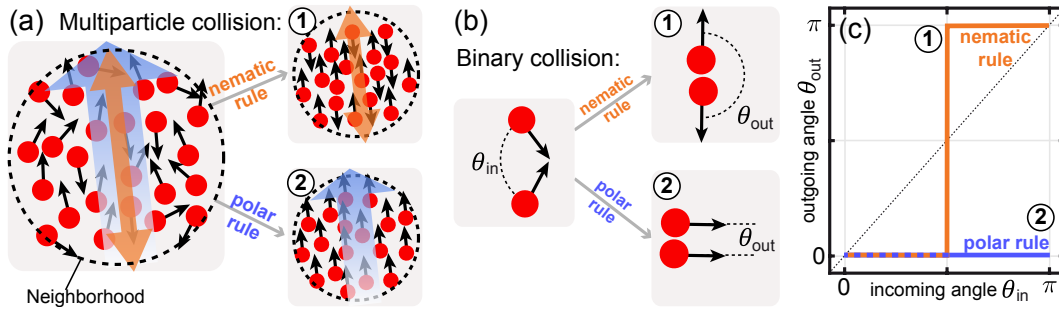


**Figure II.2** (a) Illustration of Vicsek alignment rules between multiple particle directions (black arrows) along the common direction (blue arrow) and the common nematic axis (orange arrow). For multiple collision partners, this is the average direction. This form is also extendible for the limiting case of binary (i.e. two-particle) interactions (b), where the reference angle is just the direction of the collision partner. (c) Vicsek response curve of pre-alignment angles  $\theta_{in}$  and post-alignment angles  $\theta_{out}$ , relative to a reference direction. (1) depicts a nematic rule, (2) a polar rule, respectively.

where  $\theta_i^t$  denotes the orientation of particle  $i$  at time  $t$ ,  $\mathcal{N}$  the averaging 'neighborhood',  $\arg$  the argument of a complex number, and  $\delta\xi_i^t$  the angular noise. The effect of these rules is illustrated in Fig. II.2. It should be noted that, separately, these two rules represent extremely simplified cases: 1) alignment is either completely polar or completely nematic, and not gradual (Fig. II.2(c)); 2) stochastic fluctuations during a collision does not depend on any orientation; 3) the interaction is discrete and nonlocal; 4) spatial extensions of particles or their arrangements do not matter. In experiments or agent-based simulations with continuous dynamics and local interactions, this is (typically) different: In particular, alignment is a strictly local process upon particle contact for many realistic systems, with pairwise contributions (Fig. II.2(b)), and microscopic correlations. In addition, the alignment symmetry may neither be perfectly polar or perfectly nematic, but rather have both contributions to different extent. In section 2, we examine the influence of this mixed interaction symmetry.

# 1 Chiral particle motion

In this section, we present the details of the analysis of an active system with chiral particle motion. In particular, we focus on how active motion of constituents along chiral, that is, clockwise (or anti-clockwise) trajectories affects the collective behavior. In the following, we present a biological, intra-cellular example of such a system, which we approach by using two complementary theoretical approaches. Both consistently predict chiral pattern formation at the onset of order, reminiscent of experimental patterns. A compact version of the results presented below was recently published in the journal *Physical Review Letters* (see section 1.6).

## 1.1 Ring formation of curved FtsZ filaments *in vitro* as a precursor to bacterial cell division

The bacterial cell division is a prominent example of intracellular self-organization and is orchestrated by a plethora of different protein machineries [97]. A vital part of this process is driven by the formation of the contractile Z-ring along the equator of the bacterial cell membrane, which marks the future site of cell division and forms the septum that invaginates the mother cell (Fig. II.3(a)). The Z-ring itself is not a continuous structure, but consists of many overlapping protofilaments of the protein FtsZ, which are attached to the cell membrane by anchoring proteins like FtsA and ZipA [98–100]. Surprisingly, lateral interactions or related motor proteins that would crosslink these filaments are absent [2, 3] - yet, the Z-ring appears very localized. Recent experiments *in vitro* showed that FtsZ filaments are, in fact, not straight polymers, but have an intrinsically curved conformation, possibly depending on the nucleotide state [4, 5]. In addition, FtsZ, which is a tubulin homologue, forms polar filaments with an asymmetric polymerization process: upon hydrolysis of ambient guanosine triphosphate (GTP), FtsZ preferentially assembles protein monomers at one end, and disassembles at the other end, performing so-called treadmilling dynamics [5]. Loose and Mitchison performed experiments of the reconstituted system using a flat membrane [6] (Fig. II.3(b)): being attached to the two-dimensional substrate, they observed that FtsZ polymers effectively become self-propelled due to treadmilling, and that they move along clockwise trajectories due to the filament curvature (Fig. II.3(c)). Because of the intra-molecule geometry of the membrane anchoring with respect to FtsZ curvature, all filaments exhibit the same chirality. For an intermediate interval of filament coverage on their substrate, the authors observed the formation of dense ring-like structures which – though arguably – resemble the structure of the bacterial Z-ring.

These observations suggest that the FtsZ assay represents a new type of active matter system, in which the constituent particles perform a chiral motion. In the following, we present a complementary theoretical ansatz to model this active

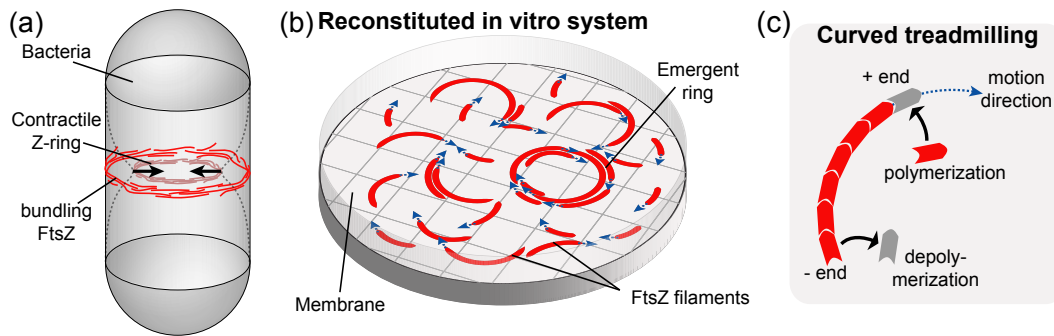


**Figure 11.3** (a) Illustration of the bacterial division ring (red filaments) which forms along the cell equator and eventually invaginates the mother cell. (b) *in vitro* experiment of Loose and Mitchison [6]. They observed the emergence of localized ring structures on a flat membrane. (c) Treadmilling dynamics of an anchored and curved FtsZ filament (red segments). The + end marks the site of preferential recruitment of FtsZ monomers or oligomers, the – end the site of preferential disassembly, respectively. This cyclic process consumes GTP as a fuel.

system from both microscopic and mesoscopic scales, respectively. In section 1.2 we emulate FtsZ filaments as extended polymers using Brownian dynamics simulations. On more general grounds we introduce a kinetic Boltzmann approach for chiral active particles (section 1.3). Both methods predict the emergence of localized ring structures or swirling vortices for intermediate filament densities, even in the absence of any adhesive forces, which is in agreement with more recent experiments [7]. The analysis also yields a new set of hydrodynamic equations for an active chiral liquid (section 1.4), which represents an interesting generalization of the famous complex Ginzburg-Landau equation [101]. The analysis presented in sections 1.2, 1.3, and 1.3 condensed to a recent publication in *Physical Review Letters*, which is reprinted in below.

## 1.2 Agent-based simulation of self-propelled, curved polymers

### 1.2.1 Model definitions

In their experiments, Loose and Mitchison observed that FtsZ polymers undergo depolymerization and polymerization processes leading to an effective translation in the direction of the polymers' backbones. In our agent-based approach we focused on these two main aspects of the microscopic physics: first, active particles are modelled as semiflexible polymers with an intrinsic curvature and second, they are translated into the polar direction of the polymer tip, while its tail is not actively advected. Stochastic fluctuations may still be present due to the complex

environment of the anchoring on the membrane, for which we assume uncorrelated white noise that diffuses and undulates the polymers.

Therefore, our agent-based model is primarily given by the equilibrium dynamics of a system of  $M$  polymers within on a two-dimensional surface of area  $A$ , with periodic boundary conditions. Each polymer is described as an inextensible worm-like chain [102, 103] of length  $L$ , persistence length  $\ell_p$ , and intrinsic curvature  $\kappa_0$ . For a given polymer conformation  $\mathbf{r}(s)$ , parameterized in terms of arc length  $s$ , the overall bending energy is given by

$$E_{\text{bend}} = \frac{1}{2} \ell_p k_B T \int_0^L ds [\kappa(s) - \kappa_0]^2, \quad (\text{II.3})$$

where  $\kappa(s) = |\partial_s^2 \mathbf{r}(s)|$  denotes the local curvature. To assure motion of the filament contour on a circular track (apart from noise), polymers are propelled with a tangential velocity  $\mathbf{v}_0(s) = v_0 \partial_s \mathbf{r}(s)$ . This accounts for the effective motion of treadmilling in a simplified fashion, without considering fluctuations of the polymer lengths. Note that for this choice of tangential motion, the area explored by a circling polymer is primarily given by the curvature radius of the polymer, and motion perpendicular to the polymer contour is purely diffusive. In the free draining limit, the dynamics of the polymer system is then determined by a set of coupled Langevin equations for the contours  $\mathbf{r}^{(m)}(t, s)$  of each polymer  $m=1, 2, \dots, M$ :

$$\zeta (\partial_t \mathbf{r}^{(m)}(s) - \mathbf{v}_0^{(m)}(s)) = - \frac{\delta E[\{\mathbf{r}^{(n)}\}]}{\delta \mathbf{r}^{(m)}(s)} + \boldsymbol{\eta}^{(m)}(s), \quad (\text{II.4})$$

balancing viscous friction with elastic and repulsive forces generated by the total energy  $E$  and Langevin noise  $\boldsymbol{\eta}$  with zero mean and  $\langle \boldsymbol{\eta}(t, s) \cdot \boldsymbol{\eta}(t', s') \rangle = 4k_B T \zeta \delta(t - t') \delta(s - s')$ . Here total energy  $E$  consists of all contributing bending energies and an additional, purely repulsive excluded volume interaction between adjacent contour points, which will be further specified below. Note how Eqs. (II.3), (II.4) break the chiral symmetry of motion: for every non-zero  $\kappa_0$ , filaments are preferentially curved. And due to the propulsion mechanism along the polymer backbone, the filament trajectories are, at least on average, chiral as well. We will further focus on the regime where the persistence length  $\ell_p$  is comparable or larger than the curvature radius,  $\ell_p \gtrsim 1/\kappa_0$ .

### 1.2.2 Implementation

To numerically solve these polymer dynamics in Eq. (II.4), we use a bead-spring model [104, 105] that comprises the following discretization scheme: a polymer of length  $L$  is subdivided into  $N$  beads at positions  $\mathbf{r}_i = (x_i, y_i)^T$  ( $i = 1, 2, \dots, N$ ), with  $N - 1$  bonds of length  $a$ ; the (normalized) bond vectors are given by  $\partial_s \mathbf{r} \approx \frac{\mathbf{r}_{i+1} - \mathbf{r}_i}{a} =:$

$\hat{\mathbf{t}}_i$ ; the bending angle between two adjacent bonds is given by  $\theta_i = \arccos(\hat{\mathbf{t}}_{i+1} \cdot \hat{\mathbf{t}}_i)$ . The discretized bending energy corresponding to the continuous version defined in Eq. (II.3) reads

$$E_{bend} = \frac{\ell_p}{2a} k_B T \sum_{i=1}^{N-2} (\theta_i - \theta_0)^2. \quad (\text{II.5})$$

where  $\theta_0 \approx a\kappa_0$  is the spontaneous bending angle. Note that we omitted the superscript polymer index  $m$  for brevity. While the contour length in the continuous description is inextensible by definition  $|\partial_s \mathbf{r}(s)| \equiv 1$ , in the bead-spring model one requires an additional energy term to enforce length conservation on average. This is achieved by connecting neighboring beads by stiff harmonic springs. The corresponding stretching energy is given by

$$E_{stretch} = \frac{k}{2} \sum_{i=1}^{N-1} (|\mathbf{r}_{i+1} - \mathbf{r}_i| - a)^2. \quad (\text{II.6})$$

In the simulations, the spring constant  $k$  is chosen larger than all other force constants to account for the fact that biopolymers are nearly inextensible; As a consequence, stretching modes relax fast compared to other dynamic processes. At the same time,  $k$  cannot be chosen arbitrarily large as this would strongly limit the maximal simulation time  $T_{max}$  (see below for values).

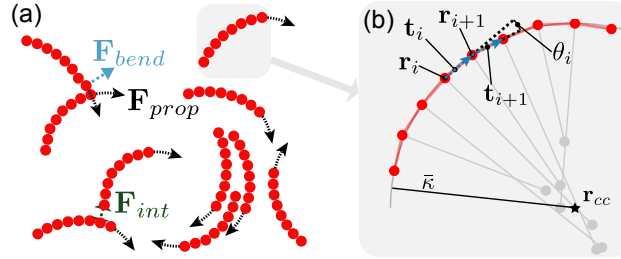


**Figure II.4** (a) Illustration of a system of semiflexible, self-propelled polymers in the bead-spring representation, which are subject to microscopic forces from intra-particle stress (bending, propulsion) and inter-particle stress (repulsion). (b) Close-up of a single filament and its discretized geometry: each contour point represents a bead (red circle) at position  $\mathbf{r}_i$  which is connected to its neighbor bead by the normalized contour vector  $\mathbf{t}_i$  (blue arrows). The preferential curvature results in nonzero average bending angles  $\theta_i$ . The curvature center  $\mathbf{r}_{cc}$  of a polymer is given as the average of all curvature centers along the contour (depicted by gray circles).

In the two-dimensional system of  $M$  polymers (Fig. II.4(a)), we assume steric repulsion between adjacent polymer segments  $\mathbf{r}_i^{(m)}$  ( $m = 1, 2, \dots, M$ ). As an

interaction potential we use a truncated Lennard-Jones potential [106–108]

$$(E_{int})_{ij}^{(mn)} = \epsilon \left[ \left( \frac{a}{r_{ij}^{(mn)}} \right)^{12} - \left( \frac{a}{r_{ij}^{(mn)}} \right)^6 \right] \Theta(a - r_{ij}^{(mn)}), \quad (11.7)$$

with  $r_{ij}^{(mn)} = |\mathbf{r}_i^{(m)} - \mathbf{r}_j^{(n)}|$ ,  $\epsilon$  the potential strength, and  $\Theta(r)$  the Heaviside step function. At distances smaller than the bond length  $a$ , the potential is strongly repulsive. In the Langevin description, the equation of motion is given by a force balance between elastic, active, thermal and dissipative terms. For the  $i$ -th bead of a polymer, the equation of motion reads

$$\begin{aligned} \zeta \partial_t \mathbf{r}_i &= -\frac{\delta E}{\delta \mathbf{r}_i} + \mathbf{F}_i^{prop} + \boldsymbol{\eta}_i \\ &= \mathbf{F}_i^{bend} + \mathbf{F}_i^{stretch} + \mathbf{F}_i^{int} + \mathbf{F}_i^{prop} + \boldsymbol{\eta}_i \end{aligned} \quad (11.8)$$

where  $E = E_{bend} + E_{stretch} + E_{int}$ ,  $\mathbf{F}_{prop}$  is the propulsive force and the amplitude of the thermal forces is given by  $\langle \boldsymbol{\eta}_i(t) \cdot \boldsymbol{\eta}_j(t') \rangle = 4k_B T \zeta \delta_{ij} \delta(t - t')$ . The bending, stretching and interaction forces  $\mathbf{F}_i^{bend}$ ,  $\mathbf{F}_i^{stretch}$ ,  $\mathbf{F}_i^{int}$  are obtained by variation of the corresponding energetic terms with respect to the position vector  $\mathbf{r}_i$  [104, 105]. We employ the following implementation of the tangential propulsive force  $\mathbf{F}^{prop} = \zeta v_0 \partial_s \mathbf{r}$ :

$$\mathbf{F}_i^{prop} = \zeta v_0 \begin{cases} \hat{\mathbf{t}}_1 & i = 1 \\ (\hat{\mathbf{t}}_{i-1} + \hat{\mathbf{t}}_i)/2 & 1 < i < N \\ \hat{\mathbf{t}}_{N-1} & i = N \end{cases} \quad (11.9)$$

For the integration of Eq. (11.8) we use an Euler-Maruyama iteration scheme [109] with sufficiently small time steps  $\Delta = 0.0001\tau$  with the unit time  $\tau = \zeta a^2 / (k_B T)$ . In our simulations, we used the following set of parameters:  $L = 9a$ ,  $\ell_p = 100a$ ,  $k = 500k_B T / a^2$ ,  $\epsilon = 1k_B T$ ,  $\theta_0 = 0.2$ ,  $\zeta = 1$  and a periodic system of area  $A = 60a \times 60a$  (such that it can contain many consecutive polymer lengths). The unit of length is set to  $a = 100 \text{ nm}$ , such that  $L = 0.9 \mu\text{m}$ ,  $\ell_p = 10 \mu\text{m}$  are roughly similar to FtsZ filaments. In the subsequent analysis, we focus on a typical paradigm of control parameters in active matter - the competition between noise and density (as a precursor for increasing order by collisions). The relevant dimensionless parameters that characterize the system are the reduced noise  $\sigma$  and density  $\rho$ . Here,  $\sigma := k_B T \ell_p / (\zeta v_0 L^2)$  relates thermal forces at length scale  $\ell_p$  with friction forces, and  $\rho := (R_0/b)^2$  denotes the squared ratio of the radius of curvature  $R_0 = \kappa_0^{-1}$  to the mean polymer distance  $b = \sqrt{A/M}$ .

### 1.2.3 Emergence of rotating rings

For dilute systems,  $\rho \ll 1$ , our simulations show that each polymer is propelled on a circular path and collisions between polymers are infrequent; likewise, for large noise  $\sigma$  the tendency to decorrelate dominates, and no collective order emerges (see Fig. II.5(a)). Upon increasing  $\rho$  or lowering  $\sigma$ , we observe that a significant fraction of filaments begin to collide, order, and collect into localized vortex structures (*vortex state*). These ring-like structures are highly dynamic. They assemble and persist for several rotations, during which their centers of mass remain relatively static; see Fig. II.5(b). Despite our simplified kinetic assumption, the phenomenology of rotating rings resembles the FtsZ patterns observed by Loose and Mitchison [6], including vortex assembly, disassembly and localization. In the dense regime,  $\rho \gtrsim 1$ , where each polymer is likely to collide, these vortices are unstable. Instead, the polymers cluster and form jammed 'trains' that travel through the system in an irregular fashion; see Fig. II.5(c).

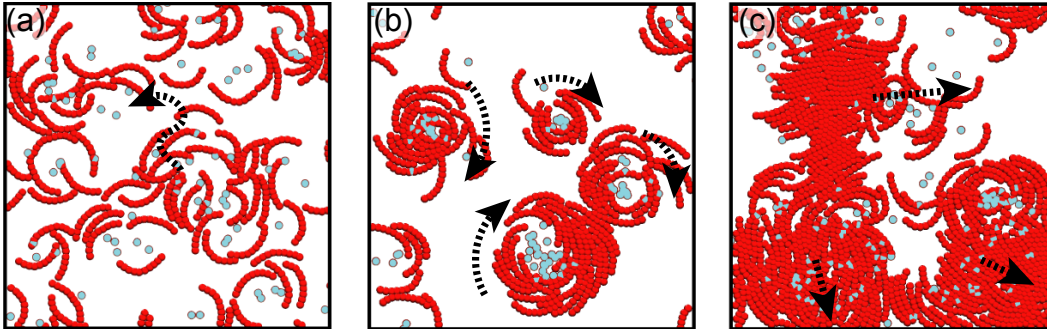


**Figure II.5** System snapshots depicting (a) disorder ( $\rho=0.556$ ,  $\sigma=0.987$ ), (b) vortices ( $\rho=0.556$ ,  $\sigma=0.247$ ) and (c) trains ( $\rho=1.389$ ,  $\sigma=0.247$ ). Dashed arrows illustrate the dynamics of patterns, which is persistently rotating only for (b); for (a) motion is disordered and for (c) it is turbulent. Blue dots depict the curvature centers of individual polymers.

In order to quantitatively distinguish between the various observed patterns and organize them into a 'phase diagram' we consider the pair correlation function  $g(d_{cc})$  [110, 111] of distances  $d_{cc} = |\mathbf{r}_{cc}^{(m)} - \mathbf{r}_{cc}^{(n)}|$ . The positions  $\mathbf{r}_{cc}^{(m)}$  are the curvature centers of each polymer, generated by averaging over the local curvature and all bead positions on a contour (see Fig. II.4(b)). In contrast to the positions  $\mathbf{r}^{(m)}$ , the curvature centers do not oscillate due to self-propulsion and hence represent a more stable measure of particle position. Figure II.6(a) displays the contour of  $g(d_{cc})$  for parameters  $k_B T = 1$  and  $v_0 = 5$  (i.e.  $\sigma = 0.247$ ). For sufficiently small  $\rho$ , the density exhibits a local minimum at  $d_{cc}^{min}$ , the diameter of a vortex. This implies that there is a preferred vortex size and structure connected to the distance  $d_{cc}^{min}$ . These minima were determined after applying a Gaussian filter to suppress

random fluctuation artefacts and then used to distinguish the observed patterns according to the following 'phase' criteria: We regard a system as *disordered* if  $g(d_{cc})$  exhibits a minimum at a distance  $d_{cc}^{\min}$  equal to the diameter of a free circular path,  $d_{cc}^{\min} \approx 2R_0$ . This is distinct from *vortex states*, where  $d_{cc}^{\min}$ , defining an effective vortex diameter, is larger than  $2R_0$ . Finally, for *train states*,  $g(d_{cc})$  does not exhibit a local minimum, indicating the absence of an isolated vortex structure (Fig. II.6(b)).

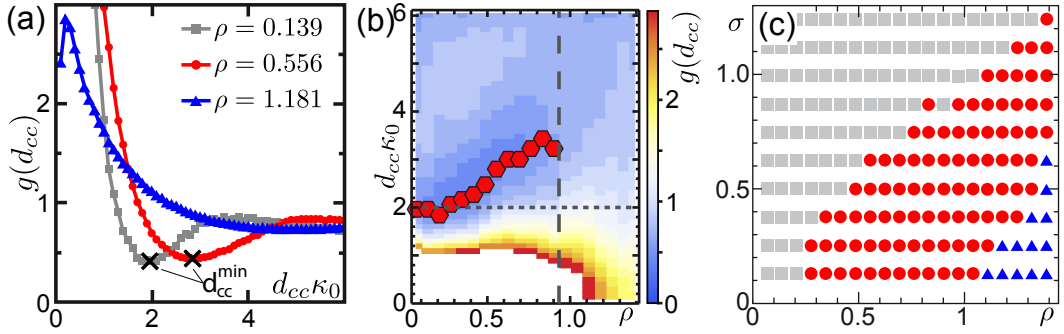


**Figure II.6** (a) Pair correlation function  $g(d_{cc})$  for the three different states with  $\sigma=0.247$  and  $\rho$  indicated in the graph. (b) Corresponding heat map of the pair correlation function for varying densities  $\rho$ . Red polygons denote the positions of  $d_{cc}^{\min}$ . The short dashed line depicts the free polymer radius and the long dashed line marks the regime where  $d_{cc}^{\min}$  vanishes. (c) Phase portrait for varying density  $\rho$  and noise  $\sigma$ : *disorder* states (gray rectangles), *vortex* states (red circles), *train* states (blue triangles).

To determine the macroscopic behavior for varying  $\sigma$  and  $\rho$ , the noise strength  $\sigma = k_B T \ell_p / (\zeta v_0 L^2)$  was varied as follows: we changed the temperature scale in the interval  $k_B T \in [0, 1]$  for  $v_0 = 5$ , and for  $k_B T = 1$  varied  $v_0$  in the range  $v_0 \in [1, 5]$ . The maximal simulation times  $T_{max}$  for all simulations were chosen such that the single polymer rotation time  $\tau_R = 2\pi / (\kappa_0 v_0)$  is much smaller. We took  $T_{max} > 400\tau_R$  and  $T_{max} > 700\tau$  for our data to provide a sufficiently large sampling interval for both convective and diffusive motion. To consolidate the results, data were recorded for 10 independent simulations for each given set of parameters. The ensuing 'phase diagram' is shown in Fig. II.6(c). As in other active systems [19, 45, 49, 54, 76, 112–114], pattern formation is favored by increasing density and decreasing noise strength. Jammed states prevail only when density is high and noise level low.

Note also that the structure of the phase diagram depends on the ratio of filament length  $L$  to radius of curvature  $R_0$ . Polymers with an arc angle close to  $\kappa_0 L = 2\pi$  (closed circles) retain mostly a single-circle structure and do not form large collective structures upon increasing  $\rho$  (Fig. II.7(a)). Conversely, reducing

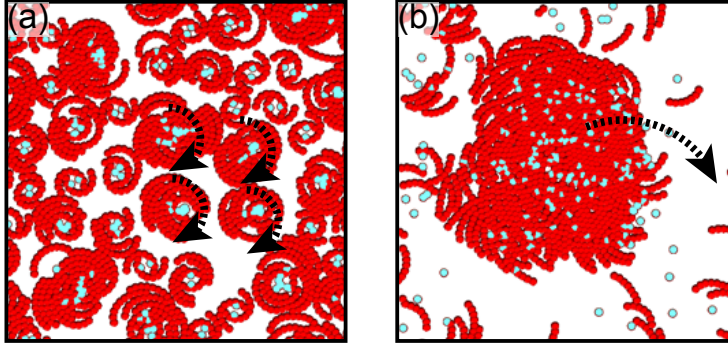


**Figure II.7** System snapshots depicting (a) compact individual circles ( $\rho=1.389$ ,  $\sigma=0$ ,  $\kappa_0 L=0.95\pi$ ) and (b) swirling patches ( $\rho=1.389$ ,  $\sigma=0.247$ ,  $\kappa_0 L=0.4\pi$ ). Green dashed arrows illustrate the dynamics of patterns.

$\kappa_0 L$  suppresses the formation of closed ring structures, due to inefficient alignment of short polymers. Instead, these polymers cluster into flocks which move on approximately circular paths (Fig. II.7(b)). Hence, we conclude that the range of arc angles of FtsZ polymers,  $\kappa_0 L \approx 0.6\pi$ , observed *in vitro* [6], facilitates the formation of closed polymer rings particularly well (Fig. II.5(b)).

In summary, closed polymer rings require explicit curvature and filament lengths larger than a certain threshold value. For other interactions than local, steric repulsion ring structures may also emerge [25, 115, 116]; straight, rotating rods may form vortex arrays but not closed rings [92].

## 1.3 Kinetic Boltzmann ansatz with curved particles

### 1.3.1 Model definitions

The results from section 1.2 demonstrate how the active FtsZ system enables the formation of dynamic rings, by explicitly considering the microscopic structure of the constituent polymers. An apparent disadvantage of this approach is the numerical limitation of system sizes due to the local complexity, restricting the ability to make statements about the generic large-scale behavior of these systems. To circumvent this, we employed a different approach for the mesoscopic limit of vanishing particle extension, using a kinetic Boltzmann ansatz for active particles [42, 52, 54, 55, 78, 117, 118]. This approach allows us to determine the collective behavior and the corresponding phase transitions, irrespective of (most of) the microscopic details of the constituent particles. In detail, we simplified the active system to one consisting of spherical particles (of diameter  $d$ ) that move on clockwise trajectories with a constant velocity  $v_0$  on circling radius  $\kappa_0^{-1} = R_0$ , which accounts for both self-propulsion and spontaneous curvature (Fig. II.8(a)). We further assume that a particle's orientation is altered by 'self-diffusion' as well as by local

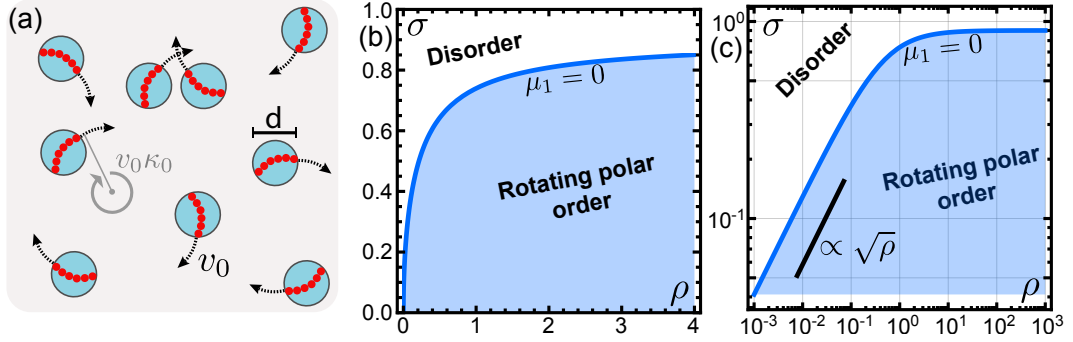


**Figure II.8** (a) Illustration of point-like chiral particles in the Boltzmann approach. The cycling frequency is given by  $v_0 \kappa_0$ . (b,c) Phase diagram in (b) linear and (c) double-logarithmic  $\rho$ - $\sigma$  space with the line  $\mu_1 = 0$  defining the onset of collective motion.

binary collisions. For self-diffusion, a particle's instantaneous orientation  $\theta$  changes at rate  $\lambda$  into  $\theta + \eta$ , where we assume  $\eta$  to be Gaussian-distributed with standard deviation  $\sigma$ . At the core of the Boltzmann approach is the behavior of particle collisions, in particular, the binary collisions of two particles: in the Brownian dynamics simulations in section 1.2, it was observed that colliding filaments tend to align in the same direction, for which their respective circling trajectories become synchronized. We therefore model, as in other particle-based active systems [54, 55, 119], binary collisions by a polar alignment rule where the orientations of the collision partners align along their average angle plus a Gaussian-distributed fluctuation<sup>1</sup>; for simplicity, we take the same noise amplitude  $\sigma$  as for self-diffusion. The kinetic Boltzmann equation [42, 52, 54, 55, 78, 117, 118] for the one-particle distribution function  $f(\mathbf{r}, \theta, t)$  then reads

$$\partial_t f + v_0 [\mathbf{e}_\theta \cdot \partial_{\mathbf{r}} + \kappa_0 \partial_\theta] f = \mathcal{I}_d[f] + \mathcal{I}_c[f, f]. \quad (\text{II.10})$$

It describes the dynamics of the density of particles in a phase-space element  $d\mathbf{r} d\theta$  which is being convected due to particle self-propulsion, and which undergoes rotational diffusion and binary particle collisions, as given by the angular self-diffusion

<sup>1</sup> It should be noted that this particular choice of alignment represents the limiting case of a polar Vicsek rule with only two collision partners, which will be discussed in more detail in Chapter III.

$\mathcal{I}_d[f]$  and the collision integral  $\mathcal{I}_c[f, f]$ , respectively:

$$\mathcal{I}_d[f] = \lambda \left\langle \int_{-\pi}^{\pi} d\phi f(\phi) [\delta(\theta - \phi - \eta) - \delta(\theta - \phi)] \right\rangle_{\eta}, \quad (\text{II.11})$$

$$\begin{aligned} \mathcal{I}_c[f, f] = & \left\langle \int_{-\pi}^{\pi} d\phi_1 \int_{-\pi}^{\pi} d\phi_2 \mathcal{S}(|\phi_1 - \phi_2|) f(\phi_1) f(\phi_2) \right. \\ & \left. \times [\delta(\theta - \frac{1}{2}(\phi_1 + \phi_2) - \eta) - \delta(\theta - \phi_1)] \right\rangle_{\eta}, \end{aligned} \quad (\text{II.12})$$

where  $\mathcal{S}(\psi) = 4d\nu_0 |\sin(\frac{\psi}{2})|$  is the scattering cross section for spherical particles of diameter  $d$  in two dimensions as detailed in Ref. [54]. The collision integral represents ferromagnetic alignment of two particles with orientation  $\phi_1$  and  $\phi_2$  along their average angle  $\theta = \frac{1}{2}(\phi_1 + \phi_2)$ . The brackets  $\langle \dots \rangle_{\eta}$  denote an averaging over a Gaussian-distributed noise variable  $\eta$ . To obtain a dimensionless form we used the rescaling

$$\begin{aligned} t & \rightarrow t \cdot \lambda^{-1}, \\ \mathbf{x} & \rightarrow \mathbf{x} \cdot \nu_0 \lambda^{-1}, \\ f & \rightarrow f \cdot \rho_0, \\ \kappa_0 & \rightarrow \kappa_0 \cdot \nu_0 \lambda^{-1}, \end{aligned}$$

with  $\rho_0 = \lambda/(d\nu_0)$ . Measuring time, space and density in units of  $\lambda^{-1}$ ,  $\nu_0 \lambda^{-1}$ , and  $\rho_0$ , respectively, allows us to set  $d = \lambda = \nu_0 = 1$  which we will use in the following. Then, the only remaining free parameters are the noise amplitude  $\sigma$ ,  $\kappa_0$ , and the mean particle density  $\bar{\rho} = A^{-1} \int_A d\mathbf{r} \int_{-\pi}^{\pi} d\theta f(\mathbf{r}, \theta, t)$  measured in units of  $\lambda/(d\nu_0)$ , i.e. the number of particles found within the area traversed by a particle between successive self-diffusion events. Note the critical difference of Eq. (II.10) to field theories for straight-moving particles [50, 51, 54, 72]: there is an additional angular derivative  $\nu_0 \kappa_0 \partial_{\theta}$  in the convection term, which reflects the fact that the particles are moving on circular orbits.

The kinetic Boltzmann equation (II.10) requires several remarks about the underlying assumption: first, only collisions between two particles are considered and higher-order interactions are neglected. Thus, this represents a *dilute limit* approximation which may or may not be realistic for the full active system. Second, particle collisions are point interactions and any correlations between particles after collisions are neglected (commonly referred to as molecular chaos). While this allows us to factorize the many-body density function in terms of the single particle density  $(\mathbf{r}, \theta, t)$ , and makes Eq. (II.10) analytically tractable, this severe assumption may

not represent the microscopic reality of active systems, where local correlations may be omnipresent.

### 1.3.2 Spectral analysis

To identify possible solutions of the Boltzmann equation and analyze their stability, we performed a Fourier transformation. Upon expanding the one-particle distribution function in terms of Fourier modes of the angular variable,  $f_k(\mathbf{r}, t) = \int_{-\pi}^{\pi} d\theta e^{i\theta k} f(\mathbf{r}, \theta, t)$ , one obtains

$$\begin{aligned} \partial_t f_k + \frac{v_0}{2} \left[ \partial_x (f_{k+1} + f_{k-1}) - i \partial_y (f_{k+1} - f_{k-1}) \right] - ik v_0 \kappa_0 f_k \\ = -\lambda (1 - e^{-(k\sigma)^2/2}) f_k + \sum_{n=-\infty}^{\infty} \mathcal{I}_{n,k} f_n f_{k-n}, \end{aligned} \quad (\text{II.13})$$

where explicit expressions for the collision kernels  $\mathcal{I}_{n,k}(\sigma)$  are given by

$$\mathcal{I}_{n,k} = \int_{-\pi}^{\pi} \frac{d\Phi}{2\pi} \mathcal{S}(|\Phi|) \left[ \hat{P}_k \cos(\Phi(n - k/2)) - \cos(\Phi n) \right]. \quad (\text{II.14})$$

Here  $\hat{P}_k = e^{-(k\sigma)^2/2}$  is the Fourier transform of the Gaussian noise with standard deviation  $\sigma$ . For  $k=0$ , Eq. (II.13) yields the continuity equation  $\partial_t \rho = -\nabla \cdot \mathbf{j}$  for the local density  $\rho(\mathbf{r}, t) := f_0(\mathbf{r}, t)$  with the particle current given by  $\mathbf{j}(\mathbf{r}, t) = v_0 (\text{Re } f_1, \text{Im } f_1)^T$ . In general, Eq. (II.13) constitutes an infinite hierarchy of equations that couples lower with higher order Fourier modes. In section 1.4 we will introduce an appropriate truncation scheme to reduce the dynamic to the dominant Fourier modes  $f_k$ . Since  $\mathcal{I}_{n,0}=0$  for all  $n$ , a state with spatially homogeneous density  $\bar{\rho}=f_0$  and all higher Fourier modes vanishing is a stationary solution to Eq. (II.13) (*disordered state*). To linear order, the dynamics of small perturbations  $\delta f_k$  with respect to this uniform state is in general given by  $\partial_t \delta f_k = \mu_k(\bar{\rho}, \sigma) \delta f_k$ , where  $\mu_k(\bar{\rho}, \sigma) = (\mathcal{I}_{0,k} + \mathcal{I}_{k,k}) \bar{\rho} - \lambda (1 - e^{-(k\sigma)^2/2})$ . For a polar collision rule as considered here, only  $\mu_1$  can become positive, and a critical density  $\rho_c(\sigma) := \frac{\pi \lambda (1 - e^{-\sigma^2/2})}{4(2e^{-\sigma^2/2} - 4/3)}$  can be defined at  $\mu_1(\rho_c, \sigma) = 0$ . For small  $\sigma$ , this density behaves as  $\rho_c \propto \sigma^2$  and diverges for  $\sigma \rightarrow (-2 \log \frac{2}{3})^{1/2} \approx 0.9$  (Fig. II.8(b,c)).

### 1.3.3 Weakly nonlinear analysis

Far above threshold of order, simple lowest-order closure relations of Eq. (II.13) may not be appropriate in general. We therefore proceeded by numerically calculating the spatially homogeneous solutions for all angular Fourier modes  $f_k$  below some

Fourier mode  $K$ . For given values of  $\bar{\rho}$  and  $\sigma$  and a desired accuracy  $\varepsilon$  of this mode truncation scheme, the cutoff is chosen such that  $|f_{K+1}| < \varepsilon$ . We find that for  $\bar{\rho} < \rho_c(\sigma)$  a spatially homogeneous state where all modes but  $f_0$  vanish is the only stable state. In contrast, above threshold ( $\bar{\rho} > \rho_c(\sigma)$ ) there is a second solution for which  $|f_1| > 0$ . It corresponds to a polar ordered state whose orientation is changing periodically in time with frequency  $v_0 \kappa_0$ . Note that the homogeneous version of Eq. (II.13) (neglecting all gradient terms) is invariant under a phase shift  $f_k \rightarrow f_k e^{ikv_0 \kappa_0 t}$ . Choosing the orientation of the polar order at  $t = 0$  to be aligned along the  $x$ -axis, Eq. (II.13) is solved by  $f_k = |f_k| e^{ikv_0 \kappa_0 t}$  with the time and space independent amplitude  $|f_k|$ , which is then determined by:

$$0 = \lambda(\hat{P}_k - 1)|f_k| + \sum_{n=-\infty}^{\infty} \mathcal{I}_{n,k} |f_n| |f_{k-n}|. \quad (\text{II.15})$$

This equation is identical to the stationary homogeneous Boltzmann equation for straight-moving particles, that is, with vanishing  $\kappa_0 = 0$  [54]. To proceed, we truncated the infinite sum in Eq. (II.15) at  $K$  and calculated the solution of all  $|f_k|$  with  $|k| \leq K$ . Fig. II.9(a) depicts the solution for the amplitude  $|f_1|$  as compared to the solution of the generalized Ginzburg-Landau equation (see section 1.4) as well as the direct numerical solutions of Eq.(II.10) obtained by SNAKE algorithm (see section 1.3.4). For decreasing noise  $\sigma$  or increasing density  $\bar{\rho}$  an increasing number of Fourier modes starts to grow (Fig. II.9). In our numerical calculations we typically included 30 – 50 Fourier modes.

In a second step, we considered wave-like perturbations of the spatially homogeneous oscillatory solution in a co-rotating frame,  $\delta f_k(\mathbf{r}, t) \sim \delta f_{k,\mathbf{q}} e^{i\mathbf{q}\cdot\mathbf{r}}$  with wave-vector  $\mathbf{q}$ .  $\delta f_{k,\mathbf{q}}$  is in general a complex amplitude assumed to be small. Periodic boundary conditions impose  $|\mathbf{q}| = n \frac{2\pi}{L}$ ,  $n \in \mathbb{Z}$ , where  $L = \sqrt{A}$  and  $A$  is the area of the (quadratic) system. With the substitution  $f_k = (|f_k| + \delta f_k) e^{ikv_0 \kappa_0 t}$  the linear system for  $\delta f_k$  then reads

$$\begin{aligned} \partial_t \delta f_k = & -\frac{v_0}{2} (\nabla \delta f_{k-1} + \nabla^* \delta f_{k+1}) + \lambda(\hat{P}_k - 1) \delta f_k \\ & + \sum_{n=-\infty}^{\infty} (\mathcal{I}_{n,k} + \mathcal{I}_{k-n,k}) |f_{k-n}| \delta f_n. \end{aligned} \quad (\text{II.16})$$

where  $\nabla := \partial_x + i\partial_y$ . Analogous to Eq. (II.15) we performed a coordinate transformation to a frame that rotates with angular frequency  $\kappa_0$  such that  $\nabla \rightarrow e^{ikv_0 \kappa_0 t} \nabla$ . To eliminate the gradient terms, we performed a Fourier transform on Eq. (II.16) which yields  $\nabla \rightarrow i\mathbf{q}$  and  $\nabla^* \rightarrow -i\mathbf{q}$  with the wave vector  $\mathbf{q} = (q_x, q_y)^T$ . Further

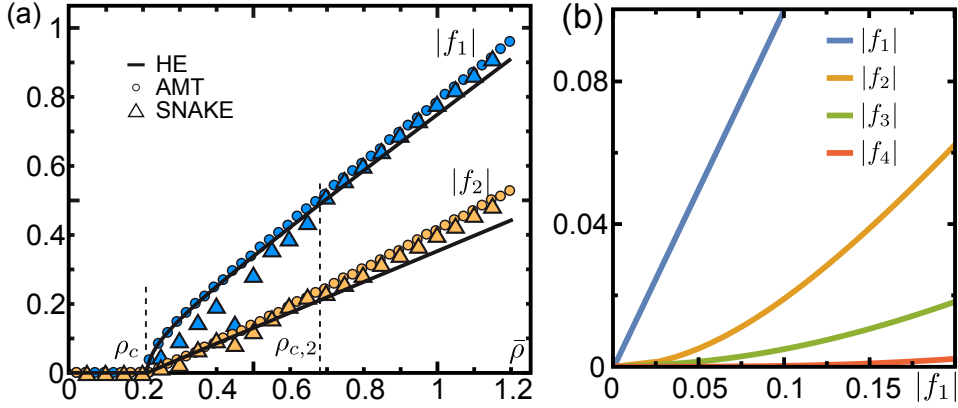


**Figure II.9** (a) Homogeneous solution for  $f_1$  (blue) and  $f_2$  (yellow) for  $\sigma = 0.5$  obtained from the adapted mode truncation scheme (AMT) in Eq. (II.15), the hydrodynamic equations Eqs. (II.20) (HE) from section 1.4, and the SNAKE algorithm from section 1.3.4. Note that within  $\rho_c$  and  $\rho_{c,2}$  (dashed vertical lines), the SNAKE algorithm yields swirl states and hence the corresponding mode values do not represent homogeneous states. (b) Solutions for the first modes as a function of  $|f_1|$  obtained from the AMT and that exhibit nonlinear scaling of higher modes.

we rewrite Eq. (II.16) in the matrix notation

$$\partial_t \delta \mathbf{f} = \Gamma(\mathbf{q}) \delta \mathbf{f} \quad (\text{II.17})$$

where  $\delta \mathbf{f} := (\delta f_0, \delta f_1, \delta f_2, \dots, \delta f_K)^T$  and  $\Gamma(\mathbf{q})$  is the Jacobian of Eq. (II.16) in Fourier space. Let  $S_k$  be an eigenvalue and  $\boldsymbol{\eta}_k$  be an eigenvector of  $\Gamma(\mathbf{q})$ , then the evolution of the perturbation for small times  $t$  can be described by

$$\delta \mathbf{f}(t) = \sum_k \boldsymbol{\eta}_k (\delta \mathbf{f}(0) \cdot \boldsymbol{\eta}_k) \exp[S_k t] \sim \exp[S(\mathbf{q})t] \quad (\text{II.18})$$

with the dispersion  $S(\mathbf{q}) = \max\{S_0(\mathbf{q}), S_1(\mathbf{q}), S_2(\mathbf{q}) \dots S_K(\mathbf{q})\}$  being the maximal eigenvalue of the Jacobian, because all terms with smaller  $S_k$  are exponentially suppressed and hence not relevant for the stationary state. In agreement to previous results [54], we found that the growth rate is maximal for  $\mathbf{q}$  parallel to the particle current. Thus we replaced, without loss of generality,  $S(\mathbf{q}) = S(q)$  where  $q$  is the parallel component of  $\mathbf{q}$ . We solved Eq. (II.16) for the maximal (real) part of an eigenvalue  $S_k$  and got the growth rate  $S(q)$  as a function of the wave number in the rotating frame (see Fig. II.10(a)). The dispersion relation  $S(q)$  exhibits a band of unstable modes, with the maximal growth rate taken over all wave numbers  $S_{\max}$  decreasing as one moves away from the threshold  $\rho_c$ . The contour plot of  $S_{\max}$  as a function of  $\bar{\rho}$  and  $\sigma$  yields the phase diagram (Fig. II.10(b)). Interestingly, there is a lobe-like regime in parameter space where  $S(q) < 0$ , and hence a homogeneously

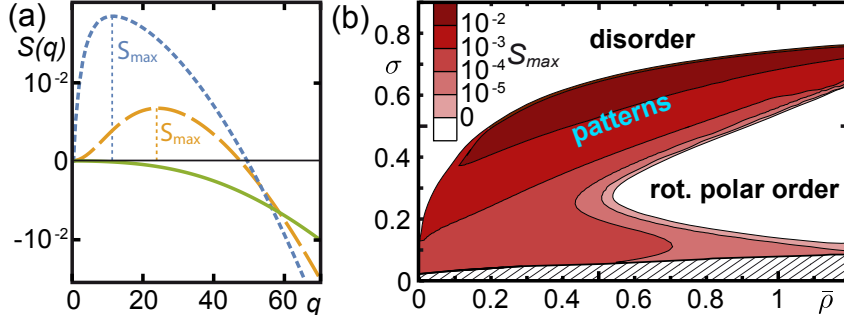


**Figure II.10** (a) Dispersion relation of  $S(q)$  ( $q$  in units of  $2\pi/\sqrt{A}$ ) for  $\bar{\rho}=0.8$  and  $\sigma=0.7$  (short dashed line),  $\sigma=0.6$  (long dashed line) and  $\sigma=0.4$  (solid line). Vertical lines indicate  $S_{max}$ . (b) Phase diagram for density  $\bar{\rho}$  and  $\sigma$  obtained from different growth rates  $S_{max}$  of the homogeneous states with respect to spatial variations  $\delta f_k(\mathbf{r}, t)$ . In the red regions, the homogeneous order is unstable.

polar state with rotating direction is stable. The dashed region in Fig. II.10(b) indicates the regime where we cannot find a nontrivial solution to Eq. (II.15) by neglecting Fourier modes above the chosen  $K = 50$ . We emphasize here that our stability portrait is independent of  $\kappa_0$  and hence equally valid for systems of straight-moving particles.

### 1.3.4 Numerical integration using SNAKE

To determine the spatiotemporal dynamics in the regime where neither a spatially homogeneous state nor a homogeneously polar ordered state are stable, we resort to a modified version of the SNAKE algorithm [55] to numerically solve Eq. (II.10). As tessellations we used a quadratic periodic regular lattice with equally sized angular slices. Circling propulsion was included by rotating the angular distribution of each lattice site with a frequency  $v_0\kappa_0$  in addition to the straight convection steps. The system was initialized with a disordered state with small random density fluctuations around the mean density  $\bar{\rho} = A^{-1} \int_A \rho(\mathbf{r}, t)$ . We used a lattice of  $200 \times 200$  grid points with lattice field size 2 and angular discretization of 24 angular slices; hence,  $A = 400 \times 400 = 160000$ .

SNAKE accurately reproduces the threshold value  $\rho_c(\sigma)$  at which the spatially homogeneous state becomes unstable (Fig. II.11(a)). Above threshold ( $\bar{\rho} > \rho_c$ ) we find that local density fluctuations quickly grow and evolve into stable swirls, that is, disc-like flocks of high density and polar order moving on circular paths; see Fig. II.11(b). These swirl patterns closely resemble the swirling flocks observed in the Brownian dynamics simulations for short polymer arc angles Fig. II.7(a) (section 1.2). In the swirl phase the swirl size grows for growing  $\bar{\rho} - \rho_c$  whereas the radius of a swirl's motion stays at approximately  $\kappa_0^{-1}$ . Fig. II.11(a) shows the

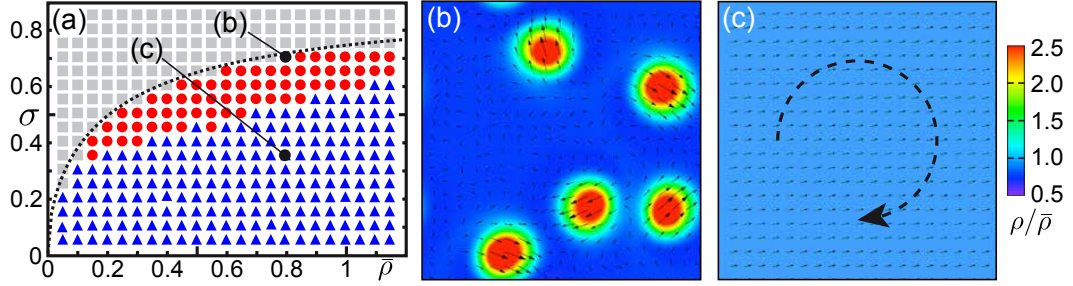


**Figure II.11** (a) Phase diagram obtained from SNAKE simulations. Gray rectangles depict isotropic, disordered states, red circles inhomogeneous vortex solutions, and blue triangles homogeneously ordered rotating states, respectively. The dashed line shows the critical line  $\mu_1 = 0$ . (b) Snapshot of swirl patterns ( $\bar{\rho}=0.8$ ,  $\sigma=0.7$ ). All swirls are moving clockwise on circular paths. (c) Snapshot of homogeneous order ( $\bar{\rho}=0.8$ ,  $\sigma=0.35$ ). The color code denotes the local density, the black arrows the polar field  $(\text{Re}f_1, \text{Im}f_1)^T$ .

parameter values of  $\bar{\rho}$  and  $\sigma$  where the SNAKE algorithm exhibits steady swirl patterns. Changing  $\kappa_0$  did not change the observed patterns qualitatively. In the limiting case of very small  $\kappa$ , we observed traveling wave patterns as reported in Refs. [45, 55, 75].

Moreover, in accordance with the spectral analysis (section 1.3.3), we find a second threshold density, above which the system settles into a homogeneously polar ordered state with a periodically changing orientation (Fig. II.11(c)). The amplitude and frequency of the polar order agree with the numerical results of the spectral analysis to high accuracy (Fig. II.9(a)), while the numerically determined phase boundaries in Fig. II.10(b) differ. The SNAKE algorithm produces stable swirl patterns only in a parameter regime where our linear stability analysis yields significant growth rates. This is mainly due to spurious noise caused by the discretization of the angular variable, which tends to suppress inhomogeneities in the regime of small growth rates. Furthermore, the finite system size constricts the band of possible modes and allows only for patterns of sufficiently short length scales.

## 1.4 Generalized complex Ginzburg-Landau equations

### 1.4.1 Derivation

While the analysis of the SNAKE solutions using the full Boltzmann equation (II.10) and the adaptive mode truncation scheme yield a quantitative comparison of the stability of the emergent nonlinear patterns, an intuitive description of the emergent phenomena is still lacking. In close proximity to the critical density  $\rho_c(\sigma)$  a lowest-order non-linear analysis yields further insights into the dynamics of the system, which was analogously derived for the case of straight-moving particles.

Here we follow Ref. [52, 54] and assume small currents  $f_1 \ll \bar{\rho}$  at onset. Since for the case of polar collisions only  $\mu_1$  can become positive, it is plausible that higher-order Fourier modes of  $f_k$  will not substantially destabilize solutions close to the onset. Still, this is a shaky argument and requires a well-controlled truncation scheme.

In order to get a closed equation for the particle current at onset, we assume small currents  $f_1 \ll \bar{\rho}$  and use the truncation scheme:  $\rho - \bar{\rho} \sim f_1$ ,  $\partial_{x/y} \sim f_1$ ,  $\partial_t \sim f_1$ ,  $f_2 \sim f_1^2$  with vanishing higher modes as presented for polar particles with ferromagnetic interaction in Ref. [52]. We retained only terms up to cubic order in  $f_1$  in the Fourier-transformed Boltzmann equation, Eq. (II.13), for  $k = 1$ . The equation for  $f_1$  then couples to the nematic order field  $f_2$  via a term  $\sim f_1^* f_2$  of order  $f_1^3$ , where the star denotes complex conjugate. Writing down contributions from Eq. (II.13) for  $k = 2$  of quadratic order in  $f_1$  yields an expression for  $f_2$  as a function of  $f_1$ . The expression for  $f_2$  can then be substituted into Eq. (II.13) for  $k = 1$  to obtain a closed equation for  $f_1$ . Together with the continuity equation, the hydrodynamic equations for the density and the particle current read

$$\partial_t \rho = -\frac{1}{2}(\nabla f_1^* + \nabla^* f_1), \quad (\text{II.19})$$

$$\begin{aligned} \partial_t f_1 = & [\alpha(\rho - \rho_c) + i\nu_0 \kappa_0] f_1 - \xi |f_1|^2 f_1 + \nu \nabla^* \nabla f_1 \\ & - \gamma f_1 \nabla^* f_1 - \beta f_1^* \nabla f_1 - \frac{\nu_0}{2} \nabla \rho \end{aligned} \quad (\text{II.20})$$

where again  $\nabla := \partial_x + i\partial_y$ . The coefficients are given by

$$\begin{aligned} \alpha & := (\mathcal{I}_{0,1} + \mathcal{I}_{1,1}), \\ \rho_c & = \frac{\lambda(1 - \hat{P}_1)}{\mathcal{I}_{0,1} + \mathcal{I}_{1,1}}, \\ \nu & := -\frac{1}{4} \frac{1}{\lambda(\hat{P}_2 - 1) + 2i\nu_0 \kappa_0 + (\mathcal{I}_{0,2} + \mathcal{I}_{2,2})\rho}, \\ \xi & := -4(\mathcal{I}_{-1,1} + \mathcal{I}_{2,1})\nu \mathcal{I}_{1,2}, \\ \beta & := 2(\mathcal{I}_{-1,1} + \mathcal{I}_{2,1})\nu, \\ \gamma & := 4\nu \mathcal{I}_{1,2}. \end{aligned} \quad (\text{II.21})$$

We note that the employed truncation scheme implies fast relaxation of the nematic order field  $f_2$  such that  $\partial_t f_2$  is assumed to be negligible on time scales of the dynamics of  $f_1$ . Then  $f_2$  is slaved to  $f_1$  via  $f_2 = -2\nu \nabla f_1 + \gamma f_1^2$ . While this equation shows the same functional dependencies on local density and current as found in systems with straight propulsion [54], the coefficients  $\alpha$ ,  $\xi$ ,  $\nu$ ,  $\gamma$  and  $\beta$  are now *complex-valued*. This can be traced back to the angular convection term in Eq. (II.10), or, equivalently, to the corresponding phase-shift term in Eq. (II.13). As a consequence, the field theory of active systems with particles moving on circular

orbits with defined chirality is generically given by a *complex Ginzburg-Landau (GL) equation with convective spatial coupling* as well as *density-current coupling*. This constitutes a highly interesting generalization of the standard (diffusive) complex GL equations [101, 120], and is qualitatively different to real GL-type equations that were previously applied in the context of self-propelled particles [52].

### 1.4.2 Homogeneous solutions and stability

*Homogeneous isotropic state:*

As for Eq. II.15, a trivial solution of equations (II.20) exists for all parameters which is the homogeneous isotropic state with  $\rho = \bar{\rho}$  and  $f_1 = 0$ . To determine its stability we substitute  $\rho = \bar{\rho} + \delta\rho$  and  $f_1 = \delta f_1$  with the wave-like perturbations of the form

$$\begin{aligned}\delta\rho(\mathbf{r}, t) &\sim \delta\rho_{\mathbf{q}} e^{i\mathbf{q}\cdot\mathbf{r}}, \\ \delta f_1(\mathbf{r}, t) &\sim \delta f_{1,\mathbf{q}} e^{i\mathbf{q}\cdot\mathbf{r}},\end{aligned}\tag{II.22}$$

where  $\delta\rho_{\mathbf{q}}$  and  $\delta f_{1,\mathbf{q}}$  are in general complex amplitudes that are assumed to be small, analogous to the more general variation of  $\delta f_{k,\mathbf{q}}$  in section 1.3.3. The linearized set of equations of motion for the perturbations  $\delta\rho_{\mathbf{q}}(t)$ ,  $\delta f_{1,\mathbf{q}}(t)$  and  $\delta f_{1,\mathbf{q}}^*(t)$  has the characteristic polynomial

$$\begin{aligned}&-q^2\alpha(\bar{\rho} - \rho_c) + q^4\text{Re}[\nu] \\ &+ (2(\alpha(\bar{\rho} - \rho_c) - \text{Re}[\nu]q^2)^2 + 2(v_0\kappa_0 - \text{Im}[\nu]q^2)^2 + q^2) S \\ &+ 4(-\alpha(\bar{\rho} - \rho_c) + \text{Re}[\nu]q^2) S^2 + 2S^3.\end{aligned}\tag{II.23}$$

where  $S$  is the eigenvalue of the linearized set of equations for  $\delta\rho_{\mathbf{q}}(t)$ ,  $\delta f_{1,\mathbf{q}}(t)$  and  $\delta f_{1,\mathbf{q}}^*(t)$ . We note that  $\text{Re}[\nu]$  is positive for all densities. For  $\bar{\rho} < \rho_c$ , all coefficients in Eq. (II.23), including the  $S$ -independent terms are positive, such that Eq. (II.23) only yields  $S$  with negative real part. Thus, the homogeneous isotropic state is linearly stable against inhomogeneous wave-like perturbations, as expected. For  $\bar{\rho} - \rho_c > 0$ , the real part of  $S$  becomes positive where the fastest growing mode is always at  $q = 0$ , meaning that the isotropic state is unstable and that the homogeneous polar order grows fastest (for small deviations).

*Homogeneous oscillatory state*

Above threshold,  $\bar{\rho} > \rho_c(\sigma)$ , the active chiral hydrodynamics described by Eq. (II.20) exhibits a uniform oscillatory solution with  $f_1 = F_1 e^{i\Omega_0 t}$ , i.e. a state in which particles move on a circular (chiral) path with an angular velocity  $\Omega_0 = v_0\kappa_0 - \alpha(\bar{\rho} - \rho_c)\text{Im}[\xi]/\text{Re}[\xi]$ ; and an amplitude  $F_1 = (\alpha(\bar{\rho} - \rho_c)/\text{Re}[\xi])^{1/2}$ . For moderate  $\bar{\rho} - \rho_c$ , this amplitude quantitatively agrees with the result from the numerical mode solver (section 1.3.3)

and SNAKE solutions (section 1.3.4).

To study the stability of the homogeneous oscillatory solution we substitute small perturbations in the basis of the homogeneous oscillating solution:

$$\begin{aligned}\rho &= \bar{\rho} + \delta\rho_{(0)} + F_1 (\delta\rho_{(1)}e^{i\Omega_0 t} + \delta\rho_{(1)}^*e^{-i\Omega_0 t}), \\ f_1 &= F_1 e^{i\Omega_0 t} + \delta f_{(0)} + F_1 (\delta f_{(1)}e^{i\Omega_0 t} + \delta f_{(2)}e^{-i\Omega_0 t}),\end{aligned}\quad (\text{II.24})$$

where the amplitudes  $\delta\rho_{(0)}$ ,  $\delta\rho_{(1)}$ ,  $\delta f_{(0)}$ ,  $\delta f_{(1)}$  and  $\delta f_{(2)}$  are again of the form Eq. (II.22). Truncating at the lowest order of  $(\bar{\rho} - \rho_c)$ , which is  $\sqrt{\alpha(\bar{\rho} - \rho_c)}$ , yields a closed set of linear equations for the amplitudes. The eigenvalue with the largest real part of this linear system determines the growth rate  $S(q)$  of wave-like perturbations. We find that the dispersion relation yields positive  $S(q)$  for finite  $q$  (see Fig II.12(a)). Hence, the oscillatory solution is linearly unstable against finite wavelength perturbations in the current and density fields, in accordance with the more general linear stability analysis presented in section 1.3.3.

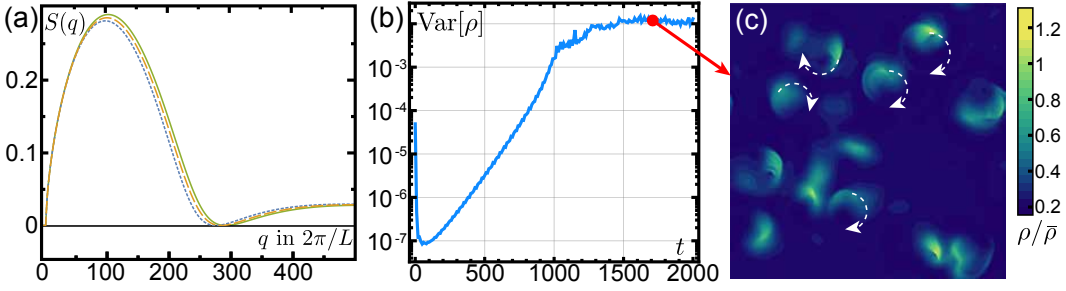


**Figure II.12** (a) Dispersion relations for  $\sigma = 0.6, 0.4$  and  $0.1$  (short-dashed, long-dashed and solid lines, respectively) at  $\bar{\rho} = 0.8$ . (b) Evolution of  $\text{Var}[\rho](t)$ , which is the variance of all densities on the grid to measure density inhomogeneities. As predicted from the stability analysis,  $\text{Var}[\rho](t)$  grows exponentially from some small initial value to some plateau value of fully developed patterns. (c) Snapshot of swirl patterns ( $\bar{\rho} = 0.25, \sigma = 0.5$ ) at time  $t = 1710$ . All swirls are moving clockwise on circular paths.

### 1.4.3 Inhomogeneous solutions

So far, we have only showed that above threshold  $\bar{\rho} > \rho_c(\sigma)$ , all homogeneous solutions of II.20 are unstable, with the system resorting to inhomogeneous solutions. An apparent advantage of the generalized complex GL equations (II.20) is their simple structure, which makes them easy to solve numerically. To this end, we implemented the generalized complex GL equations (II.20) in a numerical program to solve partial differential equations, using the open-source software XMDS2 [121]. Simulating a system with random initial and periodic boundary conditions, a size  $A = 160 \times 160 = 25600$ ,  $\bar{\rho} = 0.25$ ,  $\sigma = 0.5$ , and  $R_0 = 5$  (hence  $\bar{\rho} > \rho_c$ ), yields

the following dynamics (Fig. II.12(b,c)) from an almost isotropic state at early stages, density gradients grow exponentially and eventually yield the formation of dense rotating swirls, which do not become stationary but rather resemble a chaotic rearrangement of patches, which is in very good agreement to the patterns that we observed in the Brownian dynamics simulations (section 1.2.3) or the numerical solutions of SNAKE (section 1.3.4). This apparent active turbulent state is qualitatively distinct from the high-density bands found for straight-moving particles [45, 75] and the vortex field of a fluid coupled to torque dipoles [122, 123].

## 1.5 Particle density and chirality control localized vortices

To summarize the previous sections, we introduced two conceptually different approaches to investigate active systems that include a chiral - or curved - motion of individual particles. Both exhibit a similar self-organization process and collective motion, namely the formation of localized, but highly dynamic rotating rings or vortex swirls. These patterns are very distinct from the case of straight-moving active systems. For the FtsZ system, our analysis yields that the formation of polymer rings requires only active motion and curved trajectories, even in the absence of any adhesive biochemical interactions. Here, the membrane density of filaments serves as a control parameter that could provide a simple and robust pattern-forming mechanism for biological systems. Recent experiments by Ramirez et al. [7], who rigorously tested different anchoring molecules of FtsZ and filament densities, have confirmed this conjecture. Furthermore, recent studies have revealed that active treadmilling is also vital for the bacterial cell division *in vivo* [8–10]. Hence, the treadmilling FtsZ system appears to be equally important for living bacteria, which makes it – arguably – one of the physiologically most relevant examples of a two-dimensional active system. As for the dividing bacteria, further questions remain: most importantly, what is the role of a different system geometry and topology, that is, an approximately cylindrical cell membrane? Given the intrinsic curvature of FtsZ, motion along the (curved) cell equator should again lift the broken chirality. In addition, what is the role of these active dynamics on the cell contraction? While active motion, as a nonequilibrium process, may provide some free energy in the system, the force generation mechanism is unclear and could be, for instance, a fine-tuned orchestration of biochemical reactions, or a collective effect of FtsZ filaments. All these aspects provide enough motivation for future research of active chiral motion, which are, however, outside the scope of this project.

On more general grounds, our analysis yielded a set of hydrodynamic equations (Eq. (II.20)) which represents a new type of a generalized complex Ginzburg-Landau equation with hydrodynamic gradients and coupling to a density field. This augmentation from real-valued coefficients for straight-moving particles to

complex-valued ones for chirally moving particles is important, since it shows that the emerging nonlinear solutions for both cases are qualitatively distinct: this is equivalent to the extension of the real Ginzburg-Landau equation to its complex counterpart [101, 120], which is accompanied by a plethora of unique nonlinear solutions. For the active chiral system, it remains to be shown to which extent different stable solutions exist, since the relevant coefficients are more or less bound by the microscopic details of the constituents.

In addition to the results shown in the previous sections, we have extended the WASP model, developed in section 2.2, to account for curved particle motion. This enables a different comparison of our results with a different agent-based technique, which is capable of simulating systems that are orders of magnitude larger than the Brownian dynamics simulations. Without going into a quantitative comparison of both models, preliminary simulations yield a remarkable agreement with the above analysis and the experimental results of Loose and Mitchison [6] (see Fig. II.13).



**Figure II.13** Self-organization of dynamic rotating ring structures in WASP simulations (section 2.2 for details) with 50 000 curved filaments. Parameters are  $L_p = 31.75L$ ,  $L_{box} = 162.5L$ ,  $\kappa_0 = 0.63/L$ ,  $\varphi_p = 0.225$ ,  $\varphi_n = 0.072$ ,  $t_{max} = 5L_p/v_0$ .

## 1.6 Publication

# Active Curved Polymers Form Vortex Patterns on Membranes

by

J. Denk<sup>\*,1</sup>, L. Huber<sup>\*,1</sup>, E. Reithmann<sup>1</sup>, and E. Frey<sup>1</sup>

<sup>\*</sup>equal contribution,

<sup>1</sup>Department of Physics, Arnold Sommerfeld Center for Theoretical Physics and  
Center for NanoScience, Ludwig-Maximilians-Universität München,  
Theresienstraße 37, 80333 München, Germany

reprinted on pages [35–40](#)

with permission ([CC BY 3.0](#)) from

*Phys. Rev. Lett.* **116**(17), 178301 (2016),

DOI: [10.1103/PhysRevLett.116.178301](https://doi.org/10.1103/PhysRevLett.116.178301),

also available on arXiv:[1602.08976](https://arxiv.org/abs/1602.08976).

© 2016 American Physical Society

Supplemental Material reproduced on pages [41–46](#).





## Active Curved Polymers Form Vortex Patterns on Membranes

Jonas Denk, Lorenz Huber, Emanuel Reithmann, and Erwin Frey\*

Arnold Sommerfeld Center for Theoretical Physics (ASC) and Center for NanoScience (CeNS), Department of Physics, Ludwig-Maximilians-Universität München, Theresienstrasse 37, D-80333 München, Germany

(Received 16 June 2015; revised manuscript received 9 December 2015; published 25 April 2016)

Recent *in vitro* experiments with FtsZ polymers show self-organization into different dynamic patterns, including structures reminiscent of the bacterial Z ring. We model FtsZ polymers as active particles moving along chiral, circular paths by Brownian dynamics simulations and a Boltzmann approach. Our two conceptually different methods point to a generic phase behavior. At intermediate particle densities, we find self-organization into vortex structures including closed rings. Moreover, we show that the dynamics at the onset of pattern formation is described by a generalized complex Ginzburg-Landau equation.

DOI: 10.1103/PhysRevLett.116.178301

Intracellular structuring is often facilitated by the active dynamics of cytoskeletal constituents. The origin of these driven dynamics and their impact on pattern formation has been extensively studied using artificial motility assays of cytoskeletal filaments [1–4]. Another intriguing example of self-organization due to driven filaments was reported recently by Loose and Mitchison [5]. *In vitro*, the bacterial protein FtsZ forms membrane-bound, intrinsically curved polymers. These seem to exhibit treadmilling dynamics (consuming guanosine triphosphate) and, as a result, move clockwise on the membrane. Depending on the protein density, polymers cluster into dynamic structures such as rotating rings or jammed bundles, despite the absence of attractive interactions [6]. These ring structures are of particular interest, since, *in vivo*, FtsZ builds the contractile Z ring which drives cell division in a yet unknown way [7–9]. But also in the *in vitro* experiments, the pattern-forming mechanism remains unclear even on a qualitative level.

Motivated by these experimental findings, we have studied pattern formation in a class of active systems, where particles move on circular tracks and interact only via steric repulsion. To assess the dynamics of this class, we consider two conceptually different models: First, we emulate active particles as elastic polymers with fixed intrinsic curvature that move with a constant tangential velocity [Fig. 1(a)] and perform Brownian dynamics simulations. Second, we employ a kinetic Boltzmann approach, where pointlike particles move on circular paths and undergo diffusion and binary collisions (with polar symmetry) according to a simplified collision rule [Fig. 1(b)]. As a result, we identify different phases of collective behavior as a function of density and noise level. With both approaches, we find flocking into vortex patterns in

the regime of intermediate density and noise strength. Our simulations for extended particles predict the formation of closed ring structures reminiscent of those found in Ref. [5], even in the absence of any attractive interactions. In the mesoscopic limit, our analysis yields that, close to the onset of vortex formation, the dynamics at the onset of ordering is characterized by a novel generalization of the complex Ginzburg-Landau equation.

In our Brownian dynamics simulations, we consider a system of  $M$  curved polymers of the same chirality embedded in a two-dimensional membrane of area  $A$  with periodic boundary conditions. Each polymer is described as an inextensible wormlike chain [10,11] of length  $L$ , persistence length  $\ell_p$ , and intrinsic curvature  $\kappa_0$ . For a given polymer conformation  $\mathbf{r}(s)$ , parameterized in terms of arc length  $s$ , the overall bending energy is given by  $E_{\text{bend}} = \frac{1}{2} \ell_p k_B T \int_0^L ds [\kappa(s) - \kappa_0]^2$ , where  $\kappa(s) = |\partial_s^2 \mathbf{r}(s)|$  denotes the local curvature. Excluded volume interaction is implemented by a repulsive truncated Lennard-Jones potential. To assure motion of the filament contour on a circular track (apart from noise), polymers are propelled with a tangential velocity  $\mathbf{v}_0(s) = v_0 \partial_s \mathbf{r}(s)$ . This accounts for the effective motion of treadmilling in a simplified way [12].

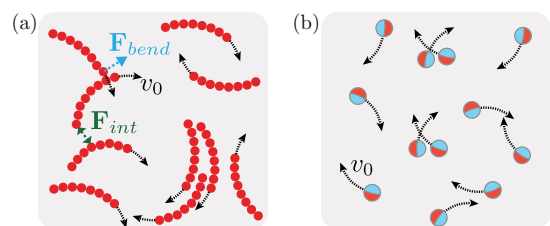


FIG. 1. Systems of active particles, which are driven on chiral, circular tracks with speed  $v_0$ : (a) *Microscopic view*: Extended, elastic polymers with intrinsic curvature, where noise and steric interaction trigger bending of filaments. (b) *Mesoscopic view*: Pointlike particles that undergo diffusion as well as binary collisions.

Published by the American Physical Society under the terms of the *Creative Commons Attribution 3.0 License*. Further distribution of this work must maintain attribution to the author(s) and the published article's title, journal citation, and DOI.

Note that, for this choice, the area explored by a circling polymer is minimal. In the free draining limit, the dynamics of the polymer system is then determined by a set of coupled Langevin equations for the contours  $\mathbf{r}^{(m)}(t, s)$  of each polymer  $m = 1, 2, \dots, M$ :  $\zeta(\partial_t \mathbf{r}^{(m)} - \mathbf{v}_0^{(m)}) = -\delta E[\{\mathbf{r}^{(n)}\}] / \delta \mathbf{r}^{(m)} + \boldsymbol{\eta}^{(m)}$ , balancing viscous friction with elastic and repulsive forces generated by the total energy  $E$  and Langevin noise  $\boldsymbol{\eta}$  with zero mean and  $\langle \boldsymbol{\eta}(t, s) \cdot \boldsymbol{\eta}(t', s') \rangle = 4k_B T \zeta \delta(t - t') \delta(s - s')$ . To numerically solve the polymer dynamics, we employ a bead-spring representation of the polymers [12,17,18]. For most simulations, we adapted length scales close to those observed in Refs. [5,8]:  $\kappa_0^{-1} = 0.5 \mu\text{m}$ ,  $L = 0.9 \mu\text{m}$ , and  $\ell_p = 10 \mu\text{m}$ . The relevant dimensionless parameters that characterize the system are the reduced noise  $\sigma$  and density  $\rho$ . Here,  $\sigma := k_B T \ell_p / (\zeta v_0 L^2)$  relates thermal forces at length scale  $\ell_p$  with friction forces, and  $\rho := (R_0/b)^2$  denotes the squared ratio of the radius of curvature  $R_0 = \kappa_0^{-1}$  to the mean polymer distance  $b = \sqrt{A/M}$ .

For dilute systems  $\rho \ll 1$ , our simulations show that each polymer is propelled on a circular path and collisions between polymers are infrequent; see Fig. 2(a) and Movie 1 in Supplemental Material [12]. The positions of the polymers' centers of curvature (CC)  $\mathbf{r}_{\text{CC}}^{(m)}$  are uncorrelated as in a gas, and we refer to this state as a *disordered state*. On increasing  $\rho$ , we observe that a significant fraction of filaments begin to collide and collect into localized vortex structures (*vortex state*). These ringlike structures are

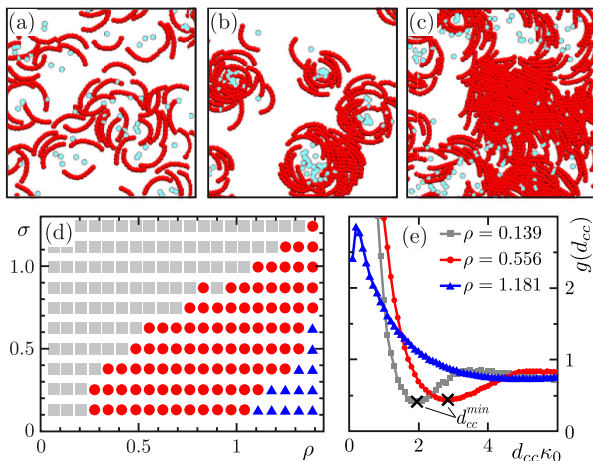


FIG. 2. System snapshots are provided to depict (a) disorder ( $\rho = 0.556$ ,  $\sigma = 0.987$ ), (b) vortices ( $\rho = 0.556$ ,  $\sigma = 0.247$ ), and (c) trains ( $\rho = 1.389$ ,  $\sigma = 0.247$ ). Curvature centers  $\mathbf{r}_{\text{CC}}^{(m)}$  are depicted by light blue dots. (d) Phase portrait for varying density  $\rho$  and noise  $\sigma$ : disorder states (gray rectangles), vortex states (red circles), and train states (blue triangles). (e) Pair correlation function  $g(d_{\text{CC}})$  for the three different states with  $\sigma = 0.247$  and  $\rho$  indicated in the graph.

highly dynamic. They assemble and persist for several rotations, during which their centers of mass remain relatively static; see Fig. 2(b) and Movie 2 [12]. Despite our simplified kinetic assumption, the overall phenomenology resembles the FtsZ patterns observed by Loose and Mitchison [5], including vortex assembly, disassembly, and localization. In the dense regime  $\rho \gtrsim 1$ , where each polymer is likely to collide, these vortices are unstable. Instead, the polymers cluster and form jammed “trains” that travel through the system in an irregular fashion; see Fig. 2(c) and Movie 3 [12].

In order to quantitatively distinguish between the various observed patterns and organize them into a “phase diagram,” we consider the pair correlation function  $g(d_{\text{CC}})$  [19,20] of distances  $d_{\text{CC}} = |\mathbf{r}_{\text{CC}}^{(m)} - \mathbf{r}_{\text{CC}}^{(n)}|$  between the centers of curvature [Fig. 2(d)]. We regard a system as disordered if  $g(d_{\text{CC}})$  exhibits a minimum at a distance  $d_{\text{CC}}^{\text{min}}$  equal to the diameter of a free circular path,  $d_{\text{CC}}^{\text{min}} \approx 2R_0$ . This is distinct from vortex states, where  $d_{\text{CC}}^{\text{min}}$ , defining an effective vortex diameter, is larger than  $2R_0$ . Finally, for train states,  $g(d_{\text{CC}})$  does not exhibit a local minimum, indicating the absence of an isolated vortex structure; for more details, see Supplemental Material [12]. The ensuing phase diagram is shown in Fig. 2(d). As in other active systems [21–28], pattern formation is favored by increasing density and decreasing noise strength. Jammed states prevail only when the density is high and the noise level low. Note also that the structure of the phase diagram depends on the ratio of filament length  $L$  to radius of curvature  $R_0$ . Polymers with an arc angle close to  $\kappa_0 L = 2\pi$  (closed circles) retain a single-circle structure and do not form any collective structures upon increasing  $\rho$  (Movie 4 [12]). Conversely, reducing  $\kappa_0 L$  suppresses the formation of closed ring structures, due to inefficient alignment of short polymers. Instead, these polymers cluster into flocks which move on approximately circular paths (Movie 5 [12]). Hence, we conclude that the range of arc angles of FtsZ polymers,  $\kappa_0 L \approx 0.6\pi$ , observed *in vitro* [5], facilitates the formation of closed polymer rings particularly well [Fig. 2(b)]. In summary, closed polymer rings require explicit curvature and filament lengths larger than a certain threshold value. For other interactions than local, steric repulsion ring structures may also emerge [1,3,29]; straight, rotating rods may form vortex arrays but not closed rings [30].

We complement the Brownian dynamics simulations of active particles that are propelled on circular tracks by considering the mesoscopic limit of a vanishing particle extension. To this end, we have employed a kinetic Boltzmann approach [24,31–36] to determine the collective behavior and the corresponding phase transitions in this limit, irrespective of the microscopic details of the constituent particles. In detail, we simplified the active system to one consisting of spherical particles (of diameter  $d$ ) moving clockwise with constant speed  $v_0$  on circular orbits of radius  $R_0$ . This accounts for both self-propulsion and

spontaneous curvature but neglects the finite extension of the polymers as compared to our Brownian dynamics simulations.

We further assume that a particle's orientation is altered by "self-diffusion" as well as by local binary collisions. In self-diffusion, a particle's instantaneous orientation  $\theta$  changes at rate  $\lambda$  into  $\theta + \eta$ , where we assume  $\eta$  to be Gaussian distributed with standard deviation  $\sigma$ . As in other particle-based active systems [32,34,37], binary collisions are modeled by a polar alignment rule where the orientations of the collision partners align along their average angle plus a Gaussian-distributed fluctuation; for simplicity, we take the same width  $\sigma$  as for self-diffusion.

The kinetic Boltzmann equation [24,31–36] for the one-particle distribution function  $f(\mathbf{r}, \theta, t)$  then reads

$$\partial_t f + v_0[\mathbf{e}_\theta \cdot \partial_{\mathbf{r}} + \kappa_0 \partial_\theta] f = \mathcal{I}_d[f] + \mathcal{I}_c[f, f]. \quad (1)$$

It describes the dynamics of the density of particles in phase-space element  $d\mathbf{r}d\theta$  which is being convected due to particle self-propulsion and which undergoes rotational diffusion and binary particle collisions, as given by the collision integrals  $\mathcal{I}_d[f]$  and  $\mathcal{I}_c[f, f]$ , respectively; for explicit expressions, please see Supplemental Material [12]. Note here the critical difference from field theories for straight-moving particles [32,38–40]; there is an additional angular derivative in the convection term, which reflects the fact that the particles are moving on circular orbits. In the following, we rescale the time, space, and density such that  $v_0 = \lambda = d = 1$ . Then, the only remaining free parameters are the noise amplitude  $\sigma$ ,  $\kappa_0$ , and the mean particle density  $\bar{\rho} = A^{-1} \int_A d\mathbf{r} \int_{-\pi}^{\pi} d\theta f(\mathbf{r}, \theta, t)$  measured in units of  $\lambda/(dv_0)$ , i.e., the number of particles found within the area traversed by a particle between successive self-diffusion events.

To identify possible solutions of the Boltzmann equation and analyze their stability, we performed a spectral analysis. Upon expanding the one-particle distribution function in terms of Fourier modes of the angular variable,  $f_k(\mathbf{r}, t) = \int_{-\pi}^{\pi} d\theta e^{i\theta k} f(\mathbf{r}, \theta, t)$ , one obtains

$$\begin{aligned} \partial_t f_k + \frac{v_0}{2} [\partial_x (f_{k+1} + f_{k-1}) - i\partial_y (f_{k+1} - f_{k-1})] - ikv_0\kappa_0 f_k \\ = -\lambda(1 - e^{-(k\sigma)^2/2}) f_k + \sum_{n=-\infty}^{\infty} \mathcal{I}_{n,k} f_n f_{k-n}, \end{aligned} \quad (2)$$

where explicit expressions for the collision kernels  $\mathcal{I}_{n,k}(\sigma)$  are given in Supplemental Material [12]. For  $k = 0$ , Eq. (2) yields the continuity equation  $\partial_t \rho = -\nabla \cdot \mathbf{j}$  for the local density  $\rho(\mathbf{r}, t) := f_0(\mathbf{r}, t)$  with the particle current given by  $\mathbf{j}(\mathbf{r}, t) = v_0(\text{Re}f_1, \text{Im}f_1)^T$ . In general, Eq. (2) constitutes an infinite hierarchy of equations coupling lower- with higher-order Fourier modes.

A linear stability analysis of Eq. (2) enables further progress. Since  $\mathcal{I}_{n,0} = 0$  for all  $n$ , a state with spatially

homogeneous density  $\bar{\rho} = f_0$  and all higher Fourier modes vanishing is a stationary solution to Eq. (2) (disordered state). To linear order, the dynamics of small perturbations  $\delta f_k$  with respect to this uniform state is given by  $\partial_t \delta f_k = \mu_k(\bar{\rho}, \sigma) \delta f_k$ , where  $\mu_k(\bar{\rho}, \sigma) = (\mathcal{I}_{0,k} + \mathcal{I}_{k,k})\bar{\rho} - \lambda(1 - e^{-(k\sigma)^2/2})$ . For a polar collision rule, as considered here, only  $\mu_1$  can become positive, defining a critical density  $\rho_c(\sigma)$  at  $\mu_1(\rho_c, \sigma) := 0$  [Fig. 3(a)]. Above the threshold ( $\bar{\rho} > \rho_c$ ), the spatially homogeneous state is unstable, the particle current grows exponentially, and collective motion may emerge.

In close proximity to the critical density  $\rho_c(\sigma)$ , a weakly nonlinear analysis yields further insights into the dynamics of the system and the ensuing steady states. Here we follow Ref. [31] and assume small currents  $f_1 \ll 1$  at the onset. Then, balancing of the terms in the continuity equation, the equation for  $f_1$ , and terms involving  $f_1$  in the equation for  $f_2$  implies the scaling  $\rho - \bar{\rho} \sim f_1$ ,  $f_2 \sim f_1^2$  as well as weak spatial and temporal variations  $\partial_{x/y} \sim f_1$ ,  $\partial_t \sim f_1$ . To include the lowest-order damping term in  $f_1$ , we retain terms up to cubic order in  $f_1$ . This yields the following hydrodynamic equation for the complex particle current  $v_0 f_1(\mathbf{r}, t) = j_x(\mathbf{r}, t) + ij_y(\mathbf{r}, t)$ :

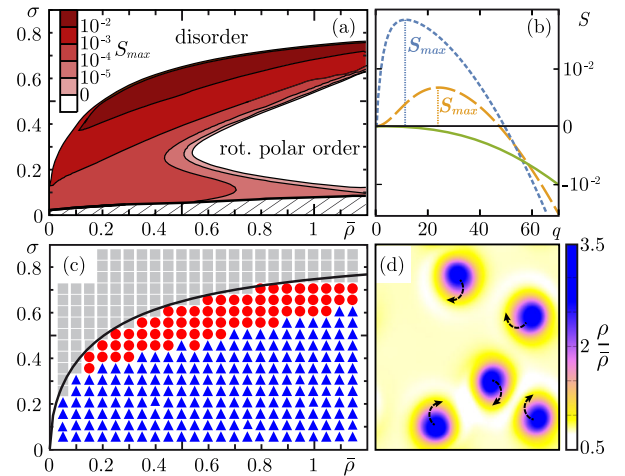


FIG. 3. (a) Stability of homogeneous solutions of Eq. (2) as a function of  $\sigma$  and  $\bar{\rho}$  in units of  $\lambda/(dv_0)$ . White and red areas denote regions where finite wavelength perturbations of the homogeneous solutions are stable and unstable, respectively. The color code denotes the value of the maximal growth rate  $S_{\max}$ . (b) Dispersion relation of  $S(q)$  ( $q$  in units of  $2\pi/\sqrt{A}$ ) for  $\bar{\rho} = 0.8$  and  $\sigma = 0.7$  (short-dashed line),  $\sigma = 0.6$  (long-dashed line), and  $\sigma = 0.4$  (solid line). Vertical lines indicate  $S_{\max}$ . (c) Phase diagram for density  $\bar{\rho}$  and  $\sigma$  displaying phases of homogeneous disorder (gray rectangles), swirls (red circles), and homogeneous order (blue triangles). The solid line marks the analytic solution of  $\rho_c(\sigma)$ . An overlay of (a) and (c) can be found in Supplemental Material [12]. (d) Snapshot of swirl patterns ( $\bar{\rho} = 0.8$ ,  $\sigma = 0.7$ ). All swirls are moving clockwise on circular paths.

$$\partial_t f_1(\mathbf{r}, t) = [\alpha(\bar{\rho} - \rho_c) + i v_0 \kappa_0] f_1 - \xi |f_1|^2 f_1 - \frac{v_0}{2} \nabla \rho - \beta f_1^* \nabla f_1 - \gamma f_1 \nabla^* f_1 + \nu \nabla^* \nabla f_1, \quad (3)$$

where  $\nabla := \partial_x + i\partial_y$ . While this equation shows similar functional dependencies on local density and current as found in systems without [41] and with straight propulsion [32], the coefficients  $\alpha$ ,  $\xi$ ,  $\nu$ ,  $\gamma$ , and  $\beta$  are now *complex valued* (for explicit expressions, please see Supplemental Material [12]). This can be traced back to the angular convection term in Eq. (1) or, equivalently, to the corresponding phase-shift term in Eq. (2). As a consequence, the field theory of active systems with particles moving on circular orbits with defined chirality is generically given by a complex Ginzburg-Landau (GL) equation with convective spatial coupling as well as density-current coupling. This constitutes a highly interesting generalization of the standard (diffusive) complex GL equations [42,43] and is qualitatively different from real GL-type equations that were previously applied in the context of self-propelled particles [31]. Above the threshold,  $\bar{\rho} > \rho_c(\sigma)$ , the active chiral hydrodynamics described by the generalized GL equation (3) exhibits a uniform oscillatory solution with  $f_1 = F_1 e^{i\Omega_0 t}$ , i.e., a state in which particles move on a circular (chiral) path with an angular velocity  $\Omega_0 = v_0 \kappa_0 - \alpha(\bar{\rho} - \rho_c) \text{Im}[\xi]/\text{Re}[\xi]$ ; the amplitude  $F_1 = \{\alpha(\bar{\rho} - \rho_c)/\text{Re}[\xi]\}^{1/2}$  gives the particle density. However, a linear stability analysis of Eq. (3) shows that for densities slightly larger than  $\rho_c$  this oscillatory solution is linearly unstable against finite wavelength perturbations in the current and density fields. Preliminary numerical solutions of the generalized GL equation [Eq. (3)] take the form of rotating spots of high density that appear to show turbulent dynamics [12,44]. This is qualitatively distinct from the high-density bands found for straight-moving particles [23,45] and the vortex field of a fluid coupled to torque dipoles [46,47].

Far above the threshold, closure relations such as those discussed above [31] may become invalid and with them the ensuing hydrodynamic equations. Therefore, we proceed with the full spectral analysis of the Boltzmann equation [Eq. (2)] as detailed in Supplemental Material [12]. First, we numerically calculate the spatially homogeneous solutions for all angular Fourier modes  $f_k$  below some cutoff wave vector  $k_{\max}$ . For given values of  $\bar{\rho}$  and  $\sigma$  and a desired accuracy  $\epsilon$  of this mode truncation scheme, the cutoff is chosen such that  $|f_{k_{\max}+1}| < \epsilon$ . We find that for  $\bar{\rho} < \rho_c(\sigma)$  a spatially homogeneous state where all modes but  $f_0$  vanish is the only stable state. In contrast, above the threshold [ $\bar{\rho} > \rho_c(\sigma)$ ], there is a second solution for which  $|f_1| > 0$ . It corresponds to a polar ordered state whose orientation is changing periodically in time with frequency  $v_0 \kappa_0$ . For moderate  $\bar{\rho} - \rho_c$ , the amplitude quantitatively agrees with the result from the generalized GL equation; see Supplemental Material [12]. In a second step, we

consider wavelike perturbations,  $\delta f_k(\mathbf{q})$  with wave vector  $\mathbf{q}$ , of the spatially homogeneous oscillatory solution in a corotating frame. The largest real part of all eigenvalues of the corresponding linearized system for  $\delta f_k$  then yields the linear growth rate  $S(q)$  [Fig. 3(b)]. In accordance with the linear stability analysis of Eq. (3), we find that for densities slightly larger than  $\rho_c$  a spatially homogeneous solution is unstable against finite wavelength perturbations. The dispersion relation  $S(q)$  exhibits a band of unstable modes, with the maximal growth rate  $S_{\max}$  decreasing as one moves away from the threshold  $\rho_c$  [Figs. 3(a) and 3(b)]. Actually, there is lobelike regime in parameter space where  $S(q) < 0$  [Fig. 3(a)], and hence a homogeneously polar ordered state with rotating direction is stable. We emphasize here that our stability portrait [Fig. 3(a)] is independent of  $\kappa_0$  and hence equally valid for systems of straight-moving particles. For our two approaches [Figs. 2(d) and 3(a)], the onset to order is governed by a similar trend [12], common for active systems [28,48]: Disorder prevails for low density or high noise, and order is promoted for high density or low noise.

To determine the spatiotemporal dynamics in the regime where neither a spatially homogeneous state nor a homogeneously polar ordered state are stable, we resort to a modified version of the SNAKE algorithm [34] to numerically solve Eq. (1). It accurately reproduces the threshold value  $\rho_c(\sigma)$  at which the spatially homogeneous state becomes unstable [Fig. 3(c)]. Above the threshold ( $\bar{\rho} > \rho_c$ ), we find that local density fluctuations quickly grow and evolve into stable swirls, i.e., disklike flocks of high density and polar order moving on circular paths; see Fig. 3(d) and Movie 6 in Supplemental Material [12]. The radius of such a path is approximately given by  $R_0$ . These swirl patterns closely resemble the swirling flocks observed in the Brownian dynamics simulations for short polymer arc angles (Movie 5 [12]), as well as our preliminary numerical solutions of the generalized GL equation [Eq. (3)] [12,44]. Moreover, in accordance with the spectral analysis, we find a second threshold density, above which the system settles into a homogeneously polar ordered state with a periodically changing orientation (Movie 7 [12]). The amplitude and frequency of the polar order agree with the numerical results of the spectral analysis to high accuracy [12], while the numerically determined phase boundaries differ. The SNAKE algorithm produces stable swirl patterns only in a parameter regime where our linear stability analysis yields significant growth rates. This is mainly due to spurious noise caused by the discretization of the angular variable, which tends to suppress inhomogeneities in the regime of small growth rates. Furthermore, the finite system size constricts the band of possible modes and allows only for patterns of sufficiently short length scales.

For active systems of circling particles that interact via steric repulsion, our microscopic and mesoscopic treatments strongly suggest that a phase of collective vortex structures is a generic feature. Within this class, our work

shows that extended polymers which as a whole follow circular tracks can form closed rings. Concerning our motivation of circling FtsZ, further research is needed to elucidate the dynamics of treadmilling; yet our minimal kinetic assumption suggests that varying the particle density alone suffices to regulate the patterns as observed by Loose and Mitchison [5]. Compared to systems of straight-moving particles, we find qualitatively new phenomena [12,44]. For those systems, it was already reported that (globally achiral) vortices can occur due to collisions of particles of asymmetric shape [49] or due to memory in orientation [3,50]. Some of our findings, like the polymer length dependence of patterns and the possible emergence of active turbulence [51,52], pose interesting questions for future work. Our analysis yields a mapping of the emergent dynamics onto a generalized Ginzburg-Landau equation, providing a connection between active matter and nonlinear oscillators [44].

We thank F. Thüroff, L. Reese, and J. Knebel for helpful discussions. This research was supported by the German Excellence Initiative via the program “NanoSystems Initiative Munich” (NIM) and the graduate school “Quantitative Biosciences Munich” (QBM), and the Deutsche Forschungsgemeinschaft (DFG) via project B02 within the Collaborative Research Center (SFB 863) “Forces in Biomolecular Systems.”

J. D. and L. H. contributed equally to this work.

\*frey@lmu.de

- [1] V. Schaller, C. A. Weber, B. Hammerich, E. Frey, and A. R. Bausch, *Proc. Natl. Acad. Sci. U.S.A.* **108**, 19183 (2011).
- [2] V. Schaller, C. A. Weber, C. Semmrich, E. Frey, and A. R. Bausch, *Nature (London)* **467**, 73 (2010).
- [3] Y. Sumino, K. H. Nagai, Y. Shitaka, D. Tanaka, K. Yoshikawa, H. Chaté, and K. Oiwa, *Nature (London)* **483**, 448 (2012).
- [4] R. Suzuki, C. A. Weber, E. Frey, and A. R. Bausch, *Nat. Phys.* **11**, 839 (2015).
- [5] M. Loose and T. J. Mitchison, *Nat. Cell Biol.* **16**, 38 (2013).
- [6] E. L. Meier and E. D. Goley, *Curr. Opin. Cell Biol.* **26**, 19 (2014).
- [7] M. Ingerson-Mahar and Z. Gitai, *FEMS Microbiol. Rev.* **36**, 256 (2012).
- [8] H. P. Erickson, D. E. Anderson, and M. Osawa, *Microbiol. Mol. Biol. Rev.* **74**, 504 (2010).
- [9] P. Szwedziak, Q. Wang, T. A. M. Bharat, M. Tsim, and J. Löwe, *eLife* **3**, e04601 (2014).
- [10] O. Kratky and G. Porod, *Recl. Trav. Chim. Pays-Bas* **68**, 1106 (1949).
- [11] N. Saitô, K. Takahashi, and Y. Yunoki, *J. Phys. Soc. Jpn.* **22**, 219 (1967).
- [12] See Supplemental Material at <http://link.aps.org/supplemental/10.1103/PhysRevLett.116.178301> for a detailed description of the numerical methods and analytical derivations, which contains Refs. [13–16].
- [13] P. Kloeden and E. Platen, *Numerical Solution of Stochastic Differential Equations* (Springer, Berlin, 1992).
- [14] R. E. Goldstein and S. A. Langer, *Phys. Rev. Lett.* **75**, 1094 (1995).
- [15] M. Hinczewski, X. Schlagberger, M. Rubinstein, O. Krichevsky, and R. R. Netz, *Macromolecules* **42**, 860 (2009).
- [16] C. Bennemann, J. Baschnagel, W. Paul, and K. Binder, *Comput. Theor. Polym. Sci.* **9**, 217 (1999).
- [17] G. Chirico and J. Langowski, *Biopolymers* **34**, 415 (1994).
- [18] H. Wada and R. R. Netz, *Europhys. Lett.* **77**, 68001 (2007).
- [19] J. K. G. Dhont, *An Introduction to Dynamics of Colloids* (Elsevier, Amsterdam, 1996).
- [20] X. Lu and Y. Hu, *Molecular Thermodynamics of Complex Systems* (Springer, Heidelberg, 2008).
- [21] T. Vicsek, A. Czirók, E. Ben-Jacob, I. Cohen, and O. Shochet, *Phys. Rev. Lett.* **75**, 1226 (1995).
- [22] I. H. Riedel, K. Kruse, and J. Howard, *Science* **309**, 300 (2005).
- [23] H. Chaté, F. Ginelli, G. Grégoire, and F. Raynaud, *Phys. Rev. E* **77**, 046113 (2008).
- [24] E. Bertin, M. Droz, and G. Grégoire, *Phys. Rev. E* **74**, 022101 (2006).
- [25] T. Ihle, *Phys. Rev. E* **83**, 030901 (2011).
- [26] F. Ginelli, F. Peruani, M. Bär, and H. Chaté, *Phys. Rev. Lett.* **104**, 184502 (2010).
- [27] F. Peruani, J. Starruß, V. Jakovljevic, L. Søgaard-Andersen, A. Deutsch, and M. Bär, *Phys. Rev. Lett.* **108**, 098102 (2012).
- [28] M. C. Marchetti, J. F. Joanny, S. Ramaswamy, T. B. Liverpool, J. Prost, M. Rao, and R. A. Simha, *Rev. Mod. Phys.* **85**, 1143 (2013).
- [29] Y. Yang, F. Qiu, and G. Gompper, *Phys. Rev. E* **89**, 012720 (2014).
- [30] A. Kaiser and H. Löwen, *Phys. Rev. E* **87**, 032712 (2013).
- [31] A. Peshkov, E. Bertin, F. Ginelli, and H. Chaté, *Eur. Phys. J. Spec. Top.* **223**, 1315 (2014).
- [32] E. Bertin, M. Droz, and G. Grégoire, *J. Phys. A* **42**, 445001 (2009).
- [33] A. Peshkov, I. S. Aranson, E. Bertin, H. Chaté, and F. Ginelli, *Phys. Rev. Lett.* **109**, 268701 (2012).
- [34] F. Thüroff, C. A. Weber, and E. Frey, *Phys. Rev. X* **4**, 041030 (2014).
- [35] C. A. Weber, F. Thüroff, and E. Frey, *New J. Phys.* **15**, 045014 (2013).
- [36] F. Thüroff, C. A. Weber, and E. Frey, *Phys. Rev. Lett.* **111**, 190601 (2013).
- [37] A. Peshkov, S. Ngo, E. Bertin, H. Chaté, and F. Ginelli, *Phys. Rev. Lett.* **109**, 098101 (2012).
- [38] J. Toner and Y. Tu, *Phys. Rev. Lett.* **75**, 4326 (1995).
- [39] A. Baskaran and M. C. Marchetti, *Phys. Rev. E* **77**, 011920 (2008).
- [40] S. Mishra, A. Baskaran, and M. C. Marchetti, *Phys. Rev. E* **81**, 061916 (2010).
- [41] I. S. Aranson and L. S. Tsimring, *Phys. Rev. E* **71**, 050901 (R) (2005).
- [42] I. S. Aranson and L. Kramer, *Rev. Mod. Phys.* **74**, 99 (2002).
- [43] V. García-Morales and K. Krischer, *Contemp. Phys.* **53**, 79 (2012).

- [44] L. Huber, J. Denk, E. Reithmann, E. Frey (to be published).
- [45] H. Chaté, F. Ginelli, G. Grégoire, F. Peruani, and F. Raynaud, *Eur. Phys. J. B* **64**, 451 (2008).
- [46] S. Fürthauer, M. Strempel, S. W. Grill, and F. Jülicher, *Eur. Phys. J. E* **35**, 89 (2012).
- [47] S. Fürthauer, M. Strempel, S. W. Grill, and F. Jülicher, *Phys. Rev. Lett.* **110**, 048103 (2013).
- [48] S. Ramaswamy, *Annu. Rev. Condens. Matter Phys.* **1**, 323 (2010).
- [49] H. H. Wensink, V. Kantsler, R. E. Goldstein, and J. Dunkel, *Phys. Rev. E* **89**, 010302 (2014).
- [50] K. H. Nagai, Y. Sumino, R. Montagne, I. S. Aranson, and H. Chaté, *Phys. Rev. Lett.* **114**, 168001 (2015).
- [51] J. Dunkel, S. Heidenreich, K. Drescher, H. H. Wensink, M. Bär, and R. E. Goldstein, *Phys. Rev. Lett.* **110**, 228102 (2013).
- [52] V. Bratanov, F. Jenko, and E. Frey, *Proc. Natl. Acad. Sci. U.S.A.* **112**, 15048 (2015).

# Supplemental Material: Active Curved Polymers form Vortex Patterns on Membranes

Jonas Denk, Lorenz Huber, Emanuel Reithmann, and Erwin Frey\*

*Arnold Sommerfeld Center for Theoretical Physics (ASC) and Center for NanoScience (CeNS),  
Department of Physics, Ludwig-Maximilians-Universität München, Theresienstrasse 37, 80333 München, Germany*

## COMMENT ON TREADMILLING

In their experiments [1], Loose and Mitchison observe that FtsZ polymers undergo depolymerization and polymerization processes leading to an effective translation in the direction of the polymers' backbones. However, the underlying molecular details are unclear, as they involve many qualitatively and quantitatively unknown reactions and a yet unstudied interplay of different auxiliary proteins (*e.g.* FtsA, ZipA). Here, we neglect these details and focus on the collective effects of many FtsZ polymers retaining only their effective movement along circular tracks. To realize this kind of motion we assume an intrinsic particle velocity.

## NUMERICAL IMPLEMENTATION OF BROWNIAN DYNAMICS

In the following, we discuss the details of the implementation of the Brownian dynamics simulations. We use a bead-spring model [2, 3] that comprises the following discretization scheme: a polymer of length  $L$  is subdivided into  $N$  beads at positions  $\mathbf{r}_i = (x_i, y_i)^T$  ( $i = 1, 2, \dots, N$ ), with  $N - 1$  bonds of length  $a$ ; the (normalized) bond vectors are given by  $\partial_s \mathbf{r} \approx \frac{\mathbf{r}_{i+1} - \mathbf{r}_i}{a} =: \hat{\mathbf{t}}_i$ ; the bending angle between two adjacent bonds is given by  $\theta_i = \arccos(\hat{\mathbf{t}}_{i+1} \cdot \hat{\mathbf{t}}_i)$ . The corresponding bending energy reads

$$E_{bend} = \frac{\ell_p}{2a} k_B T \sum_{i=1}^{N-2} (\theta_i - \theta_0)^2. \quad (\text{S1})$$

where  $\theta_0 \approx a\kappa_0$  is the spontaneous bending angle. In the bead-spring model, neighboring beads are connected by stiff harmonic springs. The corresponding stretching energy is given by

$$E_{stretch} = \frac{k}{2} \sum_{i=1}^{N-1} (|\mathbf{r}_{i+1} - \mathbf{r}_i| - a)^2. \quad (\text{S2})$$

In the simulations, the spring constant  $k$  is chosen larger than all other force constants to account for the fact that biopolymers are nearly inextensible; as a consequence, stretching modes relax fast compared to other dynamic processes. At the same time,  $k$  cannot be chosen arbitrarily large as this would strongly limit the maximal simulation time  $T_{max}$  (see below for values).

In the two-dimensional system of  $M$  polymers, we assume steric repulsion between adjacent polymer segments

$\mathbf{r}_i^{(m)}$  ( $m = 1, 2, \dots, M$ ). As an interaction potential we use a truncated Lennard-Jones potential [4-6]

$$(E_{int})_{ij}^{(mn)} = \epsilon \left[ \left( \frac{a}{r_{ij}^{(mn)}} \right)^{12} - \left( \frac{a}{r_{ij}^{(mn)}} \right)^6 \right] \Theta(a - r_{ij}^{(mn)}), \quad (\text{S3})$$

with  $r_{ij}^{(mn)} = |\mathbf{r}_i^{(m)} - \mathbf{r}_j^{(n)}|$ ,  $\epsilon$  the potential strength, and  $\Theta(r)$  the Heaviside step function. At distances smaller than the bond length  $a$ , the potential is strongly repulsive.

In the Langevin description, the equation of motion is given by a force balance between elastic, active, thermal and dissipative terms. For the  $i$ -th bead of a polymer, the equation of motion reads

$$\zeta \partial_t \mathbf{r}_i = - \frac{\delta E}{\delta \mathbf{r}_i} + \mathbf{F}_i^{prop} + \boldsymbol{\eta}_i \\ = \mathbf{F}_i^{bend} + \mathbf{F}_i^{stretch} + \mathbf{F}_i^{int} + \mathbf{F}_i^{prop} + \boldsymbol{\eta}_i \quad (\text{S4})$$

where  $E = E_{bend} + E_{stretch} + E_{int}$ ,  $\mathbf{F}_i^{prop}$  is the propulsive force and the amplitude of the thermal forces is given by  $\langle \boldsymbol{\eta}_i(t) \cdot \boldsymbol{\eta}_j(t') \rangle = 4k_B T \zeta \delta_{ij} \delta(t - t')$ . The bending, stretching and interaction forces  $\mathbf{F}_i^{bend}$ ,  $\mathbf{F}_i^{stretch}$ ,  $\mathbf{F}_i^{int}$  are obtained by variation of the corresponding energetic terms with respect to the position vector  $\mathbf{r}_i$  [2, 3]. We employ the following implementation of the tangential propulsive force  $\mathbf{F}_i^{prop} = \zeta v_0 \partial_s \mathbf{r}$ :

$$\mathbf{F}_i^{prop} = \zeta v_0 \begin{cases} \hat{\mathbf{t}}_1 & i = 1 \\ (\hat{\mathbf{t}}_{i-1} + \hat{\mathbf{t}}_i)/2 & 1 < i < N \\ \hat{\mathbf{t}}_{N-1} & i = N \end{cases} \quad (\text{S5})$$

For the integration of Eq. (S4) we use an Euler-Maruyama iteration scheme [7] with sufficiently small time steps  $\Delta = 0.0001\tau$  with the unit time  $\tau = \zeta a^2 / (k_B T)$ . In our simulations, we used the following set of parameters:  $L = 9a$ ,  $\ell_p = 100a$ ,  $k = 500k_B T / a^2$ ,  $\epsilon = 1k_B T$ ,  $\theta_0 = 0.2$ ,  $\zeta = 1$  and a periodic system of area  $A = 60a \times 60a$  (such that it can contain many consecutive polymer lengths). In the main text, the unit of length is set to  $a = 100 \text{ nm}$ , such that  $L = 0.9 \mu\text{m}$ ,  $\ell_p = 10 \mu\text{m}$  are roughly similar to FtsZ filaments. The noise strength  $\sigma = k_B T \ell_p / (\zeta v_0 L^2)$  was varied as follows: we changed the temperature scale in the interval  $k_B T \in [0, 1]$  for  $v_0 = 5$ , and for  $k_B T = 1$  varied  $v_0$  in the range  $v_0 \in [1, 5]$ . The maximal simulation times  $T_{max}$  for all simulations in the main text were chosen such that the single polymer rotation time  $\tau_R = 2\pi / (\kappa_0 v_0)$  is much smaller. We

took  $T_{max} > 400\tau_R$  and  $T_{max} > 700\tau$  for our data to provide a sufficiently large sampling interval for both convective and diffusive motion. To consolidate the results, data were recorded for 10 independent simulation for each given set of parameters.

### ANALYSIS OF THE PAIR CORRELATION FUNCTION

To analyze the patterns observed in the Brownian dynamics simulations, we consider the pair correlation function  $g(d_{cc})$  [8, 9] of center distances  $d_{cc} = |\mathbf{r}_{cc}^{(m)} - \mathbf{r}_{cc}^{(n)}|$ . The positions  $\mathbf{r}_{cc}^{(m)}$  are the curvature centers of each polymer, generated by averaging over the local curvature and all local reference positions on a contour (see Fig. S1(a)). In contrast to the positions  $\mathbf{r}^{(m)}$ , the curvature centers do not oscillate due to self-propulsion and hence represent a more stable measure of particle position.

Figure S1(b) displays the contour of  $g(d_{cc})$  for parameters  $k_B T = 0.5$  and  $v_0 = 5$  (i. e.  $\sigma = 0.247$ ). For sufficiently small  $\rho$ , the density exhibits a local minimum at  $d_{cc}^{min}$ , the diameter of a vortex. This implies that there is a preferred vortex size and structure connected to the distance  $d_{cc}^{min}$ . These minima were determined after applying a Gaussian filter to suppress random fluctuation artifacts and then used to distinguish the observed patterns according to the 'phase' criteria introduced in the main text: *disordered states* for  $d_{cc}^{min} \approx 2R_0$ , *vortex states* for  $d_{cc}^{min} > 2R_0$  and *train states* without  $d_{cc}^{min}$ .

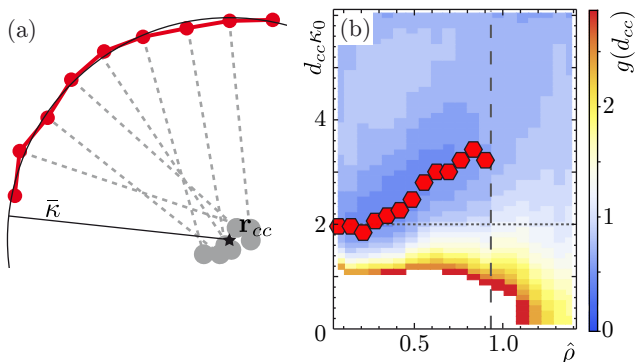


FIG. S1. (a) Illustration of the curvature center  $\mathbf{r}_{cc}$  as determined by averaging over local centers with a mean contour curvature  $\bar{\kappa}$  (polymer in red). (b) Heat map of the pair correlation function for  $\sigma = 0.247$  in terms of distances  $d_{cc}$  and densities  $\rho$ . Red polygons denote the positions of  $d_{cc}^{min}$ . The short dashed line depicts the free polymer radius and the long dashed line marks the regime where  $d_{cc}^{min}$  vanishes.

### DERIVATION OF THE HYDRODYNAMIC EQUATIONS

To assess the dynamics at larger scales, we employed a kinetic Boltzmann approach. The corresponding generalized Boltzmann equation for  $f(\theta, \mathbf{r}, t)$  is given by Eq. (1). The self-diffusion and collision integrals  $\mathcal{I}_d$  and  $\mathcal{I}_c$ , respectively, are given by

$$\mathcal{I}_d[f] = \lambda \left\langle \int_{-\pi}^{\pi} d\phi f(\phi) [\delta(\theta - \phi - \eta) - \delta(\theta - \phi)] \right\rangle_{\eta}, \quad (\text{S6})$$

$$\mathcal{I}_c[f; f] = \left\langle \int_{-\pi}^{\pi} d\phi_1 \int_{-\pi}^{\pi} d\phi_2 \mathcal{S}(|\phi_1 - \phi_2|) f(\phi_1) f(\phi_2) \times [\delta(\theta - \frac{1}{2}(\phi_1 + \phi_2) - \eta) - \delta(\theta - \phi_1)] \right\rangle_{\eta}, \quad (\text{S7})$$

where  $\mathcal{S}(\psi) = 4dv_0 |\sin(\frac{\psi}{2})|$  is the scattering cross section for spherical particles of diameter  $d$  and velocity  $v_0$  in two dimensions as detailed in Ref. [10]. The collision integral represents ferromagnetic alignment of two particles with orientation  $\phi_1$  and  $\phi_2$  along their average angle  $\theta = \frac{1}{2}(\phi_1 + \phi_2)$ . The brackets denote an average over a Gaussian-distributed noise variable  $\eta$ . To obtain a dimensionless form we used the rescaling

$$\begin{aligned} t &\rightarrow t \cdot \lambda^{-1}, \\ \mathbf{x} &\rightarrow \mathbf{x} \cdot v_0 \lambda^{-1}, \\ f &\rightarrow f \cdot \rho_0, \\ \kappa_0 &\rightarrow \kappa_0 \cdot v_0 \lambda^{-1}, \end{aligned}$$

with  $\rho_0 = \lambda/(dv_0)$ . Measuring time, space and density in units of  $\lambda^{-1}$ ,  $v_0 \lambda^{-1}$ , and  $\rho_0$ , respectively, allows to set  $d = \lambda = v_0 = 1$ . Then, the only remaining free parameters are the noise amplitude  $\sigma$ ,  $\kappa_0$ , and the mean particle density  $\bar{\rho} = A^{-1} \int_A d\mathbf{r} \int_{-\pi}^{\pi} d\theta f(\mathbf{r}, \theta, t)$ . To proceed, we performed a Fourier transformation of the angular variable:  $f_k(\mathbf{r}, t) = \int_{-\pi}^{\pi} d\theta e^{i\theta k} f(\mathbf{r}, \theta, t)$ . This leads to the Boltzmann equation in Fourier space, Eq. (2), where the Fourier transforms  $\mathcal{I}_{n,k}$  are given by

$$\mathcal{I}_{n,k} = \int_{-\pi}^{\pi} \frac{d\Phi}{2\pi} \mathcal{S}(|\Phi|) \left[ \hat{P}_k \cos(\Phi(n - k/2)) - \cos(\Phi n) \right]. \quad (\text{S8})$$

$\hat{P}_k = e^{-(k\sigma)^2/2}$  is the Fourier transform (characteristic function) of the Gaussian noise with standard deviation  $\sigma$ . Note that  $\mathcal{I}_{n,0} = 0$  for all  $n$ . For  $k = 0$ , Eq. (2) hence yields the continuity equation  $\partial_t \rho = -\frac{1}{2}(\nabla f_1^* + \nabla^* f_1) = -\nabla \cdot \mathbf{j}$  for the local density  $\rho(\mathbf{r}, t) := f_0(\mathbf{r}, t)$  with the particle current given by  $\mathbf{j}(\mathbf{r}, t) = v_0(\text{Re}f_1, \text{Im}f_1)^T$ . In order to get a closed equation for the particle current at onset, we assume small currents  $f_1 \ll 1$  and use the

truncation scheme:  $\rho - \bar{\rho} \sim f_1$ ,  $\partial_{x/y} \sim f_1$ ,  $\partial_t \sim f_1$ ,  $f_2 \sim f_1^2$  with vanishing higher modes as presented for polar particles with ferromagnetic interaction in Ref. [11]. In analogy to Ref. [10], we retained only terms up to cubic order in  $f_1$  in the Boltzmann equation, Eq. (2), for  $k = 1$ . The equation for  $f_1$  then couples to the nematic order field  $f_2$  via a term  $\sim f_1^* f_2$  of order  $f_1^3$ , where the star denotes complex conjugate. Writing down contributions from Eq. (2) for  $k = 2$  of quadratic order in  $f_1$  yields an expression for  $f_2$  as a function of  $f_1$ . The expression for  $f_2$  can then be substituted into Eq. (2) for  $k = 1$  to obtain a closed equation for  $f_1$ . Together with the continuity equation, the hydrodynamic equations for the density and the particle current read

$$\partial_t \rho = -\frac{1}{2}(\nabla f_1^* + \nabla^* f_1), \quad (\text{S9a})$$

$$\begin{aligned} \partial_t f_1 = & [\alpha(\rho - \rho_c) + iv_0\kappa_0] f_1 - \xi |f_1|^2 f_1 + \nu \nabla^* \nabla f_1 \\ & - \gamma f_1 \nabla^* f_1 - \beta f_1^* \nabla f_1 - \frac{v_0}{2} \nabla \rho, \end{aligned} \quad (\text{S9b})$$

where  $\nabla := \partial_x + i\partial_y$ . The coefficients are given by

$$\begin{aligned} \alpha &:= (\mathcal{I}_{0,1} + \mathcal{I}_{1,1}), \\ \rho_c &= \frac{\lambda(1 - \hat{P}_1)}{\mathcal{I}_{0,1} + \mathcal{I}_{1,1}}, \\ \nu &:= -\frac{1}{4} \frac{1}{\lambda(\hat{P}_2 - 1) + 2iv_0\kappa_0 + (\mathcal{I}_{0,2} + \mathcal{I}_{2,2})\rho}, \\ \xi &:= -4(\mathcal{I}_{-1,1} + \mathcal{I}_{2,1})\nu\mathcal{I}_{1,2}, \\ \beta &:= 2(\mathcal{I}_{-1,1} + \mathcal{I}_{2,1})\nu, \\ \gamma &:= 4\nu\mathcal{I}_{1,2}. \end{aligned} \quad (\text{S10})$$

We note that the employed truncation scheme implies fast relaxation of the nematic order field  $f_2$  such that  $\partial_t f_2$  is assumed to be negligible on time scales of the dynamics of  $f_1$ .  $f_2$  is then slaved to  $f_1$  via  $f_2 = -2\nu\nabla f_1 + \gamma f_1^2$ .

### Linear stability analysis

For  $\rho < \rho_c$  Eqs. (S9) are solved by the homogeneous isotropic state:  $\rho = \bar{\rho} = \text{const.}$ ,  $f_1 = 0$ . For  $\rho > \rho_c$  there is a second solution given by the homogeneous oscillatory state:  $\rho = \bar{\rho}$ ,  $f_1 = F_1 e^{i\Omega_0 t}$  with  $F_1 = (\alpha(\bar{\rho} - \rho_c)/\text{Re}[\xi])^{1/2}$  and  $\Omega_0 = v_0\kappa_0 - \alpha(\bar{\rho} - \rho_c)\text{Im}[\xi]/\text{Re}[\xi]$ .

#### Homogeneous isotropic state

To study the stability of the homogeneous isotropic state we substitute  $\rho = \bar{\rho} + \delta\rho$  and  $f_1 = \delta f_1$  with the wave-like perturbations of the form

$$\begin{aligned} \delta\rho(\mathbf{r}, t) &\sim \delta\rho_{\mathbf{q}} e^{i\mathbf{q}\cdot\mathbf{r}}, \\ \delta f_1(\mathbf{r}, t) &\sim \delta f_{1,\mathbf{q}} e^{i\mathbf{q}\cdot\mathbf{r}}, \end{aligned} \quad (\text{S11})$$

where  $\delta\rho_{\mathbf{q}}$  and  $\delta f_{1,\mathbf{q}}$  are in general complex amplitudes that are assumed to be small. Periodic boundary conditions in our numeric solution impose  $|\mathbf{q}| = n\frac{2\pi}{L}$ ,  $n \in \mathbb{Z}$ , where  $L = \sqrt{A}$  and  $A$  is the area of the (quadratic) system. The linearized set of equations of motion for the perturbations  $\delta\rho_{\mathbf{q}}(t)$ ,  $\delta f_{1,\mathbf{q}}(t)$  and  $\delta f_{1,\mathbf{q}}^*(t)$  has the characteristic polynomial

$$\begin{aligned} &-q^2\alpha(\bar{\rho} - \rho_c) + q^4\Re[\nu] \\ &+ (2(\alpha(\bar{\rho} - \rho_c) - \Re[\nu]q^2)^2 + 2(v_0\kappa_0 - \Im[\nu]q^2)^2 + q^2)S \\ &+ 4(-\alpha(\bar{\rho} - \rho_c) + \Re[\nu]q^2)S^2 + 2S^3. \end{aligned} \quad (\text{S12})$$

where  $S$  is the eigenvalue of the linearized set of equations for  $\delta\rho_{\mathbf{q}}(t)$ ,  $\delta f_{1,\mathbf{q}}(t)$  and  $\delta f_{1,\mathbf{q}}^*(t)$ . We note that  $\Re[\nu]$  is positive for all densities. For  $\bar{\rho} < \rho_c$ , all coefficients in (S12), including the  $S$ -independent terms are positive, such that (S12) only yields  $S$  with negative real part. Thus, for  $\bar{\rho} < \rho_c$  the homogeneous isotropic state is linearly stable against inhomogeneous wave-like perturbations. For  $\bar{\rho} - \rho_c > 0$ , the real part of  $S$  becomes positive where the fastest growing mode is always at  $q = 0$ .

#### Homogeneous oscillatory state

To study the stability of the homogeneous oscillatory solution we substitute small perturbations in the basis of the homogeneous oscillating solution:

$$\begin{aligned} \rho &= \bar{\rho} + \delta\rho_{(0)} \\ &+ \sqrt{\frac{\alpha(\bar{\rho} - \rho_c)}{\Re[\xi]}} \delta\rho_{(1)} e^{i\Omega_0 t} + \sqrt{\frac{\alpha(\bar{\rho} - \rho_c)}{\Re[\xi]}} \delta\rho_{(1)}^* e^{-i\Omega_0 t}, \\ f_1 &= F_1 e^{i\Omega_0 t} + \delta f_{(0)} \\ &+ \sqrt{\frac{\alpha(\bar{\rho} - \rho_c)}{\Re[\xi]}} \delta f_{(1)} e^{i\Omega_0 t} + \sqrt{\frac{\alpha(\bar{\rho} - \rho_c)}{\Re[\xi]}} \delta f_{(2)} e^{-i\Omega_0 t}, \end{aligned} \quad (\text{S13})$$

where the amplitudes  $\delta\rho_{(0)}$ ,  $\delta\rho_{(1)}$ ,  $\delta f_{(0)}$ ,  $\delta f_{(1)}$  and  $\delta f_{(2)}$  are again of the form (S11). Truncating at the lowest order of  $(\bar{\rho} - \rho_c)$ , which is  $\sqrt{\alpha(\bar{\rho} - \rho_c)}$ , yields a closed set of linear equations for the amplitudes. The eigenvalue with the largest real part of this linear system determines the growth rate  $S(q)$  of wave-like perturbations. We find that the dispersion relation yields positive  $S(q)$  for finite  $q$  (see Fig S2).

### NUMERICAL LINEAR STABILITY ANALYSIS IN THE FULL PHASE SPACE

In the derivation and the stability analysis of Eqs. (S9) we rely on the assumption of small particle currents which might be justified at onset. However, this assumption is in general questionable and not well justified for

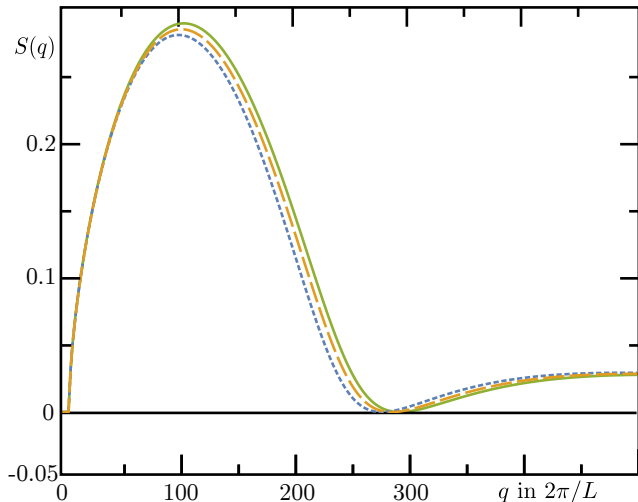


FIG. S2. Dispersion relations for  $\sigma = 0.6, 0.4$  and  $0.1$  (short-dashed, long-dashed and solid lines, respectively) at  $\bar{\rho} = 0.8$ .

densities much larger than  $\rho_c$ . To obtain a stability map for the full phase space (Fig. 3), we first calculated the homogeneous solution of Eq. (2) retaining only modes up to  $k_{\max}$ . Given some values of  $\bar{\rho}$  and  $\sigma$  and a desired accuracy  $\epsilon$  of this mode truncation scheme the cutoff is chosen such that  $|f_{k_{\max}+1}| < \epsilon$ . As a next step, we linearized Eq. (2) with respect to this solution and calculated the maximal growth rate  $S(\mathbf{q})$  of wave-like perturbations with wave vector  $\mathbf{q}$ . If  $S(\mathbf{q}) > 0$  for some  $|\mathbf{q}|$ , the homogeneous solution is unstable whereas if  $S(\mathbf{q}) < 0$  for all  $|\mathbf{q}|$ , the corresponding homogeneous solution is stable.

Note that the homogeneous version of Eq. (2) (neglecting all gradient terms) is invariant under a phase shift  $f_k \rightarrow f_k e^{ikv_0\kappa_0 t}$ . Choosing the orientation of the polar order at  $t = 0$  to be aligned along the  $x$ -axis, Eq. (2) is solved by  $f_k = |f_k| e^{ikv_0\kappa_0 t}$  with the time and space independent amplitude  $|f_k|$ .  $|f_k|$  is then determined by the stationary homogeneous version of Eq. (2):

$$0 = \lambda(\hat{P}_k - 1)|f_k| + \sum_{n=-\infty}^{\infty} \mathcal{I}_{n,k} |f_n| |f_{k-n}|. \quad (\text{S14})$$

This equation is identical to the stationary homogeneous Boltzmann equation for straight moving particles; i.e. where  $\kappa_0 = 0$ . Hence, the solutions for the amplitudes  $|f_k|$  are identical to the solutions for the Fourier modes in systems of straight moving particles [10]. To proceed, we truncate the infinite sum in Eq. (S14) at  $k_{\max}$  and calculate the solution of all  $|f_k|$  with  $|k| \leq k_{\max}$ . Fig. S3 depicts the solution for the amplitude  $|f_1|$  as compared to the solution of the generalized Ginzburg-Landau equation as well as the SNAKE algorithm. The explicit solution for  $|f_1|$  and higher modes justifies the scaling scheme used to derive Eqs. (S9) in the vicinity of  $\rho_c$  [Fig. S3, inset]. For decreasing noise  $\sigma$  or increasing density  $\bar{\rho}$

an increasing number of Fourier modes starts to grow [Fig. S3, inset]. In our numerical calculations we typically included 30 – 50 Fourier modes. The dashed region in Fig. 3(a) indicates the regime where we cannot find a nontrivial solution to Eq. (S14) by neglecting Fourier modes above the chosen  $k_{\max} = 50$  and where we would have to choose a larger  $k_{\max}$ .

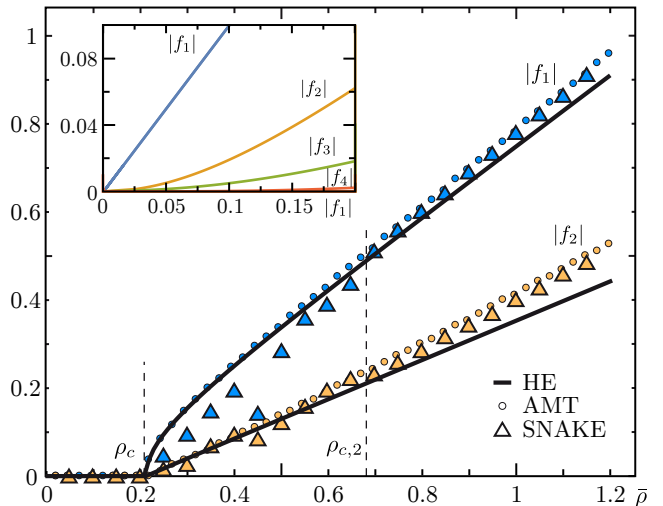


FIG. S3. Homogeneous solution for  $f_1$  and  $f_2$  for  $\sigma = 0.5$  obtained from the hydrodynamic equations Eqs. (S9) (HE), the adapted mode truncation scheme (AMT), and the SNAKE algorithm. Note that within  $\rho_c$  and  $\rho_{c,2}$  (dashed vertical lines), the SNAKE algorithm yields swirl states and hence the corresponding mode values do not represent homogeneous states. The inset depicts the solutions for the first modes obtained from the AMT and shows nonlinear scaling of higher modes with respect to  $|f_1|$ .

With the substitution  $f_k = (|f_k| + \delta f_k) e^{ikv_0\kappa_0 t}$  the linear system for  $\delta f_k$  then reads

$$\partial_t \delta f_k = -\frac{v_0}{2} (\nabla \delta f_{k-1} + \nabla^* \delta f_{k+1}) + \lambda(\hat{P}_k - 1) \delta f_k + \sum_{n=-\infty}^{\infty} (\mathcal{I}_{n,k} + \mathcal{I}_{k-n,k}) |f_{k-n}| \delta f_n. \quad (\text{S15})$$

Here, we performed a coordinate transformation to a frame rotating with angular frequency  $\kappa_0$  such that  $\nabla \rightarrow e^{ikv_0\kappa_0} \nabla$ . Assuming wave-like perturbations as in Eq. (S11), we solved Eq. (S15) for the maximal eigenvalue and get the growth rate as a function of the wavenumber in the rotating frame (see Fig. 3(b)). The maximum taken over all wavenumbers  $|\mathbf{q}| > 0$  then defines the maximal growth rate  $S_{\max}$  of wave-like perturbations. In agreement to previous results [10], we found that the growth rate is maximal for  $\mathbf{q}$  parallel to the particle current. The contour plot of  $S_{\max}$  as a function of  $\bar{\rho}$  and  $\sigma$  yields the phase diagram Fig. 3(a). Note again, that our stability analysis and the resulting phase diagram Fig. 3(a) is independent of curvature and also valid for the well-studied system of propelled particles without

curvature [10, 12, 13]. Hence, Fig. 3(a) shows that the Boltzmann approach is capable of reproducing phases of all states observed in [12, 14] including a transition from travelling wave patterns to global homogeneous order.

### NUMERICAL SOLUTION OF THE BOLTZMANN EQUATION WITH SNAKE

In order to study the resulting steady states in the regime where our linear stability analysis predicts inhomogeneities, we numerically solved the generalized Boltzmann equation, Eq. (1). To this end we employed the SNAKE algorithm as introduced in Ref. [15]. As tessellations we used a quadratic periodic regular lattice with equally sized angular slices. Circling propulsion was included by rotating the angular distribution of each lattice site with a frequency  $v_0\kappa_0$  in addition to the straight convection steps. The system was initialized with a disordered state with small random density fluctuations around the mean density  $\bar{\rho} = A^{-1} \int_A \rho(\mathbf{r}, t)$ . Changing  $\kappa_0$  did not change the observed patterns qualitatively. In the limiting case of very small  $\kappa$ , we observed traveling wave patterns as reported in Refs. [12, 14, 15]. For Fig. 3(c), Movie 6, and Movie 7 we used a lattice of of  $200 \times 200$  grid points with lattice field size 2 and angular discretization of 24 angular slices; hence,  $A = 400 \times 400 = 160000$ . In the swirl phase the swirl size grows for growing  $\bar{\rho} - \rho_c$  whereas the radius of a swirl's motion stays at approximately  $\kappa_0^{-1}$ . Fig. S4 shows the parameter values of  $\bar{\rho}$  and  $\sigma$  where the SNAKE algorithm exhibits steady swirl patterns together with the phase diagram obtained from the adapted mode truncation scheme.

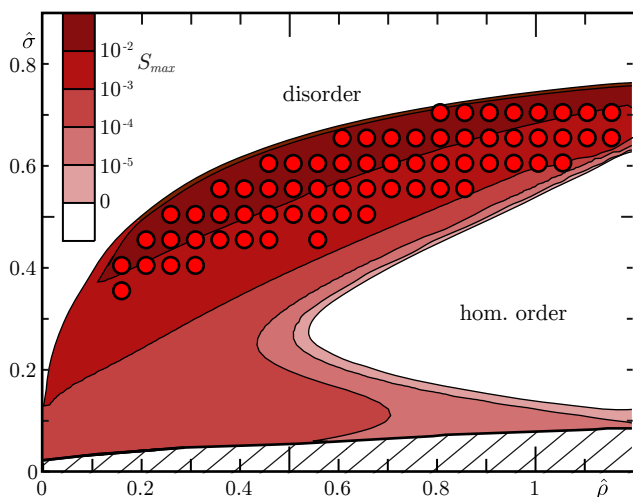


FIG. S4. Overlay of the parameter values where the SNAKE algorithm exhibits steady swirl patterns (red dots) together with the phase diagram obtained from the adapted mode truncation scheme (with  $k_{\max} = 50$ ). In the shaded region, neglected Fourier modes become important.

### REMARK ON THE SHAPE OF THE PHASE CURVES

When comparing the transition to order in the phase diagrams 2 and S4 it should be noted that our particle-based and continuum approaches are distinct in the following features: polymer fluctuations vs. effective diffusion, multi-particle collisions vs. binary alignment, extended polymers vs. point particles. The functional form of  $\rho_c(\sigma)$  (S10) depends on the choice of diffusion and collision noise (e.g. equally Gaussian distributed). In contrast, the form of the transition line in our Brownian dynamics simulations depends on the choice of the phenomenological criteria (*disordered states* for  $d_{cc}^{min} \approx 2R_0$ , *vortex states* for  $d_{cc}^{min} > 2R_0$  and *train states* without  $d_{cc}^{min}$ ). These differences result in different shapes of the phase boundaries. In addition, the observed patterns in the vortex phase are distinct. While for our particle-based model we find closed, rotating rings, dense, rotating swirls are observed in the continuum model (Fig. 2(b) and Fig. 3(d)). These differences are interesting and should be considered as part of the results we obtained. For example, these differences will guide future model building for specific models, e.g. the dynamics of FtsZ, as they emphasise what molecular details need to be accounted for. For the discussion of this work, however, our emphasis was on the topology of the phase diagram (similar trend of the onset to order) and the fact that in both models one finds a vortex phase.

### MOVIE DESCRIPTIONS

**Movie1.mp4:** Brownian dynamics simulation of a system with  $M = 10$  polymers with  $v_0 = 5, k_B T = 1$  and hence  $\rho = 0.069, \sigma = 0.247$ .

**Movie2.mp4:** Brownian dynamics simulation of a system with  $M = 80$  polymers with  $v_0 = 5, k_B T = 1$  and hence  $\rho = 0.556, \sigma = 0.247$ .

**Movie3.mp4:** Brownian dynamics simulation of a system with  $M = 200$  polymers with  $v_0 = 5, k_B T = 1$  and hence  $\rho = 1.389, \sigma = 0.247$ .

**Movie4.mp4:** Brownian dynamics simulation with parameters as in Movie 3, except for a changed curvature angle  $\theta_0 = 0.333$ , resulting in an polymer arc angle  $L\kappa_0 = 3$ .

**Movie5.mp4:** Brownian dynamics simulation with parameters as in Movie 3, except for a changed contour length  $L = 6$ , resulting in an polymer arc angle  $L\kappa_0 = 1.2$ .

**Movie6.mp4:** SNAKE solution for  $\bar{\rho} = 0.2$  and  $\sigma = 0.45$  with  $\kappa_0 = 0.1$ . The colour code denotes the local density  $\rho/\bar{\rho}$ . The orientation and length of the arrows indicates the orientation and amplitude of the local particle current.

**Movie7.mp4:** SNAKE solution for  $\bar{\rho} = 0.75$  and  $\sigma = 0.2$  with  $\kappa_0 = 0.1$ . The colour code denotes the local density  $\rho/\bar{\rho}$ . The orientation and length of the arrows indicates the orientation and amplitude of the local particle current.

**Hydroswhirl.mp4:** Preliminary results of the explicit integration [16] of the hydrodynamic Eqs. (S9). The video shows the time evolution of the density field  $\rho(\mathbf{r}, t)$ , for parameters close above threshold  $\bar{\rho} > \rho_c$ . The system size is  $A = 80 \times 80 = 640$ ,  $\bar{\rho} = 0.5$ ,  $\sigma = 0.6$ , and  $R_0 = 5$ .



\* [frey@lmu.de](mailto:frey@lmu.de)

- [1] M. Loose and T. J. Mitchison, *Nat. Cell Biol.* **16**, 38 (2013).
- [2] G. Chirico and J. Langowski, *Biopolymers* **34**, 415 (1994).
- [3] H. Wada and R. R. Netz, *Europhys. Lett.* **77**, 68001 (2007).
- [4] R. E. Goldstein and S. A. Langer, *Phys. Rev. Lett.* **75**, 1094 (1995).
- [5] M. Hinczewski, X. Schlagberger, M. Rubinstein, O. Krichevsky, and R. R. Netz, *Macromol.* **42**, 860 (2009).
- [6] C. Bennemann, J. Baschnagel, W. Paul, and K. Binder, *Comput. Theor. Polym. Sci.* **9**, 217 (1999).
- [7] P. Kloeden and E. Platen, *Numerical Solution of Stochastic Differential Equations* (Springer, Berlin, 1992).
- [8] J. K. G. Dhont, *An Introduction to Dynamics of Colloids* (Elsevier, Amsterdam, 1996).
- [9] X. Lu and Y. Hu, *Molecular Thermodynamics of Complex Systems* (Springer, Heidelberg, 2008).
- [10] E. Bertin, M. Droz, and G. Grégoire, *J. Phys. A-Math. Theor.* **42**, 445001 (2009).
- [11] A. Peshkov, E. Bertin, F. Ginelli, and H. Chaté, *Eur. Phys. J.-Spec. Top.* **223**, 1315 (2014).
- [12] H. Chaté, F. Ginelli, G. Grégoire, F. Peruani, and F. Raynaud, *Eur. Phys. J. B* **64**, 451 (2008).
- [13] T. Ihle, *Phys. Rev. E* **83**, 030901 (2011).
- [14] H. Chaté, F. Ginelli, and F. Raynaud, *Phys. Rev. E* **77**, 046113 (2008).
- [15] F. Thüroff, C. A. Weber, and E. Frey, *Phys. Rev. X* **4**, 041030 (2014).
- [16] In preparation.

## 2 Mixed symmetry of alignment interactions

In this section, we investigate the collective phenomena of active systems with microscopically realistic interactions, which are much more detailed than simplified alignment assumptions like the Vicsek rules (Eq. (II.2)). In particular, we employ the paradigmatic actomyosin gliding assay which was found to lack a clear symmetry preference of the microscopic alignment, despite finding collective order. We present a two-pronged approach of theory and experiment to analyze how microscopic symmetries affect the self-organization and emerging order of an active system. Both investigations exhibit a remarkable agreement on all relevant length and time scales. The results of this work were recently published in the journal *Science* (see section 2.5).

It should be noted that the introduced computational model represents a new simulation paradigm for active matter systems, which is flexible enough to be extended to a variety of different model systems. It is therefore also a key method for project 1 in chapter III.

### 2.1 The actomyosin gliding assay

#### 2.1.1 Background

In general, gliding assays are *in vitro* experiments that assess the active mechanics of protein filaments and motor domains, which are found in many living systems. They require several key ingredients: 1) protein filaments, 2) molecular motors, 3) a 'fuel', and 4) a proper biochemical environment, that is, a substrate surface and an aqueous bulk that stabilize the filament-motor complex. In the following, we concentrate on the *actomyosin gliding assay* or *actin motility assay*, which was first introduced by Sheetz et al. in 1983 [124] (another prominent example would be microtubule gliding assays [24, 25, 125]).

In the actomyosin gliding assay, actin filaments move on a flat 'lawn' of immobilized *heavy mero-myosin* (HMM) motors (Fig. II.14), similar to 'crowd-surfing' singers at a concert: HMM is a part of the non-processive motor protein myosin II of animal muscles, and consists of a head and a tail domain; HMM tail domains are then 'glued' to a flat cover slip using nitrocellulose, with the active head domain being able to bind to ambient actin filaments (F-actin). Upon hydrolysis of adenosine-tri-phosphate (ATP) as an energy source, HMM exerts a unidirectional power stroke on the actin filament - this is the active force (Fig. II.14(b)). Typically, actin filaments are a few  $\mu\text{m}$  long and each filament is simultaneously pushed by many motors in the same direction, resulting in a processive and polar propulsion along the filament contour. This creates a two-dimensional active motion of actin

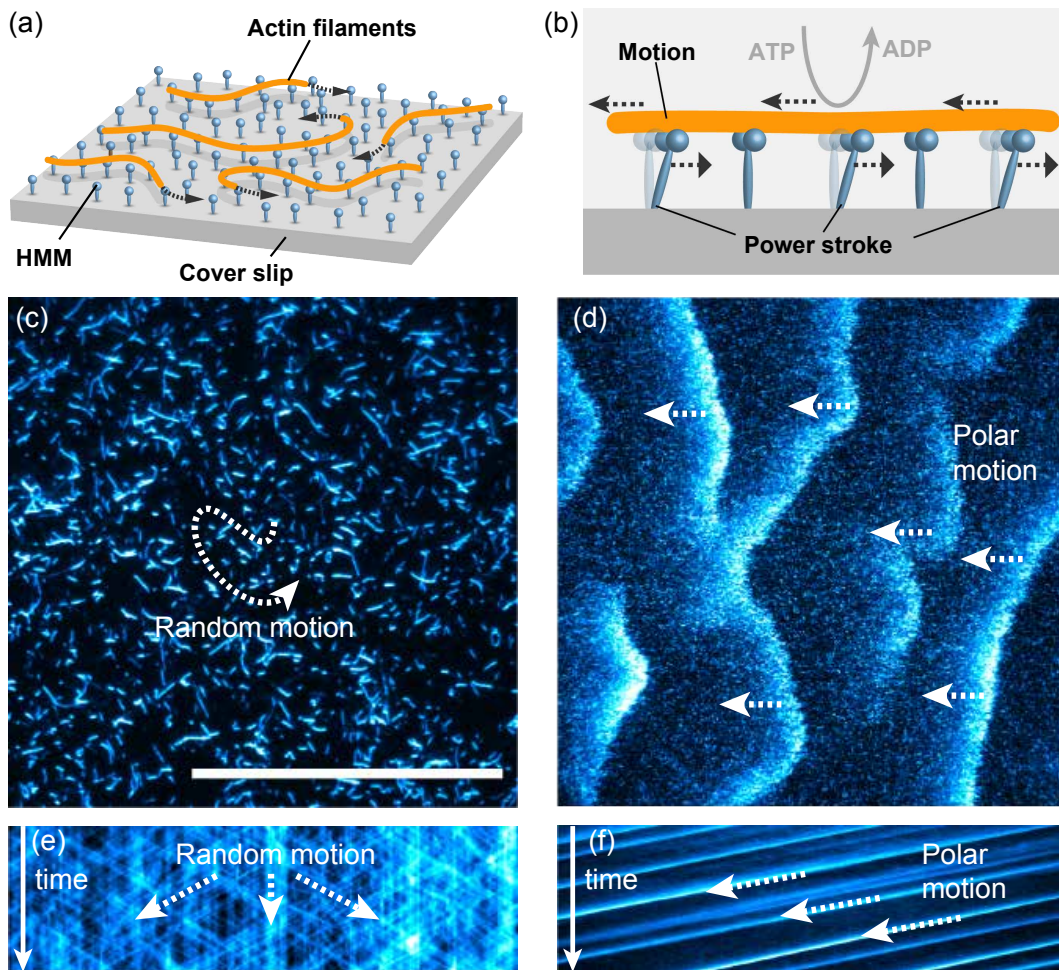


**Figure II.14** (a) Illustration of the actomyosin gliding assay. HMM motor proteins are fixed to the surface of a coverslip and actin filaments (orange) can bind to them. (b) Side view of the actomyosin complex: HMM motors can perform unidirectional power strokes upon ATP consumption, which effectively pushes the actin filament forward. (c,d) Fluorescence images of the gliding assay at (c) low actin densities (monomeric concentration  $1\mu M$ ) and (d) large actin densities ( $10\mu M$ ) exhibit a disordered global state and the large-scale formation of polar fronts, respectively. The white arrows depict the collective orientations (absent in (a)), which is also reflected by the corresponding kymographs in lower panels of (c,d) to illustrate the motion of patterns (arbitrary time scale). Scale bar corresponds to  $50\mu m$ . Please refer to section 2.3 for further details.

polymers on the cover slip. The interplay between the discrete and fluctuating nature of force generation with the elastic properties of actin leads to anomalous filament bending [126], and importantly, to random reorientations of the filament tip which result in orientational diffusion and hence a persistent random walk.

### 2.1.2 Controlling collective motion

While actomyosin gliding assays at low filament densities are useful to understand the mechanisms of single filament dynamics (Fig. II.14(c)), gliding assays at high filament densities have proven themselves as a standard experiment to examine collective motion in active systems. In the latter case, actin filaments self-organize into large-scale, coherently moving clusters or front-like structures [21, 22] (Fig. II.14(d)), akin to the phenomenology of the polar active system of the Vicsek model: beyond a critical actin filament density polar order emerges, accompanied by a subsequent phase separation into dilute disordered regions and dense ordered regions. It was shown that colliding actin filaments in the assay exhibit alignment interaction (Fig. II.15(a)), possibly mediated by short-ranged biochemical, hydrodynamic, or steric interactions [26, 37].

Yet, it is misleading and dangerous to interpret these phenomenological similarities with an overall equivalence of experiment and theory. In fact, the properties of microscopic interactions of actin filaments - which are indispensable for the ordering transition - refute theoretical predictions about the onset of order [26, 118]. In essence, it is not clear how the character of local alignment, that is, binary collisions between two actin filaments (Fig. II.15(b)), can be reconciled with simplified collision rules which are at the heart of active matter theories like the Vicsek model (compare also with Fig. II.2(b,c)): first, the overall degree of alignment is too weak to lead to collective ordering at any density, at least if higher-order interactions and correlations are neglected. Second, the *symmetry* of alignment is not perfect but a malleable hybrid of both polar and nematic contributions, with gradual instead of full alignment. Overall, a framework is lacking that explains both why collective order emerges at all, and how a particular symmetry is chosen.

Motivated by these questions, our collaborator Ryo Suzuki recently sought to gain experimental control over the microscopic interactions, which are at the root of collective motion. To this end, he added the crowding agent polyethylene glycol (PEG 35kD) to the assay buffer to change alignment interactions of filaments by additional depletion forces (Fig. II.15(c)) mediated by large PEG molecules, which press actin filaments down on the HMM lawn. The so-enhanced excluded-volume interactions are intrinsically nematic in nature. As a result, the statistics of binary collisions in the dilute system changed very slightly - towards a gradually stronger and more nematic alignment (Fig. II.15(a)). For more details on the experimental method, please refer to section 2.3.3. Surprisingly, for large actin densities, the collective effects changed drastically: instead of polar order, large-scale nematic order emerged. Also, the system phase-separated into a network of dense, nematic trails or streams (Fig. II.15(d)): while single filaments move to equal amounts in both directions and eventually exit or enter a trail from the surrounding dilute

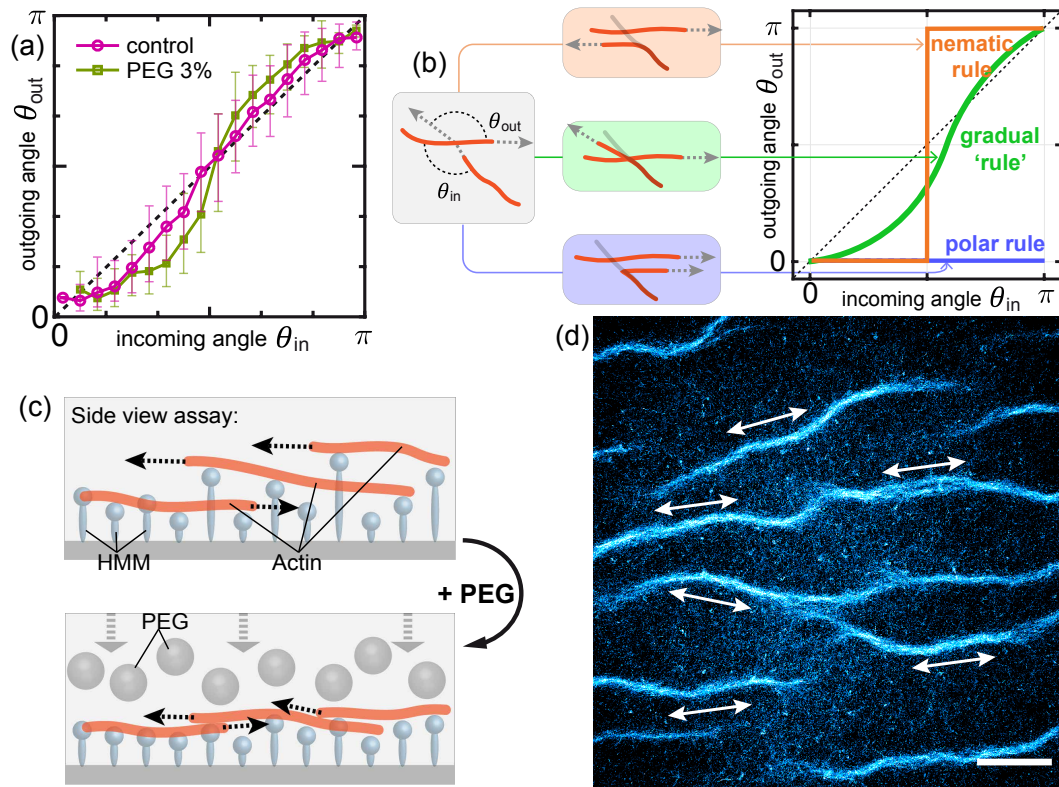


**Figure II.15** (a) Alignment of binary collision curves of the actomyosin assay: the standard assay (purple line) exhibits a small bias towards polar scattering (data taken over 1113 collisions, see also Ref. [26]). With 3% PEG (w/v, green line) alignment becomes stronger for both polar and anti-polar parts (389 collisions). Error bars: 1 standard deviation. (b) Illustrative comparison of Vicsek-like alignment rules (blue line: polar, orange line: nematic) with gradual alignment of mixed symmetry (green line) of binary filament collisions. (c) Illustration of the effect of PEG on filament interactions: PEG molecules 'squeeze' filaments tighter on the HMM lawn which increases excluded-volume, nematic interactions. (d) Fluorescence image of self-organized nematic trails in the PEG-assay (3% PEG and  $5\mu M$  monomeric actin). While individual filaments are motile, the pattern itself is almost static. Image is a time-average over 100s, scale bar is  $50\mu m$ . White arrows denote the nematic axis. Please refer to section 2.3 for further details. The data from (a,d) is also published in Ref. [127].

regions, the network itself appears rather static (please refer to section 2.3.2 for a detailed analysis). It was unexpected to see that the phenomenology of the collective effects was so sensitive with respect to minuscule changes on the microscopic scale, for which there was no proper theoretical framework available. These experimental results were the starting point for our subsequent investigation

and will be characterized more thoroughly after the presentation of our theoretical approach in the next section.

## 2.2 Multi-scale simulations of the gliding assay

The incompatibility of the kinetic Boltzmann approach for Vicsek-like theories [42, 54] with the collision properties of the motility assay (which predicted a negative critical density of the ordering transition [26]) indicated that the underlying assumptions - the negligence of many-body interactions and correlations - may actually be essential for the formation of collective effects. We therefore resorted to a computational model to overcome these analytical limitations, and to simply simulate the motility assay 'bottom-up'. Still, this was not just straightforward to achieve, and merely shifted the challenge towards different requirements: 1) the microscopic details of propelled actin filaments and their interactions must be described sufficiently well, 2) simulations need to be 'all scale' with feasible simulation times, i.e. without introducing any truncation bias, 3) identification of relevant parameter regimes, phenomena, and mechanisms. Unfortunately, the full Brownian dynamics simulations of semiflexible polymers introduced in section 1.2 are not directly applicable, since alignment is not explicit here but only results from steric effects. Furthermore, displaying the full two-dimensional diffusion dynamics of thousands of polymers is neither necessary nor computationally feasible. In the next sections we will first introduce the model details and their computational implementation, followed by the analysis of properties on the smallest 'particle' scales, and then the full specification of collective phenomena.

### 2.2.1 Modelling weakly-aligning self-propelled polymers (WASP)

Intuitively, the key element of any model of the actin gliding assay is the actin filament, which is attached to a cover slip by a number of HMM motors that provide the active force (Fig. II.14(b)). Since the full microscopic dynamics are neither completely known nor necessary to understand the physical processes of the system, we have to coarse-grain the microscopic picture sufficiently. For simplicity, we model actin filaments as identical polymers of length  $L$  and width  $d$ , with a slender aspect ratio  $L/d \gg 1$  (Fig. II.16(a)). Actin in the experiment is roughly  $1 - 10 \mu m$  long and has a molecular diameter of  $10 nm$ . While the effective interaction range for alignment processes is unknown, it is likely on the same scale as the diameter  $d$ . Hence, as long as the aspect ratio is  $L/d \gg 1$  this uncertainty should not be relevant for the scattering kinetics. Furthermore, filaments are discretized into  $N$  beads which are smoothly connected by  $N - 1$  segments. In general,  $N$  needs to be as large as possible to properly resolve a deformed polymer contour, which is at the expense of numerical performance. As will be detailed later, strong filament

bending will however only rarely occur for our relevant parameter regime, which allows us to set  $N \approx 5 - 10$  at relatively small values.

The filament propulsion due to HMM also requires coarse-graining and is modelled as a continuous active force that acts strictly parallel to the local contour, rather than a full stochastic process that involves a complicated interplay of the mechanical properties of actin and myosin (Fig. 11.14(b)). Furthermore, due to the anchoring of the filament onto the two-dimensional substrate, filament motion perpendicular to the contour is strongly suppressed, except for the front tip of the actin filament. Consequently in our model, motion of the polymer tail is only determined by the active force, and merely follows the front tip. This 'trailing' motion drastically affects the collective behavior when compared with non-trailing rods, as was recently observed in Brownian dynamics simulations of penetrable bead-spring rods [128], where the interplay of crowding, elastic frustration, and active forces lead to large-scale sideways motion of filaments, resembling a 'snow-plow' structure. For the actin gliding assay, such a behavior is not observed. As for the actin tip, the underlying microscopic processes are unclear and may involve an interplay of thermal forces, environmental heterogeneities, and HMM motor strains with the elastic properties of the free polymer end. Irrespective of these details, their effect amounts to an effective persistent random walk of the filament contour with a two-dimensional persistence length of about  $12\mu m$  [129]. Likewise, the polymer tip in our model has an internal direction of motion, which is subject to angular diffusion that results in a persistent random walk.

Taken together, a contour has different dynamics for the tip (at contour index  $i = 0$ ) and for the tail (at contour indices  $i \in \{1, \dots, N - 1\}$ ). The corresponding equations of motion for a single, *unperturbed* filament  $n$  read<sup>2</sup>:

$$\frac{\partial}{\partial t} \mathbf{r}_0^{(n)} = v_0 \mathbf{u}_0^{(n)} = v_0 \begin{pmatrix} \cos \theta_0^{(n)} \\ \sin \theta_0^{(n)} \end{pmatrix}, \quad (11.25)$$

$$\frac{\partial}{\partial t} \theta_0^{(n), \text{unperturbed}} = \sqrt{\frac{2v_0}{L_p}} \xi^{(n)}, \quad (11.26)$$

$$\frac{\partial}{\partial t} \mathbf{r}_i^{(n)} = K_s \frac{\mathbf{u}_{i-1}^{(n)} + \mathbf{u}_i^{(n)}}{2} \left( \left| \mathbf{r}_i^{(n)} - \mathbf{r}_{i-1}^{(n)} \right| - \frac{L}{N-1} \right), \quad (11.27)$$

where  $\mathbf{r}_0^{(n)}$  is the position,  $\mathbf{u}_0^{(n)}$  the director, and  $\theta_0^{(n)}$  the direction of the tip (note that we omitted the superscript *unperturbed* for brevity).  $v_0$  is the (constant) propulsion velocity,  $L_p$  the persistence length, and  $\xi^{(n)}$  an angular random white

<sup>2</sup> It is very easy to extend the equations of motion towards chiral active matter as in section 1 by adding a rotation rate  $\omega_0 = v_0 \kappa_0$  to Eq. (11.26) ( $\kappa_0$  being the curvature of motion).

noise with zero mean and unit variance. Note the equivalence of Eqs. (II.25, II.26) with the equations for a simple active particle Eqs. (II.1). Eq. (II.27) describes the trailing of tail segments  $i$ , which is formally similar to an asymmetric spring force (i.e. only acts onto the tail-sided neighbor) that maintains a constant cylinder length of  $\frac{L}{N-1}$ , where  $K_s$  is a sufficiently strong spring constant ( $K_s \gg v_0(N-1)/L$ ). The tail directors  $\mathbf{u}_i^{(n)}$  are given by the renormalized connecting vectors  $\mathbf{r}_{i-1}^{(n)} - \mathbf{r}_i^{(n)}$ .

Up to now, the model only describes the stochastic dynamics of a polymer tip with a strictly following tail end. To couple a system of many active filaments, interactions with realistic assumptions are needed (Fig. II.15(a)): specifically, for colliding actin filaments, we expect only local interactions when a tip touches another filament segment, or comes sufficiently close to it. Since actin polymers are smooth objects (apart from cues on the submolecular scale), this interaction should only depend on the local geometry (i. e. positions and orientations) of the collision partners, and only act on polymer tips which are not anchored to the substrate. In general, these interactions may have an arbitrary contribution of forces and torques that act upon the tip position and its orientation, respectively. Yet it was observed that interactions in the actin motility assay are extremely weak [26]: upon collision, filaments will most likely cross each other without noticeable stopping, which might come from the roughness of the HMM surface with many filament layers. In addition, filaments experience a very slight reorientation depending on the relative incoming collision angle (Fig. II.15(a)). Hence in our strictly two-dimensional model we further assume that filaments are penetrable objects which are dominated by local alignment interactions. Repulsive forces may still be present, but small. We will henceforth refer to our active objects as **Weakly-Aligning Self-propelled Polymers (WASP's)**.

In the WASP model, alignment is provided by the presence of a local alignment potential along any filament contour. This potential has both polar and nematic contributions, respectively, and, since it acts only upon tip directions, gives rise to canonical torques that add up to the Langevin Eq. (II.26):

$$\frac{\partial}{\partial t} \theta_0^{(n)} = -\frac{\delta H_0^{(n)}}{\delta \theta_0^{(n)}} + \sqrt{\frac{2\nu}{L_p}} \xi^{(n)}. \quad (\text{II.28})$$

Here  $H_0^{(n)} = \sum_m \int_0^L ds U_{m,s}^{(n)}$  is the total sum of all alignment potentials that are present at the tip  $n$ , running over all filaments  $m$  and respective contours  $s$ . Since we require both potentials and torques to be local and continuous, every potential is a smooth ramp which is only present in the area covered by a polymer, and has

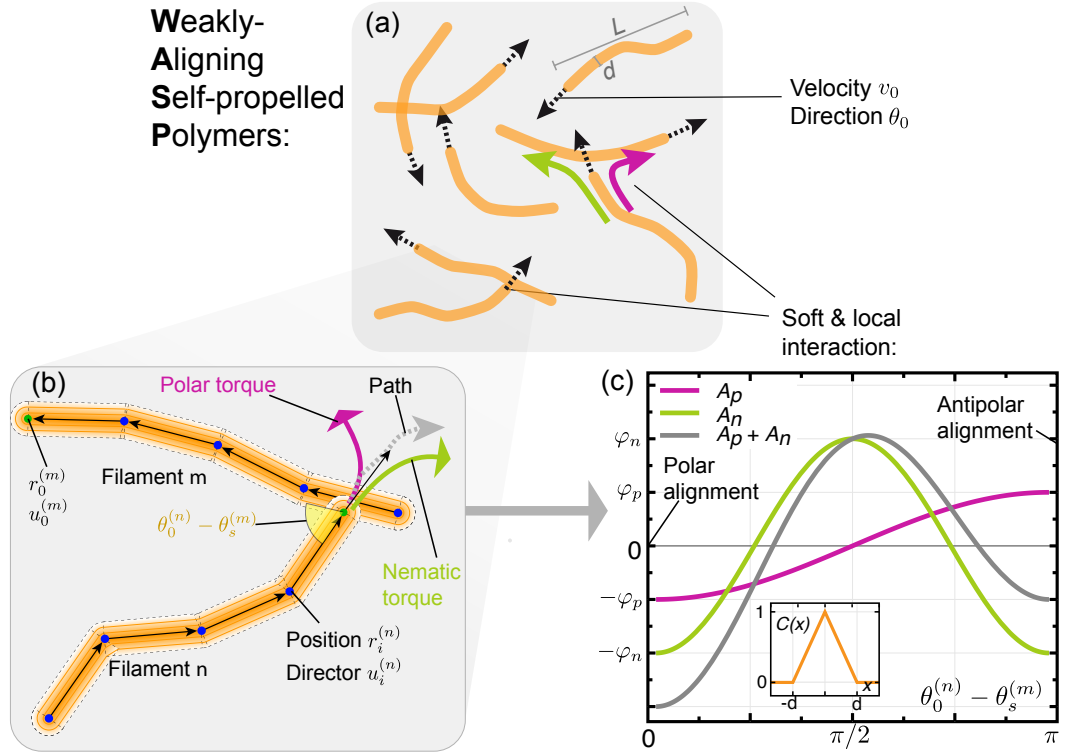


**Figure II.16** (Illustration of the WASP model: (a) a system of  $M$  filaments of length  $L$ , width  $d$ , velocities  $v_0$ , and tip orientations  $\theta_0^{(m)}$  which interact via gradually-aligning collisions. (b) Close-up of filament collision shows the continuous envelope of a filaments' contour and its local tangential direction (orange lines). The collision is a continuous process of the filament tip (green point) in the landscape of the adjacent tail contour, acting as a polar and a nematic torque on the tip director. (c) Angular part of the alignment potential Eq. (II.30) visualizes the minima of polar and nematic symmetry (purple and green line, respectively) and the mixed case (gray). Inset: linear ramp of potential cross section Eq. (II.31).

the form:

$$U_{m,s}^{(n)} = C \left( \left| \mathbf{r}_0^{(n)} - \mathbf{r}_s^{(m)} \right|_{shDist} \right) \times [A_p(\theta_0^{(n)} - \theta_s^{(m)}) + A_n(\theta_0^{(n)} - \theta_s^{(m)})] \quad (II.29)$$

with the polar and nematic terms

$$A_p(\theta) = -\frac{\varphi_p v_0}{d} \cos \theta, \quad A_n(\theta) = -\frac{\varphi_n v_0}{d} \cos 2\theta, \quad (II.30)$$

and a linearly increasing ramp

$$C(x) = \begin{cases} 0 & \text{for } x > d \\ (d - x)/d & \text{else} \end{cases}. \quad (\text{II.31})$$

The amplitudes  $\varphi_{p,n}$  are scales of the typical angular displacement upon a single collision, which can be obtained by  $\theta_0^{(n)} \cdot \Delta t_{cross} \propto \frac{\varphi_{p,n} v_0}{d} \Delta t_{cross} = \varphi_{p,n}$  since the crossing time is  $\Delta t_{cross} \propto d/v_0$ . Note how the angular dependencies in Eq. (II.30) discriminate the polar direction (via  $\cos\theta$ ) and the nematic axis (via  $\cos 2\theta$ ) of a filament (Fig. II.16(c)). In Eq. (II.29),  $|\dots|_{shDist}$  denotes the shortest possible distance between the tip position and the contour of an adjacent polymer.  $\theta_s^{(m)}$  is the local tangential direction at the contour position  $s$ . In this way, alignment of filaments strictly takes place upon local contact, which allows to resolve collisions continuously in space and time without needing some averaging procedure like in Vicsek-type models [49, 91, 130]. Yet these definitions require a fine resolution of contours to obtain faithful values of the tangential direction  $\theta_s^{(m)}$  and the tangential position  $\mathbf{r}_s^{(m)}$ . Fig. (Fig. II.16(b)) shows the continuous envelope of a filament; ambiguous regions exist at the inner and outer bends of segment joints which cannot be approximated by cylinders. Outer gaps are therefore 'filled' by circular sectors and the inner ones by the average potentials of the overlapping segment cylinders. While this is numerically tedious to implement, it creates a smooth filament shape without spurious friction effects, like it would be the case for the bead-spring model presented in section 1.2. Alignment is hence exclusively set by the alignment parameters  $\varphi_p, \varphi_n$ .

So far, no repulsive force has been considered. However, for purely aligning filaments, there exists an unphysical fixed point of the alignment dynamics: since alignment maximizes contour overlap which is amplified by the amount of filaments, a singularity with all particles of a system on top of each other would be possible. Therefore, we added a very weak repulsion force  $-S \frac{\partial H_0^{\{n\}}}{\partial \mathbf{r}_0^{\{n\}}}$  with a small amplitude  $S \ll v_0$  to Eq. (II.25) acting only on tips and being proportional to the sum of all linear ramps (Eq. (II.31)). This caps the amount of locally overlapping filaments, proportional to  $v_0/S$ , which did not change the phenomenology of self-organization. To complete the model preferences, we insert  $M$  active filaments into a system of size  $L_{box}$  with periodic boundary conditions and variable initial conditions, and let the dynamics defined by Eqs. (II.25-II.31) evolve until a simulation time  $t_{max}$ .

The parameters of the WASP model are summarized in Table II.1. In the following chapters we will fix many of the above quantities, and only vary a few. If not stated otherwise, we fixed  $L, d, N, v_0, K_s$ , and  $S$  as displayed above. While  $N$  and  $K_s$

Single particle variable	Typical values	Explanation
$L$	6.3	Length of a contour.
$d$	0.3	Width of a contour, such that $L/a \gg 1$ .
$N$	5	Contour discretization. For weakly bending contours, $N$ can be assumed small.
$v_0$	1	Active velocity of a contour.
$L_p$	200	Persistence length of the contour and the path of polymer.
$K_s$	200	Segment stretching constant, such that $K_s \gg v_0(N - 1)/L$ maintains the segment length.
Interaction variable	Typical values	Explanation
$\varphi_p$	-	Polar alignment strength.
$\varphi_n$	-	Nematic alignment strength.
$S$	0.1	Repulsive force amplitude.
System variable	Typical values	Explanation
$L_{box}$	-	Box length of the system, with an area $A = L_{box}^2$
$M$	-	Number of particles, defining a density $\rho_0 = M/A$ .
$t_{max}$	-	Simulation time.

**Table II.1** Typical parameters of the WASP simulations. If not explicitly stated otherwise, we fixed the corresponding values as given here. A '-' signals a variable parameter.

are only auxiliary values to control the discrete nature of the model,  $L$  is a typical length scale that drops out when one rescales the particle density with  $\rho_0 L^2$ . When the aspect ratio  $L/d$  is large, filaments become slender objects with effectively no dependence on  $d$ . Likewise,  $v_0$  only sets the time scale of the dynamics and can be set to 1. The remaining physical quantities are hence the persistence length  $L_p$ , the alignment strengths  $\varphi_p, \varphi_n$ , and the density  $\rho_0 L^2$ . For future relevance we will further define the *relative alignment strength*  $\alpha := \varphi_n/\varphi_p$ , which measures the balance between the polar and the nematic term.

### 2.2.2 Implementation of WASP simulations

The computational implementation of the WASP model defined above is relatively straightforward. Using the C++ language, the simulation program creates a collection of  $M$  polymer objects and embeds them into a global system. Using a simple Euler forward integration, the forces and torques that act on every contour point are first calculated using Eqs. (II.25,II.28,II.27) and then displaced by a small amount  $\Delta t \ll 1$  to obtain the updated positions and orientations. While the program structure appears easy, the implementation of the interaction needs to be handled with great care: naively,  $M$  filament tips would in principle be able to each interact with all  $M$  filaments, each with  $N$  beads, requiring  $\mathcal{O}(M^2)$  operations at every time step. This would drastically reduce performance and restrict the maximally feasible  $M$  to a few hundred. Of course, only a small fraction of all possible interactions really contribute to the dynamics because interactions are strictly local. It remains to efficiently identify those few collisions. This can be done by decomposing the system into sufficiently small compartments or cells, and only consider interactions inside cells and to neighboring cells (Fig. II.17), which formally reduces the computational effort to  $\mathcal{O}(M)$  [131]. Note that the iteration over cells requires proper bookkeeping to avoid repeated calculations. Furthermore, we can assume that particles will only be displaced by a small amount  $\sim v_0 \Delta t$ . As a result, a re-iteration of the cell lists is not necessary at every time step: when calculating interactions of a particle, a new interaction partner would first have to cross the layer of neighboring cells to come close enough. Reassigning the cell list only before this distance is crossed further reduces the computational effort, which is referred to as Verlet algorithm [131]. Using OpenMP allowed us to heavily parallelize the simulation program, and to achieve large simulation times for systems of more than  $\mathcal{O}(10^6)$  discretized polymers using a single 32-core CPU. In practice, we fixed  $\Delta t = 10^{-3}$  which is small enough to even resolve the shortest crossing of polymer contours very smoothly within  $v_0 \cdot d/\Delta t = \mathcal{O}(10^3)$  steps.

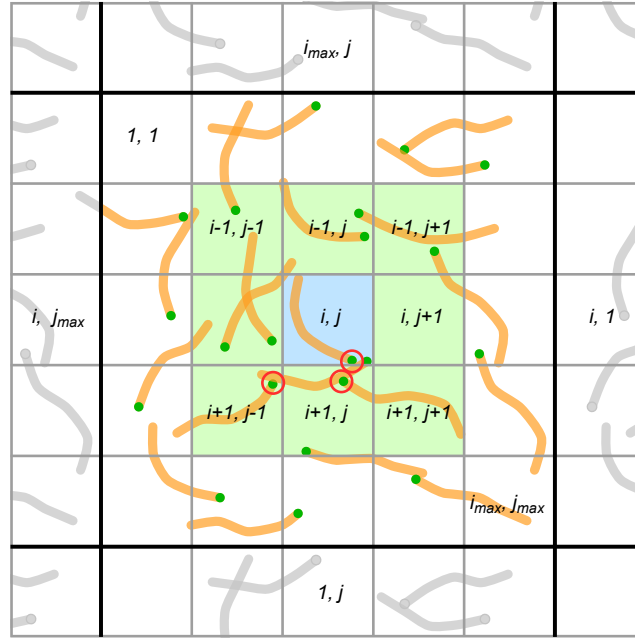


**Figure II.17** Illustration of the cell algorithm of a WASP system to calculate interactions with periodic boundary conditions: first, all  $N \cdot M$  discretized contour points are cast into a periodic list of dimension  $(i_{max}, j_{max})$ . Then, for every filament tip (green dots) in a cell  $(i, j)$  (blue color), all pairwise interactions with all contour points within the cell and the adjacent cells (green color) are calculated. This is then iterated over the array of cells. The minimal cell size to include all possible interactions within the shell of neighbor cells is given by  $L_{cell} \geq \sqrt{(L/(N-1))^2 + (d/2)^2}$ . Note that only very few interactions take place (red circles).

### 2.2.3 Single filament properties

Before we investigate the full dynamics of a crowded model simulation which is similar compared to the actin motility assay, we will briefly present the physical properties of individual WASP's and the features of the microscopic interaction, which is the basis on which we will compare local properties with the experiment. For simplicity, we set  $L = 6.3$  throughout this section.

#### Orientational decorrelation:

For a single filament without interaction, the dynamics follow Eqs. (II.25-II.27) and hence perform a persistent random walk as noted in the introduction of this chapter. As can be seen in Fig. II.18(a), the autocorrelation function of the tip orientation follows the predicted decay law  $\langle \mathbf{u}_0(t) \mathbf{u}_0(0) \rangle = \exp(-t v_0 / L_p)$  almost perfectly; likewise, the mean-squared displacement of a filament is very close to the prediction  $\langle (\mathbf{r}(t) - \mathbf{r}(0))^2 \rangle = 2L_p v_0 t (1 - \frac{L_p}{v_0 t} (1 - \exp(-v_0 t / L_p)))$  and shows the cross over

from ballistic to diffusive motion at a length scale of  $L_p$  in Fig. II.18(b). This agreement is not particularly surprising, since the dynamics is, so far, exclusively set by the dynamics of the filament tip.

### Binary collisions:

Next we turn towards the effect of the alignment interactions defined in Eqs. (II.28- II.31). To this end, we only consider binary interactions as in the experiment and slightly modify the simulation: we randomly distribute two filaments in a small system and let it evolve until the first filament contact, which defines the pre-collision angle  $\theta_{in}$  between the director of the colliding tip and the 'target' contour. Then, subsequently, aligning torques act on the tip until it has completely crossed the adjacent contour (see illustration in Fig. II.16(b)). At this point, the post-collision angle  $\theta_{out}$  is recorded. After this event, the iteration begins anew until sufficiently many collisions have been recorded to obtain statistical properties. Similar to the experiment where the addition of a depletion agent alters the nematic alignment, we will first set the polar alignment strength to a fixed value  $\varphi_p = 0.036 \cong 2.1^\circ$  and concentrate on varying the nematic strength  $\varphi_n$  (and hence the relative alignment symmetry  $\alpha = \varphi_n/\varphi_p$ ). Figure II.18(c) depicts 20,000 individual collision events and an averaged curve  $\bar{\theta}_{out}(\theta_{in})$  at  $\alpha = 2.75$  and a persistence length  $L_p = 200 = 31.7L$ . Interestingly, the binary collision statistics hardly yields a significant signal  $\bar{\theta}_{out}(\theta_{in})$  in the background of fluctuations, similar to the experimental curve at zero PEG (Fig. II.15(a)); in particular, the standard deviation at any given  $\theta_{in}$  is larger than the deflection  $\Delta := \bar{\theta}_{out} - \theta_{in}$  (see error margins in Fig. II.18(d)). Furthermore,  $\bar{\theta}_{out}$  is slightly biased in a polar fashion, that is, acute incoming angles  $\theta_{in} < \pi/2$  are gradually more aligned than obtuse angles  $\theta_{in} > \pi/2$  (Fig. II.18(c)). When the relative alignment strength is increased to  $\alpha = 6.25$  (Fig. II.18(d)), the shape of  $\bar{\theta}_{out}$  becomes more nematic and more pronounced, albeit still very close to the previous curve. This behavior is very similar to the actin motility assay with PEG, and correctly captures the microscopic interactions. Fig. II.18(f) shows how the symmetry of alignment gradually changes from a polar symmetry (low  $\alpha$ ) to a nematic symmetry (large  $\alpha$ ) with  $\Delta$  being anti-symmetric around  $\pi/2$ . Furthermore, the binary collision statistics is sensitive to the persistence length, because there is a finite duration of every collision during which angular diffusion takes places. The resulting randomization of the outgoing angle  $\theta_{out}$  is thus strongest for acute angles  $\theta_{in} \rightarrow 0$  and obtuse angles  $\theta_{in} \rightarrow \pi$ , as can be seen by comparison with the deterministic case for  $L_p = \infty$  (Fig. II.18(d)). Note that even for this limiting case there is a finite variance of  $\theta_{out}$  due to averaging over arbitrary impact parameters of the collision partners. In the limit  $L_p \rightarrow 0$ ,  $\theta_{out}$  approaches  $\pi/2$  which is the average angle between two random orientations.

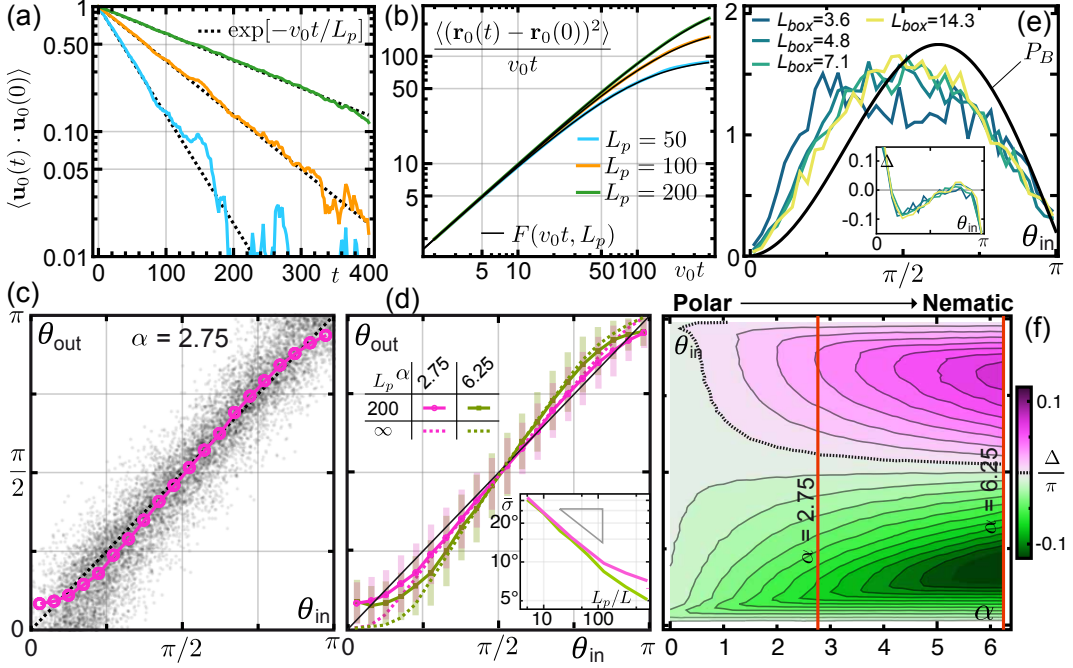


**Figure II.18** (a) Orientational autocorrelation  $\langle \mathbf{u}_0(t) \cdot \mathbf{u}_0(0) \rangle$  of polymer tips for different values of  $L_p$ , each averaged over 2000 filaments. Dashed black lines depict the theoretical prediction  $\exp(-v_0 t / L_p)$ . (b) Rescaled mean-squared displacement  $\langle (\mathbf{r}(t) - \mathbf{r}(0))^2 \rangle / (v_0 t)$  of WASP filaments for different values of  $L_p$ . Black solid lines denote the theoretical prediction  $F(v_0 t, L_p) := 2L_p(1 - \frac{L_p}{v_0 t}(1 - \exp(-v_0 t / L_p)))$ . For both (a,b): blue line:  $L_p = 50$ , orange line:  $L_p = 100$ , green line:  $L_p = 200$ . (c) Binary collision statistics at  $\alpha = 2.75$  for 20,000 individual collisions (grey dots). The averaged curve  $\bar{\theta}_{out}$  was obtained by subdividing the range  $\theta_{in} \in [0, \pi]$  into bins of size  $\pi/20$ . (d) Comparison of binary collision curves for different values of  $\alpha$  and  $L_p$ . Light purple and light green error bars denote 1 standard deviation for the curves  $L_p = 200$ . Inset: dependence of the averaged deviation  $\bar{\sigma} = \int_0^\pi d\theta_{in} \sqrt{\text{Var}[\theta_{out}]}$  on the persistence length for  $\alpha = 2.75$  (green line) and  $\alpha = 6.25$  (purple line). (e) Distribution function  $\Gamma(\theta_{in})$  for different box sizes and  $\alpha = 1.75$ . The black line depicts the Boltzmann cylinder approximation Eq. (II.32). Inset: corresponding deflection  $\Delta$ . (f) Contour map of the deflection  $\Delta$  as a function of  $\alpha$  ( $L_p = \infty$  for simplicity) shows the transition from a polar to predominantly nematic collision character, which is anti-symmetric around  $\pi/2$ . Vertical red lines depict the corresponding curves from (d).

For  $L_p = 200 = 31.7L$ , the averaged deviation  $\bar{\sigma} = \int_0^\pi d\theta_{in} \sqrt{\text{Var}[\theta_{out}]}$  is about  $15^\circ$  (inset of Fig. II.18(d)) which roughly matches the corresponding values of the actin experiment in Fig. II.15(a). Therefore, we will fix  $L_p = 200$  in the following analysis of the collective properties. To test the robustness of the collision algorithm, we also recorded the distribution  $\Gamma(\theta_{in})$  of incoming angles  $\theta_{in}$  as a function of the simulation box size  $L_{box}$ , and compared it with the theoretical prediction of the Boltzmann scattering cylinder of rods  $P_B(L/d, \theta_{in})$ , which can be derived by considering the scattering cross section of a rod that moves relative to the rest frame of the other one [26]:

$$P_B(L/d, \theta_{in}) \propto \left| \sin \frac{\theta_{in}}{2} \right| \left( 1 + \frac{L/d - 1}{2} \sin \theta_{in} \right). \quad (\text{II.32})$$

As can be seen in Fig. II.18(e) there is indeed a dependence on the box sizes for values of  $L_{box} \lesssim 10L$  which comes from a selection bias of  $\theta_{in}$ . For larger  $L_{box}$ ,  $\Gamma$  still deviates from the rod approximation  $P_B(L/d, \theta_{in})$  (using  $L/d = 21$ ) such that acute angles  $\theta_{in} < \pi/2$  are more frequent, which also coincides with the scattering statistics of the experiment [26, 129]. Note that irrespective of  $L_{box}$ , the angular deflection  $\Delta$  remains unaffected.

#### Low-density correction of decorrelation:

When we consider a system with a sufficiently low homogeneous density  $\rho_0 L^2$ , no collective order emerges and the system resembles a disordered, isotropic gas (Fig. II.19(a)) similar to the experimental state (Fig. II.14(c)). For this weakly-interacting system we have to correct the single filament dynamics with respect to random collision which, on average, do not create macroscopic order. Let us re-derive an expression for the orientational autocorrelation  $\langle \mathbf{u}_0(t) \mathbf{u}_0(0) \rangle = \langle \cos[\Delta\theta] \rangle$  with  $\Delta\theta = \theta_0(t) - \theta_0(0)$ : using Isserlis' theorem [132] to express arbitrary even modes as  $\langle \Delta\theta^{2n} \rangle \equiv \frac{(2n)!}{2^n n!} \langle \Delta\theta^2 \rangle^n$  we obtain in general

$$\begin{aligned} \langle \cos[\Delta\theta] \rangle &= \left\langle \sum_{n=0}^{\infty} \frac{(-1)^n \Delta\theta^{2n}}{(2n)!} \right\rangle \stackrel{!}{=} \sum_{n=0}^{\infty} \frac{(-1)^n (2n)! \langle \Delta\theta^2 \rangle^n}{(2n)! 2^n n!} \\ &= \sum_{n=0}^{\infty} \frac{1}{n!} \left( -\frac{\langle \Delta\theta^2 \rangle}{2} \right)^n = \exp \left( -\frac{\langle \Delta\theta^2 \rangle}{2} \right) =: \exp(-Dt), \end{aligned} \quad (\text{II.33})$$

where we exploited that  $\langle \Delta\theta^2 \rangle = 2Dt$  corresponds to angular diffusion with a diffusion constant  $D$  that needs to be further specified. Without loss of generality,  $D = \frac{v_0}{L_p} + \frac{\epsilon^2}{\delta t}$  since decorrelation due to angular noise and random scattering are independent. Here  $\epsilon$  is the typical scale of deflection upon random scattering, and  $\delta t$  is the time between successive events. The former can be

estimated by the average angular displacement due to an alignment potential,  $\epsilon = \overline{|A_x d/v_0|} = \frac{1}{2\pi} \int_0^\pi d\theta |A_x(\theta) d/v_0| \approx \sqrt{\frac{1}{2\pi} \int_0^\pi d\theta (A_x(\theta) d/v_0)^2}$ , where the  $x$  in  $A_x(\theta)$  from Eq. (II.30) stands for polar ( $p$ ) or nematic ( $n$ ). Due to the independence of both contributions,  $\epsilon^2 = \overline{|A_p d/v_0|}^2 + \overline{|A_n d/v_0|}^2 \approx (\varphi_p^2 + \varphi_n^2)/2$ . Now  $\delta t$  is given by inter-particle distance  $l_{pp} = 1/\sqrt{\rho_0}$  divided by  $v_0$  and the hitting probability  $d_0/l_{pp}$  where  $d_0 = L/2$  is the scattering cross section of a rod of length  $L$ . Taken together, we obtain an expression for the angular persistence at finite density  $\rho_0$ :

$$D(L_p, \rho_0, \varphi_p, \varphi_n) = v_0 \left( \frac{1}{L_p} + \frac{\rho_0 L}{4} (\varphi_p^2 + \varphi_n^2) \right). \quad (\text{II.34})$$

Figures II.19(b-d) show the fitted decay constants for systems with different density  $\rho_0 L^2$  and  $\alpha$ , which all agree well with Eq. (II.34). Hence, we conclude that here collective effects are absent and do not influence the properties of single filaments.

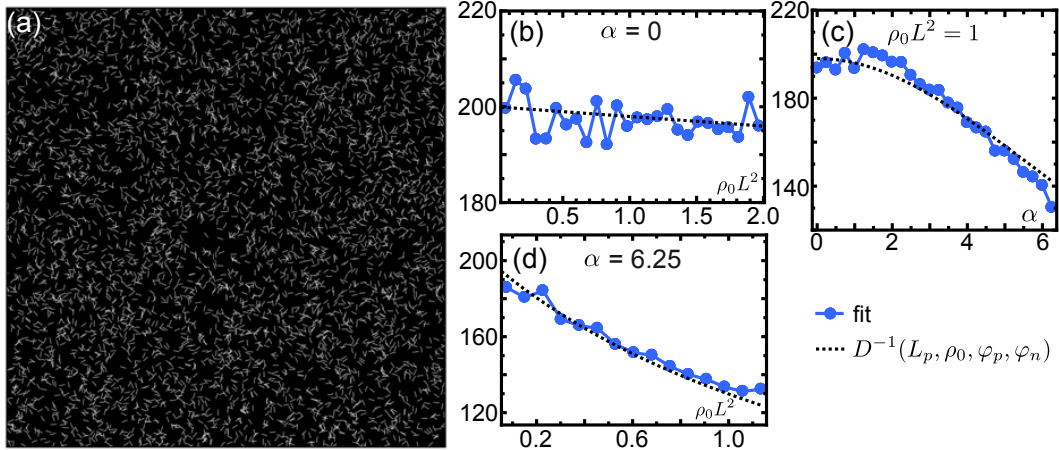


**Figure II.19** (a) Isotropic state of a low-density simulation of WASP's with  $\alpha = 0$ ,  $M = 5000$ ,  $L_{box} = 512$ , and hence  $\rho_0 L^2 = 0.76$ . (b-d) Fitted decay length  $\tau$  for  $\langle \mathbf{u}_0(t) \mathbf{u}_0(0) \rangle = \exp(-t/\tau)$  (blue circles) for (b,d) varying density and (c) varying relative alignment strength. The black dashed line depicts the prediction of Eq. (II.34). For (a-d),  $L_p = 200$ .

### 2.2.4 Emergence of collective order and patterns

Until now, we only considered the properties on the level of individual filaments. We showed that even in the presence of a few interactions in a system at low density or low interaction strength, the dynamics of individual filaments is still well described by a persistent random walker, and hence collective effects are absent. Rather paradoxically, orientational order decorrelates faster as  $\rho_0$  or  $\alpha$  is increased

(Eq. (II.34)). Yet, when these values are sufficiently large, macroscopic order and patterns emerge, as we will elaborate below.

As in the previous section, we first fix  $\varphi_p = 0.036$  and  $L_p = 200$  such that the collision curves of theory (Fig. II.18(d)) and experiment (Fig. II.15(a)) agree well. Note that setting  $L = 6.3$  we recover stiff polymers with a persistence length  $L_p/L = 31.7$ . Since the resulting filament path does not exhibit large bending events,  $N = 5$  is sufficient to resolve the dynamics. To analyze the collective order of the systems, we introduce the polar and nematic order parameters  $\mathcal{P}$ ,  $\mathcal{N}$ :

$$\mathcal{P} = |\langle \exp(i\theta_0) \rangle| \quad \text{and} \quad \mathcal{N} = |\langle \exp(2i\theta_0) \rangle|, \quad (\text{II.35})$$

where  $\theta_0$  are the tip orientations of filaments. Alternatively, one could have taken other definitions of a particles' orientation, like the angle of the end-to-end vector, which is equivalent on average. When a system is fully oriented in the same direction  $\mathcal{P}$  and  $\mathcal{N}$  both approach 1. Similarly, when it is fully disordered,  $\mathcal{P} \rightarrow 0$  and  $\mathcal{N} \rightarrow 0$ . Note that when the system perfectly nematically ordered, that is, all directors are equally split up into two opposite directions,  $\mathcal{P} = 0$  and  $\mathcal{N} = 1$ .

Upon simulating a more crowded system of WASP's with a density  $\rho_0 L^2 = 1.51$  in the presence of actin-like alignment interactions  $\alpha = 2.75$ , filaments begin to align and create macroscopic polar order  $\mathcal{P}$ , as can be seen in Fig. II.20(a-c). As a result, the system phase-separates into a high-density, polar-ordered moving front embedded in a low-density background, closely resembling the polar patterns found in the actin motility assay (Fig. II.14(d)) and similar to polar pattern formation in other types of active matter models [40, 42, 43, 45, 47, 51]. Within a short time, the system evolves a stationary global polar order  $\mathcal{P}$  (Fig. II.20(c)). In this stationary state, the orientational (or polar) autocorrelation  $\langle \cos[\Delta\theta(t)] \rangle$  as well as the nematic autocorrelation  $\langle \cos[2\Delta\theta(t)] \rangle$  drops from 1 to a nonzero value given by the corresponding order parameter (Fig. II.20(b)). Figs. II.20(d,e) show that the transition from a disordered to the ordered state is very discontinuous. We postpone an appropriate analysis of this phase transition towards the next chapter III. As can be seen by the self-organized pattern in Fig. II.20(a) the shape and orientation is enslaved to the periodicity of the finite simulation box, and may not illustrate the phenomenology of an infinitely large system. To this end, we have also simulated extremely large systems (Fig. II.20(f)) which does not exhibit a preferred box direction within the simulation time. Here one can observe that order emerges locally, and successively, but slowly, coarsens towards larger structures.

Interestingly, when increasing the relative alignment strength  $\alpha$  towards more nematically dominated collisions in Fig. II.20(e), the order parameter  $\mathcal{P}$  drops to zero, while  $\mathcal{N}$  remains finite. This indicates a transition of the global order from polar to nematic, as it was seen in the actin experiments. Indeed, when we closer examine the collective phenomena for  $\alpha = 6.25$ , the resulting pattern formation

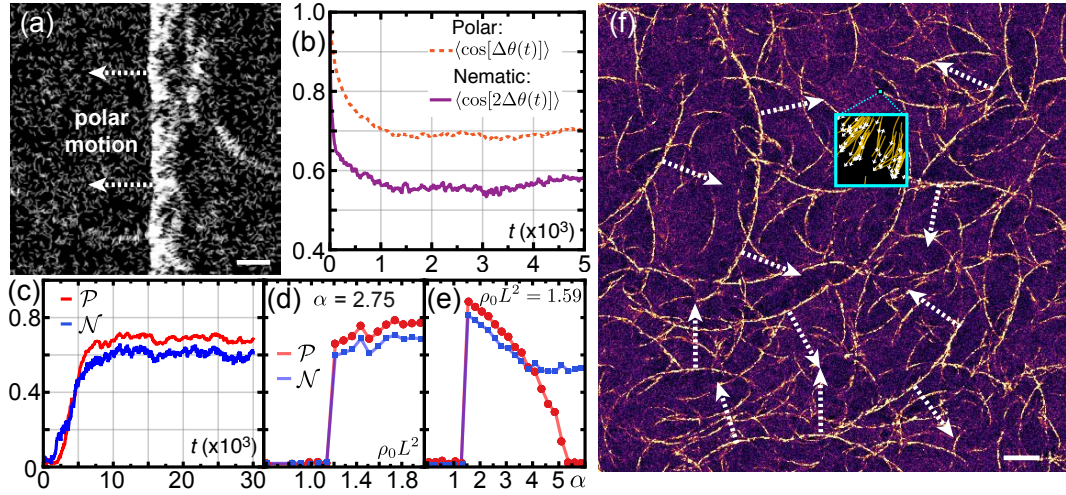


**Figure II.20** (a-c) Self-organization of polar order from disordered initial conditions for  $\alpha = 2.75$  and  $\rho_0 L^2 = 1.51$ . (a) Emergence of a travelling polar front of filaments, which exhibits a sharp front side and a smooth back side (white scale bar:  $20L$ ) in a system of 10,000 filaments. (b) Corresponding polar and nematic autocorrelation functions remain at a finite plateau values set by  $\mathcal{P}$  and  $\mathcal{N}$ . The decay time is dominated by the dwell time of filaments within the polar front. (c) Evolution of order parameters. (d,e) Stationary order parameters as a function of  $\rho_0$  and  $\alpha$ , respectively, show a discontinuous transition towards polar order. Note that for large  $\alpha > 5$  polar order vanishes completely while  $\mathcal{N}$  remains finite, indicating global nematic order. (f) Ultra-large-scale simulations of  $M = 2,176,000$  WASP's organize into polar patterns ( $\alpha = 3$ ,  $\rho_0 L^2 = 1.29$ ,  $L_{\text{box}} = 8192$ ). At a time  $t_{\text{max}} = 10^4$  the system is still far from stationarity. White arrows illustrate the motion of wave patterns, the white scale bar is  $100L$  long. The inset shows local filaments and their orientations.

has drastically changed: instead of polar fronts, a dense band of filaments emerges very quickly, with a globally nematic order (Fig. II.21(a-c)). The band itself remains static, while single particles locally move parallel to the band, and to equal amounts in opposite directions which is also reflected by the orientational autocorrelations (Fig. II.21(d)); while a nematic orientation remains, the polar orientation decays within a time  $\tau \approx 461$ , which represents the time scale upon which filaments flip their direction. Fig. II.21(e) shows that the transition towards nematic order is less discontinuous as the polar case.

While these simulations with system sizes  $L_{\text{box}} = 512$  exhibit nematic order and an accompanied phase separation into a high-density nematic trail surrounded by a dilute, disordered gas similar to Vicsek-type theories of active rods [52, 76, 78], it is still hard to assess if the emergent structures are really equivalent to those observed in the actin motility assay. This is owed to the small system sizes, which forbid a proper comparison of the patterns on the larger length scales. To this

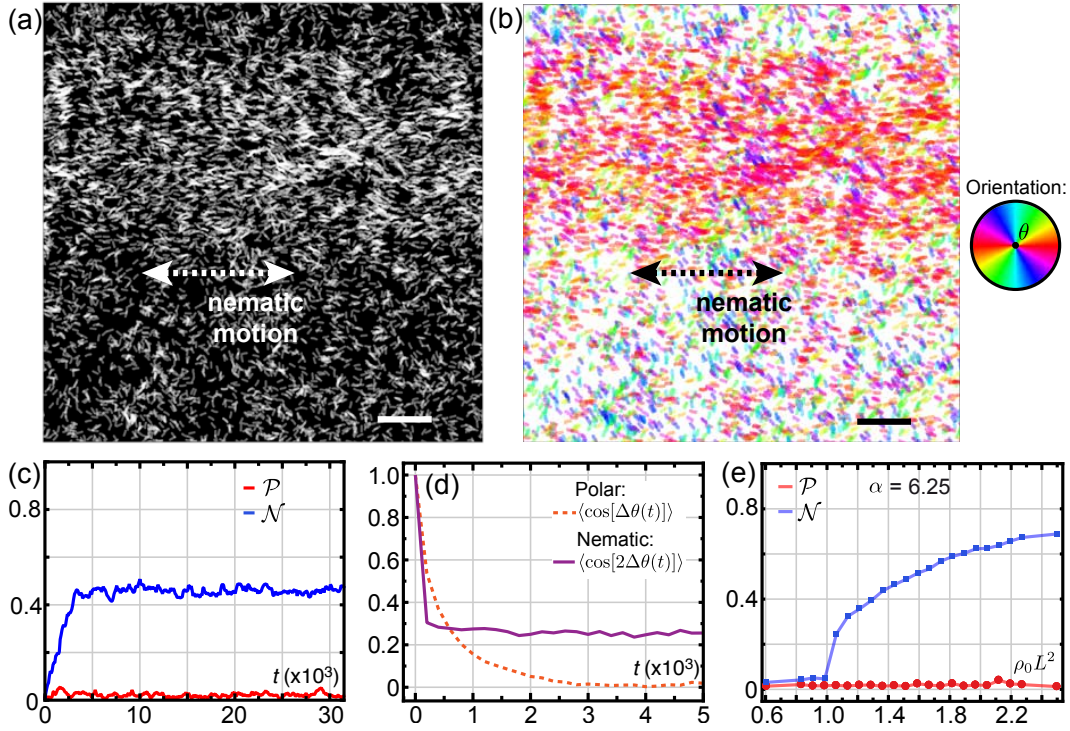


**Figure II.21** (a-d) Self-organization of nematic order from disordered initial conditions for  $\alpha = 6.25$  and  $\rho_0 L^2 = 1.51$ . (a) Emergence of a dense nematic trail of filaments in a system of 10,000 filaments. The local order can be visualized when coloring filaments with a  $\pi$ -periodic colormap (b). Scale bars are  $20L$ . (c) Evolution of order parameters. (d) Polar and nematic autocorrelation functions. While the former decays within a characteristic time of  $\tau \approx 4.61$  to zero, the latter remains finite due to the global nematic order. (e) Stationary order parameters as a function of  $\rho_0$  for  $\alpha = 6.25$  show the presence of global nematic order above  $\rho_0 L^2 \gtrsim 1$ .

end, we repeated the simulations with a 16-fold system size of  $L_{box} = 8192$  and  $M = 2,176,000$  filaments and observe the coarsening dynamics in Fig. II.22. Within very short time  $t \sim 1000$  nematic trails form locally as in the small simulation boxes as in Fig. II.21, but with random orientations on the global scale. This creates a large nematic network structure with an intriguing spatio-temporal dynamics: as time progresses, smaller branches become successively depleted or merge, creating ever larger trails. It is interesting to note that there are (temporary) symmetric junctions of three branches exchanging filaments, and that open trail ends persistently feed filaments back into the disordered regions. At least qualitatively, this looks very similar to the patterns observed in the experiment (Fig. II.15(d)). It remains to be shown experimentally if the predicted dynamics are also present in the actin motility assay. To this end, please refer to section 2.3.2.

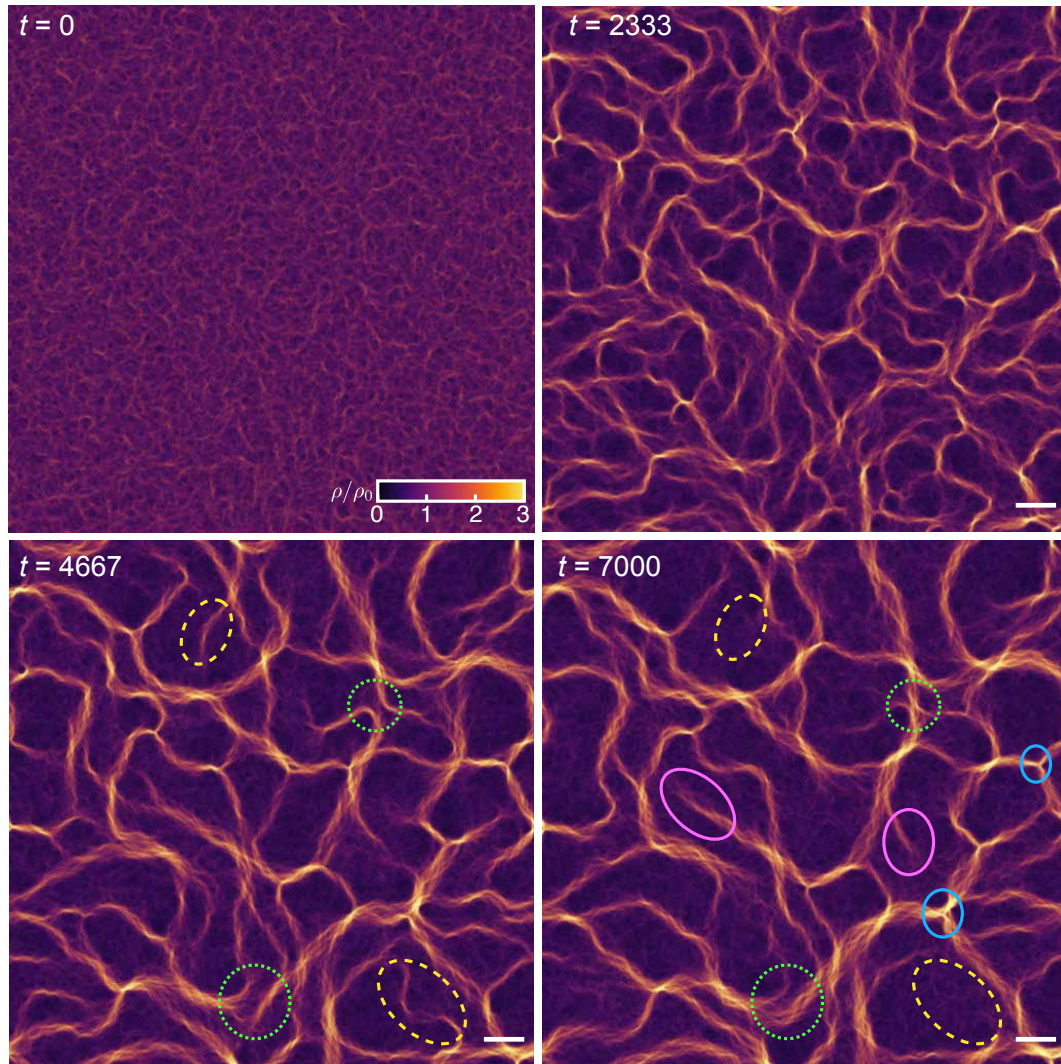


**Figure II.22** Snapshots of an ultra-large-scale simulation of nematic trails at different times with  $\rho_0 L^2 = 1.29$  and  $\alpha = 6.25$  ( $L_{box} = 8192$  and  $M = 2,176,000$ ). For better visualization, every image is an average over 24 snapshots over a period of  $\Delta t = 480$ . For illustration we marked some features in the bottom images: junctions (blue circle), loose ends (pink circles), depleting branches (long-dashed yellow circles), and merging branches (short-dashed green circles). Scale bars:  $100L$ .

### 2.2.5 Hysteresis analysis

In the above analysis we saw that the WASP model is capable of producing both global polar order as well as global nematic order accompanied by a self-organization of collective patterns, respectively. In particular, we showed that this can be controlled by tuning the relative alignment strength  $\alpha$ , from small to larger values. This can be seen in Fig. II.20(e), where we let the system equilibrate within a time  $t_{max} = 10^4$  for each value of  $\alpha$ , and then slowly increased  $\alpha$ . Here the patterns of the corresponding system undergo a transformation from a moving polar front towards a nematic trail. In general, this represents an ordering transition of active matter that was hardly examined previously. In a study by Ngo et al. [130] with stochastically switching populations of purely polar and purely nematic Vicsek particles it was found that the transition is discontinuous. This is plausible since polar and nematic order are obviously not compatible but mutually exclusive, and there is no possible way to continuously convert moving polar fronts (which extent perpendicular to the particle motion) into static nematic trails (which extent parallel to the particle motion). Yet, studying this toy model does not give further insight into our system, because the micro-physics including alignment interactions are inherently different, and there is no stochastic switching between two types of particles.

Surprisingly, when we start simulations with random initial conditions instead of the quasi-static increase of  $\alpha$ , the phenomenology changes drastically (Fig. II.23(a)): for intermediate values of  $\alpha$ , repeated simulations (with different random initial conditions) at times yield the emergence of polar order, at other times nematic trails form. Within the observed time interval, we did not observe any switching between these patterns. Therefore we conclude that the polar and nematic state are distinct stable attractors of the dynamics within a multistable parameter regime, which are robust against small local fluctuations. To quantify these regions, we searched for hysteresis effects, by using the quasi-static sweep performed in Fig. II.20(e) from small to large  $\alpha$  ('+' direction), and a similar sweep in the opposite direction from large to small  $\alpha$  ('-' direction). We recorded the corresponding order parameters  $\mathcal{P}_+$ ,  $\mathcal{N}_+$  and  $\mathcal{P}_-$ ,  $\mathcal{N}_-$ , respectively, and observed that there is hysteresis in the polar order parameter, while the nematic order parameter remained relatively unchanged: as note above, when  $\alpha$  is increased, the polar order  $\mathcal{P}_+$  smoothly drops to zero at a value  $\alpha_+$ , however for decreasing  $\alpha$  the polar order  $\mathcal{P}_-$  remains zero until it sharply jumps to a large value at  $\alpha_-$ . This can be seen in Fig. II.23(a) where we quantified the hysteresis loop - and hence the region of multistability - using  $\delta\mathcal{P} := \mathcal{P}_+ - \mathcal{P}_-$  for a density  $\rho_0 L^2 = 1.51$ . Furthermore, we performed this procedure in the whole experimentally relevant parameter space of varying density  $\rho_0 L^2$  and relative alignment strength  $\alpha$ , creating an effective phase diagram (Fig. II.23(b,c)). Unexpectedly, we find a broad parameter regime where polar and

nematic order are simultaneously stable. This is in contrast to Ref. [130] and the consensus that there are distinct symmetry classes in active matter systems, which predict universal features in the vicinity of a critical transition point [18, 52, 57].

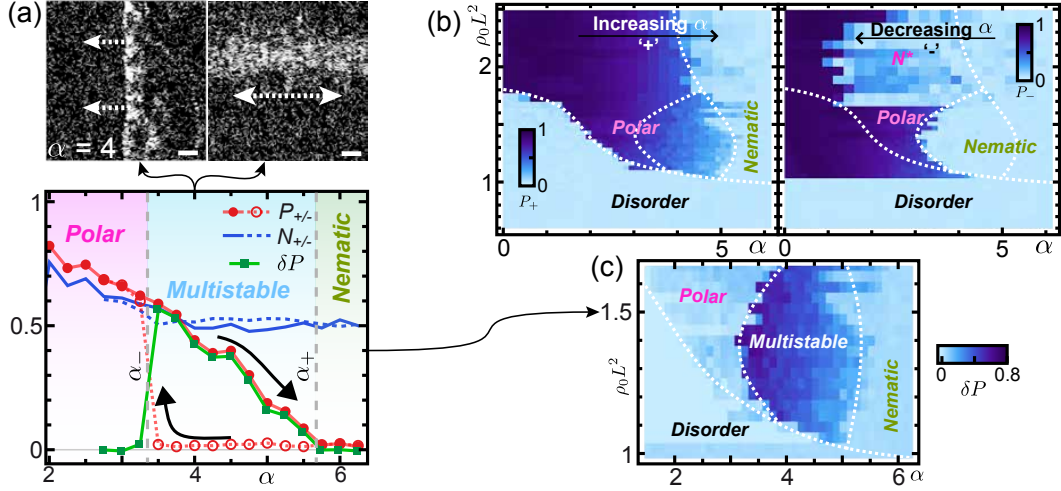


**Figure II.23** (a) Multistability of polar and nematic order for a density  $\rho_0 L^2 = 1.51$  in smaller systems of box size  $L_{box} = 512$ . For  $\alpha = 4$  we observe that both types of orders can emerge and are stable (upper panels). Lower panels: hysteresis analysis of the polar order quantifies the region of multistability within a relative alignment strength interval  $[\alpha_-, \alpha_+]$  using the quantity  $\delta P := P_+ - P_-$ . (b) Polar order of increasing (left panel) and decreasing (right panel) sweep directions for different  $\rho_0 L^2$  and  $\alpha$ . White dashed lines are guides to the eye to separate the respective domains of different order. In the region marked by  $N^*$  the polar order is relatively small, despite having local polar order. In these simulations, polar waves collide head-on (see also Fig. II.25(d)). Note that for the decreasing direction, there is also a large subcritical region of polar order coexisting with the disordered state. This will be studied more thoroughly in the next chapter. (c) Multistable parameter region obtained by subtracting both panels of (b). Data is also published in Ref. [127].

### 2.2.6 Three-phase coexistence, breakdown of universality, and emergent symmetry of order

Until now, we have only analyzed the multistability on the basis of rather small systems, for which the hysteresis sweep is numerically feasible. If this peculiar feature is not just an artefact of finite systems, it suggests that multistability could be a prerequisite of large-scale coexistence of polar and nematic patterns. Indeed, we performed ultra-large simulations and found that both polar fronts and nematic networks can emerge simultaneously, embedded in a dilute background with no order (Fig. II.24(a)). The resulting state is highly dynamic, with polar clusters disrupting

or infiltrating nematic trails, while also losing filaments to the environment which again feed back into the trail network. We saw coexistence of both orders within the maximal time of these simulations, and did not see the extinction of one type as for small systems like in Fig. II.23(a), suggesting that the coexisting state is stable in the thermodynamic limit. To this end, we performed a finite-size scaling analysis of the relevant time scales of the dynamics of pattern selection: for a given system size  $L_{box}$ , we simulate an ensemble of systems with different random initial conditions and tracked their evolution of order parameters. Note that in addition to  $\mathcal{P}$  and  $\mathcal{N}$ , we introduced new order parameters  $\langle \pi_c \rangle$  and  $\langle \nu_c \rangle$ , the so-called *local cluster polar and nematic order*, which will be introduced in section 1.2 of the next chapter III. In essence,  $\langle \pi_c \rangle$  and  $\langle \nu_c \rangle$  measure the degree of local order of patterns without suffering from artefacts of the global orientation, for example when two polar waves are counter-oriented. As can be seen by Fig. II.24(b,c), both types of order are simultaneously present at intermediate times, but at the terminal stage only one type remains, either polar or nematic order. The underlying dynamics can be readily resolved by  $\langle \pi_c \rangle$  and  $\langle \nu_c \rangle$ : within a very short time  $t_0$ , filaments organize into small clusters with a local polar order as is reflected by the first plateau value of  $\langle \pi_c \rangle$ . From this time on global order builds up with subsequent coarsening; still locally, both types of order are still present. At the end of this 'coexistence time' one type of order becomes extinct: when polar order 'wins' (Fig. II.24(b)),  $\langle \pi_c \rangle$  grows successively from small values due to the local appearance of a polar cluster (see inset snapshots) and eventually hits  $\langle \nu_c \rangle$  at a time  $t_{fix}$ , which is comparable to the global polar order. On the other hand, when nematic order 'wins' (Fig. II.24(c)),  $\langle \pi_c \rangle$  drops from its initial plateau where both types of order are still present (see inset snapshots) to a smaller, stationary value at time  $t_{fix}$ . Note that even in the fully nematic state here, local filament clusters are still partly polar (since  $\langle \pi_c \rangle$  is nonzero).

By fitting  $t_0$  and  $t_{fix}$  in these simulations we obtained the time scale statistics of fixation times in Fig. II.24(d,e). While the initial time scale  $t_0$  remains constant for all different system sizes (as it should since it tracks initial pattern formation), the fixation time  $t_{fix}$  appears to grow linearly with the system size  $L_{box}$ . This is plausible since the competition of the polar and nematic subpopulations are represented by the coarsening dynamics of two different pattern domains with a length scale  $l$  which is bounded by  $L_{box}$ ; since they are active, their spreading velocity should be initially linear in time, that is  $l \propto t$ . We speculate that for very large times, this velocity should in principle become slower  $l \propto \sqrt{t}$  since the underlying active particles are ultimately diffusing. Thus, for very large system sizes beyond our numerical resolution, the fixation times should even scale with  $t_{fix} \propto L_{box}^2$ . In any case, in the statistical limit of infinite system sizes  $t_{fix} \rightarrow \infty$ , hence the coexistence of polar and nematic order is indeed a stable state of the active system.

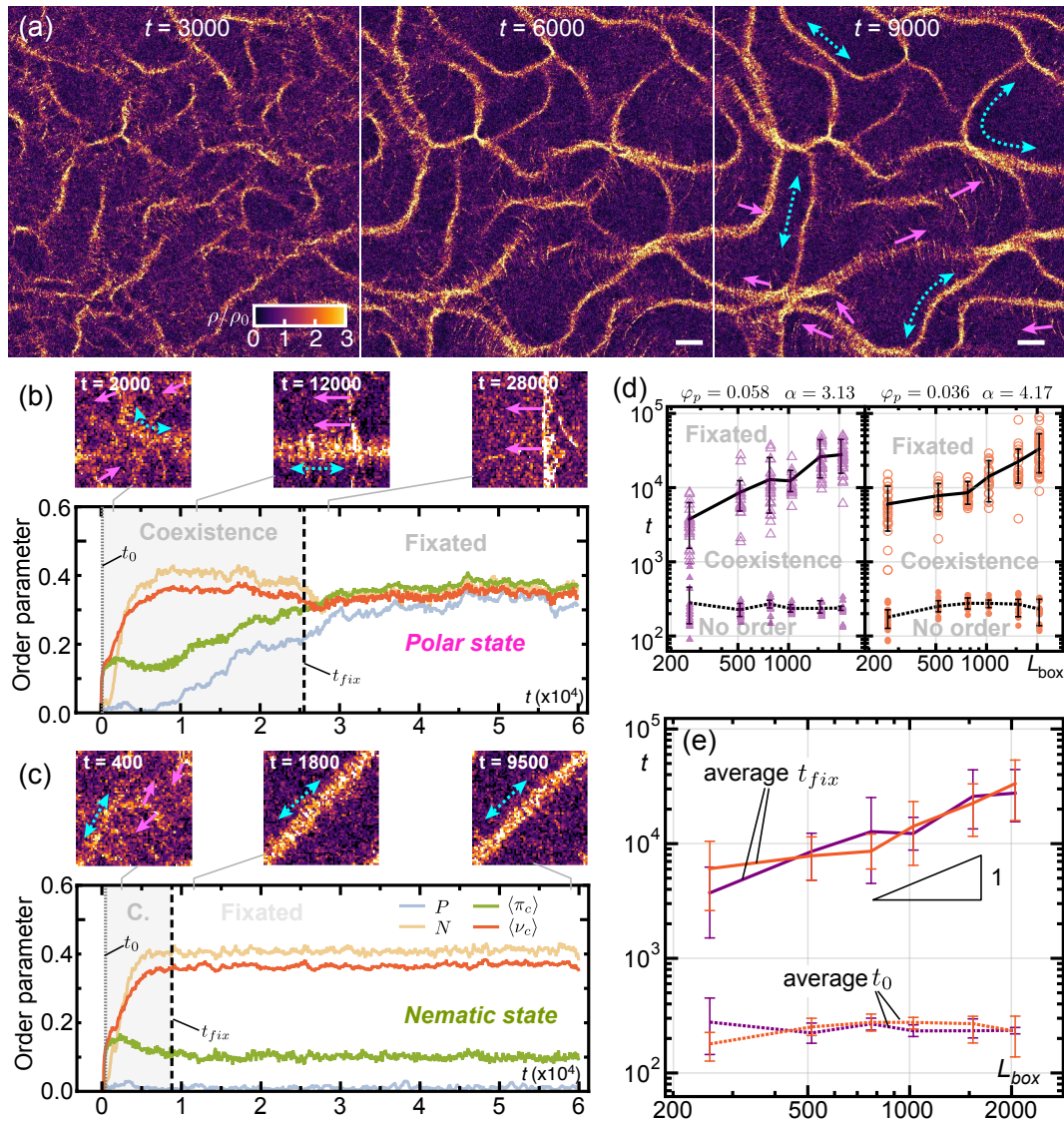


**Figure II.24** (a) Snapshots of an ultra-large WASP simulation in the multistable parameter region at different times shows the simultaneous formation of polar fronts and nematic networks. In the right panel, pink arrows depict moving polar fronts, and light-blue bi-directional arrows illustrate nematic trails. Parameters:  $\alpha = 3.13$ ,  $\rho_0 L^2 = 1.29$ , and  $L_{box} = 8192$ . Scale bars:  $100L$ . (b,c) Fixation process of (b) polar order and (c) nematic order as visualized by the evolution of order parameters  $\mathcal{P}$ ,  $\mathcal{N}$ ,  $\langle \pi_c \rangle$ ,  $\langle \nu_c \rangle$ . Parameters are the same as in (a) but with  $L_{box} = 512$ . At time  $t_0$  local order builds up, while at time  $t_{fix}$  the systems settles on a distinct type of order. (d) Statistics of time scales  $t_0$ ,  $t_{fix}$  as a function of the system size  $L_{box}$  at two different parameter points. The black lines denote respective average values. (d) Comparison of average times scales  $t_0$ ,  $t_{fix}$  from (d) reveals linear scaling law. Error bars depict the 15th, respective 85th percentiles of data points. (b-e) are also published in Ref. [127].

The mechanism that underlies the coexistence and multistability remains to be explained. A crucial difference of the particle interactions of the WASP model and actin motility assay with other theories is that alignment is extremely faint. While for the latter, the order and its symmetry is already imprinted at the smallest scales, for the former it is even unclear at which length scales significant order emerges at all. In the WASP model, we hypothesize that during the process of order formation, multiparticle correlations build up and many different particle configurations with gradual order are stochastically explored. In this space of configurations, full polar and nematic order represent local attractors in which the system will ultimately end up as coarsening progresses. In this picture, the malleability or ambiguity of order at the intermediate scale is essential for the emergence of multistability, as a system might end up in different order attractors depending on random fluctuations (see illustration in Fig. II.25(a)). If this were true, then eliminating this ambiguity would also extinguish multistability and hence coexistence: To this end, we increased the total interaction strength, that is, both  $\varphi_p$  and  $\varphi_n$  towards stronger alignment, which fixes the emergent order on ever smaller length scales, and thus suppress large fluctuations of particle configurations. Figs. II.25(b-d) show the repeated hysteresis analysis for this case ( $L_{box} = 512$ ). As can be seen by Fig. II.25(d) the region of multistability indeed shrinks and eventually vanishes as both alignment parameters are increased, leaving a sharp transition between polar and nematic order similar to the Vicsek toy model of Ref. [130]. Consequently, weak interactions, which are amplified by multiparticle correlations, are essential for multistability and coexistence to occur. Note that we tested the robustness of this phase diagram with respect to the system size, and found no significant change for doubled  $L_{box} = 1024$ .

Let us shortly remark on additional features of the phase spaces Figs. II.23 and II.25. In addition to the symmetry-broken polar fronts, we also saw the emergence of head-on colliding polar fronts (Fig. II.26(a)), which possess no distinct global order  $\mathcal{P}$  and appear to be analogous to an 'excitation' of the polar 'ground state'. In particular, this appears to be a common decay channel of nematic trails depending on the periodic boundary conditions, in which the two counter-propagating filament populations inside a fully straight nematic trail start to nucleate polar order. When  $\varphi_p$  increases, polar patterns seem to become gradually more irregular, resembling single clusters rather than large fronts (Fig. II.26(b)). Unexpectedly, for large total interaction strength, global order ceases to exist and the system becomes disordered again (see upper right corners of Figs. II.25(b-d) and II.26(c)). For this case, we also recorded the orientational decay length  $\tau$  of single particles and found that in this disordered phase, it roughly follows the predicted law  $D^{-1}$  (Eq. (II.34)) which excludes the presence of large collective effects. This behavior seems to be reminiscent of previous results in Ref. [83], where strong excluded-volume interactions (which are a proxy for nematic alignment) may suppress collective order.

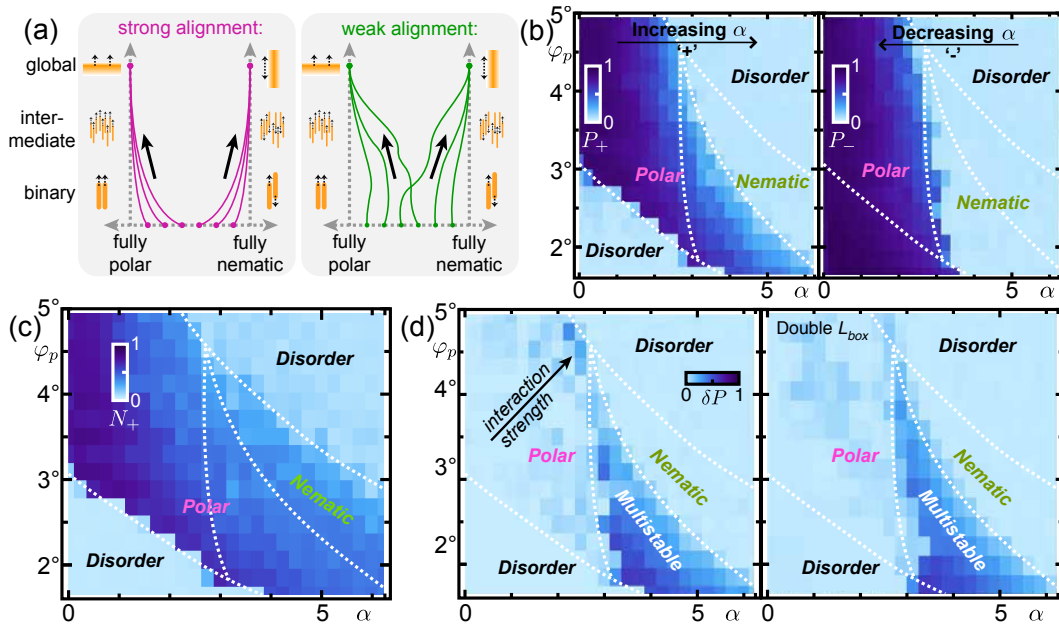


**Figure II.25** (a) Illustration of the malleable order in the space of emergent order and length scales, for different initial conditions: for strong interactions (left panel), order is already determined at small scales. For weak interactions (right panel), increased fluctuations allow to reach both order attractors. (b) Polar order of increasing (left panel) and decreasing (right panel) sweep directions for different  $\alpha$  and  $\varphi_p$  (in degrees). (c) Nematic order for the increasing sweep shows the reentrance of the disordered phase for large alignment interactions. (d) Corresponding hysteresis  $\delta P$  depicting multistable regions. Left panel:  $L_{box} = 512$ , right panel:  $L_{box} = 1024$ . Note that the total interaction strength increases along the diagonal of (b-d), and  $\rho_0 L^2 = 1.29$ . White dashed lines are guides to the eye to separate the respective domains of different order. (b-d) are also published in Ref. [127].

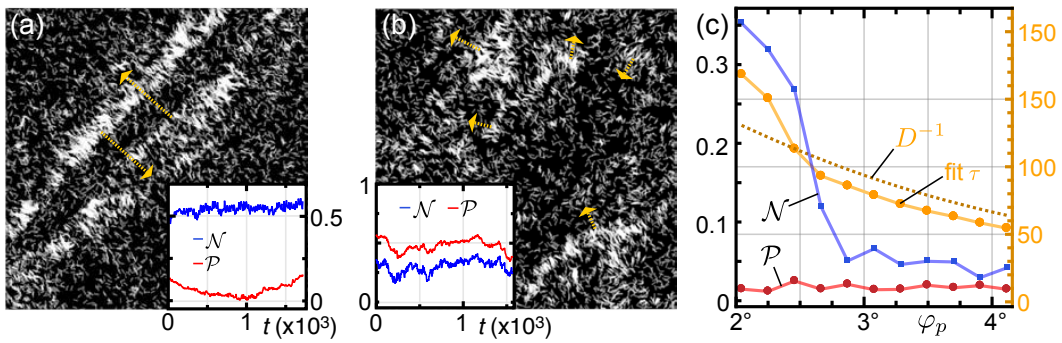


**Figure II.26** (a) Colliding polar fronts with overall nematic order ( $\rho_0 L^2 = 1.51$ ,  $\alpha = 4.5$ ,  $\varphi_p = 2.1^\circ$ ). (b) Chaotic polar clusters without dominant long-range order ( $\rho_0 L^2 = 1.29$ ,  $\alpha = 2$ ,  $\varphi_p = 5.^\circ$ ). Insets of (a,b): evolution of order parameters. (a,b) are also published in Ref. [127]. (c) Transition towards dense disorder depicted by the stationary values of  $\mathcal{P}$ ,  $\mathcal{N}$  (left axis), and the fitted orientational decay length  $\tau$  compared with  $D^{-1}$  from Eq. (II.34) (right axis). Parameters as in Fig. II.25.

## 2.3 Experimental verification

In addition to the theoretical approach in the previous section, we were able to test our predictions directly in experiments with the actomyosin gliding assay. Being properly instructed by Ryo Suzuki and Andreas Bausch, Timo Krüger and I conducted many experiments over a time period of 6 months in the biophysics laboratory facilities of the Technische Universität Munich. In the following we will present a short introduction to experimental methods, which we will subsequently use to analyze the properties of collective phenomena of the actin motility assay with crowding agents.

### 2.3.1 Setup of the gliding assay

In essence, the actomyosin gliding assay exhibits a rather simple experimental setup, which is also suitable for student workshops. Before the assay itself can be initialized, we prepared flow chambers from microscope slides (Carl Roth, Germany) to which we glued cover slips (Carl Roth, Germany) using heated parafilm (see Fig. II.27(a)). The cover slips were coated with a 0.1% nitrocellulose solution, which was made by diluting a 2% solution (Electron Microscopy Sciences, Hatfield, PA) in amyl acetate (Roth), and were left to dry overnight under a fume hood to reduce dust contamination. A smooth and clean coating turned out to be essential for creating reproducible experiments. The chamber typically has dimensions of ca.  $7\text{mm} \times 20\text{mm} (\times 1\text{mm})$ , and is hence about three orders of magnitude larger than the length of a single filament, to avoid boundary effects. The actin filaments (F-actin) were bred from a monomeric actin solution (G-actin), which was prepared by dissolving lyophilized G-actin obtained from rabbit skeletal muscle [133, 134] in deionized water and dialyzing against fresh G-buffer ( $2\text{mM}$  Tris pH 7.5,  $0.2\text{mM}$  ATP,  $0.2\text{mM}$   $\text{CaCl}_2$ ,  $0.2\text{mM}$  DTT and  $0.005\%$   $\text{NaN}_3$ ) overnight at  $4^\circ\text{C}$ . Polymerization of actin was initiated by adding one volume of tenfold concentrated F-buffer ( $20\text{mM}$  Tris,  $20\text{mM}$   $\text{MgCl}_2$ ,  $2\text{mM}$  DTT and  $1\text{M}$  KCl) to nine volumes of the G-actin sample. Within a time of roughly 2 hours, a stationary distribution of long actin filaments had formed. These filaments are quite sensitive to mechanical shearing - any pipetting process needs to be performed gentle and with care to avoid rupture. The resulting F-actin solution was then used within 48 hours. For fluorescence microscopy, we also prepared a solution of fluorescently labelled filaments which were stabilized with Alexa Fluor 488 phalloidin (Invitrogen). If not stated otherwise, we used a labelled-to-unlabelled fraction of 1:25. Prior to the experiment, both solutions were added such that a defined fraction of filaments was labelled. Heavy meromyosin (HMM) was prepared by dialyzing rabbit skeletal muscle against myosin buffer ( $0.6\text{M}$  NaCl,  $10\text{mM}$   $\text{NaH}_2\text{PO}_4$ ,  $2\text{mM}$  DTT,  $2\text{mM}$   $\text{MgCl}_2$ ,  $0.05\%$   $\text{NaN}_3$ ) at  $4^\circ\text{C}$  [135]. We used the same batch of HMM for all our experiments, which was stored at a constant temperature of  $-80^\circ\text{C}$ .

Prior to experiments, HMM was diluted in the assay buffer (25mM imidazole hydrochloride pH 7.4, 25mM KCl, 4mM MgCl<sub>2</sub>, 1mM EGTA and 1mM DTT). Unless stated otherwise, the HMM concentration was fixed at 0.1mg/ml. The actin solution was then added to assay buffer that had been premixed with PEG 35,000kD (Sigma) to yield a final PEG concentration of 0-3% (w/v). To vary the surface density of actin filaments, we diluted the initial breeding concentration of F-actin correspondingly. For the used range of 0 – 20μM F-actin we assumed a linear dependence of both values. The flow chamber was incubated with the HMM dilution for 3 min and the surfaces were then passivated with BSA (10mg/ml BSA (Sigma) dissolved in assay buffer). The actin solution was then incubated for 2 min to allow for saturated HMM binding. To initiate an experiment, 2mM ATP dissolved in assay buffer was injected into the flow chamber, together with a standard antioxidant buffer supplement (GOC, containing 2mg glucose oxidase (Sigma) and 0.5mg catalase (Fluka)) to prevent oxidation of the fluorophore. For the last two steps, careful pipetting was crucial: because of the strongly increased viscosity due to PEG, buffer mixing required multiple pipette strokes which, on the other hand, increased shearing forces and filament rupture. After all components had been combined, the flow chamber was sealed with vacuum grease (Bayer Silicones) and quickly put under the appropriate microscope.

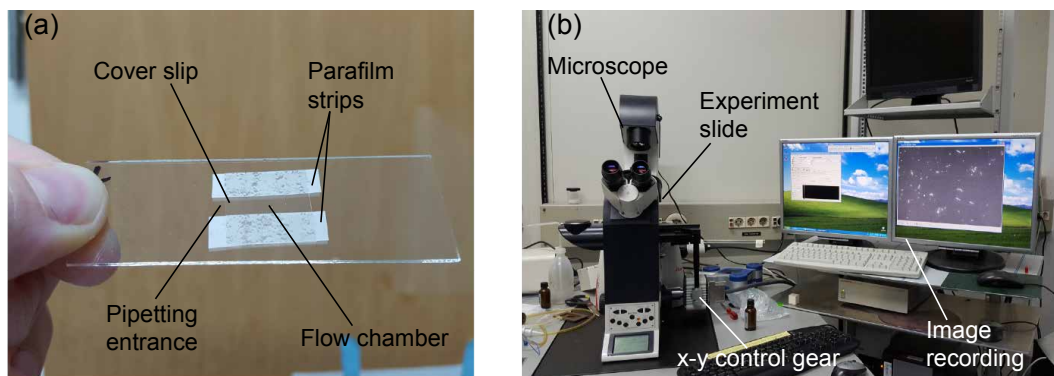


**Figure II.27** (a) Image of a prepared coverslip before the addition of HMM. (b) Fluorescence microscope setup including image recording device.

### 2.3.2 Analysis of single particle and collective properties

For the imaging of our experiments we mainly used a Leica DMI 6000B inverted microscope equipped with a 40x oil-immersion objective (NA: 1.25) to acquire data (see Fig. II.27(b)). Images were captured at a resolution 1344 x 1024 pixels with a charge-coupled device (CCD) camera (C4742-95, Hamamatsu) attached to a

0.35x or 1x camera mount. The optimal frame rate for this device was 0.5s and the region of view was on the scale of  $0.5\text{mm}$ , which allowed for a proper observation of the large-scale dynamics of the crowded motility assay. To track individual filaments, we preferred to use a high-contrast TIRF microscope (Leica DMI 6000B, 100x oil-immersion objective (NA: 1.47), Andor iXon-Ultra-9369 camera with a resolution of  $512 \times 512$  pixels), which has a smaller and stabilized region of view of  $82\mu\text{m} \times 82\mu\text{m}$  and a frame rate of 0.0853s.

#### Single particle properties:

To study the binary collision statistics as depicted in Fig. II.15(a) we used a dilute system with conditions as in Ref. [26] but with a PEG concentration of 3%. The acquired images were first converted into binary images and filaments were then identified by skeletonization using a standard library 'bwmorph' available in Matlab. From this, the coordinates of the filament contour were extracted by using a cubic spline fit to obtain  $\theta_1$ ,  $\theta_2$ , and  $\theta'_1$ ,  $\theta'_2$ , to determine the incoming angle  $\theta_{in}$  and outgoing angle  $\theta_{out}$  (Fig. II.28(a)). As in the WASP simulations, the analysis of a collision began once the images of two filaments intersect. In Fig. II.28(a), the snapshots framed by red boxes represent a detected collision event. The incoming angle  $\theta_{in}$  is obtained 1 frame (0.13 sec) before the detected collision event, and the outgoing angle  $\theta_{out}$  is taken 1 frame after the filaments cease to intersect. We only studied binary collisions, neglecting all collisions involving 3 or more filaments. Figure II.28(b) shows all recorded collision events that were used to create Fig. II.15(a).

As elaborated above, we attribute the effect of PEG to the increased steric forces that promote a nematic alignment (Fig. II.15). To test this, we investigated the degree of processivity of the actomyosin complex by varying the motor concentration: for low processivity HMM motors only bind occasionally to actin filaments, and adding more motors to the substrate successively increases the transport 'efficiency', that is, filaments become faster. For large processivity on the other hand, motor binding is already saturated for lower values of the HMM concentration. Therefore, when the saturation level of filament velocities is sensitive to the concentration of PEG, this would imply a change in processivity and hence the degree of steric forces. Indeed, as can be seen in Fig. II.28(c), we recorded the filament velocities as a function of HMM and PEG concentration and found that processivity increases with PEG, which confirms the assumption of that PEG promotes nematic alignment.

Depending on the quality of the batches of monomeric actin and HMM motors, the distribution of polymerized filament lengths varied, which complicates a quantitative comparison between different batches. Furthermore, the enhanced processivity due to PEG was found to drastically increase the rupture of filaments into smaller pieces. However, the same phase diagram can be recovered by an appropriate rescaling of the filament membrane density with the average length of a batch

$\langle L \rangle$  [26]. Therefore, we only monitored the filament length distribution when we were interested in directly comparing experiments with different actin concentrations to maintain a quantitative significance. This was done when we recorded the experimental phase diagram of collective behavior (see below), such that we could estimate the critical actin density above which order is observed. For this batch, we measured many individual filament lengths for two different experiments in the absence of PEG, and found an exponential distribution of lengths with a mean of  $\langle L \rangle \approx 1\mu\text{m}$  (Fig. II.28(d-f)). This constitutes rather short filaments when compared to other studies [21, 26], which are however more robust against rupture due to PEG and represent stiff polymers  $L_p/L \gg 1$  similar to the parameters used in the WASP simulations of section 2.2.

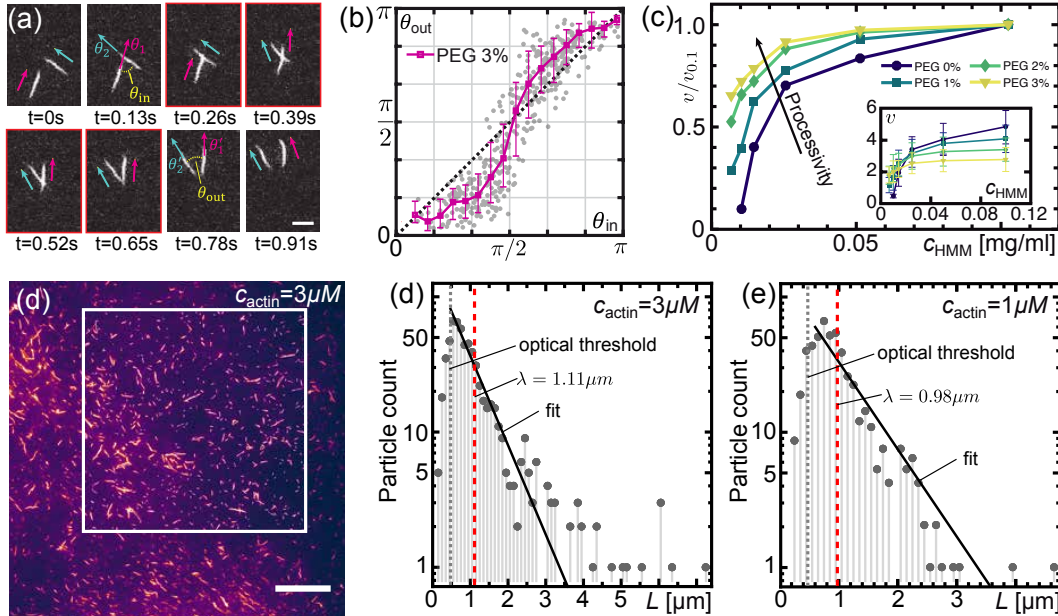


**Figure II.28** (a) Illustration of collision angles during a binary collision. Scale bar:  $2\mu\text{m}$ . (b) Full binary collision statistics of 389 collision events at a PEG concentration of 3%. Error bars depict one standard deviation. (c) Filament velocity  $v$  as a function of HMM concentration for different PEG values. Processivity increases as indicated by the earlier saturation of normalized filament velocities.  $v_{0.1}$  is the velocity at a concentration of  $c_{\text{HMM}} = 0.1\text{mg/ml}$  HMM. Inset: absolute filament velocities  $v$ . (d) Fluorescence image of a dilute region at an actin concentration of  $c_{\text{actin}} = 3\mu\text{M}$ . Within the white rectangle we measured 631 filament lengths (scale bar:  $20\mu\text{m}$ ). (e,f) Statistics of filament lengths of a single actin batch at an actin concentration of (e)  $3\mu\text{M}$  and (f)  $1\mu\text{M}$ . To obtain the average length we fitted an exponential  $\sim \exp(-L/\lambda)$  with  $\langle L \rangle = \lambda$  while discarding lengths that are below the optical threshold  $< v\tau_0 = 0.47\mu\text{m}$  where  $\tau_0 = 120\text{ms}$  is the exposure time of the camera ( $v \approx 4\mu\text{m/s}$ ). (a-c) are also published in Ref. [127].

Collective properties:

In section 2.1.2 we already gave an overview over the self-organization phenomena of the actin motility assay, which can be triggered by a sufficiently large actin substrate density via increasing the actin concentration, and by changing the aligning character of particle collisions via tuning the amount of the crowding agent PEG. While the formation of polar fronts has been previously observed in the motility assay [21, 22], collective nematic order and the corresponding pattern formation has not been seen before and hence requires a proper analysis of the dynamics, on the scale of single filaments as well as on large scales. For the latter, we recorded the time evolution of experiments at large actin concentrations and at 2% PEG which yield the large-scale formation of nematic trails. As can be seen in Fig. II.29, the nematic network is not entirely static, but rearranges slowly; trails may form new connections and branches, or become depleted by an imbalanced transport of filament mass along the trails. As in the ultra-large WASP simulations the branches are almost stable in the transversal direction, and only move in the vicinity of junctions or other branches. In addition, trails may also have free ends with filaments draining into the disordered, dilute environment.

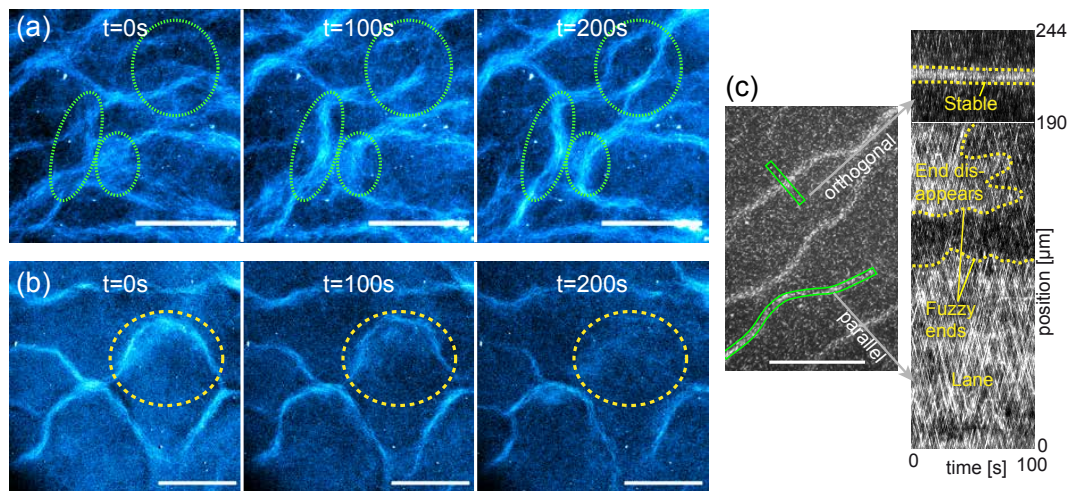


**Figure II.29** (a) Snapshots of close-by nematic trails merging and forming new branches (indicated by dashed green circles) at different times. This happens on the time scale of minutes (actin concentration  $5\mu M$ , 2% PEG, labelled filament ratio 1:30). (b) Snapshots of a nematic branch which becomes depleted on the time scale of minutes (outlined by dashed yellow circles). Actin concentration:  $10\mu M$ , 2% PEG, labelled filament ratio: 1:50. (c) Kymographs of trail structures, taken orthogonally to (lower right panel) and parallel to a trail past its end (upper right panel). Dashed yellow lines illustrate the trails edges, which are stable in transversal direction but fluctuating in longitudinal direction. (c) is also published in Ref. [127]. All scale bars are  $100\mu m$ .

As a next step, we will analyze the experiments on the smaller scales. Quantifying the observed dynamics and capturing the underlying order of the system requires to identify the motion of single filaments, locally and with high precision. For this reason we resorted to a high-contrast TIRF microscope with a pixel size of  $\Delta x = 160\text{nm}$  and a frame rate of  $\Delta t = 0.085\text{s}$ , which allows to follow individual filaments between consecutive images in an automated fashion. First, we recorded a nematic lane at  $5\mu\text{M}$  actin and 2% PEG concentration, and a polar cluster as well as a disordered region at  $10\mu\text{M}$  actin and 1% PEG concentration (upper panels of Figs. II.30(a-c)). Then, we segmented the images into  $8 \times 8$  local bins and used the Kanade-Lucas-Tomasi feature-tracking algorithm in Mathematica 11.0.0.0, which is a robust estimator of the optical flow velocity, by maximizing the local intensity gradient correlation for each segment, in order to obtain a large number ( $\sim \mathcal{O}(10^5)$ ) of displacement vectors of filaments between consecutive image frames over an acquisition time of about a minute. From this we obtained probability densities  $P(\mathbf{v})$  of filament velocities (lower left panels of Figs. II.30(a-c)), as well as the local polar and nematic order parameters  $P$ ,  $N$  at a given time in the region of interest (ROI), respectively, over the acquisition time (lower right panels of Figs. II.30(a-c)). To account for the shape of the nematic trail, we only included bins that covered the trail (Fig. II.30(a)). Note that for the polar and nematic order parameters, the respective amplitudes are comparable to those from simulations. Apart from the case of a polar cluster (Fig. II.30(b)), which is inherently not static within the fixed ROI, the order of a nematic trail is stationary over an interval corresponding to filaments crossing the ROI about 2 times.

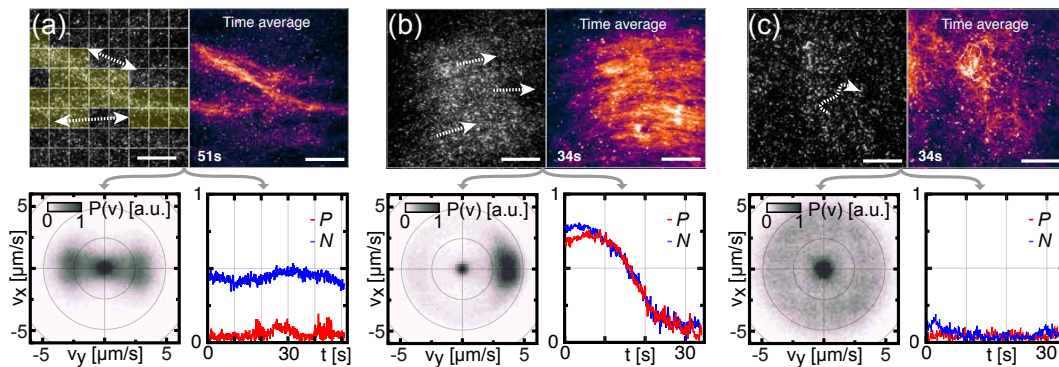


**Figure II.30** Local dynamics of filaments within nematic trails (a), polar clusters (b) and in disordered regions (c): Upper left panels are plain snapshots. In (a), the yellow area denotes the subgrid in which filaments were tracked. Upper right panels are averaged images over the acquisition time to display the average motion of structures. Lower left and right panels depict two-dimensional probability densities  $P(\mathbf{v})$  and evolution of corresponding polar  $P$  and nematic  $N$  order parameters, respectively. Figure is also published in Ref. [127]. Scale bars are  $20\mu\text{m}$ .

Furthermore, we tracked the motion of individual filaments within a nematic trail to assess the orientational correlations on the particle scale. Using a single close-up image sequence of nematic trail (Fig. II.31(a-b)) we recorded the trajectories of 39 individual filaments by hand, and extracted the orientations  $\delta\theta(t) = \theta(t) - \theta(0)$  from each path at different times (Fig. II.31(b)). From this, the polar and nematic autocorrelation functions  $\langle \cos[\delta\theta(t)] \rangle$  and  $\langle \cos[2\delta\theta(t)] \rangle$  for different filaments were obtained and averaged over every time point (Fig. II.31(d)). Comparing the evolution of two individual trajectories (Figs. II.31(a,c)) one observes that filaments mostly follow the trail axis but may occasionally reverse their directions, exit or re-enter the trail. Correspondingly this is reflected in  $\langle \cos[\delta\theta(t)] \rangle$  and  $\langle \cos[2\delta\theta(t)] \rangle$ , with the former one decaying to zero and the latter one remaining at a finite value, very similar to the WASP simulations in Fig. II.21(d). This shows that the trail network has indeed an overall nematic order.

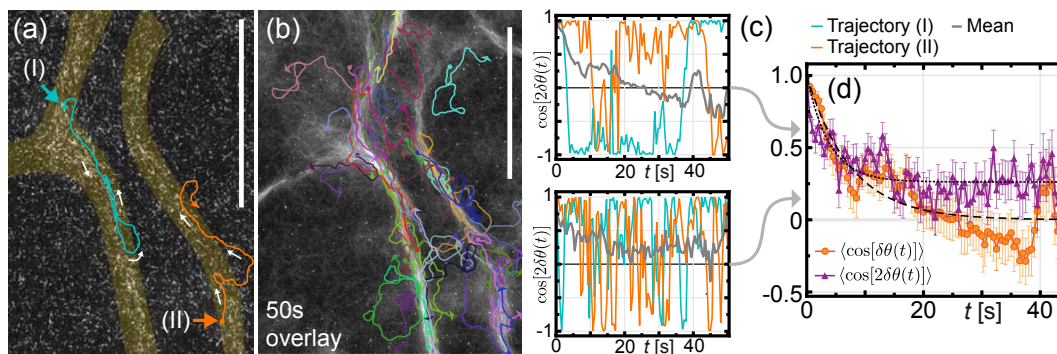


**Figure II.31** (a) Single filaments move inside nematic trails (yellow region). Two representative trajectories are shown (turquoise and orange) at  $10\mu M$  actin and 2% PEG. (b) Time-averaged over a period of 50s, including all 39 tracked filament trajectories. (c) Time evolution of  $\cos[\delta\theta(t)]$  and  $\cos[2\delta\theta(t)]$  for the two trajectories of (a) (colors accordingly). Reversal events are manifested by jumps in the amplitude from  $\cos[\delta\theta(t)]$  1 to -1 or back. (d) Autocorrelation functions of filament orientation inside trails; dashed gray lines are fits to guide the eye. Error bars depict one standard deviation, scale bars are  $100\mu m$ . (a,c,d) are also published in Ref. [127].

### 2.3.3 Three-phase coexistence

Until now, we have omitted the discussion about the transition from polar to nematic order. Of course, this transition is obviously of high interest, also because the agent-based WASP model predicted a multistable parameter region and coexisting patterns of both polar and nematic order. Therefore, we performed experiments for large actin density and intermediate PEG concentrations and found exactly this state, as it is shown in Fig. II.32: polar cluster explore the system in juxtaposition

to nematic networks (Fig. II.32(a)). These patterns emerge simultaneously and quickly after the initialization of the experiment (left panel of Fig. II.32(b) and a corresponding kymograph in Fig. II.32(c)), and remain for the whole duration of the experiment (see right panel of Fig. II.32(b)) until the ATP in the buffer solution runs out. The patterns themselves are not static but highly dynamic and interacting: clusters may invade regions that are covered by trails and locally disrupt them (Fig. II.32(e)). Likewise, clusters may lose filaments via their trailing edges forming a nematic band (Fig. II.32(d)). This cyclic competition for filament mass stabilizes the coexistence and prevent a dominance of one type of order.

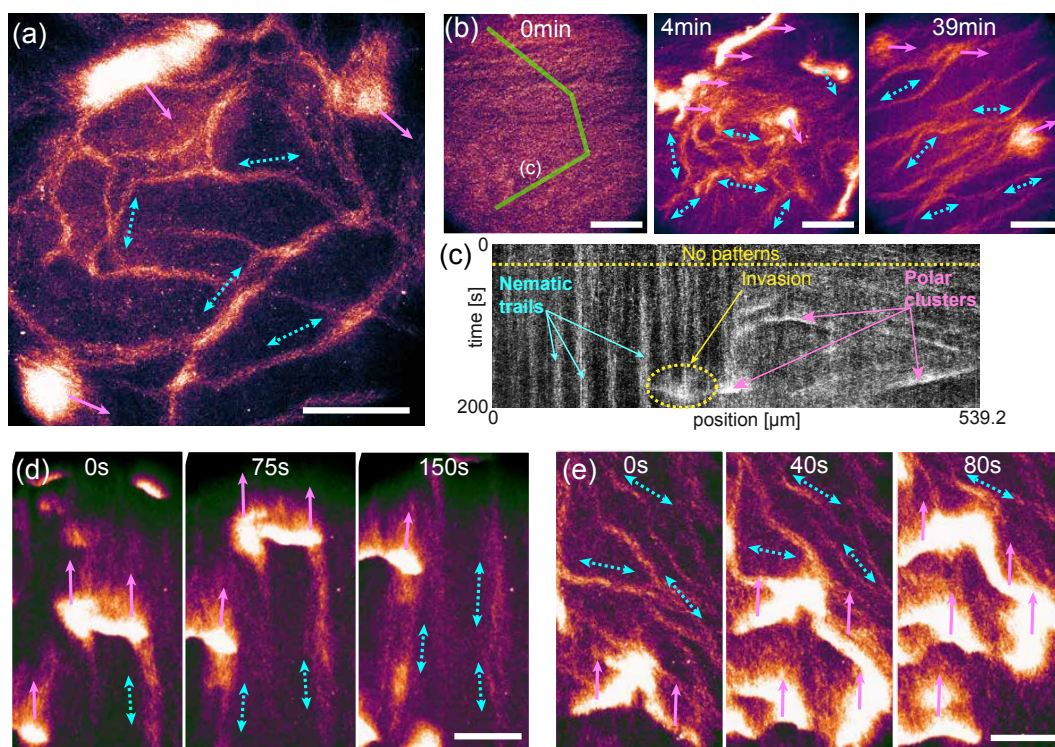


**Figure II.32** (a) Simultaneous coexistence of polar clusters and nematic trails at 2% PEG and  $5\mu M$  actin. (b) Evolution of coexisting patterns during an experiment, visualized by snapshots at different times after ATP addition. Within a few minutes (roughly 2 min), both polar clusters and nematic trails are fully developed (middle panel). At the end of the experiment, coexistence is still present (right panel). (c) Kymograph of the intensity along the curved green line in (b) shows the time evolution and emergence of patterns. In the left part, nematic trails form as can be seen by the static bright regions. On the right, polar clusters appear as can be seen by the skewed, propagating spots, that even invade the nematic regions in the middle. (d) Time evolution of a polar cluster that leaves nematic bands trailing from its 'wing-tips'. (e) Time evolution of polar clusters engulfing nematic trails by running over them. (a,b,d,e) are also published in Ref. [127]. All scale bars are  $100\mu m$ .

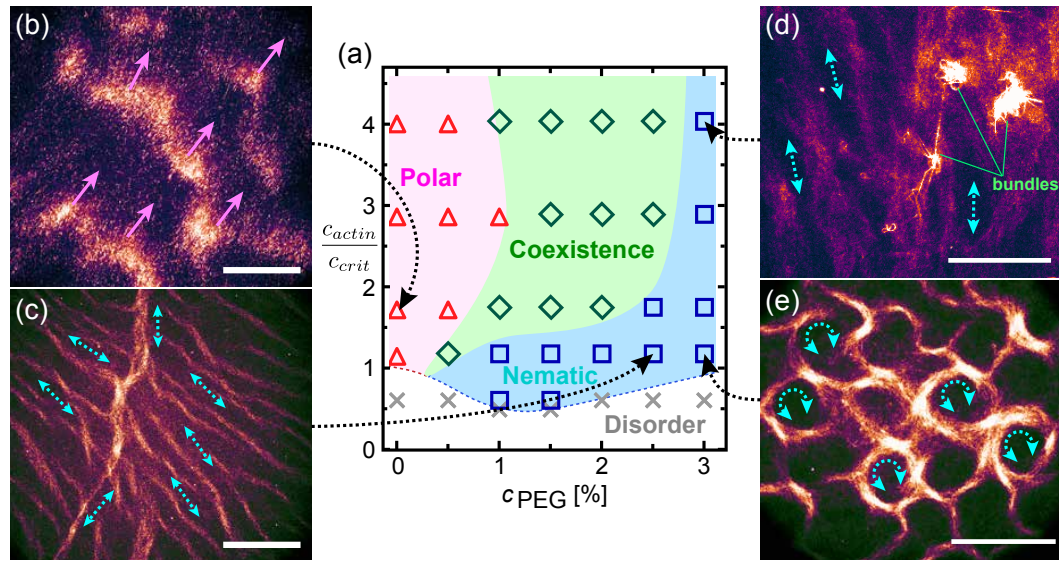


**Figure II.33** (a) Experimental phase diagram of emergent patterns for varying monomeric actin and PEG concentrations,  $c_{actin}$  and  $c_{PEG}$ . Gray crosses: disorder. Red triangles: polar clusters. Blue squares: nematic trails. Green diamonds: coexisting polar and nematic structures.  $c_{actin}$  was normalized with respect to the estimated critical concentration in the absence of PEG,  $c_{crit} \approx 1.75\mu M$ . (b) Polar fronts or clusters at  $c_{actin} = 3\mu M$  and zero PEG. (c) Purely nematic network at  $c_{actin} = 2\mu M$  and 2.5% PEG. (d) Trail network with occasional dynamic actin bundles ( $c_{actin} = 7\mu M$  and 3% PEG). (e) Vortex-like mesh of nematic branches ( $c_{actin} = 2\mu M$  and 3% PEG). (a,d,e) are also published in Ref. [127]. All scale bars are  $100\mu m$ .

In a final step we mapped out the parameter regions of the observed patterns, in the space of actin and PEG concentration,  $c_{actin}$  and  $c_{PEG}$ . To obtain meaningful and reproducible data, it was required to perform many comparable experiments in which we varied  $c_{actin}$  and  $c_{PEG}$  in a controlled fashion. Therefore, we prepared a single actin batch (incubated at  $10\mu M$  monomeric actin), with which we performed individual 39 experiments within 36 hours, at final concentrations  $c_{actin}$  between 0.8 and  $10\mu M$ . For every experiment, the assay buffer was freshly prepared with one out of seven different PEG premixes of  $c_{PEG}$  (0%, 0.5%, 1%, 1.5%, 2%, 2.5%, 3%). Note that it would in principle be more desirable to have a more universal and reproducible measure of the actin abundance like the filament surface density  $\rho$  or the normalized version  $\rho\langle L \rangle^2$ . However, it was not feasible to directly measure these values in every experiment due to the high-throughput and emergent density inhomogeneities, and also because counting filaments and their lengths always suffers from a selection bias if not performed rigorously during many observations. To circumvent this, we normalized  $c_{actin}$  with respect to the interpolated critical actin concentration  $c_{crit}$  of  $\sim 1.75\mu M$  (at zero PEG) for this specific actin batch. At this critical concentration, the filament density was roughly 9.2 filaments per

$\mu\text{m}^2$  and filament lengths were exponentially distributed as specified above in Fig. II.28. The resulting 'phase diagram' can be seen in Fig. II.33(a). As expected, the parameter domain of coexisting patterns is located in between the purely polar and purely nematic phase, and covers a vast region in accordance to the theoretical prediction (Fig. II.23). Figs. II.33(b-e) display fluorescence images of different experiments, which were cast into the corresponding phases upon visual inspection of their respective order. Interestingly, for very high PEG concentrations nematic trails seem to form an additional super-structure that resembles an array of vortex rings (Fig. II.33(e)), similar to previous results in microtubule gliding assays [24, 25]. When also the actin concentration is large, we observed the occasional appearance of large and dense actin bundles (Fig. II.33(d)) in addition to the nematic trails.

## 2.4 Summary and Outlook

In the previous chapters, we combined theory (section 2.2) and experiment (section 2.3) to investigate the role of weak alignment interactions and a gradual influence of their underlying symmetries. Here, the results of the agent-based simulations reproduce the experiments on all relevant length scales - from the interaction of individual filaments to the full self-organization of millions of collectively moving particles. Therefore, we expect that our all-scale WASP model is also capable of representing a variety of similar active systems, which rely on realistic physical interactions on the local scale, rather than simplified ad-hoc collision rules as assumed in Vicsek-type models.

Our central result of this section is the discovery of a state with coexisting polar and nematic structures in the parameter region of mixed alignment symmetries. These dense, ordered regions are formed simultaneously and are embedded in a dilute and disordered background. This represents an intriguing new state of three coexisting phases - polar, nematic, and disorder - that has no analogue to equilibrium physics: first, it violates the so-called Gibbs phase rule [28], which is a fundamental property of equilibrium statistical mechanics and connects the number of phases  $p$  with macroscopic degrees of freedom  $f$  (i.e. the dimensionality of the phase in parameter space) and the number of components  $c$ , stating that  $p = c + 2 - f$ . Thus for a one-component equilibrium system,  $p = 3$  only at one point in phase space ( $f = 0$ ), which is in contrast to our extended coexistence region ( $f > 0$ ). Second, our analysis shows that, for microscopic interactions with mixed alignment symmetries, a macroscopic polar or nematic state represent stable attractors of the same dynamical system; as a consequence, the order of the system itself is not predetermined but emerges spontaneously. Rather paradoxically, the coexisting or multistable state seems to rely on the weakness of local interactions and disappears otherwise. This is in contrast to the universality principle [29, 30], which asserts that the major features of emergent phenomena in equilibrium can

be deduced from a few relevant aspects of the microscopic interactions, most importantly their symmetry. For critical phenomena, this principle successfully explains why phase transitions can be classified into only a few universality classes. Or rephrased in simple words: details must not matter in equilibrium, but in active systems they do. Hence, our investigation challenges the generic validity of symmetry class arguments in active matter systems, especially at the boundaries of these 'classes'. Unfortunately, many theoretical approaches in literature, including Vicsek-like models [45, 76, 77, 130, 136] or kinetic approaches [18, 42, 50, 52, 78] have typically adapted this symmetry-class paradigm.

From a biological point of view, the phenomenology of the actomyosin gliding assay implies that the emergence of order in living systems is not necessarily constrained by underlying constituent symmetry, but is flexible to produce different types of order from identical building blocks and conditions. For example this may be important for 'multi-tasking' of the cellular actin network, which forms actin stress fibers and filopodia in the same system [31, 32], or the variable motility and structure of migrating cell layers [33, 34]. Moreover, the strong sensitivity of self-organization and collective order with respect to minuscule manipulations of the microscopic interactions in both theory and experiment imply that active matter can be 'adaptive'; that is, upon slightly changing local interactions by, for instance, an external stimulus or spatial cues the active system would react distinctly and actively amplify these variations by expressing different types of patterns. Yet, it remains to be shown if it is possible to control emergent order on system scales, or to even create functional machines out of the dynamic nature of active patterns. A few questions remain for the simulation results of the actomyosin assay. Above, we mostly focused on the global and stationary properties, without considering the local and intrinsic dynamics. What are the microscopic processes that lead to macroscopic order? What is the nature of the corresponding phase transitions towards order? We will try to address some of these aspects in the next section. Furthermore, due to its flexibility, the implementation of the WASP model enables us to address a variety of different issues in active matter systems. For instance, instead of using systems of identical WASP's one can readily investigate the effect of polydisperse filament populations that are ubiquitous for real active systems, with a distribution of their properties such as their lengths, persistence, velocity, or interactions. This can also be extended to a spatial dependence of these properties. So far, a generic description of such systems on all relevant length and time scales is lacking.

In the next section we have reprinted the accepted manuscript that was published in *Science* in July 2018, which represents a combination of the above theoretical and experimental results. For a critical commentary on our work, please also refer to a recent article published in the *Physik Journal* of the German Physical Society [137].

## 2.5 Publication

# Emergence of coexisting ordered states in active matter systems

by

L. Huber<sup>\*,1</sup>, R. Suzuki<sup>\*,2,3,4</sup>, T. Krüger<sup>\*,1</sup>, E. Frey<sup>1</sup> and A. R. Bausch<sup>2</sup>

<sup>\*</sup>equal contribution, <sup>1</sup>Department of Physics, Arnold Sommerfeld Center for Theoretical Physics and Center for NanoScience, Ludwig-Maximilians-Universität München, Theresienstraße 37, 80333 München, Germany,

<sup>2</sup>Lehrstuhl für Biophysik (E27), Technische Universität München, James-Franck-Strasse 1, 85748 Garching, Germany,

<sup>3</sup>Graduate School of Medicine, Kyoto University, 606-8501 Kyoto, Japan,

<sup>4</sup>Institute for Integrated Cell-Material Sciences, Kyoto University, 606-8501 Kyoto, Japan

Accepted manuscript reprinted on pages [87–99](#)

with permission from *Science* **361.6399** (2018): 255-258,

DOI: [10.1126/science.aao5434](https://doi.org/10.1126/science.aao5434),

Link to article: [science.sciencemag.org/content/361/6399/255](https://science.sciencemag.org/content/361/6399/255).

© 2018 AAAS

Supplemental Material reproduced on pages [101–119](#).





**Title:**

**Emergence of coexisting ordered states in active matter systems**

**Authors:** L. Huber<sup>1,†</sup>, R. Suzuki<sup>2,3,4,†,‡</sup>, T. Krüger<sup>1,†</sup>, E. Frey<sup>1,\*</sup>, and A.R. Bausch<sup>2,\*</sup>

**Affiliations:**

<sup>1</sup>Arnold-Sommerfeld-Center for Theoretical Physics and Center for NanoScience, Department of Physics, Ludwig-Maximilians-Universität München, D-80333 Munich, Theresienstrasse 37, Germany

<sup>2</sup>Lehrstuhl für Biophysik (E27), Technische Universität München, James-Franck-Strasse 1, D-85748 Garching, Germany

<sup>3</sup>Graduate School of Medicine, Kyoto University, 606-8501 Kyoto, Japan

<sup>4</sup>Institute for Integrated Cell-Material Sciences, Kyoto University, 606-8501 Kyoto, Japan

\*Correspondence to: [frey@lmu.de](mailto:frey@lmu.de) (E.F.), [abausch@mytum.de](mailto:abausch@mytum.de) (A.B.).

† These authors contributed equally.

‡ Current address: Center for Integrative Medicine and Physics, Institute for Advanced Study, Kyoto University, 606-8501 Kyoto, Japan

**Abstract:**

Active systems can produce a far greater variety of ordered patterns than conventional equilibrium systems. Especially, transitions between disorder and either polar- or nematically-ordered phases have been predicted and observed in two-dimensional active systems. However, coexistence between phases of different types of order has not been reported. We demonstrate the emergence of dynamic coexistence of ordered states with fluctuating nematic and polar symmetry in an actomyosin motility assay. Combining experiments with agent-based simulations, we identify sufficiently weak interactions that lack a clear alignment symmetry as a prerequisite for coexistence. Thus, the symmetry of macroscopic order becomes an emergent and dynamic property of the active system. These results provide a pathway in which living systems can express different types of order by using identical building blocks.

**One Sentence Summary:**

Generic triple-phase coexistence of local order with different symmetries reveals versatility of active systems.

## Main Text:

The distinctive feature of active matter is the local supply of energy that is transduced into mechanical motion. Examples include assemblies of self-propelled colloidal particles (1-5), self-organising systems comprised of biopolymers and molecular motors (6-9), and layers of migrating cells (10, 11). These systems exhibit a rich phenomenology of collective phenomena and emergent properties, with features absent in passive, equilibrium systems. Self-propelled colloidal particles interacting solely by steric repulsion have been predicted (12, 13) to show phase separation into an ordered, solid-like phase with a disordered gas-like phase, similar to experimental observations (2-4). Active systems comprised of rod-shaped particles, cytoskeletal filaments, or colloidal particles with velocity alignment interactions show an even broader range of collective behaviour including polar clusters (1, 5-7), nematic lanes (9), and vortex patterns (8, 14), which in all cases phase-separate with a dilute isotropic, disordered background. Theoretical studies have shown that, in principle, alignment interactions can explain how these different types of orientational order and transitions between them emerge based on either agent based (15-21) or mean-field models (20-28). All these studies tacitly assume that, as in systems in thermal equilibrium, the symmetry of the observed macroscopic order is largely dictated by the symmetry of local alignment interactions. But to what degree is the symmetry of the macroscopic order constrained by the symmetry of the microscopic interactions? More broadly, can active systems depart from these constraints and express a multitude of different ordering simultaneously, as is the case for living systems like actin stress fibres and filopodia (29, 30)?

To study these fundamental questions, we employ the high-density actomyosin motility assay (Fig. 1A), which is ideally suited to address the microscopic processes that underlie pattern formation in active systems (6, 7, 31-34). By sensitively tuning the interactions between the myosin-driven filaments with a depletion agent, we are able to observe the emergence of a phase in which nematic and polar order stably coexist. The complete phase diagram is recovered from agent-based simulations of self-propelled filaments, in which weak alignment interactions quantitatively reproduce the experimentally determined microscopic collision statistics. We show that sufficiently weak interactions generically lead to dynamic coexistence of three phases (isotropic, nematic, and polar).

In the actomyosin motility assay, hydrolysis of adenosine triphosphate (ATP) enables actin filaments to actively glide over a lawn of non-processive heavy meromyosin motor proteins (31, 32). Previous studies have shown that increasing the filament density beyond a critical value results in the emergence of polar clusters and waves (6, 7) (Fig. 2A). These patterns are produced by collisions in which filaments may align in a polar or nematic fashion. The degree and symmetry of the alignment depends on the change in the relative orientation of the interacting filaments,  $\Delta = \theta_{out} - \theta_{in}$ , where  $\theta_{in}$  and  $\theta_{out}$  are the angles before and after a collision event, respectively (Fig. 1B). In theoretical studies (15-28) these collisions have been idealized by assuming that filaments either align in a strictly polar or strictly nematic fashion upon colliding (Fig. 1C). However, in actual experimental active-matter systems (8, 9, 34, 35), the degree of alignment caused by a single collision event is weak, i.e. the relative change in filament orientation is small,  $|\theta_{out} - \theta_{in}| \ll \pi$  (Fig. 1D). Moreover, the resulting alignment exhibits neither perfectly nematic nor perfectly polar symmetry. Instead, depending on the collision angle  $\theta_{in}$ , in the motility assay there is a weak tendency to favor either alignment or anti-alignment of the filaments (Figs. 1C, D). How then can such weak interactions without a clear alignment symmetry on a local scale lead to collective order

at the system level, and what features of the local interactions determine the global symmetry of the macroscopic state?

To answer this question we tuned the local interactions between the filaments, by adding polyethylene glycol (PEG, 35 kD), a depletion agent, at concentrations of up to 3% (w/v) to the assay (Fig. 1D, Fig. S1). The observed change in the binary collision statistics can be attributed to the excluded-volume effect of the PEG molecules, which forces the filaments closer to the bottom surface covered with motors, enabling each to interact with more motors on average, with a concomitant increase in motor processivity (Fig. 1E). This reduces the incidence of collisions where filaments just pass over each other (9), and increases the likelihood that filaments will repel each other sterically, thus enhancing the tendency to align nematically (Fig. 1D, (36)). This technique enabled us to continuously modulate the symmetry of alignment interactions at the microscopic level, and probe the robustness of pattern formation in the gliding assay at high filament densities. Despite the rather minute changes in interaction characteristics caused by adding PEG at a concentration of 3% (Fig. 1D), we found that polar flocks no longer form. Instead, the moving filaments quickly, within a few minutes, self-organize into a network of ‘ant trails’ (Fig. 2B, Movie S1). In contrast to the unidirectional filament motion found within polar clusters, the filaments that form these ‘lanes’ move bi-directionally, as do many colonial ant species (37). Since the filaments move along these tracks in either direction with equal probability (Fig. 2C, Fig. S2), the overall order is nematic, not polar, and stable; this is quantified by the local nematic order (Fig. S2A) and the autocorrelation function of the filament orientations (Figs. S2D,E). Moreover, while polar clusters propagate through the system at uniform speed, nematic lanes form static networks with branches spanning up to several 100  $\mu\text{m}$  in length (Fig. 2B). Filaments are also seen to continuously leave and enter the trails (Fig. 2D, Movie S2), such that these branches remain fixed in orientation and slowly grow and shrink at their ends (Fig. S2F). These processes, operating on a timescale of minutes, lead to a slow reorganization of network architecture, with new branches forming (Movie S3) while others contract (Movie S4). Note that these networks are isotropically oriented and that no significant actin bundling was observed below 3% PEG.

This fundamental qualitative change in macroscopic order, from propagating waves of polar order to branched networks of stable lanes within which filaments move bidirectionally, induced by relatively minor changes in interaction characteristics at the microscopic scale, is puzzling. To reveal the underlying mechanism, we developed an agent-based computational model that goes beyond simple collision rules and faithfully reproduces the experimentally observed (microscopic) binary collision statistics, and used it to predict the collective dynamics at large scales. Propelled actin filaments are modeled as discrete, slender chains of length  $L$  (Fig. 3A, Fig. S3, (36)). Each filament is assumed to move at a constant speed  $v$  with the body of the filament following the tip. The direction of motion changes upon interaction with other filaments, as well as through interaction with molecular motors. When the leading segment of a given filament collides with a segment of another filament at a relative orientation  $\theta$ , an alignment potential  $U(\theta)$  acts upon the tip. This potential is assumed to be the sum of terms with polar and nematic symmetry,  $U(\theta) \propto \varphi_p \cos \theta + \varphi_n \cos 2\theta$ , where  $\varphi_p$  and  $\varphi_n$  represent the respective mean change in orientation during a collision. We adjusted  $\varphi_p$  and  $\varphi_n$  such that the binary collision statistics of the computational model (Fig. 3B) closely resemble those observed experimentally (Fig. 1D).

Having validated the computational model at the microscopic level, we asked whether it captures the collective dynamics of the high-density actomyosin motility assay. We first performed large-scale simulations for model parameters corresponding to the absence of PEG. Starting from a

random uniform distribution of filaments, we observed that high-density wave fronts of polar ordered filaments rapidly form, surrounded by disordered, low-density regions (Fig. 3C, Movie S5). This matches the phenomenology observed in the motility assay. Next, we performed simulations in a parameter regime corresponding to 3% PEG. Again, in agreement with our experiments, we found networks of high-density nematic lanes surrounded by disordered, low-density regions (Fig. 3D), reminiscent to chaotic structures that were predicted for active nematics (21). The overall network architecture changed slowly, with trails extending or retracting from their ends, and some lanes merging on longer time scales (Fig. S4A, Movie S6).

The model was then used to predict the dependence of nematic vs. polar order on the filament density  $\rho_0$  and the ratio of nematic to polar alignment strength,  $\alpha = \varphi_n/\varphi_p$ . To facilitate simulations over a broad parameter range, we considered smaller systems with a box size of  $81.3 L$ . We monitored the (global) polar and nematic order parameters,  $P = |\langle \exp(i\theta) \rangle|$  and  $N = |\langle \exp(2i\theta) \rangle|$ , respectively, measured over all filaments after the dynamics had become stationary (Fig. S4B). In initial parameter sweeps we observed that, within certain intervals of  $\alpha$ , simulations starting from different realizations of randomly distributed filaments, but with identical parameter sets, sometimes resulted in polar and sometimes in nematic patterns (Fig. 3E, lower panel). Similar observations were made in a Vicsek-type model, but only if strong additional memory in the particle movement is included (17). The patterns in our simulation were stable within the simulation times and no switching between them was observed, suggesting the existence of a regime of interaction strengths in which the dynamics exhibit multistability. To probe these initial observations further, we checked for hysteresis effects in the collective dynamics (Fig. S5, (36)). To this end, we initiated our simulations in a parameter regime in which the system shows polar waves only ( $\alpha = 2.75$ , Fig. 3E, left panel), waited until the dynamics became stationary, and then quasi-statically increased the value of  $\alpha$  (i.e. giving the system sufficient time to equilibrate between successive adjustments of  $\alpha$ ), and monitored both nematic and polar order parameters (Fig. 3F, closed symbols). After reaching a regime in which the system gave rise to nematic lanes only ( $\alpha = 6$ , Fig. 3E, right panel), we reduced the value of  $\alpha$  quasi-statically (Fig. 3F, open symbols). While the nematic order parameter remained essentially unchanged, we observed a hysteresis loop in the polar order parameter  $P$ . As the relative strength of nematic to polar alignment is increased, the degree of polar order ( $P_+$ ) gradually declines until it reaches zero at some critical value  $\alpha_+$ . Conversely, in the reverse direction, polar order ( $P_-$ ) remains negligible up to a different critical value  $\alpha_-$ , and then suddenly jumps to a rather large value. The phase diagram in Fig. 4A was obtained using  $\delta P = P_+ - P_-$  to quantify the degree of multistability.

To test these predictions, we performed experiments over a broad range of actin and PEG concentrations, and obtained a phase diagram (Fig. 4B) whose topology closely resembles that obtained from the computational model (Fig. 4A). In particular, upon varying the strength of interaction between the filaments by changing the PEG level and thus  $\alpha$ , we find a broad regime of non-equilibrium steady states where polar waves and nematic lanes coexist simultaneously. Moreover, both simulations of large systems (Fig. 4C, Movie S7) and experiments (Fig. 4D, Movie S8) consistently show that the equilibrium is highly dynamic. Polar waves may invade regions containing nematic trails and thereby disrupt their network structure (Fig. S6A). After the passage of these waves, nematic lane networks are observed to re-form locally, often close to their original positions. The formation of nematic lanes was also observed at the left and right edges of polar waves (Fig. S6B, Movie S9). While in experiments, this coexistence remained stable during the full experiment duration (Fig. S6C), in simulations we performed a scaling analysis to probe the

lifetime of coexistence  $t_{fix}$  as a function of the finite system size, at different points in the multistable parameter region. We found that this lifetime grows linearly with the system size, while the time of initial pattern formation  $t_0$  remains small and constant (Figs. 4F, S7, (36)), implying a diverging time scale separation and stable coexistence in the thermodynamic limit.

These observations from experiment and theory imply that polar waves and nematic lanes are both intrinsically stable structures, suggesting that the non-equilibrium steady state represents a dynamic equilibrium between different patterns, which - although they have conflicting polar and nematic symmetries - coexist in a dilute, disordered background. We attribute their coexistence to the weak interaction between the active particles, which determines macroscopic order not at the microscopic level but renders the symmetry of collective order itself to become an emergent property, which is dynamic in space and time. If this picture is valid, then an increase in the alignment strength at the binary level should eliminate the ambiguity in symmetry and prevent the emergence of coexistence. To test this hypothesis, we performed extensive numerical simulations by varying  $\alpha$  and  $\varphi_p$  (Fig. 4E) and looking for multistability. Indeed, we find that as the total degree of alignment, i.e. both  $\varphi_n$  and  $\varphi_p$ , is increased, the multistable region contracts and eventually vanishes completely. In this limit there appears to be a sharp transition between a polar and nematic phase, similar to previous findings in a Vicsek-type toy model (18). We therefore conclude that the coexistence of patterns with mutual polar and nematic symmetries depends upon sufficiently weak alignment interactions between individual filaments. Furthermore, it seems to be crucial that the computational model includes arbitrary pairwise interactions and spatiotemporal correlations without relying on any ad hoc truncation. This allows for coarsening dynamics, where many different mesoscale filament configurations are explored until they take the form of either polar clusters or nematic lanes. These patterns become local attractors of the dynamics, such that - despite their conflicting symmetries - they can exist in juxtaposition within the same system. This indicates that the celebrated Gibbs phase rule - stating that in thermal equilibrium, one-component systems a three-phase coexistence only occurs at a singular point in parameter space - is invalid in active systems. Overcoming this thermodynamic constraint may be an essential and simple prerequisite for biological systems to produce heterogeneous, multitasking structures out of a single set of constituents, like it is the case for the cellular actin network (29, 30) and migrating cell layers (10, 11).

#### References and Notes:

1. J. Deseigne, O. Dauchot, H. Chaté, Collective Motion of Vibrated Polar Disks. *Physical Review Letters* **105**, 098001 (2010).
2. I. Theurkauff, C. Cottin-Bizonne, J. Palacci, C. Ybert, L. Bocquet, Dynamic Clustering in Active Colloidal Suspensions with Chemical Signaling. *Physical Review Letters* **108**, 268303 (2012).
3. J. Palacci, S. Sacanna, A. P. Steinberg, D. J. Pine, P. M. Chaikin, Living Crystals of Light-Activated Colloidal Surfers. *Science* **339**, 936 (2013).
4. I. Buttinoni *et al.*, Dynamical Clustering and Phase Separation in Suspensions of Self-Propelled Colloidal Particles. *Physical Review Letters* **110**, 238301 (2013).
5. A. Bricard, J. B. Caussin, N. Desreumaux, O. Dauchot, D. Bartolo, Emergence of macroscopic directed motion in populations of motile colloids. *Nature* **503**, 95-98 (2013).
6. V. Schaller, C. Weber, C. Semmrich, E. Frey, A. R. Bausch, Polar patterns of driven filaments. *Nature* **467**, 73-77 (2010).

7. T. Butt *et al.*, Myosin motors drive long range alignment of actin filaments. *J Biol Chem* **285**, 4964-4974 (2010).
8. Y. Sumino *et al.*, Large-scale vortex lattice emerging from collectively moving microtubules. *Nature* **483**, 448-452 (2012).
9. D. Inoue *et al.*, Depletion force induced collective motion of microtubules driven by kinesin. *Nanoscale* **7**, 18054-18061 (2015).
10. K. Kawaguchi, R. Kageyama, M. Sano, Topological defects control collective dynamics in neural progenitor cell cultures. *Nature*, (2017).
11. T. B. Saw *et al.*, Topological defects in epithelia govern cell death and extrusion. *Nature* **544**, 212-216 (2017).
12. J. Tailleur, M. E. Cates, Statistical Mechanics of Interacting Run-and-Tumble Bacteria. *Physical Review Letters* **100**, 218103 (2008).
13. Y. Fily, M. C. Marchetti, Athermal Phase Separation of Self-Propelled Particles with No Alignment. *Physical Review Letters* **108**, 235702 (2012).
14. M. Loose, T. J. Mitchison, The bacterial cell division proteins FtsA and FtsZ self-organize into dynamic cytoskeletal patterns. *Nature cell biology* **16**, 38 (2014).
15. F. Ginelli, F. Peruani, M. Bär, H. Chate, Large-scale collective properties of self-propelled rods. *Phys Rev Lett* **104**, 184502 (2010).
16. G. Grégoire, H. Chaté, Onset of Collective and Cohesive Motion. *Physical Review Letters* **92**, 025702 (2004).
17. K. H. Nagai, Y. Sumino, R. Montagne, I. S. Aranson, H. Chate, Collective motion of self-propelled particles with memory. *Phys Rev Lett* **114**, 168001 (2015).
18. S. Ngo, F. Ginelli, H. Chate, Competing ferromagnetic and nematic alignment in self-propelled polar particles. *Phys Rev E Stat Nonlin Soft Matter Phys* **86**, 050101 (2012).
19. T. Vicsek, A. Czirók, E. Ben-Jacob, I. Cohen, O. Shochet, Novel Type of Phase Transition in a System of Self-Driven Particles. *Physical Review Letters* **75**, 1226-1229 (1995).
20. J. Denk, L. Huber, E. Reithmann, E. Frey, Active Curved Polymers Form Vortex Patterns on Membranes. *Phys Rev Lett* **116**, 178301 (2016).
21. S. Ngo *et al.*, Large-scale chaos and fluctuations in active nematics. *Phys Rev Lett* **113**, 038302 (2014).
22. R. Aditi Simha, S. Ramaswamy, Hydrodynamic fluctuations and instabilities in ordered suspensions of self-propelled particles. *Phys Rev Lett* **89**, 058101 (2002).
23. J. Toner, Y. Tu, Flocks, herds, and schools: A quantitative theory of flocking. *Physical Review E* **58**, 4828-4858 (1998).
24. T. B. Liverpool, M. C. Marchetti, Instabilities of isotropic solutions of active polar filaments. *Physical review letters* **90**, 138102 (2003).
25. K. Kruse, J. F. Joanny, F. Jülicher, J. Prost, K. Sekimoto, Asters, Vortices, and Rotating Spirals in Active Gels of Polar Filaments. *Physical Review Letters* **92**, 078101 (2004).
26. E. Bertin, M. Droz, G. Gregoire, Boltzmann and hydrodynamic description for self-propelled particles. *Phys Rev E Stat Nonlin Soft Matter Phys* **74**, 022101 (2006).
27. A. Baskaran, M. C. Marchetti, Hydrodynamics of self-propelled hard rods. *Phys Rev E Stat Nonlin Soft Matter Phys* **77**, 011920 (2008).
28. S. Mishra, A. Baskaran, M. C. Marchetti, Fluctuations and pattern formation in self-propelled particles. *Phys Rev E Stat Nonlin Soft Matter Phys* **81**, 061916 (2010).

29. D. A. Fletcher, P. L. Geissler, Active biological materials. *Annu Rev Phys Chem* **60**, 469-486 (2009).
30. L. Blanchoin, R. Boujemaa-Paterski, C. Sykes, J. Plastino, Actin dynamics, architecture, and mechanics in cell motility. *Physiological reviews* **94**, 235-263 (2014).
31. M. P. Sheetz, R. Chasan, J. A. Spudich, ATP-dependent movement of myosin in vitro: characterization of a quantitative assay. *J. Cell Biol* **99**, 1867-1871 (1984).
32. T. Yanagida, M. Nakase, K. Nishiyama, F. Oosawa, Direct observation of motion of single F-actin filaments in the presence of myosin. *Nature* **307**, 58-60 (1984).
33. S. Hussain, J. E. Molloy, S. M. Khan, Spatiotemporal dynamics of actomyosin networks. *Biophys J* **105**, 1456-1465 (2013).
34. R. Suzuki, C. A. Weber, E. Frey, A. R. Bausch, Polar Pattern Formation in Driven Filament Systems Require Non-Binary Particle Collisions. *Nat Phys* **11**, 839-843 (2015).
35. D. Nishiguchi, K. H. Nagai, H. Chaté, M. Sano, Long-range nematic order and anomalous fluctuations in suspensions of swimming filamentous bacteria. *Physical Review E* **95**, 020601 (2017).
36. Materials and methods are available as supplementary materials on Science Online.
37. I. D. Couzin, N. R. Franks, Self-organized lane formation and optimized traffic flow in army ants. *Proceedings of the Royal Society of London B: Biological Sciences* **270**, 139-146 (2003).
38. S. MacLean-Fletcher, T. D. Pollard, Identification of a factor in conventional muscle actin preparations which inhibits actin filament self-association. *Biochemical and biophysical research communications* **96**, 18-27 (1980).
39. J. A. Spudich, S. Watt, The regulation of rabbit skeletal muscle contraction I. Biochemical studies of the interaction of the tropomyosin-troponin complex with actin and the proteolytic fragments of myosin. *Journal of Biological Chemistry* **246**, 4866-4871 (1971).
40. S. J. Kron, Y. Y. Toyoshima, T. Q. Uyeda, J. A. Spudich, Assays for actin sliding movement over myosin-coated surfaces. *Methods in enzymology* **196**, 399-416 (1991).
41. J. Howard, Mechanics of motor proteins and the cytoskeleton. (2001).
42. D.-B. Wang, F.-B. Hsiao, C.-H. Chuang, Y.-C. Lee, Algorithm optimization in molecular dynamics simulation. *Computer Physics Communications* **177**, 551-559 (2007).
43. H. Chate, F. Ginelli, G. Gregoire, F. Raynaud, Collective motion of self-propelled particles interacting without cohesion. *Phys Rev E Stat Nonlin Soft Matter Phys* **77**, 046113 (2008).
44. F. Peruani, F. Ginelli, M. Bär, H. Chaté, Polar vs. apolar alignment in systems of polar self-propelled particles. *Journal of Physics: Conference Series* **297**, 012014 (2011).
45. F. Thüroff, C. A. Weber, E. Frey, Numerical Treatment of the Boltzmann Equation for Self-Propelled Particle Systems. *Physical Review X* **4**, (2014).
46. A. Peshkov, I. S. Aranson, E. Bertin, H. Chate, F. Ginelli, Nonlinear field equations for aligning self-propelled rods. *Phys Rev Lett* **109**, 268701 (2012).
47. V. Schaller, C. Weber, E. Frey, A. R. Bausch, Polar pattern formation: hydrodynamic coupling of driven filaments. *Soft Matter* **7**, 3213 (2011).
48. H. H. Wensink *et al.*, Meso-scale turbulence in living fluids. *Proc Natl Acad Sci U S A* **109**, 14308-14313 (2012).

**Acknowledgments:****Funding:**

E.F acknowledges support from the DFG via project B02 within SFB 863. A.R.B. acknowledges support from the European Research Council in the framework of the Advanced Grant 289714-SelfOrg and the partly support by the DFG via project B01 within the SFB 863. All authors acknowledge the continuous support of the German Excellence Initiatives via the ‘NanoSystems Initiative Munich (NIM)’.

**Author contributions:**

L.H., R.S., T.K. and A.R.B. performed and designed the experiments. L.H., T.K. and E.F. performed and designed the simulations. All authors participated in interpreting the experimental and theoretical results and in writing the manuscript.

**Competing interests:**

The authors declare no competing financial interests.

**Data and materials availability:**

All relevant data are provided in the paper and its Supporting Information files, or can be found online at <https://github.com/LorenzHuber/ActivePolymerDataRepository/>.

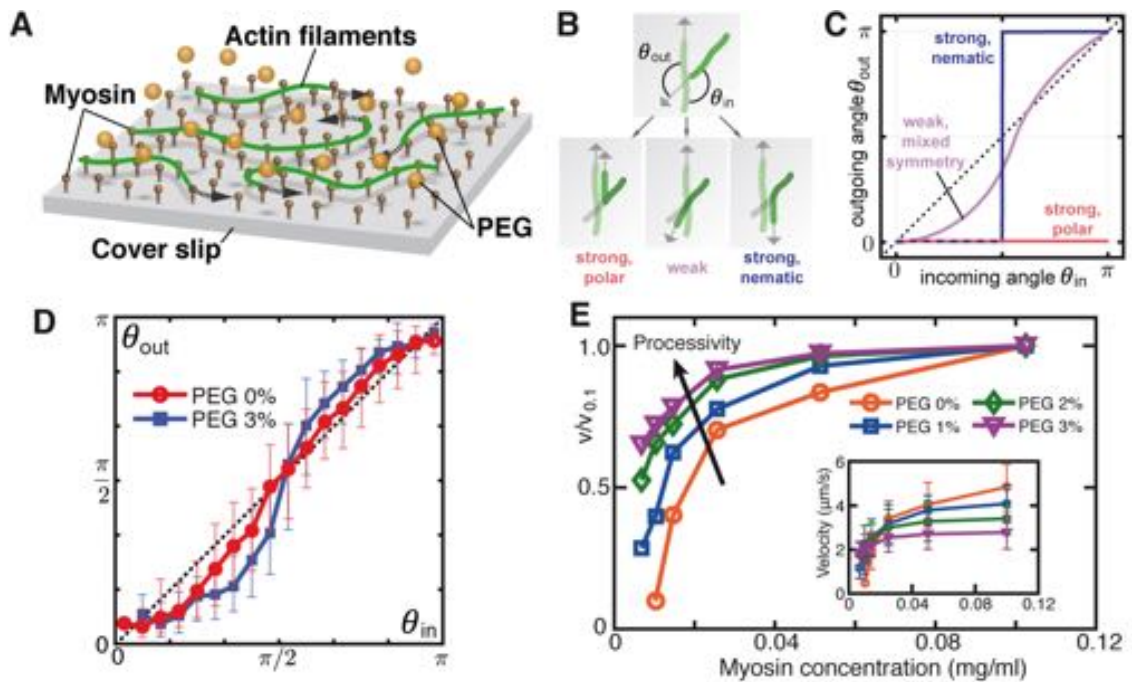


**Fig. 1. Interactions in the actomyosin assay.** (A) Schematic of the actomyosin motility assay. PEG acts as a depletion agent. (B) Illustration of different filament collision geometries with an incoming angle  $\theta_{in}$ , and corresponding binary collision curves (C). While strong polar or nematic collision rules lead to full alignment or anti-alignment, weak collisions cause a gradual change of orientation and may exhibit both polar and nematic features (purple line). The dashed line depicts neutral collisions ( $\theta_{out} = \theta_{in}$ ). (D) Binary collision statistics. Blue squares: PEG 3% (389 collisions). Red circles: no PEG (1113 collisions; data from ref. (34)). Error bars,  $\pm$  SD. (E) Processivity increases with PEG concentration, as indicated by the earlier saturation of normalized filament velocities as a function of motor density.  $v_{0.1}$  is the velocity at 0.1 mg/ml non-processive heavy meromyosin. Inset: absolute filament velocities.

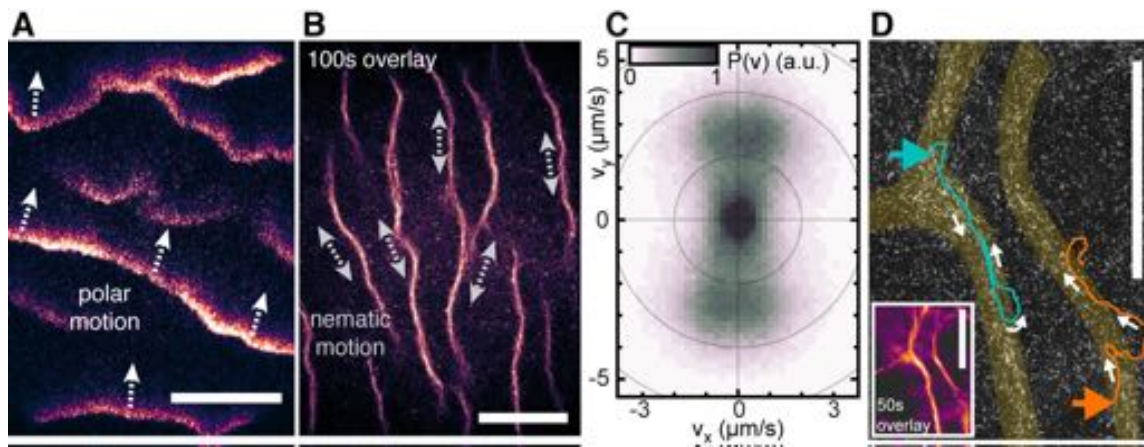


**Fig. 2. Experimental phenomenology.** (A) Polar actin clusters formed in the absence of PEG, moving in the same direction as the filaments (the fraction of fluorescently labelled filaments is 1:50, monomeric actin concentration 10  $\mu\text{M}$ ). (B) Large network of high-density nematic lanes formed at a PEG concentration of 3% and 5  $\mu\text{M}$  actin. The image is an overlay covering a period of 100 s to demonstrate that the structure is frozen and stable. Filaments move along the lane contours in opposite directions (labelled filament fraction is 1:60). (C) Probability density  $P(v_x, v_y)$  of instantaneous velocities shows the preferred bi-directional motion of filaments within a lane. (D) Single filaments move inside lanes (bright region). Two representative trajectories are shown (turquoise and orange) at 10  $\mu\text{M}$  actin and 2% PEG. Inset: overlay covering a period of 50 s. Polar (A) and nematic (B) motion are depicted by bi- and unidirectional arrows, respectively. Scale bars: 100  $\mu\text{m}$ .

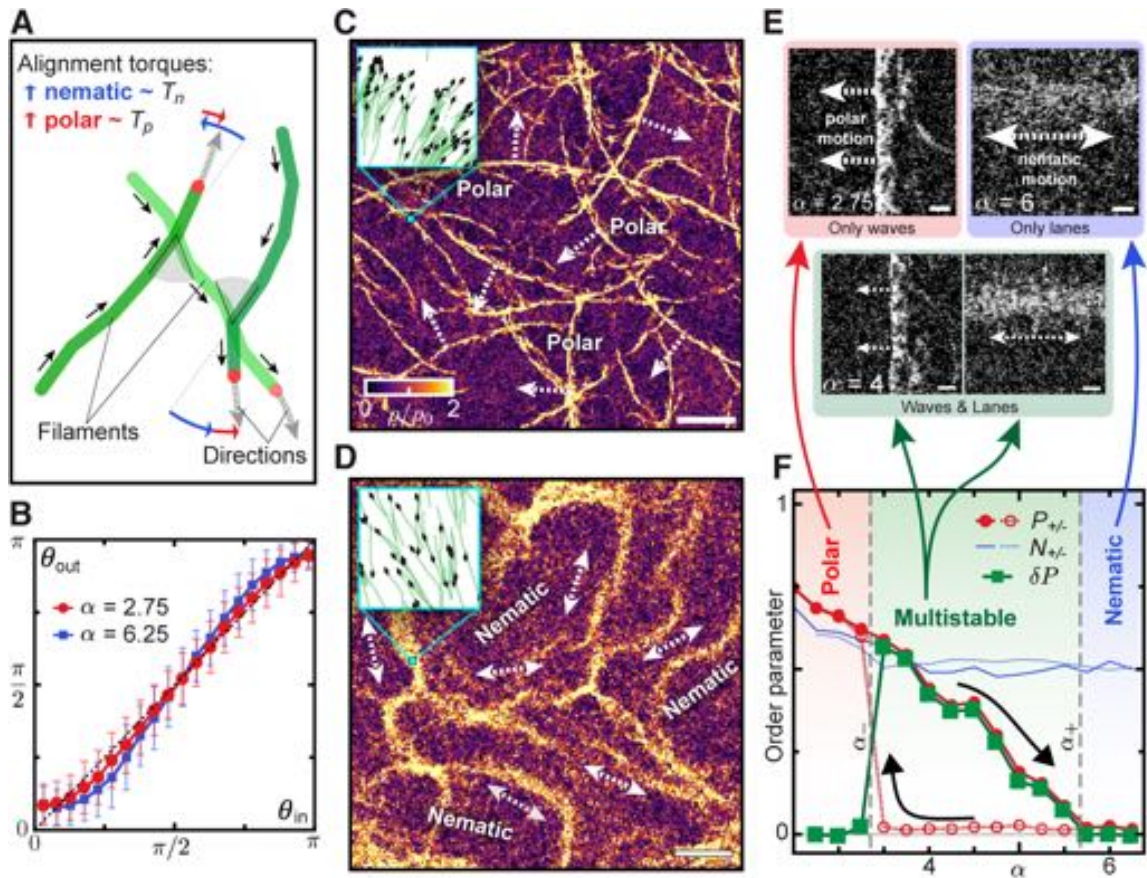


**Fig. 3. Simulation model and phenomenology.** (A) Illustration of the simulation model: filaments (green) are propelled along their contour (solid black arrows). Upon collision, the orientations of tips (gray arrows) are redirected in proportion to the polar and nematic alignment strengths (red and blue arrows). (B) Binary collision data from simulations for two selected curves with different  $\alpha$ . Error bars, 1 standard deviation. (C, D) Emergence of (C) polar waves ( $\alpha = 3$ ) and a (D) network of nematic lanes ( $\alpha = 6.25$ ) in large-scale systems. Insets: filaments within a single pixel with local density  $\rho$  and local polar (C) or nematic (D) order. In both panels, 544,000 filaments were simulated in a box of length  $650.2L$ , with a homogeneous density  $\rho_0 = 1.29/L^2$ . Scale bars:  $100L$ . Uni- and bidirectional arrows denote local polar and nematic filament motion. (E) Different steady states for small simulation boxes, with  $\rho_0 = 1.29/L^2$ : while  $\alpha = 2.75$  always produces polar waves and  $\alpha = 6$  always nematic lanes, at  $\alpha = 4$  either waves or lanes can be obtained in different realizations. Scale bars:  $10L$ . (F) Global order parameters during a hysteresis loop in  $\alpha$ . Black arrows denote the direction of the loop. Regions of non-zero  $\delta P$  (shaded in green) exhibit multistable behavior. For (B-F),  $\varphi_p = 2.1^\circ$ .

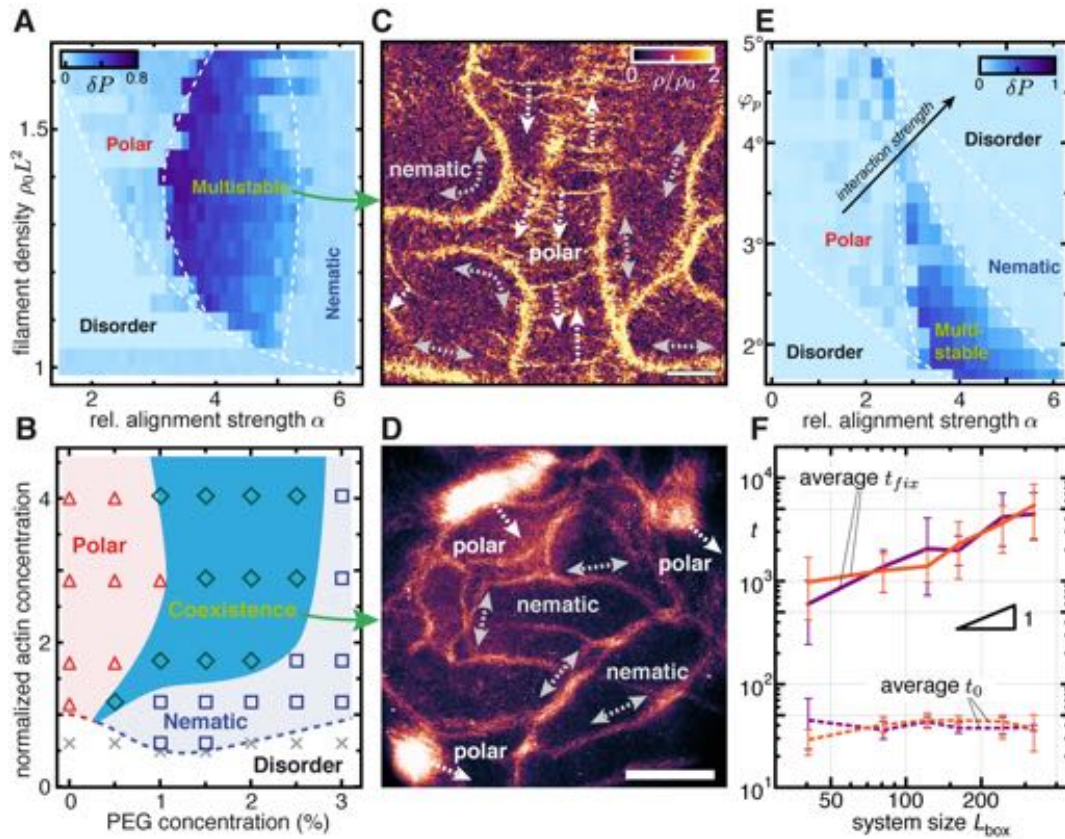


**Fig. 4. Phase diagrams and coexisting symmetries in experiment and simulation.** (A) Simulation phase diagrams for different filament densities  $\rho_0$  and relative alignment strengths  $\alpha$ . (B) Experimental phase diagram of emergent patterns for varying monomeric actin and PEG concentrations. Gray crosses: disorder. Red triangles: polar clusters. Blue squares: nematic lanes. Green diamonds: coexisting polar and nematic structures. Actin concentrations were normalized with respect to the estimated critical concentration in the absence of PEG (see Supplementary Materials for details). (C) Emergence of both polar waves and nematic lanes in large-scale simulations (scale bar:  $100L$ ) for  $\alpha = 4$  and a homogeneous density  $\rho_0 = 1.29/L^2$ . (D) Coexistence of polar clusters and nematic lanes in the motility assay at 2% PEG and  $5 \mu\text{M}$  actin. Scale bar:  $100 \mu\text{m}$ . (E) Phase diagrams for different polar alignment strengths  $\varphi_p$  and  $\rho_0 = 1.29/L^2$ . The total strength of alignment increases with both  $\varphi_p$  and  $\alpha$ . The shape of the phase diagram only slightly changes for larger system sizes (see Fig. S7A). (F) Scaling analysis of time scales at two different parameter sets (orange data:  $\varphi_p = 2.1^\circ$ ,  $\alpha = 4.17$ ; purple data:  $\varphi_p = 3.3^\circ$ ,  $\alpha = 3.13$ ). The average coexistence lifetime  $t_{fix}$  (solid lines) grows roughly linear with system size, while the average initial order time  $t_0$  (dashed lines) remains small and constant. Averages taken over 25 simulations per size, error bars represent 15<sup>th</sup> and 85<sup>th</sup> percentiles (see Supplemental Material and Fig. S7 for details). (A,E) Phase diagrams were obtained by hysteresis analysis in  $\alpha$ , white dashed lines depict the domain boundaries of the observed steady states. For (A,C),  $\varphi_p = 2.1^\circ$ .

**Supplementary Materials:**

Materials and Methods

Figures S1-S7

Table S1

Movies S1-S9

References (38-48)





## Supplementary Materials for

Emergence of coexisting ordered states in active matter systems

L. Huber, R. Suzuki, T. Krüger, E. Frey, and A.R. Bausch

correspondence to: [frey@lmu.de](mailto:frey@lmu.de) (E.F.), [abausch@mytum.de](mailto:abausch@mytum.de) (A.B.).

**This PDF file includes:**

Materials and Methods  
Figs. S1 to S7  
Table S1  
Captions for Movies S1 to S9

**Other Supplementary Materials for this manuscript includes the following:**

Movies S1 to S9

## Materials and Methods

### Assay preparation

G-actin solutions were prepared by dissolving lyophilized G-actin obtained from rabbit skeletal muscle (38, 39) in deionized water and dialyzing against fresh G-buffer (2 mM Tris pH 7.5, 0.2 mM ATP, 0.2 mM CaCl<sub>2</sub>, 0.2 mM DTT and 0.005% NaN<sub>3</sub>) overnight at 4°C. Polymerization of actin was initiated by adding one volume of tenfold concentrated F-buffer (20 mM Tris, 20 mM MgCl<sub>2</sub>, 2 mM DTT and 1 M KCl) to nine volumes of the G-actin sample. Heavy meromyosin (HMM) was prepared by dialyzing rabbit skeletal muscle against myosin buffer (0.6 M NaCl, 10 mM NaH<sub>2</sub>PO<sub>4</sub>, 2 mM DTT, 2 mM MgCl<sub>2</sub>, 0.05% NaN<sub>3</sub>) at 4°C (40). For fluorescence microscopy, fluorescently labelled filaments stabilized with Alexa Fluor 488 phalloidin (Invitrogen) were used.

Flow chambers were prepared by fixing coverslips (Carl Roth, Germany) to microscope slides (Carl Roth, Germany) with parafilm. The coverslips were coated with a 0.1% nitrocellulose solution, which was made by diluting a 2% solution (Electron Microscopy Sciences, Hatfield, PA) in amylacetate (Roth), and were left to dry overnight, prior to constructing the flow chambers. The chamber is typically three orders of magnitude larger than the length of a single filament, to avoid boundary effects. Prior to experiments, HMM was diluted in assay buffer (25 mM imidazole hydrochloride pH 7.4, 25 mM KCl, 4 mM MgCl<sub>2</sub>, 1 mM EGTA and 1 mM DTT), and actin was added to assay buffer that had been premixed with PEG 35,000 (Sigma) to yield a final PEG concentration of 0-3% (w/v). The flow chamber was briefly incubated with the HMM dilution and the surfaces were then passivated with BSA (10 mg/ml BSA (Sigma) dissolved in assay buffer), prior to addition of the actin solution. To initiate an experiment, 2 mM ATP dissolved in assay buffer was injected into the flow chamber, together with a standard antioxidant buffer supplement (GOC, containing 2 mg glucose oxidase (Sigma) and 0.5 mg catalase (Fluka)) to prevent oxidation of the fluorophore. After all components had been combined, the flow chamber was sealed with vacuum grease (Bayer Silicones).

### Assay concentrations

A list of all actin and PEG concentrations used for the figures and movies can be found in table S1. Unless stated otherwise, the HMM concentration was fixed at 0.1 mg/ml. Depending on the quality of the actin batch and the HMM motor proteins, filaments vary in length. Hence, critical densities in terms of monomeric actin concentrations vary between batches. Moreover, filament lengths appeared to be sensitive to PEG level, perhaps owing to enhanced filament rupture due to the increase in effective processivity. To obtain a reproducible, quantitative phase diagram from the patterns observed for different actin and PEG concentrations, we prepared a single actin batch (incubated at 10 μM monomeric actin), with which we performed 39 experiments within 36 h, at final concentrations of between 0.8 and 10 μM monomeric actin (the fraction of fluorescently labelled filaments was 1:25). For every experiment, the assay buffer was freshly prepared with one or other of seven different PEG premixes (0%, 0.5%, 1%, 1.5%, 2%, 2.5%, 3%). In figure 4B every actin concentration was normalized with respect to an estimated critical actin concentration of 1.75 μM (at zero PEG) for this specific actin batch. At this critical concentration, the filament density was roughly 9.2 filaments μm<sup>-2</sup> and filament lengths were exponentially distributed with a mean in the range of 0.5-0.7 μm.

### Image acquisition

A Leica DMI 6000B inverted microscope equipped with a 40x oil-immersion objective (NA: 1.25) was used to acquire data. Images were captured at a resolution 1344 x 1024 pixels with a charge-coupled device (CCD) camera (C4742-95, Hamamatsu) attached to a 0.35x or 1x camera mount. To track filament velocities, a TIRF microscope (Leica DMI 6000B, 100x oil-immersion objective (NA: 1.47), Andor iXon-Ultra-9369 camera with a resolution of 512 x 512 pixels) was used.

### Experimental binary collision statistics

To study the binary collision statistics (34), the acquired images were first converted into binary images and filaments were then identified by skeletonization using a standard library “bwmorph” available in Matlab. The coordinates of the filament contour were extracted by using a cubic spline fit to obtain  $\theta_1$ ,  $\theta_2$  and  $\theta_1'$ ,  $\theta_2'$  to determine the incoming angle  $\theta_{in}$  and outgoing angle  $\theta_{out}$  (Fig. S1A). Analysis of a collision begins once the images of two filaments intersect. In figure S1A, the images that are framed by red boxes are representative of a detected collision event. The incoming angle  $\theta_{in}$  is obtained 1 frame (0.13 sec) before the detected collision event, and the outgoing angle  $\theta_{out}$  is taken 1 frame after the filaments cease to intersect. Here, only binary collisions are studied and all collisions involving more than 3 filaments were discarded. Figure S1B shows all recorded collision events for a PEG concentration of 3%.

### Processivity

To study the change in the filament-motor interaction as a function of the PEG concentration, the degree to which filaments were forced onto the HMM motor lawn as a result of the excluded-volume effect was evaluated by measuring the effective processivity. Processivity is a measure of the ability of a single motor to execute a power stroke continuously without releasing the filament. While HMM is non-processive, i.e. always releases the actin filament after the power stroke, an effective processivity at the single (actin) filament level can be assumed, since many motors act simultaneously along a filament and also the number of active motors should increase due to the filaments being pressed down onto the motor lawn by the PEG. The effective processivity was evaluated by monitoring the change in filament velocity as a function of changing the motor density; the absence of a change in velocity with a decrease in HMM density demonstrates maximal effective processivity, while decrease in velocity with decrease in HMM density indicates that the interaction is effectively non-processive in nature (41).

### Velocity distribution and local order

Recording the nematic type of motion requires identification of single-filament motion, since opposing filament fluxes cancel each other out on larger length scales. For this reason, images were obtained by TIRF microscopy, which affords higher contrast and high temporal resolution (cycle time  $\Delta t = 0.0853s$ ), to track the local motion of individual filaments between consecutive frames. We recorded a nematic lane at 5  $\mu M$  actin and 2% PEG concentration, and a polar cluster and a disordered region at 10  $\mu M$  actin and 1% PEG concentration (Figs. S2A-C). We then segmented the images into 8 x 8 local bins and used the Kanade-Lucas-Tomasi feature-tracking algorithm in Mathematica 11.0.0.0, which is a robust estimator of the optical flow velocity, by maximizing the local intensity gradient

correlation for each segment, in order to obtain a large number ( $\sim O(10^5)$ ) of displacement vectors of filaments between consecutive image frames over an acquisition time of about a minute. From this we calculated smooth probability densities  $P(v)$  of filament velocities (lower left panels of Figs. S2A-C), as well as the local polar and nematic order parameters  $P = |\langle \exp(i\theta) \rangle_{ROI}|$  and  $N = |\langle \exp(2i\theta) \rangle_{ROI}|$  at a given time in the region of interest (ROI), respectively, over the acquisition time (lower right panels of Figs. S2A-C). To account for the shape of the lane structure, we only included bins that covered the lane (Fig. S2A). Note that for the polar and nematic order parameters, the respective amplitudes are comparable to those from simulations. Apart from the case of a polar cluster (Fig. S2B), which is inherently not static within the fixed ROI, the order of a nematic lane (Fig. S2A) is stationary over an interval corresponding to filaments crossing the ROI about 2 times.

### Autocorrelation function

Using an image sequence of a lane (Movie S2), we tracked 39 individual filaments starting inside lanes by eye and extracted the orientations  $\delta\theta(t) = \theta(t) - \theta(0)$  out of the recorded path at different times (Fig. 2D, Fig. S2D). From this the polar and nematic autocorrelation functions  $\langle \cos \delta\theta(t) \rangle$  and  $\langle \cos[2\delta\theta(t)] \rangle$  for different filaments (Fig. S2E) were obtained and averaged over every time point. As can be seen from the differences in decay times, polar order decays much faster than nematic order.

### Additional observations

At high concentrations of PEG and low actin concentration, the nematic lanes evolved into a packed vortex-like arrangement of branches after long times (roughly 15 min after the beginning of the experiment), indicating the emergence of additional types of order in this parameter region (Fig. S6D). For large concentrations of both actin and PEG, we observed the occasional bulk formation of long actin bundles (Fig. S6E) which attach to the motor lawn already shortly after experiment initialization, indicating additional depletion forces in-plane of the motility assay and suggesting a possible bundling transition for PEG concentrations above 3%. Note that the presence of bundles did not affect the formation of nematic lanes.

### Computational Model

Propelled actin filaments are modeled as discrete, slender chains of  $N-1$  cylindrical segments of length  $L$  and width  $a$  ( $L \gg a$ ), with the leading segment (tip) of each filament moving at a speed  $v$ , and the body of the filament following the tip. The direction  $\theta_0$  in which a filament tip is moving changes upon interaction with other filaments, as well as through interaction with molecular motors. The latter is described by a Gaussian white-noise process with a path persistence length  $L_p > L$ . The body of the filament with index  $n$  is pulled by its tip, parallel to its backbone. Hence, the motion of a cylinder segment with director  $u_i^{(n)}$  is given by  $v_i^{(n)} = K_s(u_{i-1}^{(n)} + u_i^{(n)})/2 [ |r_i^{(n)} - r_{i-1}^{(n)}| - L/(N-1) ]$ , where the index  $i \in \{1, \dots, N-1\}$  represents the contour position, and  $K_s$  is a sufficiently strong spring constant to ensure cylinder length conservation. Note that the direction of propulsion of every position  $r_i^{(n)}$  is the average of its' neighboring cylinder orientations, to provide a smooth lateral motion. When the leading segment of a given filament  $n$  collides with a segment of another filament  $m$  at a relative segment orientation  $\theta$ , an alignment potential

$U(\theta)$  acts on the tip's orientation; see figure S3A. The alignment potential is present within the area occupied by a filament of length  $L$  and width  $a$ , and acts on the tips of other filaments. To avoid artifacts such as surface roughness caused by discontinuous jumps and potential superpositions of bent filaments, cylinder potentials at inner bends are averaged, and at outer bends the cylinder gap is filled with a circular potential segment. In this way, local features of this potential do not change significantly when the contour moves, and discretization effects are small. Figure S3A depicts the geometry of filaments. The equations of motion (with unitary friction) are then given by

$$\begin{aligned}\frac{\partial}{\partial t} r_0^{(n)} &= v \cdot u_0^{(n)} = v \cdot (\cos[\theta_0^{(n)}], \sin[\theta_0^{(n)}])^T, \\ \frac{\partial}{\partial t} r_i^{(n)} &= K_s (u_{i-1}^{(n)} + u_i^{(n)}) / 2 \left( |r_i^{(n)} - r_{i-1}^{(n)}| - \frac{L}{N-1} \right), \text{ for } i > 0, \\ \frac{\partial}{\partial t} \theta_0^{(n)} &= -\frac{\delta H_0^{(n)}}{\delta \theta_0^{(n)}} + \sqrt{2v/L_p} \xi^{(n)},\end{aligned}$$

where  $\xi^{(n)}$  is random white noise with zero mean and unit variance, and

$$H_0^{(n)} = \sum_m \sum_j U_{m,j}^{(n)}$$

is the total alignment potential acting onto the direction of a given tip of a filament; the sum runs over all overlapping filaments  $m$  and all cylindrical segments  $j$  of each of those filaments. For the alignment potential, we assume

$$\begin{aligned}U_{m,j}^{(n)} &= C \left( |r_0^{(n)} - r_j^{(m)}|_{shDist} \right) \left[ A_n (\theta_0^{(n)} - \theta_j^{(m)}(r_0^{(n)})) + A_p (\theta_0^{(n)} - \theta_j^{(m)}(r_0^{(n)})) \right], \\ A_p(\theta) &= \frac{\varphi_p v}{a} \cos[\theta], \quad A_n(\theta) = \frac{\varphi_n v}{a} \cos[2\theta],\end{aligned}$$

where  $A_p$  and  $A_n$  are the polar and nematic parts of the alignment potential, respectively (Fig. S3B). The cutoff function  $C(x)$  is zero for  $x > a$  and otherwise  $(a-x)/a$ . The argument of the cutoff function,  $|\dots|_{shDist}$ , is the shortest distance between the tip and the cylindrical segment with which it is interacting. The values of local orientations  $\theta_j^{(m)}(r_0^{(n)})$  are determined by the direction tangent to the potential at contour position  $j$  of filament  $m$  and the relative tip position of  $r_0^{(n)}$ . The parameters  $\varphi_p, \varphi_n$  give the scale of typical reorientations during a collision, as can be easily seen by rescaling time in units of the collision time, i.e.  $t \rightarrow t \frac{a}{v}$ . During a multiparticle simulation, these alignment potentials may gradually lead to a maximal overlap of all contours at their centerline. Adding a weak repulsion force with a small amplitude  $s$  ( $s \ll v$ ) which acts on tips and is proportional to  $C(x)$  did not change the phenomenology, but avoided the unphysical and numerically very costly case of hundreds of filaments overlapping simultaneously.

### Numerical implementation

For the time integration, we used an Euler scheme. To ensure maximal performance, the code was implemented in C++ and designed to operate on a parallelized architecture. Despite the sophisticated interaction geometry, which requires many machine operations

per iteration, we were able to realize large simulation times for systems of many filaments, by exploiting the localized nature of filament interactions: for each filament tip, a Verlet (42) list was used to store all filaments which were located within a certain cutoff range. After a certain number of time steps a cell list algorithm (42) was used to update the Verlet lists. The cutoff distance was chosen such that no interaction occurring between consecutive updates could be overlooked. The cell algorithm used for the update of the Verlet lists divides the surface into squares of a sufficient size. Instead of calculating the distances to all other filaments in the whole system, only the distance to filaments in the same or in a neighboring cell must be checked. We further used OpenMP to parallelize the code. To further increase performance, we applied an additional averaging procedure by replacing the individual relative angles  $\theta$  in the alignment potential with the mean value over all interaction partners of a respective tip. This allows for a better numerical convergence for larger temporal step sizes, while the properties of the system remain the same.

### Simulation parameters

For the simulations in the paper, we fixed the following filament parameters (length units are given in filament lengths, i.e.  $L = 1$ ): filament aspect ratio  $L/a = 21$ , persistence length  $L_p = 31.75 L$ , velocity  $v = 1$ , and filaments were discretized into  $N = 5$  segments. In these units,  $t = L/v = 1$  corresponds to the time in which a filament travels a distance equal to its own length  $L$ . A fixed time increment of  $\delta t = 3.17 \cdot 10^{-4}$  was sufficient to achieve minimal numerical errors. The range of interaction strengths  $\varphi_p, \varphi_n$  was set between  $2.1^\circ$  and  $12.9^\circ$ , which is comparable to the average amount of reorientation observed in the experiments (up to  $14.6^\circ$  for 3% PEG). The sensitivity of the onset and type of collective motion with respect to other parameters like persistence length and aspect ratio will be the subject of a subsequent study.

### Computational binary collision statistics

Using a small system with two filaments and random initial conditions, the change in polymer orientation (measured from front to back) during a collision was recorded. A collision begins at the time when two filaments first touch, i.e. approach to within a distance smaller than  $a$ , and ends when the distance between them becomes larger than  $L/4$ , or, when the filaments have nearly aligned, after propagating a cutoff distance  $2L$ . The resulting scatter plot of incoming and outgoing angles is then binned into intervals of different incoming angles and averaged to produce the binary collision curve displayed in figure 3B. Figure S3C shows the continuous variation of the average reorientation  $\Delta = \langle \theta_{out} \rangle - \theta_{in}$  as a function of  $\alpha$ . Note that angular fluctuations  $\sigma = \sqrt{Var[\theta_{out}]}$  for  $L_p = 31.75L$  are of the same order as  $|\Delta|$ , similar as in the experiment (Fig. 1D). Figures S3D, E visualize the effect of noise during binary collisions.

### Macroscopic states in simulations

In large-scale simulations ( $L_{box} = 650.2L$ , 544,000 filaments), stationarity was not reached within feasible simulation times, but we observed a subsequent coarsening dynamics of the emergent patterns (Movies S5-7). We emphasize the striking similarity between the nematic lane network and the dynamics of its branches (Fig. S4A, Movie S6)

and the patterns seen in our experiments. To visualize these simulations, the system was subdivided into a grid of  $256 \times 256$  bins with well-defined local variables: Per bin, the local density  $\rho$ , polar order  $p = |\langle \exp[i\theta] \rangle_{bin}|/\rho_0$ , and nematic order  $n = |\langle \exp[2i\theta] \rangle_{bin}|/\rho_0$  are calculated and normalized by the average density  $\rho_0 = 544,000/L_{box}^2 = 1.29/L^2$ .

For the smaller systems (box length  $L_{box} = 81.3L$ ), stationarity was typically achieved by  $t < 1,500$  (Fig. S4B) and the states were characterized by the value of the global order parameters  $P$ ,  $N$ . The observed polar steady states appear to be very similar to those already reported in Refs. (26, 43-45), in spite of the conceptually different definitions of the underlying microscopic particles and their interactions that rely on idealized alignment rules. In the nematic steady state, the orientational autocorrelations resemble their experimental counterparts in exhibiting non-vanishing nematic correlations (Fig. S4C). Similar to the polar case, the observed phase separation into a high-density nematic band and a low-density gas resembles the patterns observed in Refs. (15, 44, 46), despite different interaction schemes. Due to the periodic boundary conditions, horizontal/vertical orientations predominate (Fig. 3E), but diagonal states were also found (Fig. S4D). We occasionally encountered the emergence of dual polar waves, which are locally polar and collide head-on, such that the global order is (almost) nematic. These states are predominantly located in the polar and multistable parameter regime, especially for large densities (roughly  $\rho_0 > 1.5/L^2$ , see figures S5A-D). While they are established by smectic decay of a nematic lane (Fig. S4D), it is not clear whether these colliding waves represent a transient phase on the way to a purely polar state or a stable solution of their own. We did not observe these patterns in our experiments, but this can be explained by hydrodynamic effects that are present in the actin motility assay (47): large polar actin clusters induce a flow field in the surrounding fluid, which suppresses any opposed local filament motion of large amplitude (in contrast to low-amplitude nematic motion within lanes). For large polar alignment strengths  $\varphi_p$ , polar states did not evolve into smooth wave profiles but persisted as a collection of erratically moving polar flocks (Fig. S4E). In this regime, the multistable region with respect to nematic lanes becomes elusive, similar to the previously reported abrupt switch between polar and nematic symmetry in a Vicsek-like model with fully aligning interactions of stochastically switching symmetry (18). For both large polar and nematic alignment strengths, filaments appear globally disordered but with some degree of local nematic order (upper right region of Fig. 4E), which appear similar to turbulent nematic states reported previously (48).

### Hysteresis analysis

To quantify the multistable region, we used smaller system sizes in our simulations ( $L_{box} = 81.3L$ ). We started our simulations in a strictly polar parameter regime ( $\alpha = 0$ ,  $\varphi_p \neq 0$ ) and waited until the dynamics had become stationary ('waiting' time  $\Delta t = 1,587.3$ ). We then incrementally increased  $\alpha$  by a small amount  $\Delta\alpha$  during the simulation, measured  $P_+$ ,  $N_+$  ("+" for increasing direction), and reiterated the procedure until  $\alpha = 6.25$  was reached. Then, we changed the direction and progressively reduced  $\alpha$  while recording the values of  $P_-$ ,  $N_-$  to complete the hysteresis loop in  $\alpha$ . We obtained two-dimensional phase diagrams by repeating the hysteresis analysis for different filament densities  $\rho_0$  and different polar alignment strengths  $\varphi_p$  (Figs. 4A,E). Figures S5A,B,E,F show the corresponding global order parameters in the "+" direction, figures S5C,D,G,H in the "-"

direction, respectively. For figure 4A, and for  $\rho_0 < 1.67/L^2$  in figures S5A-D, we used  $\Delta\alpha = 0.175$ ; for all other data  $\Delta\alpha = 0.25$ . Note that the multistable parameter region depends only weakly on the system size: upon doubling  $L_{box} = 162.5L$  the boundaries only shift slightly in parameter space (Fig S7A).

As can be seen in figure 3F the transition from a nematic lane into a polar wave is rather discontinuous; a lane becomes completely destabilized by a randomly emerging polar flock. The transition from polar waves to nematic lanes is quite different: the global polar order amplitude seems to vanish smoothly, although spatial structures change from a wave (orthogonal to particle motion) into a lane (parallel to the particle motion). It should be noted that a single polar wave, once formed, is very stable, even when  $\alpha$  is decreased in the minus direction far below the onset of collective motion (see the lower left corners of figures S5C,G); occupying almost all filaments, the wave profile becomes extremely dense and ordered (Fig. S4F), which represents a limiting case of the model assumptions (polar flocks do not stop to accumulate filaments for increasing density).

#### Time scale analysis of coexistence

To quantify and extrapolate the long-time behavior of coexisting polar and nematic structures in the simulations, we analyzed different time scales of pattern formation as a function of the (finite) system size. To this end, we tracked the evolution of the local order parameters, which are reliable indicators of the nature of the ordered state, and determined the fixation times  $t_{fix}$  upon which a system adapted either a distinctly polar ordered or nematically ordered state, as a function of the system size  $L_{box}$ . The local order parameters are defined as follows: any system of  $M$  filaments can be decomposed into a set of clusters of overlapping filaments,  $\{c\}$ . A cluster  $c$  has the following properties: cluster size  $m_c$ , cluster polar order  $\pi_c = |\sum_{j=1}^{m_c} \exp[i\theta_j]|/m_c - \Delta(m_c)$ , cluster nematic order  $\nu_c = |\sum_{j=1}^{m_c} \exp[2i\theta_j]|/m_c - \Delta(m_c)$ , where  $\Delta(l) = |\sum_{j=1}^l \exp[iU_j]|/l$ ,  $\{U_j\} \in U(0,2\pi)$  is the expected random order of a finite-size cluster. Hence, the local polar and nematic order  $\langle\pi_c\rangle = \sum_{\{c\}} \pi_c m_c/M$ ,  $\langle\nu_c\rangle = \sum_{\{c\}} \nu_c m_c/M$  are given by the mean cluster orders, taken over the whole cluster population. Note that with this definition, the local order parameters do not depend on the global orientation and arrangement of the whole system.

Figures S7D,E show the evolution of local order parameters  $\langle\pi_c\rangle$ ,  $\langle\nu_c\rangle$  with corresponding snapshots of the underlying simulations, for different initial conditions but identical parameters. Note that an initial plateau value of  $\langle\pi_c\rangle$ ,  $\langle\nu_c\rangle$  is achieved extremely fast, within a time scale  $t_0$  which we call the initial pattern formation time as it corresponds to the emergence of local, polar clusters. Before the system has reached a stationary state, which is either polar or nematic in nature, it exhibits coexisting structures of both types, which is reflected in the behavior of the local order parameters: when the system becomes fully polar (Fig. S7D), the local polar order  $\langle\pi_c\rangle$  eventually approaches the local nematic order  $\langle\nu_c\rangle$ , at the fixation time (or coexistence time)  $t_{fix}$ . When the system becomes fully nematic (Fig. S7E), the local polar order  $\langle\pi_c\rangle$  drops to a value below its initial plateau value and saturates at a lower (but finite) level at  $t_{fix}$ . Figures 4F, S7B,C show the statistics of these time scales, which were obtained by fitting piecewise-linear functions or crossing times of  $\langle\pi_c\rangle$ ,  $\langle\nu_c\rangle$  at any simulation, and for two different sets of  $\alpha$ ,  $\varphi_p$  in the multistable

parameter region. Note that the linear dependence of  $t_{fix}$  on  $L_{box}$  has a very large amplitude ( $t_{fix}/t_0 \approx 100$  for  $L_{box} = 325.1L$ ), and that there are strong variations towards very large fixation times. Unexpectedly, neither  $t_0$ , nor  $t_{fix}$  seem to not depend much on the overall strength of filament interaction (given the different parameter sets  $\alpha, \varphi_p$ ), and hence on the exact position in multistable parameter domain.

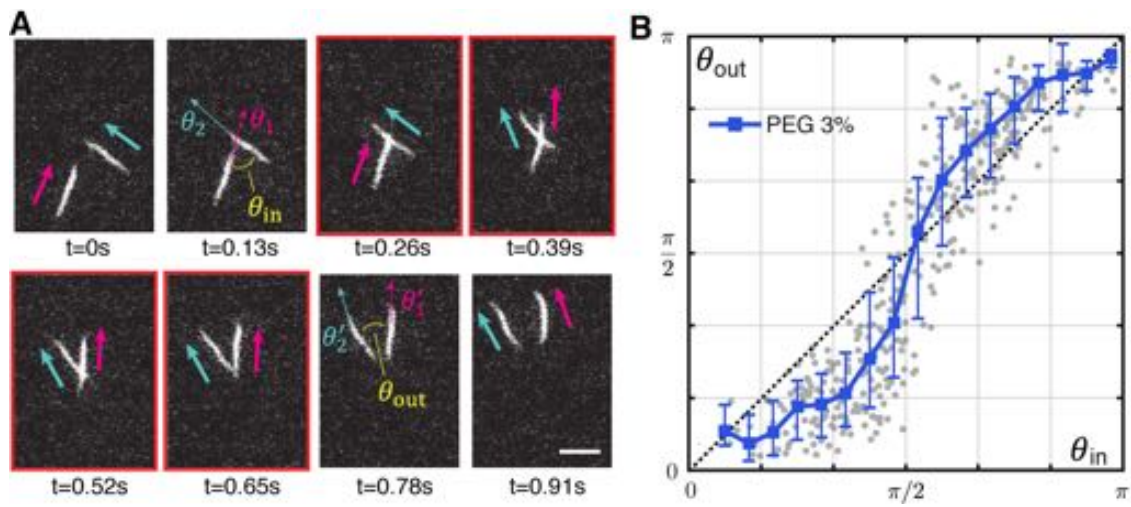


**Fig. S1. Collision measurements.**

(A) Illustration of collision angles during a binary collision. Scale bars: 2  $\mu\text{m}$ . (B) Full binary collision statistics at a PEG concentration of 3%. Error bars,  $\pm$  SD.

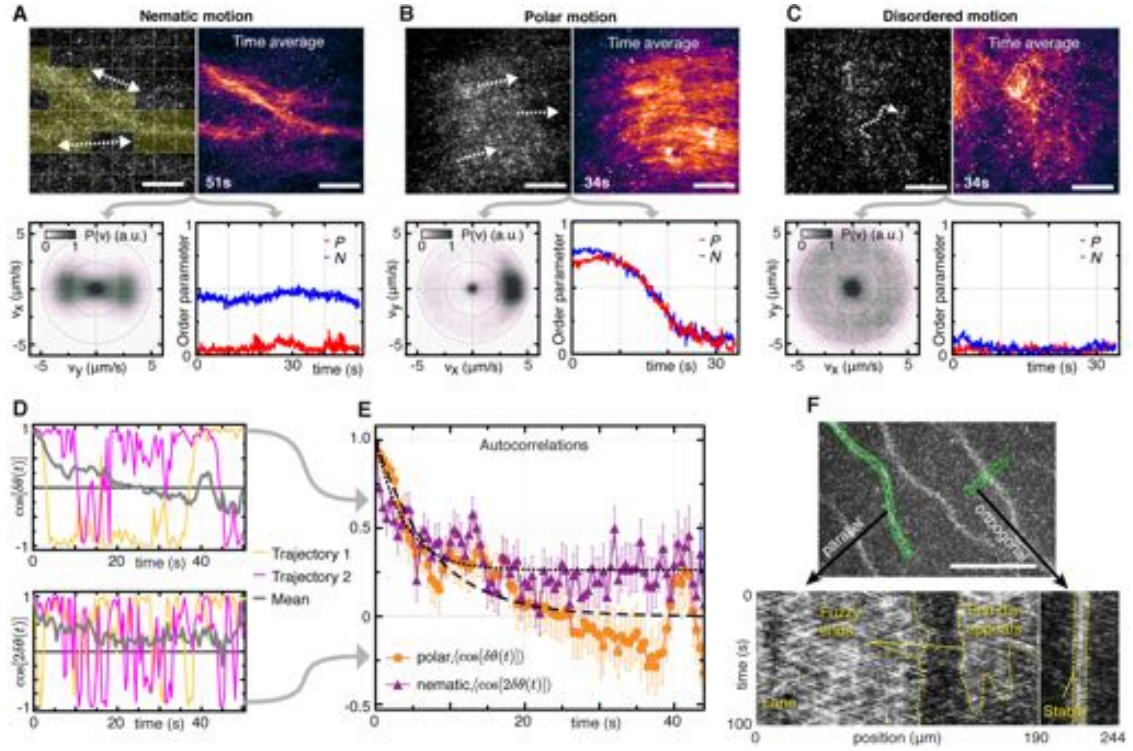


**Fig. S2. Filament dynamics.**

(A-C) Local dynamics of filaments within nematic lanes (A), polar clusters (B) and in disordered motion (C): Upper left panels are plain snapshots. In (A), the yellow area denotes the subgrid in which filaments were tracked. Upper right panels are time-averaged images over a time period indicated in the graphs to display the average motion of structures. Lower left and right panels depict two-dimensional probability densities  $P(v)$  and evolution of corresponding polar (red line) and nematic (blue line) order parameters during acquisition time, respectively. (D) Time evolution of  $\cos[\delta\theta(t)]$  and  $\cos[2\delta\theta(t)]$  for two selected trajectories (yellow and pink traces in figure 2D). Reversal events are manifested by jumps in the amplitude from 1 to -1 or back. (E) Autocorrelation functions of filament orientation inside lanes ( $n = 39$ ); dashed gray lines are fits to guide the eye. Error bars,  $\pm$  SD. (F) Kymographs of lane structures, taken orthogonally to a lane (lower left panel) and parallel to, and past the end of a lane (lower right panel). Dashed yellow lines depict lane edges. Scale bars are  $20 \mu\text{m}$  in (A-C),  $100 \mu\text{m}$  in (F).

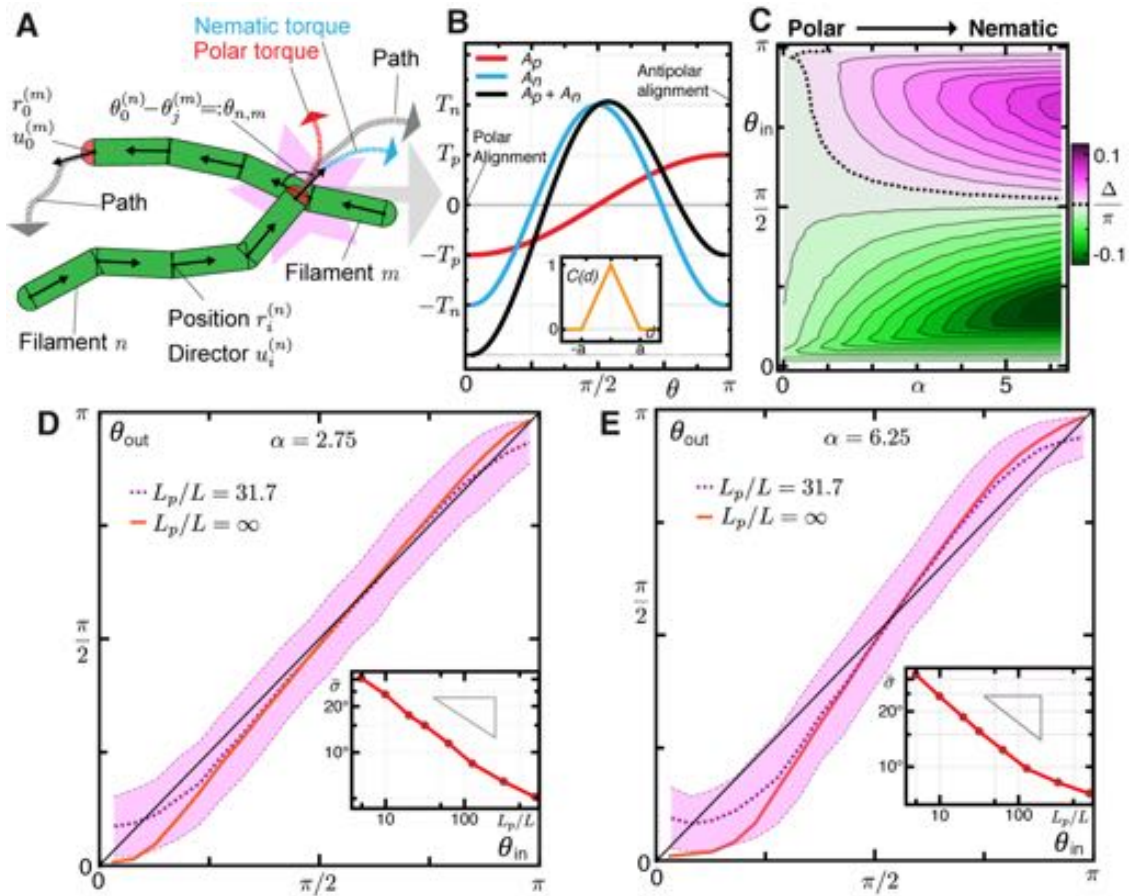


**Fig. S3. Collisions in the simulation model.**

(A) Illustration and annotation of the filament geometry. The collision occurs at the point marked by the pink region. (B) Nematic (blue line) and polar (red line) alignment potential and the mixed symmetry of their superposition (black line) plotted as a function of the relative orientation  $\theta$ . Inset: cutoff potential  $C(d)$ . (C) Average reorientation  $\Delta = \langle \theta_{out} \rangle - \theta_{in}$  during binary collisions plotted as a function of the incoming angle  $\theta_{in}$  and the relative alignment strength  $\alpha$  ( $L_p = \infty$ ). (D, E) Binary collision statistics for  $\alpha = 2.75$  (D) and  $\alpha = 6.25$  (E) with different  $L_p$  ( $\varphi_p = 2.1^\circ$ ). The shaded area marks the regions within the standard deviation  $\sigma$  for  $L_p = 31.7L$ . Inset: Dependence of the average standard deviation  $\bar{\sigma} = \langle \sigma \rangle_{\theta_{in}}$  for different angles on  $L_p$ ; the gray triangle corresponds to a scaling of  $L_p^{-1/3}$ .

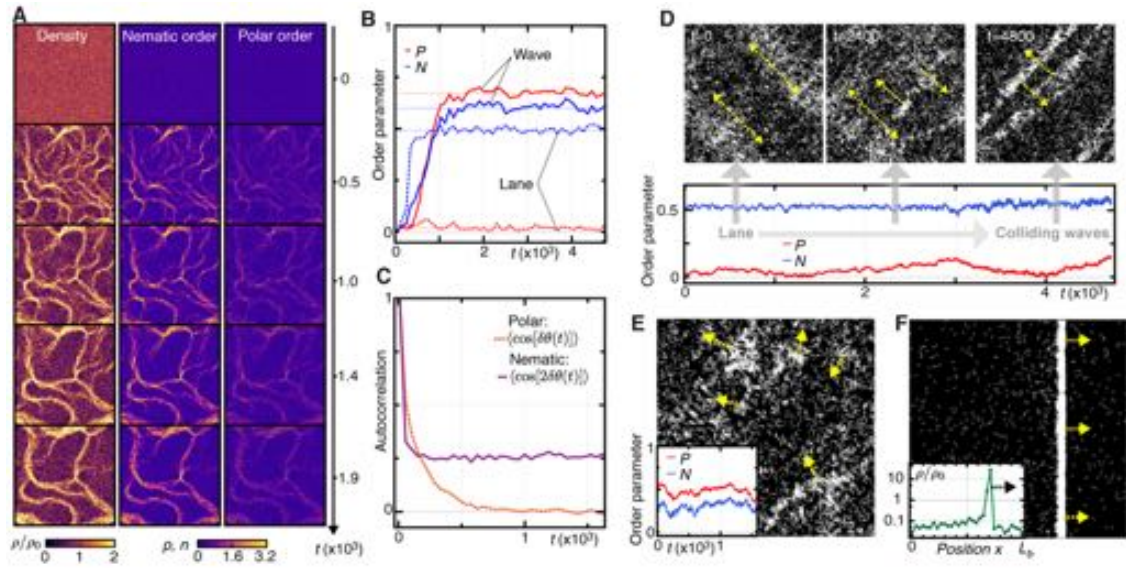


**Fig. S4. Evolution of patterns in simulations.**

(A) Dynamics of large nematic networks ( $\varphi_p = 2.1^\circ$ ,  $\alpha = 6.25$ ,  $\rho_0 = 1.29/L^2$ ,  $L_{box} = 650.2L$ ). The panels depict the evolution of the local density  $\rho$  (left), nematic order  $n$  (middle) and polar order  $p$  (right). (B) Evolution of global order parameters  $P$ ,  $N$  in systems with waves (solid lines, from the simulation of figure 3F, upper left panel) and lanes (dashed lines, from the simulation in figure 3F, upper right panel). (C) Autocorrelation of filament orientations within a lane (from the simulation in figure 3F, upper right panel). (D) Decay of a nematic lane (upper left panel) towards colliding waves (upper right panel) along the diagonal axis of the system ( $\varphi_p = 2.1^\circ$ ,  $\alpha = 4.5$ ,  $\rho_0 = 1.51/L^2$ ). Note that the decay process does not involve large jumps in the global order parameters (lower panel). (E) Irregular polar cluster. Inset: evolution of its order parameters ( $\varphi_p = 5.0^\circ$ ,  $\alpha = 2$ ,  $\rho_0 = 1.29/L^2$ ). (F) Very narrow and dense polar wave in a subcritical parameter region ( $\varphi_p = 3.6^\circ$ ,  $\alpha = 0$ ,  $\rho_0 = 1.29/L^2$ ). Inset: density profile of the wave in  $x$ -direction. For (B-F),  $L_{box} = 81.3L$ .

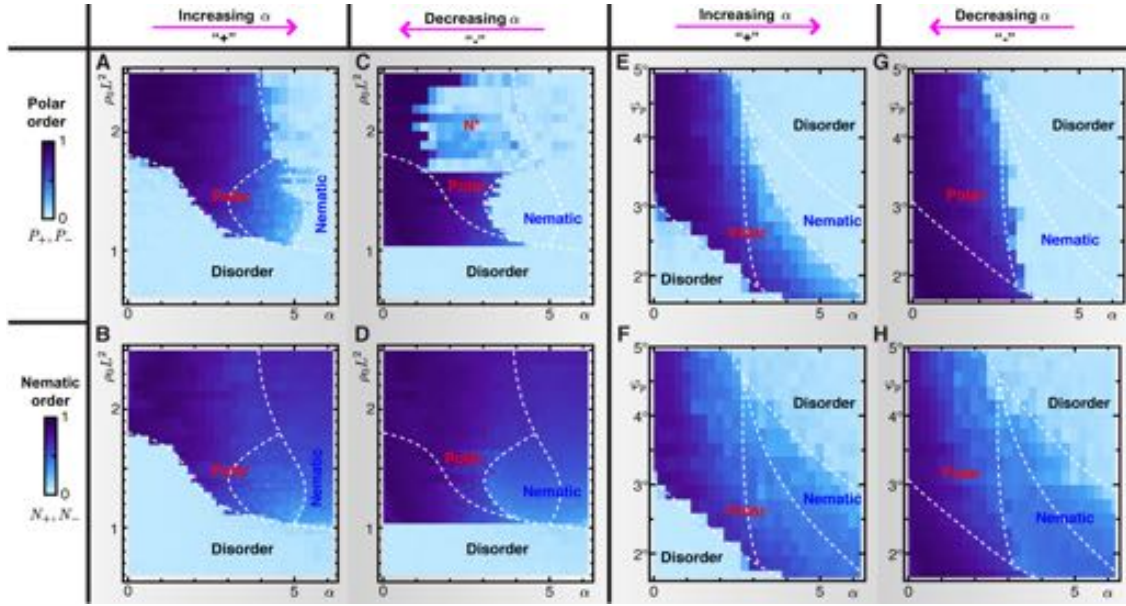


**Fig. S5. Hysteresis analysis of global order parameters.**

Global order parameters plotted as a function of the relative alignment strength  $\alpha$  for (A-D) different filament densities  $\rho_0$  (at  $\varphi_p = 2.1^\circ$ ) and for (E-H) different polar alignment strengths  $\varphi_p$  (at  $\rho_0 = 1.29/L^2$ ). The direction of increasing  $\alpha$  is depicted in (A, E) ( $P_+$ ) and (B, F) ( $N_+$ ), the decreasing direction is given by (C, G) ( $P_-$ ) and (D, H) ( $N_-$ ). White dashed lines represent critical values between domains of different patterns to guide the eye. The region  $N^*$  in (C) corresponds to states which were dominated by waves colliding head-on.

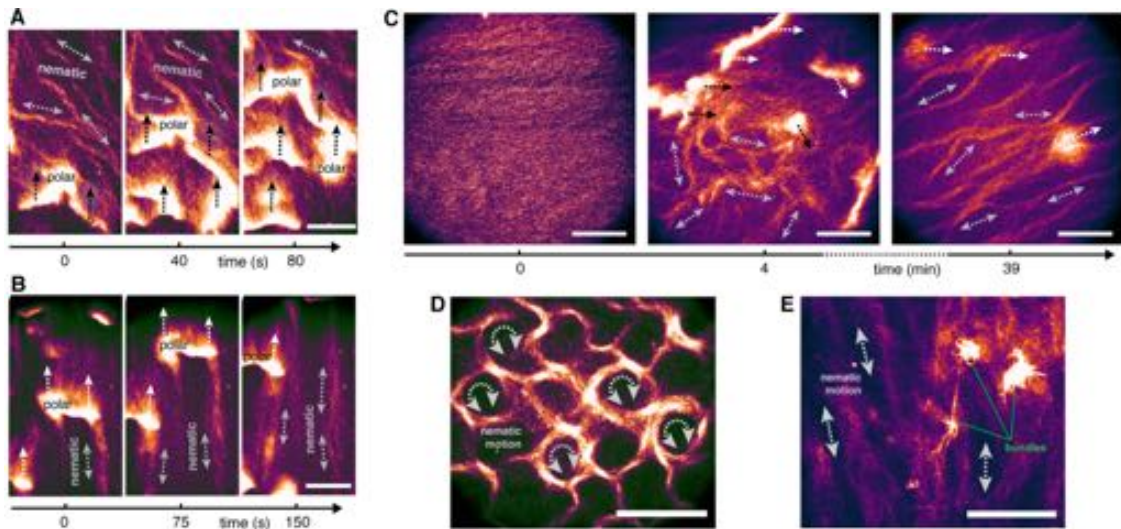


**Fig. S6. Interplay and dynamics of macroscopic structures.**

(A) Time evolution of polar clusters engulfing nematic lanes by running over them. (B) Time evolution of a polar cluster that leaves nematic lanes trailing from its 'wing-tips'. (C) Evolution of coexisting patterns during an experiment, visualized by snapshots at different times after ATP addition. Within a few minutes (roughly 2 min), both polar clusters and nematic lanes are fully developed (middle panel). At the end of the experiment, coexistence is still present (right panel). (D) Vortex-like mesh of nematic branches. (E) Lane network with occasional dynamic actin bundles. Scale bars are 100 μm in (A-C), and 50 μm in (D, E). Uni- and bi-directional arrows denote polar and nematic motion, respectively.

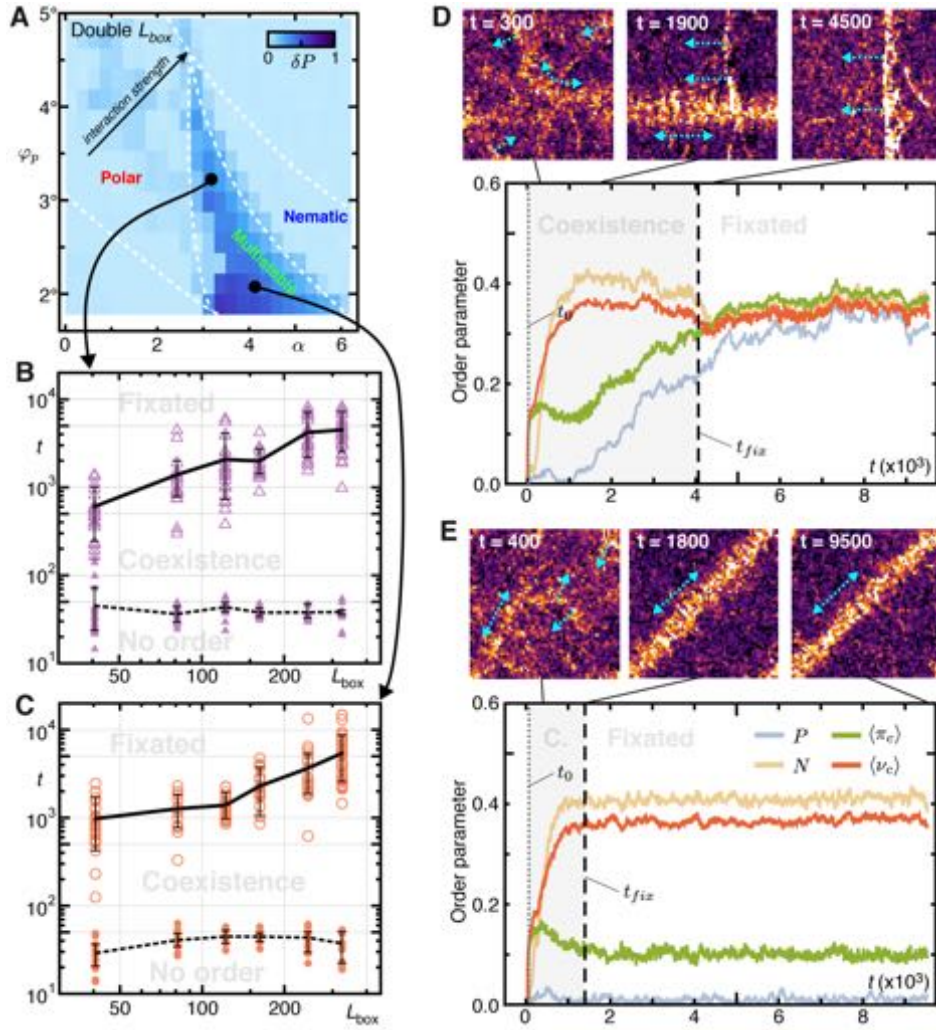


**Fig. S7. System size dependence of dynamics observed in simulations.**

(A) Multistable parameter region obtained by hysteresis analysis, with doubled system size  $L_{box} = 162.5L$  as compared to Figs. 4E, S5E-H with otherwise identical parameters. White dashed lines denote the approximate stability domain boundaries of half-sized systems which are already shown in Figs. 4E, S5E-H. (B, C) System size scaling analysis at (B)  $\varphi_p = 2.1^\circ, \alpha = 4.17$  and (C)  $\varphi_p = 3.3^\circ, \alpha = 3.13$ . Open purple triangles and open orange circles denote individual  $t_{fix}$  events, full symbols depict  $t_0$ , respectively. Black lines and arrow bars are average values and 15<sup>th</sup>/85<sup>th</sup> percentiles (as in Fig. 4F). (D, E) Examples of time evolutions of local ( $\langle \pi_c \rangle$ : green line;  $\langle v_c \rangle$ : red line) and global ( $P$ : light blue line;  $N$ : light orange line) order parameters, fixating in either a polar wave (D) or a nematic lane (E). Vertical lines denote respective time scales upon which local order emerges ( $t_0$ , short-dashed line) and finally fixates at a distinct type of order ( $t_{fix}$ : long-dashed line). Note that panels (D, E) share identical parameters:  $\varphi_p = 2.1^\circ, \alpha = 4.17, \rho_0 = 1.29/L^2, L_{box} = 162.5L$ .

**Table S1.** List of actin ( $\mu\text{M}$ ) and PEG (w/v) concentrations used for figures and movies.

Experiment from	Actin concentration ( $\mu\text{M}$ )	PEG concentration (%)
Fig. 2A	10.0	0.5
Fig. 2B, Movie S1	5.0	3.0
Fig. 2C, Fig. S2A	5.0	2.0
Fig. 2D, Fig. S2D,E, Movie S2	10.0	2.0
Fig. 5B, Movie S8	5.0	2.0
Fig. S2B	10.0	1.0
Fig. S2C	10.0	1.0
Fig. S2F	4.0	2.0
Fig. S6A-C, Movie S9	2.5	2.0
Fig. S6D	2.0	3.0
Fig. S6E	7.0	3.0
Movie S3	5.0	2.0
Movie S4	10.0	2.0

**Movie S1 (movie1.mov). Large network of nematic lanes.**

In this movie actin filaments form nematic high-density structures which constitute branches of a large network, surrounded by disordered regions. This movie is associated with figure 2B and has dimensions 605  $\mu\text{m}$  times 461  $\mu\text{m}$ . Visible filaments are labelled with a GFP tracer and represent a fraction of 1:60 of all filaments.

**Movie S2 (movie2.mov). Close-up of a nematic lane.**

This movie shows the dynamics of single actin filaments, which are exchanged between nematic lanes and the disordered environment. Within a lane, reversal of filament orientations occurs. The movie is associated with figure 2D and has dimensions 212  $\mu\text{m}$  times 161  $\mu\text{m}$  (labelling ratio 1:60).

**Movie S3 (movie3.mov). Nematic lanes merging.**

Movie of close-by nematic lanes that merge and form a new branch, indicated by white arrows. This happens on the time scale of minutes. The movie dimensions are 328  $\mu\text{m}$  times 246  $\mu\text{m}$  (labelling ratio 1:30).

**Movie S4 (movie4.mov). Nematic lanes shrinking.**

In this movie, nematic lanes indicated by white arrows become depleted on the time scale of minutes. The movie dimensions are 295  $\mu\text{m}$  times 222  $\mu\text{m}$  (labelling ratio 1:50).

**Movie S5 (movie5.mov). Simulation of polar density waves.**

This movie (associated with figure 3C) shows a large system that produces polar density waves which coarsen over time. Left panel: density field. Upper right panel: local nematic order. Lower right panel: local polar order. Parameters:  $\alpha = 3$ ,  $\varphi_p = 2.1^\circ$ , box size  $650.2L$  (periodic boundaries, random initial conditions),  $\rho_0 = 1.29/L^2$ , simulation time 0-3175.

**Movie S6 (movie6.mov). Simulation of nematic high-density lanes.**

This movie (associated with figure 3D) shows the evolution of a large system, forming a network of nematic lanes. Left panel: density field. Upper right panel: local nematic order. Lower right panel: local polar order. Parameters:  $\alpha = 6.25$ ,  $\varphi_p = 2.1^\circ$ , box size  $650.2L$  (periodic boundaries, random initial conditions),  $\rho_0 = 1.29/L^2$ , simulation time 0-3175.

**Movie S7 (movie7.mov). Simulation with simultaneously emerging polar and nematic structures.**

This movie shows the emergence of both nematic and polar structures, which interact and coarsen over time. Left panel: density field. Upper right panel: local nematic order. Lower right panel: local polar order. Parameters:  $\alpha = 4.25$ ,  $\varphi_p = 2.1^\circ$ , box size  $650.2L$  (periodic boundaries, random initial conditions),  $\rho_0 = 1.29/L^2$ , simulation time 0-3175.

**Movie S8 (movie8.mov). Coexisting polar and nematic structures.**

Polar clusters are embedded between nematic lanes, which get spatially rearranged by interacting with the clusters. The movie has dimensions 605  $\mu\text{m}$  times 461  $\mu\text{m}$  and is associated with figure 4D (labelling ratio 1:30).

**Movie S9 (movie9.mov). Filament exchange processes between structures of different symmetry.**

This movie shows exchange processes between polar and nematic structures within a single experiment in the coexistence regime. Left panel: polar clusters “eat up” nematic lanes by crossing them. Right panel: polar cluster “leaves” a nematic lane. The movie is associated with figures S6A,B (labelling ratio 1:30).



### III Dynamical processes, phase transitions and criticality

In chapter I we introduced the Vicsek ordering paradigm (VOP), which represents a generic motif of order and pattern formation in active systems without hydrodynamical coupling (often referred to as *dry active matter* [19]) and with aligning interactions. According to the VOP – and in contrast to the results of the previous section – these systems have been speculated to be dividable into different symmetry ‘classes’ depending on the symmetry of alignment rules [52, 77], with an arguable analogy to universality classes (see discussion of the previous section). In the following, we will mostly concentrate on systems with emergent polar order – that is, flocking of propelled agents – and investigate more subtle details of the VOP: for instance, studies suggested [42, 50, 52] that the onset of collective order is described by a pitchfork bifurcation scenario of the ensuing hydrodynamic equations (see Eqs. (II.20, III.18) for the slow mode  $f_1$ ) at the homogeneous level. Mathematically, this can be expressed by  $\dot{\mathcal{P}} \propto (a - b|\mathcal{P}|^2)\mathcal{P}$ , with  $\mathcal{P}$  being the polar order parameter. Above the onset  $a > 0$  there exists a stationary, homogeneous solution of the polar order  $\mathcal{P}_1 \sim \sqrt{\frac{a}{b}}$  (Fig. III.1(a)). Note that  $a, b$  depend in general on the local values of control parameters such as noise, alignment, and density (hence defining a critical control parameter value  $c_1$  such that  $a(c_1) = 0$ ). Close to the onset, the homogeneous state with polar order  $\mathcal{P}_1$  is unstable with respect to inhomogeneous perturbations (i.e. a long-wavelength band of unstable modes, see Fig. III.1(b)). As a result, spatial patterns emerge and enforce a phase separation into a dilute and a dense phase, creating a discontinuous transition to polar order. Note that there is a subcritical shell of stable patterns below the onset point  $c_1$  [26, 43, 46, 47, 55, 138]. While it has been widely established that this process resembles a non-equilibrium analogue of a gas-liquid phase transition [43, 44, 46], there is an ongoing discussion about the dynamic nature of these patterns (see list below and Fig. III.1(c)). Deeper in the polar phase of the VOP and beyond a second transition line  $c_2$ , homogeneous order becomes stable and patterns are absent [19, 45, 50, 53–55]. What determines the value and behavior of  $c_2$  as a function of the system properties is not known, since simple lowest-order hydrodynamic equations (see Eqs. (II.20, III.18)) are no longer valid as the dynamics depends successively on higher-order Fourier modes.

Put into the perspective of different active matter systems in the literature, there are several unresolved issues concerning this seemingly universal behavior of VOP:

1. It is unclear what the underlying microscopic processes of order formation are, how they interact to create order on the macroscopic scale, and at which length scale collective effects arise. It was already shown that onset behavior of the Vicsek model is very sensitive with respect to the functional dependence of particle noise [45, 139].<sup>1</sup> Yet, due to the different validity domains of theoretical models (Fig. III.1(d)), it is notoriously difficult to find a framework that fully bridges the physical processes from microscopic to macroscopic length scales.
2. It is unclear if the VOP and its corresponding flocking transition really describes order formation in experimental systems and microscopic models. For example, in the actomyosin gliding assay as well as in the WASP model we only found the formation of inhomogeneous polar clusters, without a homogeneous phase at large densities (see previous chapter in section 2.3). Furthermore, flocking in these systems seems to be dominated by nucleation events and a very large density spread of the separated phases (Figs. III.2(a,b)); here the density of the dilute background, being the subcritical threshold value for coexisting patterns (i.e. the binodal), is  $\sim 1/\mu m^2$  and much smaller than the approximate transition density  $\sim 5/\mu m^2$  (possible spinodal). VOP does neither provide an explanation for the large binodal region, nor the specific transition density value, nor if there is any significance of the bifurcation scenario (Fig. III.1(a)) for the actual ordering transition.
3. What are generic features of polar pattern formation beyond the Vicsek ordering paradigm, and how do they depend on the properties of active matter systems? For example, Lam et al. [38, 56] have shown that for a specific model of aligning discs the transition to order is driven by a discontinuous, subcritical bifurcation at the homogeneous level, instead of the supercritical instability that defines the onset of order in the VOP (Fig. III.2(c)). It remains to be clarified if this is an exceptional case, or a more common trend in the space of all possible model configurations.

In this chapter, we attempt to illuminate some of these issues and provide a better understanding of order formation in active systems; in particular, we investigate the effect of realistic physical processes on the microscopic scale of individual particles. In section 1, we employ the multiscale WASP model which was developed in the previous chapter II to detail the transition towards polar order in an experimentally relevant parameter region. Here we develop a powerful analysis technique in terms

---

<sup>1</sup> A related issue is the question of pattern selection: while mean-field theories predict different stable patterns at the onset of order [43, 44, 46, 47], Vicsek simulations with particle noise always yield a particular solution that exhibits so-called micro-phase separation (periodic waves in Fig. III.1(c)).

of a cluster decomposition to extract kinetic processes on all relevant length scales of the system, and cast these intrinsic dynamics on an effective model of interacting cluster species.

In section 2, we study the robustness of the VOP scenario as a function of microscopic collision properties. Specifically, we use a two-fold approach of a kinetic Boltzmann ansatz and Vicsek-like model simulations to assess if and when the picture of a Vicsek universality class breaks down in the presence of generic alignment models.

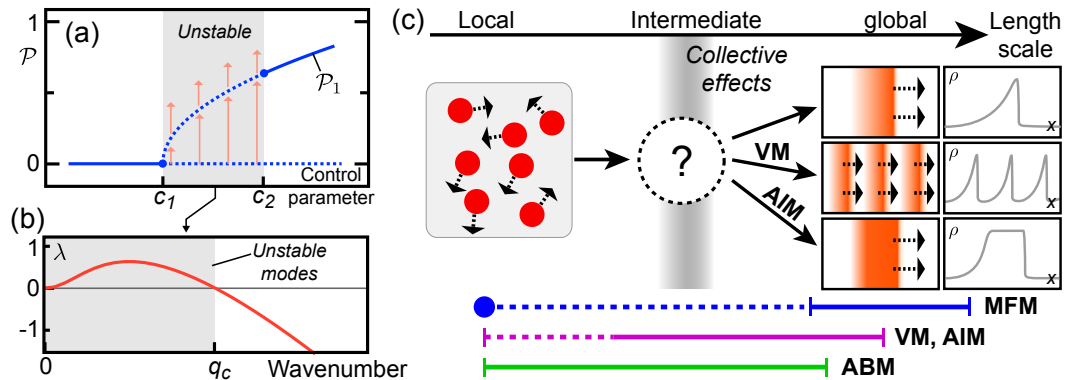


**Figure III.1** (a) Illustration of the flocking onset as predicted by hydrodynamic equations of Vicsek-like models ( $c$  is an arbitrary control parameter): at  $c_1$  a supercritical pitchfork bifurcation occurs, where a homogeneous branch  $\mathcal{P}_1$  emerges. Between  $c_1$  and  $c_2$ ,  $\mathcal{P}_1$  is unstable against spatial perturbations. (b) A typical dispersion relation of inhomogeneous perturbations of  $\mathcal{P}_1$ . Within a band of  $q \in [0, q_c]$ , field fluctuations grow exponentially as  $\sim e^{\lambda t}$ . (c) Assessment of different length scales of polar active matter systems: most models are formally dependent on local particle dynamics, yielding global, collective phenomena on the scale where individual particle fluctuations become negligible (left panels: patterns, right panels: corresponding density profiles). Possible dynamic phenomena include solitary waves (upper panels), periodic waves (middle panels), and droplet interfaces (lower panels). In the statistical limit, periodic states lead to *micro-phase separation* as found in the Vicsek model (VM) and droplet states to *macro-phase separation* as found in the active Ising model (AIM). Note that a clear picture of the kinetic processes at intermediate scales, where collective effects emerge, is elusive. (d) Validity domains of different theories: mean-field theories (MFM) describe the system on large scales, depending only on point-like interactions at the lowest scale and neglecting all intermediate effects. Vicsek (VM) or active Ising (AIM) models foot on smaller scales, but only with an effective collision rule instead of a continuously resolved process. Agent-based models (ABM) may properly describe microscopic processes but struggle to achieve large-scale properties.

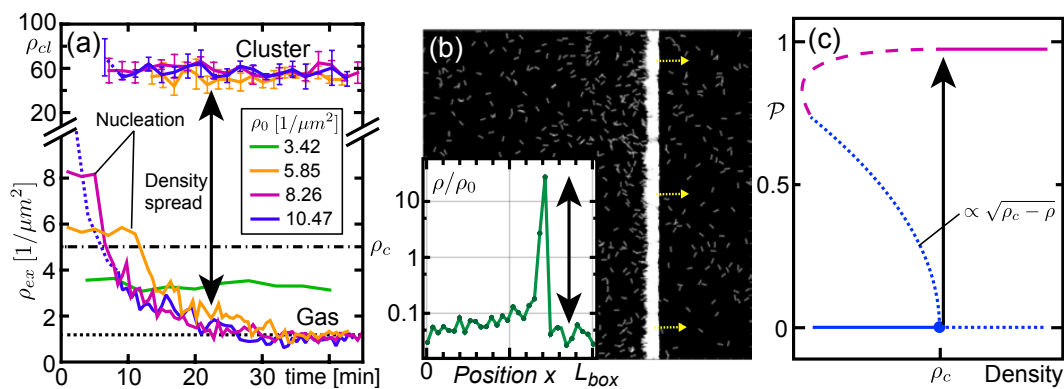


**Figure III.2** (a) Phase separation in the actomyosin gliding assay for different initial actin filament densities  $\rho_0$ . Above  $\rho_0 > 5/\mu m^2$ , polar clusters emerge by spontaneous nucleation, leading to a separation of disordered regions with density  $\rho_{ex}$  and ordered regions with density  $\rho_{cl}$ .  $\rho_0 \rightarrow \rho_{ex}$  is also the lower bound of stable clusters. Note the very large density spread  $\rho_{cl}/\rho_{ex} \approx 60$ . Data cordially provided by Ryo Suzuki [129]. (b) Sharp polar front in WASP simulations ( $\varphi_p = 0.063$ ,  $\alpha = 0$ ,  $\rho_0 L^2 = 1.29$ ) with density profile (inset) also exhibits a density spread factor of ca. 100. (c) Illustration of a subcritical transition of homogeneous polar states similar to Ref. [38, 56]. Upon changing a control parameter (here: density) a subcritical bifurcation occurs at  $\rho_c$  (blue lines, dashed depicts unstable branches), and  $\mathcal{P}$  jumps from zero to almost perfect order (pink line). (b) is also published in Ref. [127].

# 1 Cluster assembly and nucleation kinetics of WASP systems

## 1.1 Background

In section 2.2 of the previous chapter we introduced the WASP model which faithfully reproduces a variety of properties of the actin motility assay, ranging from local binary collision statistics to collective phenomena on large length scales. So far, we have quantified emerging effects using mostly stationary global order parameters, without considering the inherent kinetic mechanisms and dynamics that give rise to self-organization. Since our WASP simulations do not rely on truncation procedures and root on continuous physical interaction on the microscopic scale, the model offers insight on these processes at the intermediate scale where the coordinated properties of individual particles give rise emergent behavior as a collective. Of course, the question remains how to extract and analyze these processes; this is a highly nontrivial task. Previous studies have already attempted to do so and found, for instance, that pattern formation in active systems is in general accompanied by anomalous number fluctuations [19, 53, 140, 141]. Here, the value  $S(r) = \sqrt{\text{Var}[N]_r} / \langle N \rangle_r \sim r^a$  quantifies the fluctuations of particle numbers relative to their mean number inside a region of radius  $r$ . While for equilibrium systems  $a = 0$ ,  $a > 0$  for active systems indicating large density inhomogeneities. However, this quantity is ill-suited to analyze the formation of global order, since already disordered active gasses experience giant number fluctuations with  $a > 0$  [142, 143]. A different way of quantifying intermediate particle structures is given by the *cluster size distribution*  $p(m)$ , which has been previously used to identify the steady state statistics of active particle aggregates or clusters of sizes  $m$ . Quite generically, it was found that for disordered active gasses the cluster size distribution is similar to a exponentially suppressed power law  $p(m) \propto m^{-b} e^{-m/c}$  [114, 144, 145] (with some specific constants  $b, c > 0$ ), while collective states with emerging patterns exhibit a heavy-tailed size distribution [45, 146–148]. Here, Peruani and coworkers introduced a simple kinetic model of cluster assembly [114, 144, 145, 149] which predicts a continuous transition from a unimodal (disordered state) to a bimodal (ordered state) distribution, marking an important step towards resolving the intrinsic processes of collective phenomena in active matter. Casting the active particles into local clusters appears to be particularly advantageous, since this implicitly assumes spatial and temporal correlations of their constituents which are notoriously neglected in coarse-grained field models. However, there are some shortcomings with this approach: 1) it does not agree with or reproduce the generic discontinuous character of the order transition in active systems, let alone with the accompanied subcritical behavior of patterns; 2) it predicts the presence of a

distinct, percolating giant cluster from the second maximum of  $p(m)$  that contains a significant fraction of the whole system. This corresponds to (macro-)phase separation, in contrast to the observed presence of micro-phase separation in polar systems [43–46]. And 3), there is no qualitative distinction between symmetries of ordered structures, that is, polar or nematic order.

In particular concerning this last point, we have made a decisive observation from simulations of the WASP model defined in the previous chapter. In the flocking state, that is, when a polar front of filaments has emerged, local filament clusters are not just random assemblies, but possess a heterogeneous internal structure (see Fig. III.3): within the front, clusters are large and filaments extremely ordered, while clusters in the dilute regions are rather small and have no significant internal ordering. Hence, we hypothesize that not only cluster size, but also *cluster order* is an emergent property that is indispensable to describe the global state of the system. In the following, we will develop a framework to systematically analyze the ordering properties of particle clusters and apply them to the different modes of collective motion. We will especially focus in-depth on the polar active system and the flocking transition, where we also develop a new kinetic model that extends the work of Peruani et al. [114, 144, 145, 149] to account for polar order of clusters. As a result, we find a new paradigm to fully describe the formation of polar order in terms of a nonlinear interplay of kinetic processes along multiple length scales without relying on mesoscopic approximations or truncation schemes. Here, we have prepared a corresponding manuscript which is about to be submitted for peer review, and that can be found in section 1.7.

## 1.2 The cluster size-order decomposition

To account for clusters with both different sizes and different order in a system of WASP's, we introduce the *cluster size-order representation*: a system  $\mathcal{S}$  of filaments  $f^{(i)}$ ,  $i \in \{1, 2, \dots, M\}$  and  $\mathcal{S} = \bigcup_{i=1}^M f^{(i)}$ , can be uniquely decomposed into a set of disjoint clusters  $\{c^{(u)}\}$  with  $\mathcal{S} = \bigcup_u c^{(u)}$  ( $c^{(u)} \cap c^{(v)} = \emptyset$  if  $u \neq v$ ). A filament belongs to a cluster  $c$  if its minimal distance to  $c$  is smaller than a cutoff length  $\gamma$  with  $\gamma \ll L$ . Numerically, we set  $\gamma = (L - d)/N$  corresponding to the length of the discretized cylinder within a WASP filament. For every cluster we can now assign a *cluster size*  $k$ , a *cluster polar order*  $p = \frac{1}{k} |\sum_{j=1}^k \exp(i\theta_j)|$ , and a *cluster nematic order*  $n = \frac{1}{k} |\sum_{j=1}^k \exp(2i\theta_j)|$ , where the indices run over all cluster filament orientations  $\theta_j$ . Note that this is formally equivalent of partitioning the system into independent fractions and calculating their respective order parameters. To obtain the respective net average cluster orders, we have to correct the observables  $\langle p \rangle_k$  and  $\langle n \rangle_k$  ( $\langle \dots \rangle_k$  runs over all clusters of size  $k$ ) by subtracting a term  $\Delta_k$  that corresponds to mean average order of a random cluster (which is nonzero, as it is particularly obvious for single-filament clusters with  $p = n \equiv 1$ ).  $\Delta_k$  can be obtained

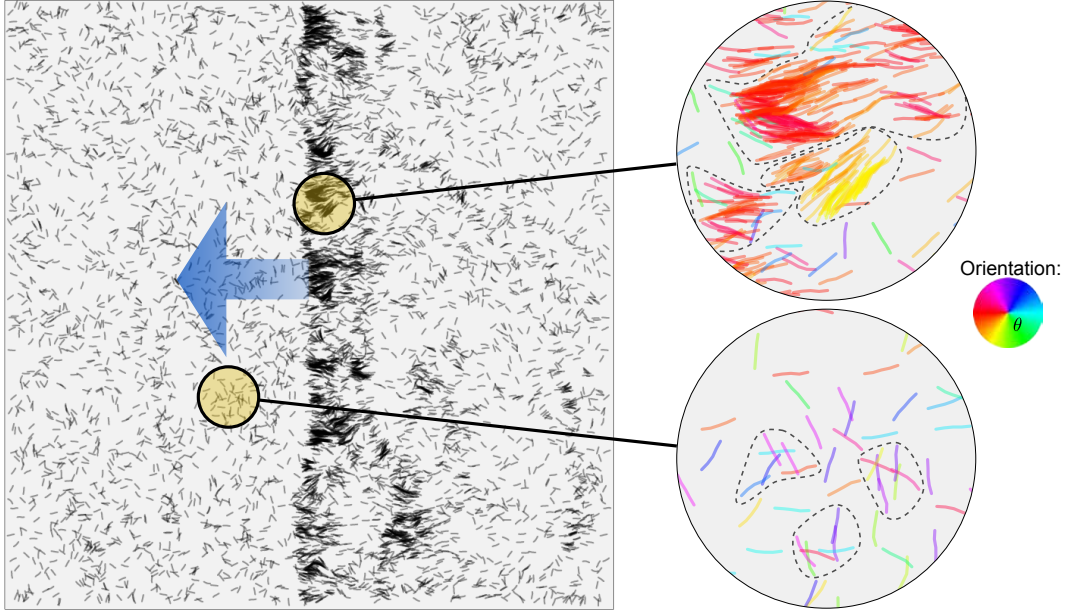


**Figure III.3** Propagating polar front in WASP simulations at parameters  $\varphi_p = 0.036$ ,  $\alpha = 4$ ,  $\rho_0 L^2 = 1.29$  (other values fixed as given in section 2.2 of chapter II) with close-ups of the local structures (right panels). Inside the polar front (upper panel), filaments are highly ordered and packed as can be seen by the angular color map of the orientation. Outside the ordered regions (lower panel), local clusters are loosely arranged and have no distinct internal orientation. Selected clusters are highlighted by dashed lines.

by calculating the average order of randomly oriented clusters as a reference: given a filament cluster of size  $k$  with uniformly random orientations  $U_j \in [-\pi; \pi]$ , and the short-cut notation  $\omega_{m,n} = U_m - U_n$ , and  $\sum_{m=1}^k \sum_{n=m+1}^k = \sum_{(m,n)}$ ,

$$\begin{aligned}
 \Delta_k &= \frac{1}{k} \langle |\sum_{j=1}^k e^{iU_j}| \rangle = \frac{1}{k} \langle \sqrt{k + 2 \sum_{(m,n)} \cos \omega_{m,n}} \rangle \\
 &= \frac{1}{k} \langle \sqrt{k} + \frac{1}{\sqrt{k}} \sum_{(m,n)} \cos \omega_{m,n} - \frac{1}{2k^{3/2}} \sum_{(m,n)} \cos^2 \omega_{m,n} \\
 &\quad + \frac{1}{2k^{5/2}} \sum_{(m,n)} \cos^3 \omega_{m,n} + \mathcal{O}(k^{-3/2}) \rangle. \tag{III.1}
 \end{aligned}$$

It can be straightforwardly shown that  $\langle \cos^2 \omega_{m,n} \rangle = \frac{1}{2}$ . Since  $\langle \cos^j \omega_{m,n} \rangle = 0$  for  $j$  odd, Eq (III.1) can be further reduced to

$$\Delta_k = \frac{1}{\sqrt{k}} \left( 1 - \frac{(k-1)}{8k} \right) + \mathcal{O}(k^{-5/2}) = \frac{1}{\sqrt{k}} \left( \frac{7}{8} + \frac{1}{8k} \right). \quad (\text{III.2})$$

This first-order correction is close to the typical scaling of mean value deviation  $\propto k^{-1/2}$ . Note that this correction is valid for both the polar and the nematic cluster order, since Eq. (III.2) is invariant upon replacing  $\omega_{m,n} \rightarrow 2\omega_{m,n}$ . This yields the *net cluster orders*  $\pi(k) = p - \Delta_k$  and  $\nu(k) = n - \Delta_k$ .

From these definitions we can introduce a set of observables that quantify processes on all length scales: first, we define global order parameters  $\Omega_p = \sum_{\{c\}} \pi(k)^{(c)} k^{(c)} / M$  and  $\Omega_n = \sum_{\{c\}} \nu(k)^{(c)} k^{(c)} / M$  by averaging the individual polar cluster orders  $p$ , respectively  $n$ , weighted by the respective cluster size  $k$ . Second, we record the statistics of  $k$  and  $p$  of the full ensemble of clusters using the corresponding distribution functions, the cluster size distribution  $\psi(k)$  and the cluster-size-order distribution  $\Psi(k, p)$ , normalized such that  $\sum_{k=1}^M k \int_0^1 dp \Psi(k, p) = \sum_{k=1}^M k \psi(k) = 1$  (this can be done likewise for the nematic order). Third, we combine  $p$  and  $k$  into an extensive quantity, the cluster polarity  $s = p \cdot k$ , which is equivalent to the amount of aligned filaments within a cluster (analogous to a cluster 'momentum'). In addition to these values, we may also record the trajectory of every particle within the cluster representation given by  $\{k, p, n\}(t)$ , and assess typical time scales of particles within this cluster space. Note that the cluster polar order  $p$  is expected to be the 'native' ordering mode of a cluster, since this means a strong coherence of its constituents; a non-trivial nematic cluster order  $n$  on the other hand indicates interactions and overlap of individual polar clusters, since there is no genuine, nematically-ordered and stable cluster. Therefore, we will mostly focus on the impact of  $p$  in sections 1.3 and 1.4.

Fig. III.4(a) shows how a system of WASP's is decomposed into individual clusters. In the following, we analyse various regions of the experimentally relevant phase diagram obtained in the chapter II, section 2.2.5 (Fig. III.4(b)).

### 1.3 Mesoscopic processes of the disordered gas

We tested the properties of the cluster size-order representation by first considering the disordered regions of the parameter space that was obtained for parameters comparable to the actin motility assay in the previous chapter (Fig. II.23). These regions do not exhibit any global ordering or large-scale pattern formation. To this end, we performed multiple simulations while sweeping the density  $\rho_0$  and the relative alignment strength  $\alpha$  along three different lines (all other parameters as given previously, in particular  $\varphi_p = 0.036$ ,  $p = 200 = 31.7L$ , and  $L_{box} = 512$ ).

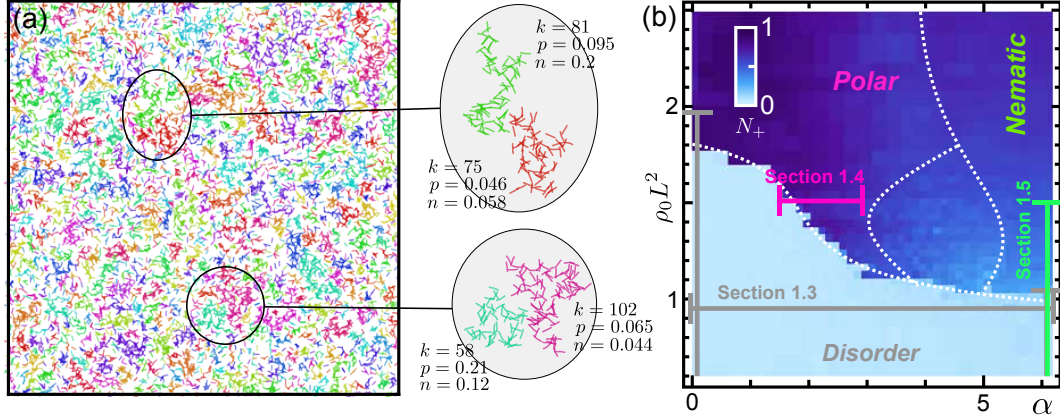


**Figure III.4** (a) Cluster decomposition for a disordered system, with 4 large clusters highlighted. Parameters are  $\alpha = 0$ ,  $\rho_0 L^2 = 1.51$  (others are default values, see section 2.2 of chapter II). (b) Phase diagram obtained by hysteresis as already depicted in Fig. II.23 including the highlighted regions that will be analyzed in the next sections.

Below, we refer to these sweeps with A (varying  $\rho_0$  for fixed  $\alpha = 0$ ), B (varying  $\alpha$  for fixed  $\rho_0 L^2 = 1.51$ ), and C (varying  $\rho_0$  for fixed  $\alpha = 6.25$ ), see also gray lines in Fig. III.4(b). First, we find that the number fluctuations  $S(r) = \sqrt{\text{Var}[N]_r} / \langle N \rangle_r$  ( $\langle N \rangle_r$  is the mean number of filaments within a region of radius  $r$ ) of the disordered system are dominated by equilibrium-like fluctuations at small scales  $r$ , but with successive deviations at larger  $r$  which increase continuously as the parameters approach the regions of collective order (Fig. III.5(a-c)). This is in agreement with Refs. [142, 143] which predicts anomalous behavior of active disordered gasses. Next, we investigate the cluster size distribution  $\psi(k)$ . For sweeps A-C,  $\psi(k)$  roughly follows an exponentially-truncated power law distribution of the form  $k^{-b} e^{-k/c}$  as can be seen in Fig. III.5(d). Upon fitting the parameters  $b$ ,  $c$  we observe that the power law exponent  $-b$  decreases linearly and the cut-off length  $c$  increases exponentially as the transition to order is approached (Fig. III.5(e)). Note that  $c$  is mostly comparable to the mean cluster size  $\langle k \rangle$ .

Not only the overall statistics of the cluster sizes seem to be strongly affected by a change of the control parameters  $\alpha$  and  $\rho_0$ , but also the character and internal structure of the clusters. This can be visualized by the properties of the cluster orders  $p$ ,  $n$ , or equivalently  $\pi$  and  $\nu$ , as can be seen in Fig. III.6. In the disordered state, the cluster size-order distribution  $\Psi(k, p)$  is composed of clusters of different sizes  $k$  and (polar) orders  $p$ . Note that this can be equivalently done for the nematic order, which has however less significance (in section 1.6 we argue that polar order is the natural ordering of clusters). In additions, if one would marginalize  $\Psi(k, p)$  over the order  $p$ , one would obtain  $\psi(k)$  of Fig. III.5(d). While the distribution is almost centered around the random deviation value  $\Delta_k$ , small but significant

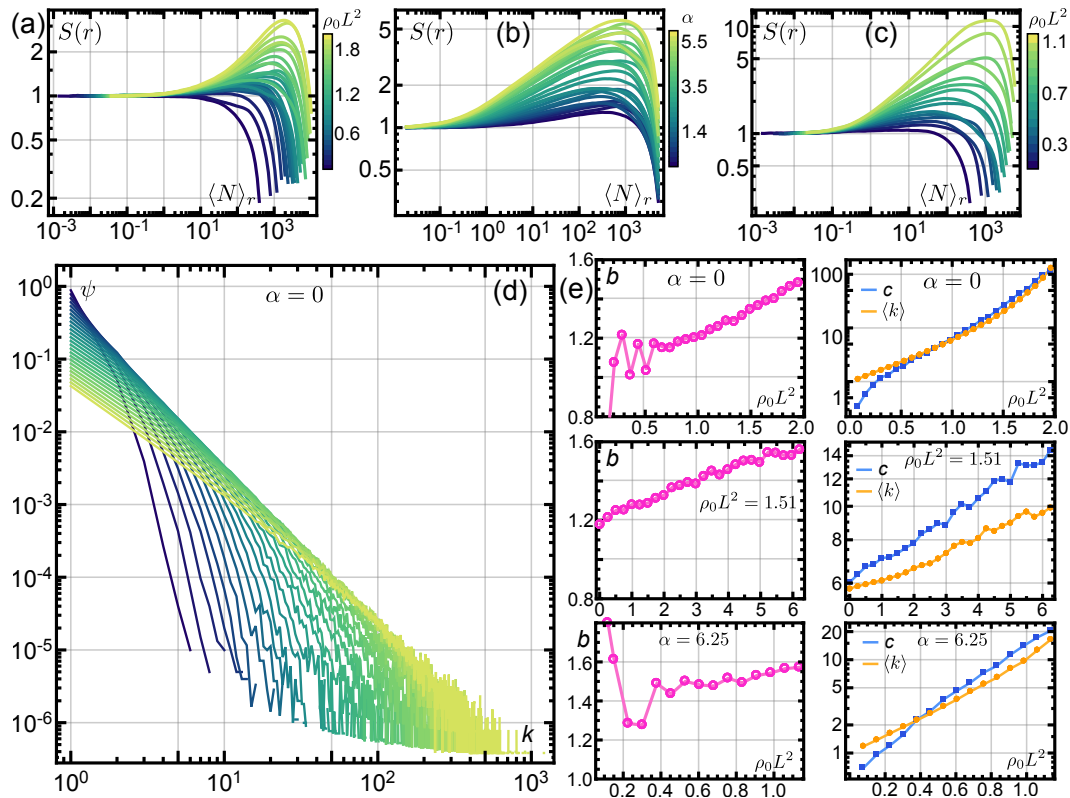


**Figure III.5** (a-c) Number fluctuation  $S(r)$  for the sweeps A (a), B (b), and C (c). The radius  $r$  is implicitly changed as  $\langle N \rangle_r$  varies. The color maps correspond to the different simulations of the sweeps A, B, C. (d) Cluster size distribution  $\psi(k)$  for cluster sizes  $k$  for sweep A. The color map is identical to the one used in (a). (e) Fit parameters  $b$ ,  $c$  for the test function  $\propto k^{-b}e^{-k/c}$ . Top row: sweep A; middle row: sweep B; bottom row: sweep C. The data for  $c$  is compared with the mean cluster size  $\langle k \rangle$  (orange data).

deviations exist especially for larger clusters as can be seen by comparison with  $\langle p \rangle_k$ . We analyzed the average net cluster orders  $\langle \pi \rangle(k)$  and the global cluster order parameters  $\Omega_p, \Omega_n$  for the different sweeps A, B, C in Fig. III.6(b) and found that this is a generic behavior: despite global disorder, clusters are genuinely ordered, but only gradually. Here, for sufficiently large  $k$ ,  $\langle \pi \rangle(k)$  approaches a plateau value. When the alignment strength  $\alpha$  is increased, so does this value. This is also reflected in the order parameters  $\Omega_p, \Omega_n$  which both grow linearly as a function of the control parameters  $\alpha, \rho_0$ . Thus, local order can be nonzero despite global disorder. For large  $\alpha$ , the character of this ordering also becomes successively nematic but is still dominated by polar cluster ordering. Note that for the largest values of  $\alpha$  and  $\rho_0$  of sweeps A and C, respectively,  $\Omega_p$  and  $\Omega_n$  already seem to have already crossed the global ordering threshold which is reflected by a strong increase. Interestingly, the statistics of individual particles appear to be unaffected by the intermediate ordering. Fig. III.6(c) displays the evolution of  $\{k, p, n\}(t)$  of a particle which exhibits strong fluctuations stemming from frequent scattering with different clusters. The Fourier spectrum of these properties appears very flat, that is, there seems to be no characteristic frequency of switching clusters (Fig. III.6(d)).

To summarize this section, we find that the disordered parameter region of a WASP system has interesting features of particle clusters at intermediate length scales, where order is still present locally. Here, the cluster size-order representation is capable of resolving heterogeneities in the population of clusters, not only for the stationary properties but also for the dynamics. In the next sections we will focus on the parameter regions where global order emerges, and how this is reflected in the cluster picture.

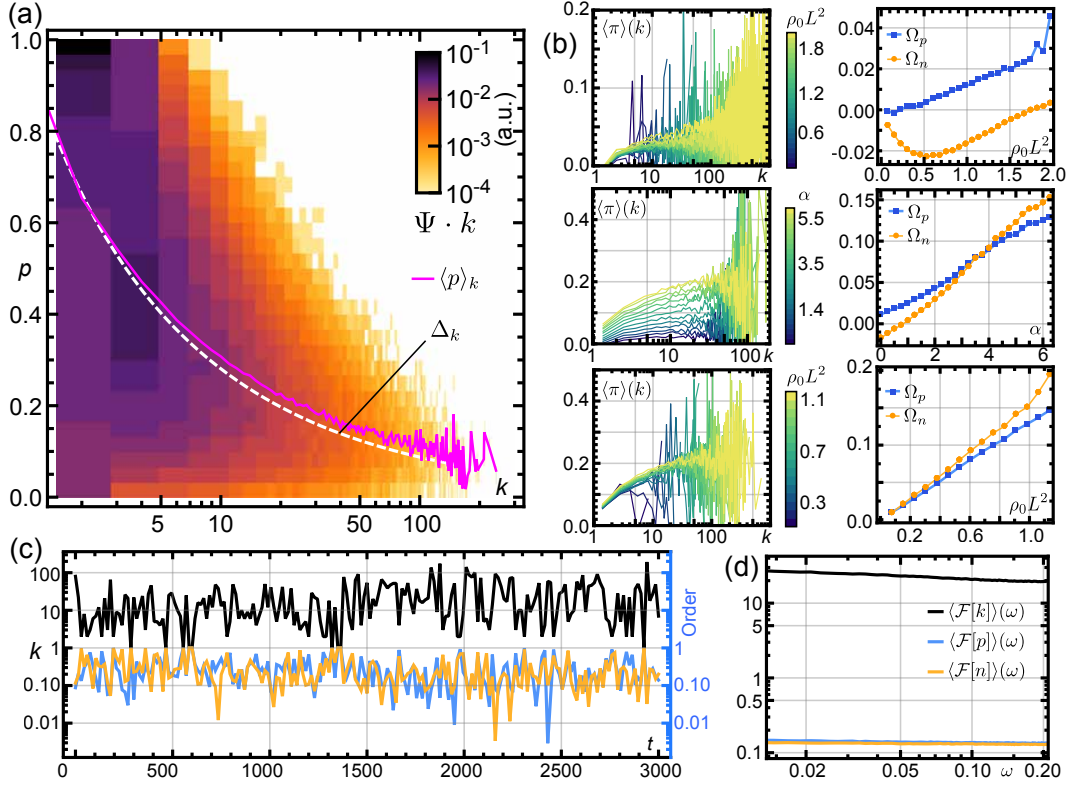


**Figure III.6** (a) Cluster size-order distribution  $\Psi(k, p)$  rescaled by  $k$  of a disordered system at  $\alpha = 0$ ,  $\rho_0 L^2 = 1.51$  like Fig. III.3(a) (arbitrary normalization constant). The pink line depicts  $\langle p \rangle_k$ , the white dashed line  $\Delta_k$ . (b) Cluster ordering for sweeps A (top row), B (middle row), and C (bottom row). The left panels depict  $\langle \pi \rangle(k)$  for different systems (color maps correspond to the control parameters), the right panels show the stationary values of the global cluster order parameters  $\Omega_p$  and  $\Omega_n$  as a function of the control parameters. For sweeps A and C, increase of local order is achieved predominantly by the emergence of larger ordered clusters while  $\langle \pi \rangle(k)$  does not significantly change, for B, the order  $\langle \pi \rangle(k)$  of the clusters increases for all  $k$ . (c) Time evolution of  $\{k, p, n\}(t)$  of a single filament. The fluctuation spectrum of  $\{k, p, n\}(t)$  in (d) shows no significant frequency dependence. Data was obtained by Fourier transformation  $\mathcal{F}[k](\omega) = \frac{1}{2\pi} \int dt e^{-i\omega t} k(t)$  over the observation interval and likewise,  $\mathcal{F}[p](\omega)$ ,  $\mathcal{F}[n](\omega)$ .

## 1.4 Mesoscopic processes at the flocking onset

In the following, we will apply the cluster size-order representation on systems close to the transition to polar order, that is, the flocking transition. As it was stressed in the beginning of this chapter, a rigorous picture of the intrinsic processes that lead to global order is elusive. Here, our approach can reveal insight on these dynamics on all length scales, and for parameters that are experimentally relevant. First, we will analyze the flocking transition in WASP systems and derive a phenomenological picture of self-organization processes. From this, we will introduce a simple kinetic model of cluster assembly to assess more general properties of the system.

### 1.4.1 Emerging clusters drive the nucleation of polar order

In Fig. II.20 we already showed that in WASP simulations, the transition towards large-scale travelling wave fronts and global polar order is very discontinuous, with the order parameter  $\mathcal{P}$  jumping from zero to almost unity. This already implies that there is a subcritical parameter region which stably exists before this threshold, which was also seen in the hysteresis analysis in Fig. II.23(b). So what determines the transition point, especially in the presence of large density fluctuations (recall the giant number fluctuations as shown in the previous section)? To this end, we simulate a system of WASP's using random initial conditions, slightly above the expected transition point with parameters  $\rho = 1.51/L^2$ ,  $\varphi_p = 0.036$ ,  $\alpha = 2$ . Within a short time  $t_i$ , the system generates a small but nonzero  $\Omega_p$  (Fig. III.7(a)), which dwells for a long time  $t_d$  (note that here and in the following we have rescaled time in units of the longest single-particle correlation time  $L_p/v$ ). This quasi-stationary, disordered system shows a cluster size distribution  $\psi(k)$  with an exponential tail as for disordered systems, similar to previous studies [144–151] (Fig. III.7(c)). The cluster size-order distribution  $\Psi(k, p)$  in Fig. III.7(d) shows that most of the clusters possess a cluster polar order  $p$  centered around  $\Delta_k$ , indicating that the individual clusters are hardly more ordered than randomly assembled clusters just as shown for the disordered regions in section 1.3. At time  $t_d$ , a sufficiently large and ordered cluster nucleates and rapidly percolates the system, as can be seen by  $\Omega_p$  growing exponentially over an order of magnitude with a growth time  $\tau$  before becoming stationary (Fig. III.7(a)). This final state is now dominated by very ordered and large clusters, as is demonstrated by the altered shape of  $\Psi(k, p)$  and  $\psi(k)$  where large clusters are almost perfectly polar while small clusters remain at small  $p$  (Fig. III.7(d)). Coloring clusters according to their order  $p$  reveals that indeed the polar front is composed of ordered clusters, surrounded by disordered ones (Fig. III.7(b)).

These results suggest that order formation and their accompanied phase separation is driven by an inherently heterogeneous population of clusters: one of which consisting of highly-ordered flocks, the other one remaining mostly unordered.

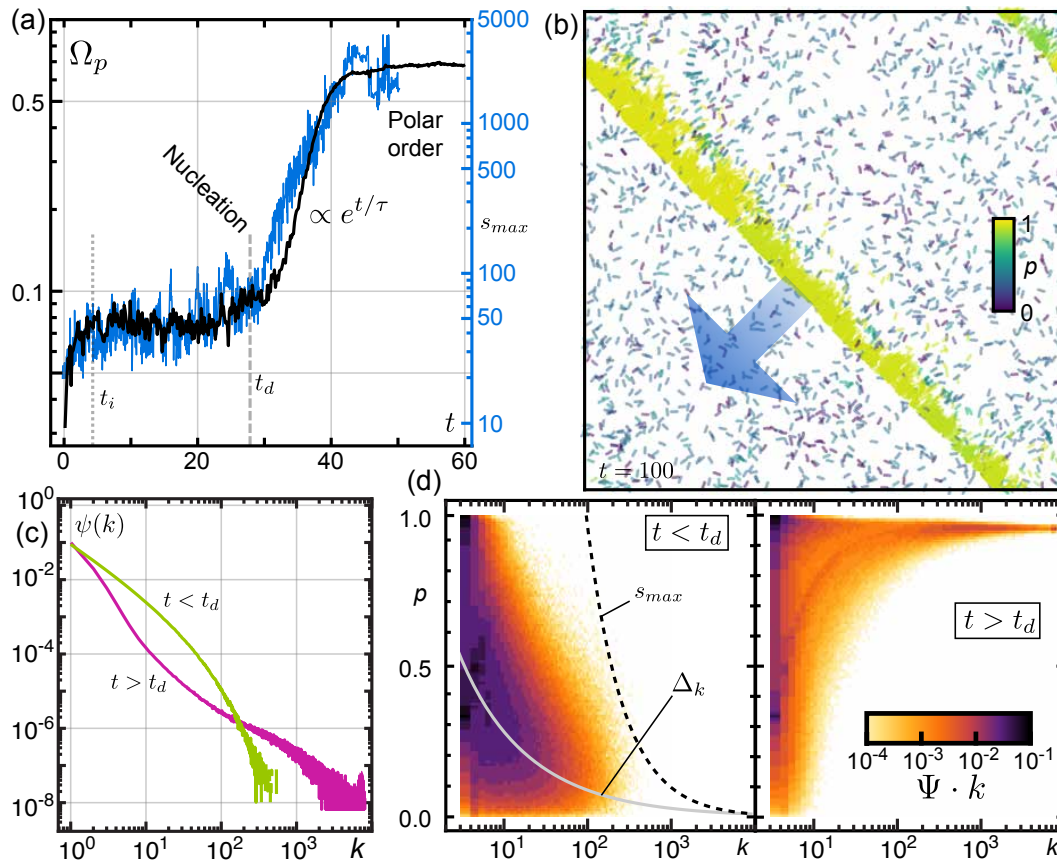


**Figure III.7** (a) Evolution of the order parameter  $\Omega_p$  (black) and  $s_{max}$  (blue, right axis). The initial time scale  $t_i$  and the nucleation time  $t_d$  are marked by short-dashed and long-dashed lines, respectively. Directly after  $t_d$ ,  $s_{max}$  increases drastically and serves as an early-stage indicator of a nucleating cluster. (b) Simulation snapshot at  $t = 200$  (in units  $L_p/v$ ) with filament coloring corresponding to the individual values of  $p$ . The polar front is distinctly marked by highly ordered clusters (yellow). (c) Cluster size distribution  $\psi(k)$  before (green) and after (purple) nucleation. (d) Cluster size-order distribution  $\Psi(k, p)$  as a function of  $k$  and  $p$ , before (left panel) and after (right panel) nucleation at time  $t_d$ . The gray solid line depicts  $\Delta_k$ , the black dashed line an estimated nucleation threshold at  $s_{crit} = p_c \cdot k \approx 90$ .

Consequently, the transition to order and the ordered state itself is driven by the dynamics of these cluster populations.

First, we investigate the dynamics of the cluster statistics during pattern formation and in the steady state in Fig. III.8. From the number fluctuations  $S(r)$  we observe a fast crossover of the anomalous scaling regime from large scales to the full domain of available length scales (the drop at the largest scales is a finite-system artefact), exhibiting a scaling exponent of 0.7 similar to other active matter systems [20]. This trend is also present when plotting the time evolution of the mean net cluster order  $\langle \pi \rangle(k)$  in Fig. III.8(d). From an initially small and constant value, a strong excitation of  $\langle \pi \rangle(k)$  at large  $k$  emerges and takes over the whole domain, with  $\langle \pi \rangle(k)$  approaching unity for large  $k$ . At small  $k$  the average order remains rather small. In the steady state, the spectra of fluctuations of single particle paths  $k^{\{i\}}(t)$ ,  $\pi^{\{i\}}(t)$  ( $i \in \{1, 2, \dots, M\}$ ) now exhibit more versatile features as compared to the white-noise-like behavior of the disordered phase (Fig. III.6(c,d)): low-frequency oscillations are much more pronounced than large-frequency oscillations, indicating that particle switching between large, ordered clusters is much slower than switching between small clusters. We can also assess the cluster scales at which order is predominantly produced and/or destroyed. This is for instance captured by calculating the mean forward order production  $\langle \Delta p(k) \rangle := \langle p_k^{\{i\}}(t + \Delta t) - p_k^{\{i\}}(t) \rangle$  which gives the difference of a filament order at time  $t + \Delta t$  at cluster size  $k$  when it was  $p(t)$  at a time  $t$ , averaged over all filaments (we fixed  $\Delta t = 0.15$ ). As can be seen in Fig. III.8(c), before time  $t_d$   $\langle \Delta p(k) \rangle$  exhibits order production at scales  $k \gtrsim 10$  and order destruction otherwise. At the polar steady state, almost no turnover of order appears to be present at the largest size scales. Since  $\langle \Delta p(k) \rangle$  is limited as a measure of particle turnover due to the possibly arbitrary-complicated coupling of clusters with different orders and sizes, we introduce a more perceivable dynamical observable (Fig. III.8(e)): by a heuristic subdivision of  $k$ - $p$  cluster space and tracking the particle fluxes  $j^{U \rightarrow P}(k, p)$ ,  $j^{P \rightarrow U}(k, p)$  between the unordered partition (U) and the ordered (P) partition, we observe at which tuples of  $(k, p)$  filaments are lost to the respective other 'species'. As a result, the system exhibits a steady-state particle current which performs a 'figure 8' trajectory in  $k$ - $p$  space. This also directly shows the non-equilibrium nature of this active system, which cannot be approximated by equilibrium-like approximations.

Next, we turn to the dynamics of the flocking transition. The evolution of the order parameter  $\Omega_p$  (Fig. III.7(a)) suggests that the order formation is dominated by the random formation of a nucleating cluster. To investigate how the corresponding time scales of nucleation depend on the control parameters, we perform multiple simulations at different values of  $\alpha$  and recorded  $t_i$ ,  $t_d$ ,  $\tau$  by fitting a piece-wise

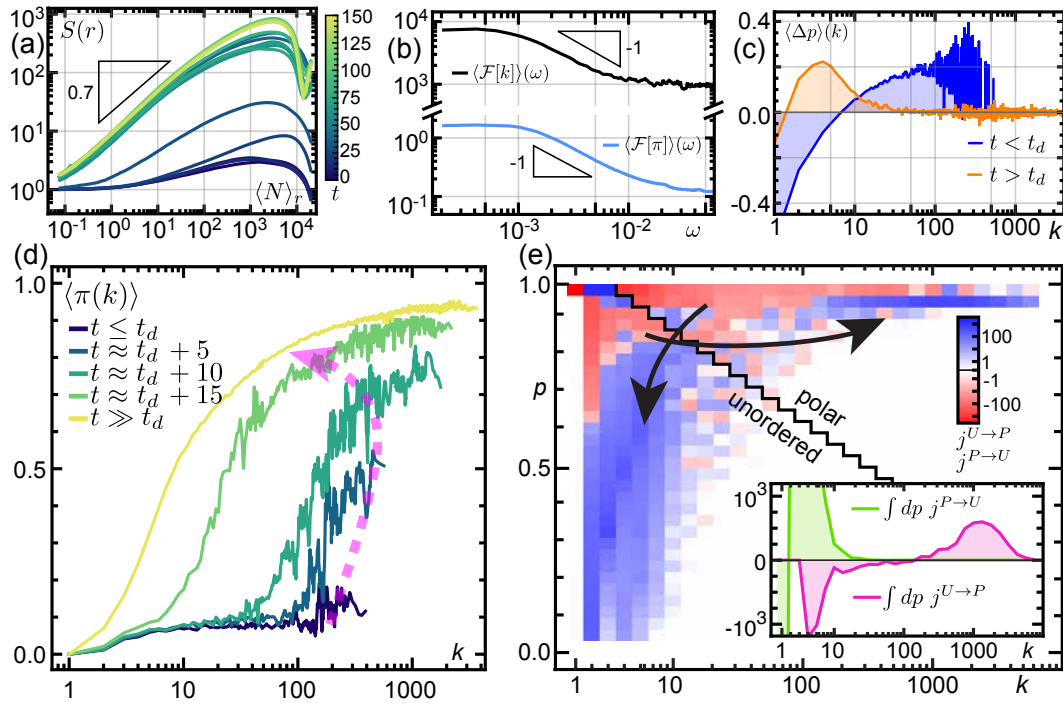


**Figure III.8** (a) Evolution of number fluctuations  $S(r)$  as a function of  $\langle N \rangle_r$ . The color map reflects different acquisition times  $t$ , and the black triangle a scaling exponent of 0.7. (b) Fourier spectrum of fluctuations of  $k^{\{i\}}(t)$ ,  $\pi^{\{i\}}(t)$  in the steady state. The black triangles denote a scaling exponent of 1. (c) Forward order production rates  $\langle \Delta p(k) \rangle$  before (blue) and after (orange) time  $t_d$ . (d) Evolution of the mean net cluster order  $\langle \pi(k) \rangle$  during order formation. (e) Steady-state particle fluxes  $j^{U \rightarrow P}(k, p)$ ,  $j^{P \rightarrow U}(k, p)$  of the polar state in  $k$ - $p$  space. The black line depicts the chosen division into an unordered (U) and a polar partition (P). Inset:  $j^{U \rightarrow P}(k, p)$ ,  $j^{P \rightarrow U}(k, p)$  integrated over  $p$ .

test function of the following form to  $\Omega_p$ :

$$f(t) = \begin{cases} a^{\frac{t}{t+t_i(1/a-1)}} & t < t_i \\ a & \text{for } t_i < t < t_d \\ a \exp[(t - t_d)/\tau] & \text{else} \end{cases} \quad (\text{III.3})$$

until  $\Omega_p(t) > 0.5$ . It should be noted that the functional form for  $t < t_i$  could also be chosen differently, as long as it captures the time scale  $t_i$  upon which  $\Omega_p$  becomes metastable. For  $\alpha \in [1.5, 3]$ , nucleation always took place if only waited sufficiently long (Fig. III.9(a)), even far below the previously reported onset of flocking (at  $\alpha \approx 1.8$  [127]). Here, the average dwell time  $\langle t_d \rangle$  grows very strongly with decreasing  $\alpha$  and the statistics resembles an exponential distribution (Fig. III.9(b)) similar to classical nucleation theory [48, 152]. For increasing  $\alpha$ , the average dwell time  $\langle t_d \rangle$  shrinks and eventually becomes comparable to the average values  $\langle t_i \rangle$ ,  $\langle \tau \rangle$ , meaning that the system effectively nucleates instantly. This can be interpreted as the spinodal point and is accompanied by a change of the underlying statistics as illustrated by the coefficient of variation  $c_v = \sqrt{\text{Var}[t_d]}/\langle t_d \rangle$  (Fig. III.9(c)), from an exponential-like  $t_d$ -distribution ( $c_v \approx 1$ ) at small  $\alpha$  to a different, less volatile distribution (note the minimum of  $c_v < 1$  at  $\alpha \approx 2.3$ ) at larger  $\alpha$ . In addition to Fig. III.9(a), we also probed the system size dependence of  $t_d$  in Fig. III.9(d) and found that  $\langle t_d \rangle$  scales inversely with the area of the system. This favors the intuitive assumption that critical fluctuations occur independently in adjacent parts of the system, hence in larger systems one has to wait less for nucleation. The constant value of the growth time  $\tau \approx 4.5$  confirms the observation of exponential cluster growth for a large range of system sizes. Note that this power-law decrease in  $\langle t_d \rangle$  competes with the exponential increase of  $\langle t_d \rangle$  as a function of parameter distance to the purely polar region in Fig. III.9(a). The thermodynamic limit is hence peculiar, and depends on the behavior of the parameter regions where nucleation times are far beyond numerically accessible simulation times, i.e. nucleation virtually never occurs.

The formation of polar order presented in Fig. III.7, in particular the shape of  $\Psi(k, p)$ , suggests that the flocking instability - above which nucleating clusters grow inexorably - depends on both sufficiently large size ( $k \gg 1$ ) and sufficiently large order ( $p \approx 1$ ), in contrast to condensation processes of equilibrium liquids. Here it is reasonable that this instability is primarily set by a critical amount of ordered filaments within a cluster  $s_{crit} = p_c \cdot k$ : if the polarity of a cluster  $s > s_{crit}$ , it will grow, or decay otherwise. Since the ensemble of clusters is stochastic and described by a distribution function  $\Psi(k, p)$ , the dwell time  $t_d$  resembles a first passage time to the instability  $s_{crit}$ . To probe the instability we perform a 'cluster stability analysis' by inserting a single, perfectly ordered cluster of size  $\tilde{k} = s$  (since  $\tilde{p} = 1$ ) into a disordered system sufficiently long after initialization

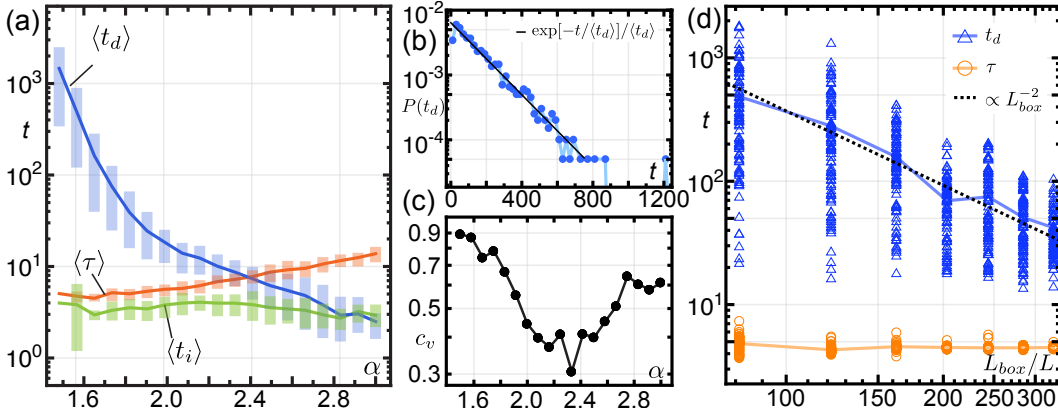


**Figure III.9** (a) Time scale analysis of  $t_d$ ,  $t_i$ , and growth times  $\tau$  as a function of  $\alpha$ . Solid lines denote average values, error bars represent the 15th, respective 85th percentiles taken over 100 realizations for every  $\alpha$ . (b) Waiting time probability density  $P(t_d)$  taken over an ensemble of 1000 simulations. The black solid line depicts an exponential distribution  $e^{-t/t_d}/t_d$  with a lifetime  $t_d$ . (c) Coefficient of variation of dwell times  $c_v$  as a function of  $\alpha$ . (d) Time scale analysis of waiting times  $t_d$  and growth times  $\tau$  as a function of the system size  $L_{box}$  in units of  $L$ . Solid lines denote average values (taken over 90-100 simulations at each point), the black dashed line shows a scaling law inversely proportional to the area of the system. Parameters:  $\alpha = 1.67$  for (b) and  $\rho L^2 = 1.51$  for (d).

while keeping the overall density of the system constant (Fig. III.10(a)). As can be seen by Fig. III.10(c), there is a critical polarity  $s_{crit}$  (and hence a critical line  $p_{crit}(k) \approx s_{crit}/k$  in Fig. III.7(d)) above which nucleation can be artificially triggered, up to stochastic fluctuations. Indeed, tracking when a cluster polarity  $s > s_{crit}$  seems to capture the earliest stages of nucleation, which can be seen when plotting the evolution of  $s_{max} = \max_{\{c\}} s = \max_{\{c\}} \rho k$  and comparing it with  $\Omega_p$  (Fig. III.7(a)). We performed the cluster stability analysis for different filament densities  $\rho$  and relative alignment strengths  $\alpha$ , creating a phase diagram of excitability (Fig. III.10(b)). Notably, the excitable region spans a very large portion of the (previously reported [127]) disordered regime. In most parts of this region, as it was assessed in Fig. III.9(a), spontaneous nucleation virtually never occurs within the time scales feasible for experiment and simulations. Yet,  $s_{crit}$  appears mostly small ( $\mathcal{O}(10^2)$ ) compared to the overall number of particles  $M$ . The above analysis suggests several kinetic mechanisms that govern polar flocking: (i) in the metastable disordered state, mostly unordered clusters emerge. (ii) At  $t_d$ , a nucleating polar cluster is spawned (Fig. III.11(c)), which behaves inherently different due to its internal ordering and coherence; it incorporates more and more disordered clusters (Fig. III.11(f,g)), but eventually splits up due to orientational splay (Fig. III.11(e)), which resembles an effective self-replication of polar clusters and creates the exponential growth of the order parameter  $\Omega_p$ . (iii) At steady

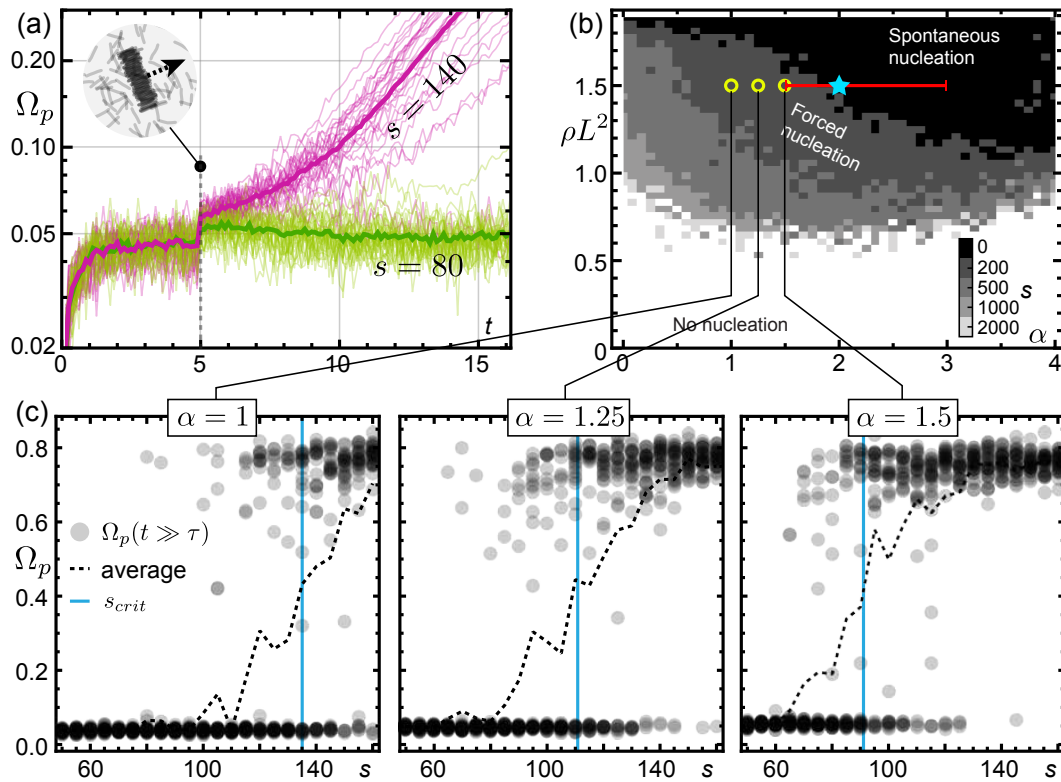


**Figure III.10** (a) Evolution of  $\Omega_p$  for disordered systems ( $\rho L^2 = 1.51$ ,  $\alpha = 1.25$ ) perturbed by a ordered cluster of polarity  $s$  at time  $t = 5$  (green:  $s = 80$ ; pink:  $s = 140$ ). Thin lines correspond to single trajectories, thick curves to the mean evolution, respectively. (b) Phase diagram as a function of  $\alpha$ ,  $\rho$ , and  $\kappa$ . The gray regions denote regimes where the final system is polar ( $\Omega_p > 0.2$ ), the gray scale corresponding to different polarity perturbations  $s$ . The red line depicts the parameters of Fig. III.9(a), the blue star Figs. III.7-III.8, respectively. (c) Cluster stability analysis as a function of the perturbing cluster size  $\tilde{k} = s$  for different values of  $\alpha$ . Gray circles denote the final order  $\Omega_p$  of single trajectories, with the dashed line being the average. Vertical blue lines depict the approximate values for the critical polarity  $s_{crit}$ .  $\rho L^2 = 1.51$ .

state, the growth of polar clusters is balanced by evaporating single particles or small clusters back into the "pool" of unordered clusters (Fig. III.11(d)), hence resembling a cyclic competition between effectively two cluster species. Some aspects of these dynamics can be directly observed in the WASP simulations; for instance, the stationary distribution of orientation angles in the polar phase shows large fluctuations in its tails which correspond to individual filaments and clusters trying to split up from the global front direction (Fig. III.11(a)). Furthermore, one can track the scattering of individual particles from clusters of different size at stationarity. The transition probability  $T(k_+, t + \Delta t | k, t)$  quantifies which fraction of filaments of a cluster  $k$  at time  $t$  scatter into a cluster of size  $k_+$  at time  $t + \Delta t$ , and it is normalized such that  $\sum_{k_+} T(k_+, t + \Delta t | k, t) = k \cdot c(k)$ . For  $\Delta t \rightarrow 0$ , this transition probability will just be a diagonal  $T(k_+, t | k, t) = \delta_{k_+, k} k c(k)$ . We recorded  $T(k_+, t + \Delta t | k, t)$  for sufficiently small  $\Delta t = 0.0125$  in Fig. III.11(b) to observe short-time processes. It can be seen that, while most clusters remain stable during this time (signal along diagonal), especially large polar clusters either frequently fragment or coalesce into similarly sized clusters (bright off-diagonal events in the upper right of Fig. III.11(b)), or evaporate very small clusters or single filaments (bottom right signal in Fig. III.11(b)).

#### 1.4.2 Effective kinetic model of flocking

To test whether these simple observations of WASP systems alone are sufficient to understand the mechanics of flocking, we introduce a kinetic toy model that describes the assembly of two competing cluster species, an unordered type  $a$  and an ordered type  $b$ . Using  $a_k = (\mathbf{a})_k$  and  $b_k = (\mathbf{b})_k$  as the cluster size distributions of the unordered species and the ordered species, respectively, the dynamics of our model is given by a set of coagulation-fragmentation equations [153–155]:

$$\dot{\mathbf{a}} = \mathbf{F}(\mathbf{a}, \mathbf{b}) \quad (\text{III.4})$$

$$\dot{\mathbf{b}} = \mathbf{G}(\mathbf{a}, \mathbf{b}) \quad (\text{III.5})$$

where the current vectors  $\mathbf{F} = (F_1, F_2, \dots, F_M)^T$  and  $\mathbf{G} = (G_1, G_2, \dots, G_M)^T$  incorporate all possible reaction channels:

$$F_1 = 2\beta_2 a_2 + \sum_{i=3}^M \beta_i a_i - \sum_{i=1}^{M-1} \alpha_{i,1} a_i a_1 + \lambda(2b_2 + \sum_{i=3}^M b_i) - \sum_{i=2}^{M-1} \gamma_{i,1} b_i a_1, \quad (\text{III.6})$$

$$F_k = \beta_{k+1} a_{k+1} - \beta_k a_k + \frac{1}{2} \sum_{i=1}^{k-1} \alpha_{i,k-i} a_i a_{k-i} - \sum_{i=1}^{M-k} \alpha_{i,k} a_i a_k - \sum_{i=2}^{M-k} \gamma_{i,k} b_i a_k - \omega_k a_k,$$

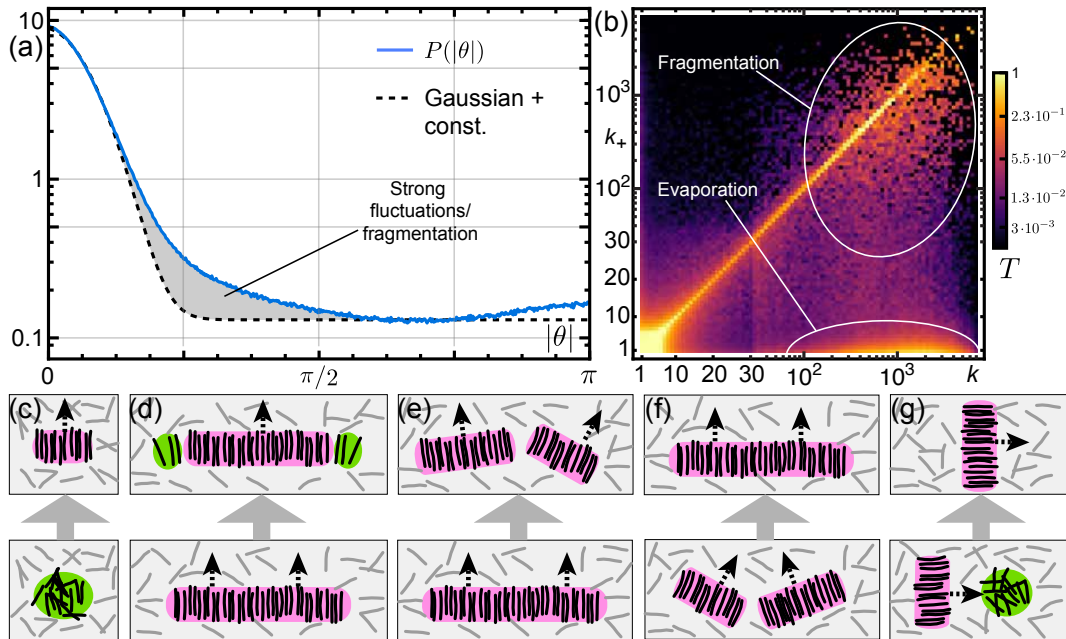


**Figure III.11** (a) Probability density  $P(|\theta|)$  of angular orientations  $\theta$  relative to the dominant direction in the stationary nucleated phase. The dashed curve corresponds to a simple Gaussian approximation of polar orientations, embedded by uniform random orientations from the disordered regions. The gray region marks the deviation from this approximation. Parameters and data are identical to Fig. III.7. (b) Transition matrix  $T(k_+, t + \Delta t | k, t)$  with  $\Delta t = 0.0125$ . As a guide to the eye, regions with dominant fragmentation or evaporation are encircled in white. Parameters:  $\rho L^2 = 1.51$ ,  $\alpha = 1.67$ . (c-g) Illustration of effective kinetic processes between unordered (green shading) and ordered clusters (pink shading): a nucleating polar cluster may spontaneously emerge from a unordered one (c); single filaments evaporate off the trailing edges of a polar flock (d); a polar flock spontaneously splits up in smaller parts due to orientational splay (e); two polar clusters coagulate to a single large cluster (f); a polar cluster 'imbibes' unordered clusters and filaments (g).

and

$$\begin{aligned}
G_1 &= 0, \\
G_k &= \lambda(b_{k+1} - b_k) - \sum_{i=2}^{M-k} \eta_{i,k} b_i b_k + \frac{1}{2} \sum_{i=2}^{k-2} \eta_{i,k-i} b_i b_{k-i} \\
&\quad + \mu \left( \sum_{i=2}^{M-k} b_{i+k} - \frac{1}{2} \sum_{i=2}^{k-2} b_k \right) + \sum_{i=2}^{k-1} \gamma_{i,k-i} b_i a_{k-i} - \sum_{i=1}^{M-k} \gamma_{k,i} b_k a_i + \omega_k a_k,
\end{aligned} \tag{III.7}$$

with  $k \in \{2, \dots, M\}$ . Note that by convention, summation over non-positive indices gives zero contribution. It can be straightforwardly checked that these currents conserve particle mass  $\sum_{k=1}^M k(F_k + G_k) \equiv 0$ . Fig. III.12(a) illustrates the corresponding interaction rates: for the unordered species  $a$ , cluster assembly occurs by the coagulation of smaller clusters of sizes  $i$  and  $j$  with a rate  $\alpha_{i,j} := v\sigma_{aa}X_{aa}(i,j)/A$ , where  $v$  is the velocity,  $A$  the area of the system,  $\sigma_{aa}$  the scattering propensity between unordered clusters, and  $X_{aa}(i,j)$  a term proportional to the scattering cross section. Likewise, for the ordered species  $b$ , there is a coagulation rate  $\eta_{i,j} := v\sigma_{bb}X_{bb}(i,j)/A$ . In addition, ordered clusters of size  $i$  'imbibe' unordered ones of size  $j$  at a rate  $\gamma_{i,j} := v\sigma_{ab}X_{ab}(i,j)/A$ . Cluster disassembly occurs via fragmentation of ordered clusters at a constant rate  $\mu_{i,j} = \mu_0$  and evaporation of single unordered particles from  $a$  and  $b$  clusters at a rate  $\beta_i := \beta_0 Y_a(i)$  and  $\lambda_i := \lambda_0 Y_b(i)$ , respectively. Finally, unordered cluster may spontaneously nucleate into an ordered cluster, at a rate  $\omega_i := \omega_0 Z(i)$ . From observations of WASP simulations (see Fig. III.11) we introduce simple, heuristic assumptions on the remaining size factors  $X_{\bullet,\bullet}$ ,  $Y_{\bullet}$ ,  $Z$ : a disordered cluster of size  $i$  has approximately spherical shape with a diameter and circumference  $\propto \sqrt{i}$  leading to  $X_{a,a}(i,j) = \sqrt{i} + \sqrt{j}$  and  $Y_a(i) = \sqrt{i}$ , respectively; ordered clusters, however, are more line-shaped with a length  $\propto i$ , hence  $X_{b,b}(i,j) = i + j$ . They evaporate particles mainly via its edges, i.e. there is no size dependence, resulting to  $Y_b(i) = 1$ . Furthermore, when colliding with unordered clusters, we assume that scattering is mainly dominated by the ordered cluster and its size  $i$ , i.e.  $X_{a,b}(i,j) = i$ . Since nucleation was observed to take only place for larger cluster sizes,  $Z(i) := 1/(1 - e^{-(i-m_c)/v_c})$  is assumed to be of sigmoidal shape with a characteristic size  $m_c = 100$  and a width  $v_c = 10$ , which we fix, for simplicity, throughout the analysis. A variation of  $m_c$  or  $v_c$  resulted only in a shifted onset of the order transition, without a qualitative difference in the ordered state. Note that without the presence of ordered clusters  $b$ , these rates would resemble previous works of Peruani et al. [144, 145, 149].

Next, we integrate the evolution using initial conditions  $a_1(t=0) = 1^2$  and a

---

<sup>2</sup> if not stated otherwise, we fix  $M = 400$ ,  $A = 800$ ,  $v = \beta_0 = \lambda_0 = 1$ ,  $\mu_0 = 0.025$ ,  $\sigma_{aa} = 1.6$ ,  $\omega_0 = 10^{-4}$

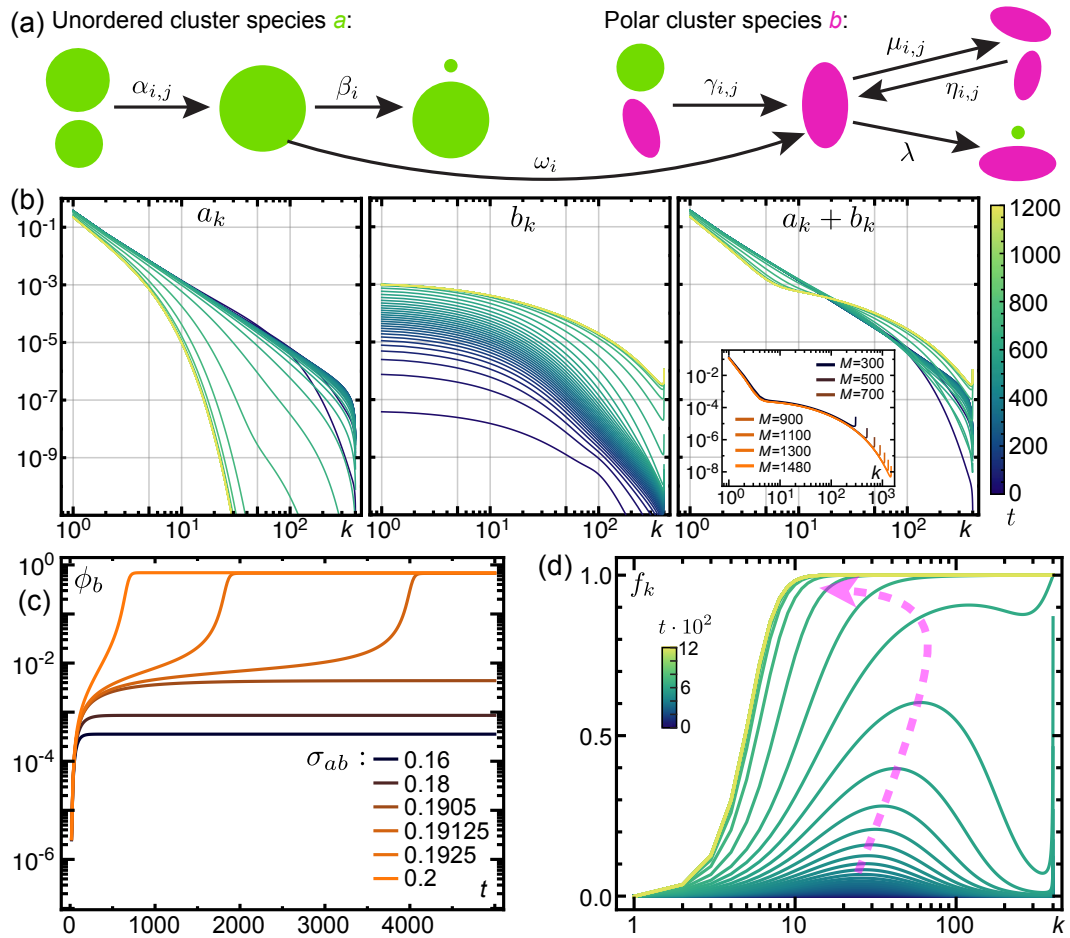


**Figure III.12** (a) Illustration of the two-species kinetic model with respective rates (compare also with Fig. III.11(c-g)). (b) Evolution of the cluster size distributions of species  $a$  (left panel) and species  $b$  (middle panel) and the sum of both (right panel) at different times (see color map). Inset: stationary total cluster distribution  $a_k + b_k$  as a function of the system size  $M$  (for  $\sigma_{aa} = 1.4$ ,  $\sigma_{ab} = 0.2$ ,  $\sigma_{bb} = 0.8$ ,  $q_0 = 0.01$ ). (c) Evolution of the mass fraction  $\phi_b$ , for different  $\sigma_{ab}$  ( $\sigma_{bb} = 1$ ). (d) Evolution of the relative fraction  $f_k$ . The color gradient depicts different times.

simple Euler scheme in C++, which, for system sizes  $M \lesssim 1000$ , we find to be numerically faster than an adaptive time-step 4th-order Runge-Kutta algorithm and much simpler than implicit integration schemes, and concentrate on the influence of the scattering propensities  $\sigma_{ab}, \sigma_{bb}$  of coagulating clusters since they couple  $a_k, b_k$  nonlinearly (note that we fix  $\sigma_{aa}$  such that  $a_k$ , in the absence of  $b$ , behaves as an exponentially truncated power law [144, 145, 149] that resembles a disordered distribution like in Fig. III.5(d)). These variables - controlling interactions of polar clusters - play a similar role as the alignment interactions in WASP systems.

For  $\sigma_{ab} = 0.2$ ,  $\sigma_{bb} = 1$ , Fig. III.12(b) shows the evolution of individual distributions  $a_k, b_k$ . It can be seen that there is little change at intermediate times, and that the dynamics only speeds up drastically when there is a significant fraction of  $b$  clusters. As a result, the total cluster size distribution  $a_k + b_k$  (right panel in Fig. III.12(b)) evolves from the initially exponentially suppressed power law to a heavy-tailed distribution with a shoulder at small  $k$  similar to Fig. III.7(c). This is driven by the rapid growth of the ordered mass fraction  $\phi_b = \sum_k k b_k$  which corresponds to the order parameter  $\Omega_p$  (Fig. III.7(a)). Similarly,  $\phi_b$  grows, after dwelling for some finite time at a small value, exponentially fast towards a distribution with many large and polar clusters (Fig. III.12(c)). In addition to these steady state properties, the internal dynamics of the kinetic model exhibit remarkable similarities to flocking in WASP systems: for both approaches, ordered clusters are initially formed from intermediate sizes  $k$  and then spread out towards larger and smaller  $k$ , which is quantified by the relative cluster fraction  $f_k = b_k / (a_k + b_k)$  (Fig. III.12(d)) and the mean net cluster order  $\langle \pi(k) \rangle_p = \int_0^1 dp \pi(k) \Psi(k, p)$  (compare with Fig. III.6(d)), respectively. The rate equations of the kinetic model allow to directly visualize the steady-state fluxes between both cluster species  $J_k^{(b \rightarrow a)}$ ,  $J_k^{(a \rightarrow b)}$ :

$$\begin{aligned} J_1^{(b \rightarrow a)} &= \lambda(2b_2 + \sum_{i=3}^M b_i) - \sum_{i=2}^{M-1} \gamma_{i,1} b_i a_1, \\ J_k^{(b \rightarrow a)} \stackrel{k \geq 1}{=} &k \cdot \left( - \sum_{i=2}^{M-k} \gamma_{i,k} b_i a_k - \omega_k a_k \right), \end{aligned} \quad (\text{III.8})$$

and

$$J_k^{(a \rightarrow b)} \stackrel{k \geq 1}{=} k \cdot \left( \lambda(b_{k+1} - b_k) + \sum_{i=2}^{k-1} \gamma_{i,k-i} b_i a_{k-i} - \sum_{i=1}^{M-k} \gamma_{k,i} b_k a_i + \omega_k a_k \right), \quad (\text{III.9})$$

which is analogous to the rates  $F_k, G_k$  (Eqs. (III.6), (III.7)) when all species-internal rates set to zero. Fig. III.13(a) shows that unordered clusters are converted to large ordered clusters over a wide range of  $k$ ; smaller ordered clusters, in turn, evaporate single filaments back into the unordered mass. In detail, Fig. III.13(b,c)

shows the individual contributions proportional to  $\lambda$ ,  $\gamma_{i,k}$ , and  $\omega_k$ , respectively. From Eq. (III.8) it is obvious that species  $a$  only gains by evaporation of ordered clusters into single, disordered filaments. In contrast, species  $b$  gains cluster mass by coalescence of smaller ordered and unordered clusters, transferring it to large cluster sizes, which is only balanced by filament evaporation. Taken together, the ordered state of the kinetic model exhibits a cyclic steady state flux, analogous to the WASP system (see Fig. III.8(e)).

Furthermore, we find that this transition towards the  $b$ -dominated state is discontinuous, and analyzed the stable solutions in the  $\sigma_{ab}$ - $\sigma_{bb}$  space (Fig. III.14), yielding a vast bistable parameter regime. This was achieved by starting the evolution from two different initial conditions, one from  $a_k(t=0) = \delta_{1,k}$ ,  $b_k(t=0) = 0$  and the other one from a set of stationary,  $b$ -dominated distributions  $a_k(t=0)$ ,  $b_k(t=0)$  (with  $\phi_b > 0.5$ ). Figs. III.14(a,b) depict the steady state values of  $\phi_b$  for varying  $\sigma_{ab}$  and  $\sigma_{bb}$  of these respective initial conditions. Fig. III.14(c) illustrates the three-dimensional structure of the bifurcation. To obtain the bistable region, we subtracted the data of both plots to obtain the hysteresis value  $\delta = \phi_b^{upper} - \phi_b^{lower}$  as shown in Fig. III.14(d). While the stability of the disorder-dominated branch (bounded by  $s_1$ ) is virtually unaffected by  $\sigma_{bb}$ , the boundary of the order-dominated branch behaves approximately like a power law  $s_2 = \sigma_{bb}^{(upper)} \propto \sigma_{ab}^{-1.4}$ . Surprisingly, there is a critical point at which the transition becomes continuous, which would correspond to a different bifurcation scenario of the flocking transition. Similarly, the bistable region and the critical point can also be analyzed in the space of density  $\rho$  and  $\sigma_{ab}$  as can be seen in Figs. III.14(e,f). Hence we hypothesize that the stability of polar nucleation and phase separation is, in principle, susceptible to varying interactions on the mesoscopic cluster level and the particle density. To visualize how of mass flux  $J_k^{(a \rightarrow b)}$  are affected by different parameters and the presence of the instability, we recorded them while varying the parameters in Figs. III.14(d-g). The amplitude of  $J_k^{(a \rightarrow b)}$  is minimal in the disordered,  $a$ -dominated phase, becomes strong in the ordered,  $b$ -dominated phase, and is maximal close to the transition. As expected, below the bifurcation point the fluxes vary continuously and increase with  $\sigma_{ab}$ , while they become discontinuous above and decrease with  $\sigma_{ab}$ .

In summary, we find a remarkable agreement of the WASP simulations and the kinetic model, despite the merely heuristic connection. The above analysis shows how microscopic processes create a nontrivial, emergent dynamics, which corresponds to a model of cyclically competing cluster species. In both approaches, the flocking state is a result of a constant turnover of particle cluster from disorder to order and back, resulting in a stationary flow in the 'phase space' of cluster size and cluster order, which breaks detailed balance. This cycling rate implies that there exist corresponding time and length scales which ultimately give rise to finite length scales of the spatio-temporal patterns of the active system, analogous to

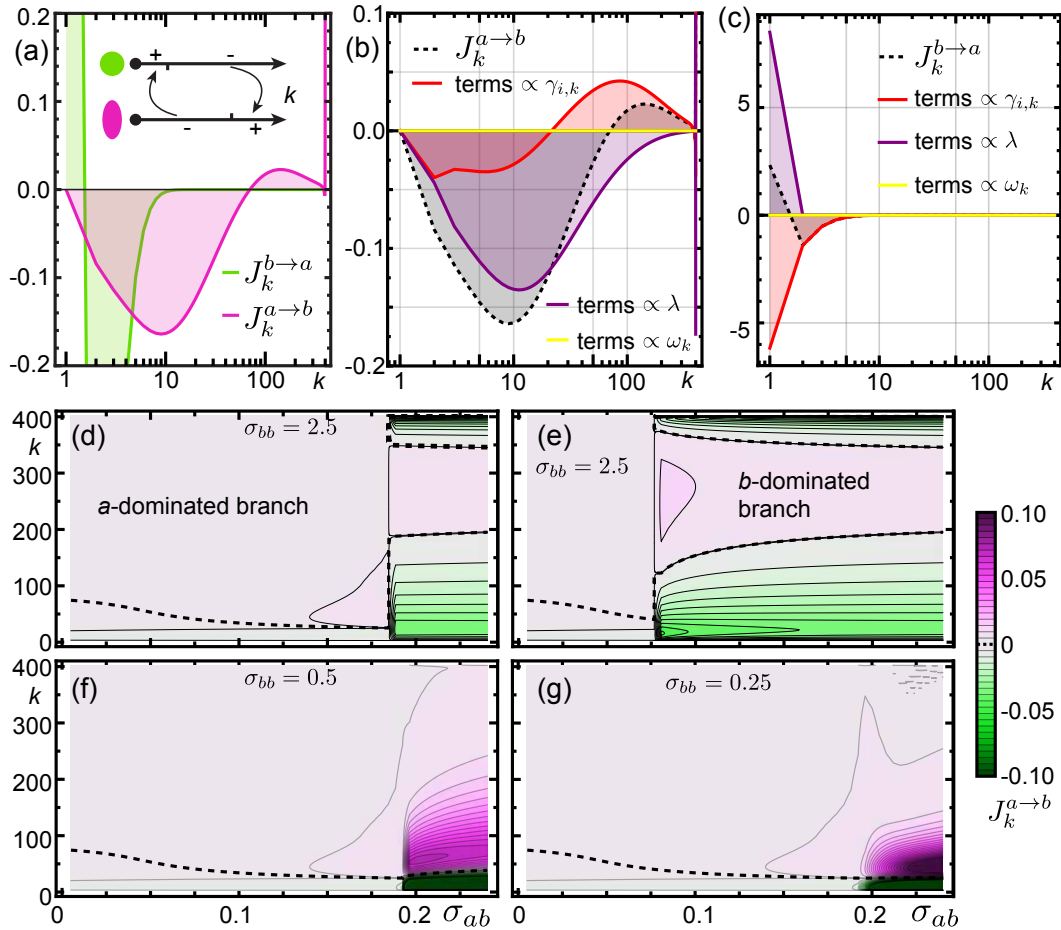


**Figure III.13** (a) Steady-state particle fluxes  $J_k^{(b \rightarrow a)}$ ,  $J_k^{(a \rightarrow b)}$  from both species as a function of  $k$ . Inset: visualization of flux directions. (b, c) Individual contributions of the inter-species particle fluxes  $J_k^{(a \rightarrow b)}$  (b) and  $J_k^{(b \rightarrow a)}$  (c) as a function of cluster size  $k$ . (d-g) Contour maps of the flux  $J_k^{(a \rightarrow b)}$  as a function of  $k$  and  $\sigma_{ab}$  at different points in parameter space,  $\sigma_{bb} = 2.5$  (d,e),  $\sigma_{bb} = 0.5$  (f), and  $\sigma_{bb} = 0.25$  (g). Above the bifurcation point at  $\sigma_{bb} \approx 0.5$ , two branches are present (d,e). Parameters are identical to Fig. III.12

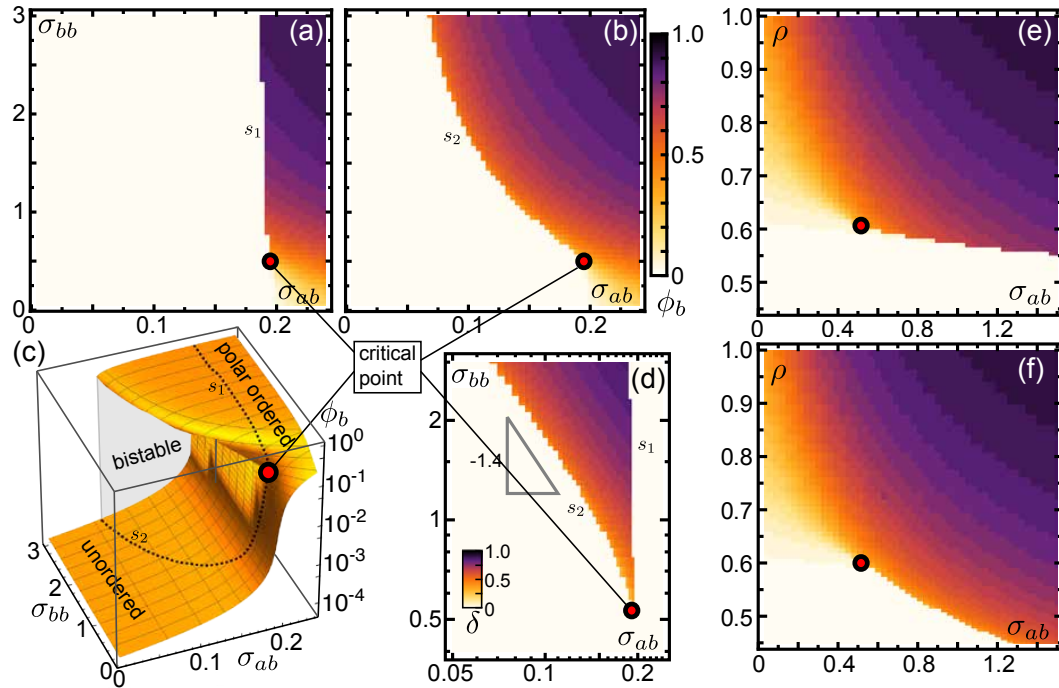


**Figure III.14** (a,b) Density plots of the stationary mass fraction  $\phi_b$  as a function of  $\sigma_{ab}$  and  $\sigma_{bb}$  with different initial conditions: (a) dominated by  $a$  clusters, and (b) dominated by  $b$  clusters. (c) Bifurcation diagram of stationary mass fractions  $\phi_b$  as a function of  $\sigma_{ab}$  and  $\sigma_{bb}$ . The dashed lines  $s_1$ ,  $s_2$  mark the upper, respectively lower, boundary of the bistable region. (d) Top view on the bistable region of (c), with the coloring corresponding to the hysteresis value  $\delta = \phi_b^{upper} - \phi_b^{lower}$ . (e,f) Density plots of the stationary mass fraction  $\phi_b$  as a function of  $\sigma_{bb}$  and the density  $\rho$  with different initial conditions: (e) dominated by  $a$  clusters, and (f) dominated by  $b$  clusters. Parameters:  $\sigma_{aa} = 1.8$ ,  $\sigma_{ab} = 0.15$ ,  $\omega_0 = 10^{-3}$ . In (a-f), bifurcation points are marked by small red and black circles.

the dynamical systems assessments of Refs. [43, 44, 46, 47]. Hence, the dynamics within the cluster-order-size representation could hint towards the microscopic mechanisms that underlie micro-phase separation in experiments and agent-based simulations. The analysis also shows that both cluster size and the locally emerging cluster order are indispensable to understand the flocking transition, nucleation time scales and the subcritical behavior of the system.

## 1.5 Mesoscopic processes at the nematic onset

In addition to the assessments of the previous section concerning the internal dynamics of the disordered and the polar parameter regions, we applied the cluster size-order representation of WASP simulations to the formation of nematic patterns. Here, we concentrate on the parameter regime that is relevant for the actin motility assay, see Fig. III.4, where  $\alpha = 6.25$ . We simulate a system with random initial conditions,  $\rho_0 L^2 = 1.51$  ( $M = 40,000$ ) and a box length  $L_{box} = 1024$  which is above the previously reported onset of nematic order (see section 2.2 and Ref [127]), and observe the evolution in Fig. III.15. As in the previous sections, we fixed  $L_p = 200$  and rescaled time with the correlation time  $L_p/v$ . Like in the case of polar flocking, local order of microscopic clusters is quickly created, with the local order parameters  $\Omega_p, \Omega_n$  growing to an intermediate plateau value (Fig. III.15(a)). Initially,  $\Omega_p \approx \Omega_n$  indicating that order on the cluster scale has a polar character. From this point, local nematic order continuously grows until it reaches a stationary value at  $\sim 0.27$ . Interestingly, the global order parameters  $\mathcal{P}, \mathcal{N}$  do not resolve this intermediate dynamics as  $\mathcal{P}$  resides around zero and  $\mathcal{N}$  exhibits a rather erratic growth. This is because the nematic patterns of the system is not globally oriented but has multiple network branches with different nematic axes at small times  $t$  (see snapshots in Fig. III.15(a)). A illustration of the physical processes is given in Fig. III.15(b), where initially, clusters with a gradual polar order emerge like in other regions of parameter space and the previous section. Then, these clusters interact and locally orient themselves along a nematic axis despite remaining polar. Subsequently, clusters intersect and mix along a nematic axis, creating a cluster nematic order  $\nu$  that exceeds the cluster polar order  $\pi$ . This is also reflected in the evolution of the mean net cluster orders  $\langle \pi \rangle(k), \langle \nu \rangle(k)$  (Fig. III.15(c)), which reveals that the continuous build-up of nematic order is caused by predominantly large clusters. In the nematic state, the cluster size distribution  $\psi(k)$  shows a rather steep, but heavy-tailed character with a tail exponent of  $\sim -2.6$  (Fig. III.15(d)). Like for the case of polar flocking, the number fluctuations  $S(r)$  at larger length scales  $r$  reflect anomalous fluctuations with  $S(r) \sim r^{0.7}$  which appear to be absent for small  $r$  (Fig. III.15(e)). In this state, single particles frequently fluctuate between clusters of different sizes and orders, which can be seen in the spectra of the trajectories  $\langle \mathcal{F}[k^{\{i\}}] \rangle(\omega), \langle \mathcal{F}[\pi^{\{i\}}] \rangle(\omega),$  and  $\langle \mathcal{F}[\nu^{\{i\}}] \rangle(\omega)$

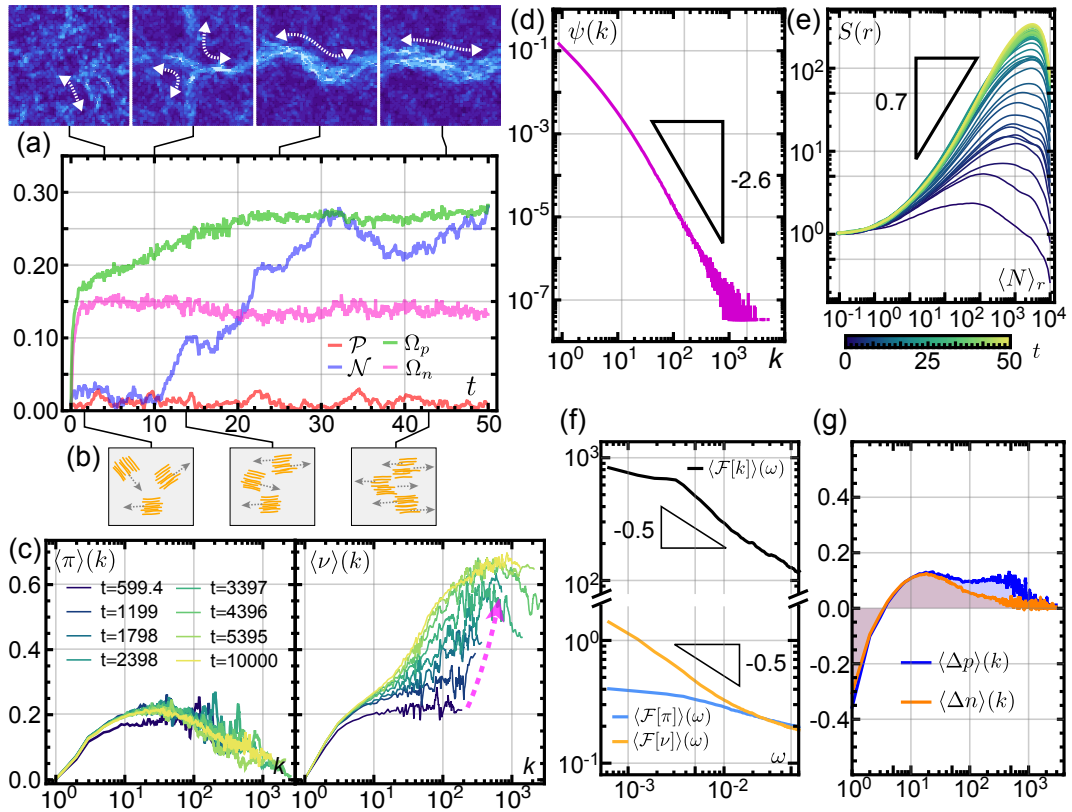


**Figure III.15** (a) Evolution of order parameters  $\mathcal{P}$ ,  $\mathcal{N}$ ,  $\Omega_p$ ,  $\Omega_n$  during nematic pattern formation. The upper panels give snapshots of the system at corresponding times. (b) Sketch of underlying mechanisms: at early times, locally polar clusters emerge; later, these cluster align nematically and gradually overlap. (c) Evolution of mean net cluster orders  $\langle \pi \rangle(k)$ ,  $\langle \nu \rangle(k)$ . (d) Stationary cluster size distribution  $\psi(k)$ . (e) Evolution of the number fluctuations  $S(r)$  as a function of the mean numbers  $\langle N \rangle_r$ . (f) Fourier spectrum of fluctuations of  $k^{\{i\}}(t)$ ,  $\pi^{\{i\}}(t)$ ,  $\nu^{\{i\}}(t)$  in the steady state. (g) Forward order production rates  $\langle \Delta p \rangle(k)$  and  $\langle \Delta n \rangle(k)$  in the stationary state. (d-f) The black triangles denote corresponding scaling exponents.

(Fig. III.15(f)). The relative frequency of switching depends on the difference in sizes and predominantly nematic order, roughly following a power law  $\sim \omega^{0.5}$ . As in the analysis of the flocking state (Fig. III.8(c)), we can also assess the cluster scales at which order is predominantly produced and/or destroyed by calculating the mean forward polar and nematic order productions  $\langle \Delta p(k) \rangle := \langle p_k^{\{i\}}(t + \Delta t) - p^{\{i\}}(t) \rangle$  and  $\langle \Delta n(k) \rangle := \langle n_k^{\{i\}}(t + \Delta t) - n^{\{i\}}(t) \rangle$  which gives the difference of a filament order at time  $t + \Delta t$  at cluster size  $k$  when it was  $p(t)$  at a time  $t$ , averaged over all filaments (we fixed  $\Delta t = 0.15$ ). Interestingly, as can be seen in Fig. III.15(g),  $\langle \Delta p(k) \rangle$  exhibits polar order production exceeding  $\langle \Delta n(k) \rangle$  at scales  $k \gtrsim 100$ . This shows that cluster polar order is constantly produced at large  $k$ , and destroyed at the smallest  $k$ , indicating that global nematic order is a result of the constant interaction of locally polar clusters instead of the formation of intrinsically stable nematic clusters, which do not exist here.

As described above, the onset of nematic order is controlled for instance by changing the homogeneous density of the system. Fig. III.16(a) gives the dependence of the stationary order parameters on  $\rho_0$  ( $\alpha = 6.25$  here again) and shows that there is a transition from a disordered to a nematically-ordered state at  $\rho_0 L^2 \approx 1.05$ . While there appears to be a distinct jump of  $\mathcal{N}$  from zero to a finite value, the corresponding change in  $\Omega_n$  seems to be rather continuous. This could indicate that the transition is predominantly driven by a global alignment of microscopically ordered clusters, and not by the creation of inherently different clusters as for polar flocking. While previous theories have predicted that this transition is first order [78, 79, 156], our analysis would need a further refinement to make a definite claim for the WASP model. To illuminate the hypothesis that the nematic onset is connected to the orientational dynamics of interacting clusters, we investigated the properties of various single particle correlation functions. In particular, we calculated the cross-correlations between the cluster size  $k^{\{i\}}(t)$ , the cluster polar order  $\pi^{\{i\}}(t)$ , and the cluster nematic order  $\nu^{\{i\}}(t)$  of single filament trajectories ( $i \in \{1, 2, \dots, M\}$ ) which are given by  $\text{Corr}[k^{\{i\}}(t), \pi^{\{i\}}(t + \Delta t)]$ ,  $\text{Corr}[k^{\{i\}}(t), \nu^{\{i\}}(t + \Delta t)]$ , and  $\text{Corr}[\pi^{\{i\}}(t), \nu^{\{i\}}(t + \Delta t)]$ . Here, the function  $\text{Corr}[A(t), B(t + \Delta t)]$  quantifies how likely a particle is found at a value  $B$  at a time  $t + \Delta$  when it had the value  $A$  at time  $t$ . Since these cross-correlators are unity when  $\Delta t = 0$  and zero when  $\Delta t \rightarrow \infty$ , we expect an exponential decay law like for the orientational autocorrelation function of single filaments:

$$\begin{aligned} \text{Corr}[k^{\{i\}}(t), \pi^{\{i\}}(t + \Delta t)] &\approx e^{-\Delta t / \tau_{k\pi}}, \\ \text{Corr}[k^{\{i\}}(t), \nu^{\{i\}}(t + \Delta t)] &\approx e^{-\Delta t / \tau_{k\nu}}, \\ \text{Corr}[\pi^{\{i\}}(t), \nu^{\{i\}}(t + \Delta t)] &\approx e^{-\Delta t / \tau_{\pi\nu}}. \end{aligned} \quad (\text{III.10})$$

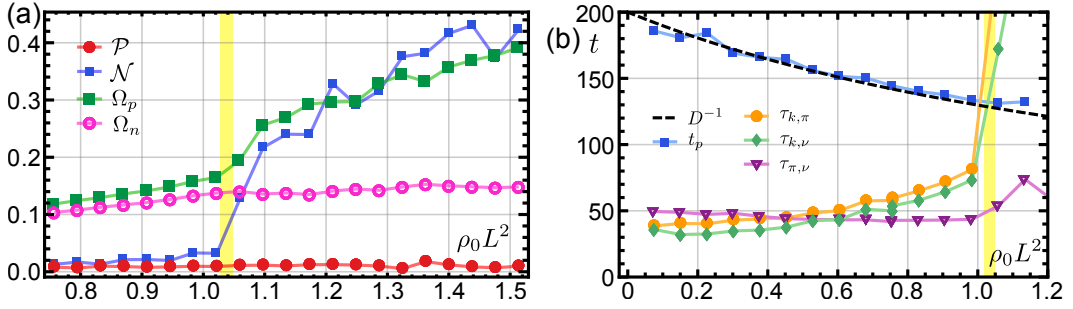


**Figure III.16** (a) Stationary order parameters  $\mathcal{P}$ ,  $\mathcal{N}$ ,  $\Omega_p$ ,  $\Omega_n$  as a function of the filament density  $\rho_0$  at  $\alpha = 6.25$  ( $L_{\text{box}} = 1024$ ). (b) Single particle correlation times of orientation ( $t_p$  and  $D^{-1}$ ) and clusters ( $\tau_{k\pi}$ ,  $\tau_{k\nu}$ ,  $\tau_{\pi\nu}$ ) as a function of  $\rho_0$ . The yellow-shaded areas illustrate the approximate position of the phase transition.

In Fig. III.16(b) we calculated the cross-correlators, fitted the corresponding decay parameters  $\tau_{k\pi}$ ,  $\tau_{k\nu}$ ,  $\tau_{\pi\nu}$  and compared them with the orientational decay time  $t_p$  of single particles (which is approximately given by Eq. (II.34) of chapter II) as a function of  $\rho_0$ . It can be seen that  $\tau_{k\pi} \approx \tau_{k\nu}$  and both continuously grow as the system gets denser, stemming from the increased coherence of locally aligning clusters; likewise  $t_p$  decreases due to enhanced scattering of individual filaments. When the onset density is reached, both  $\tau_{k\pi}$ ,  $\tau_{k\nu}$  jump to large values as expected for the enhanced coherence of the ordered state. Interestingly, the transition takes place when  $\tau_{k\pi} \approx \tau_{k\nu} \approx 0.5t_p$ . This could point to a connection of these time scales at the nematic threshold, and implies that nematic order may emerge when the correlation times of single particles become synchronized with the correlation times of locally polar clusters. For the whole domain there appears to be no mechanism that directly couples polar cluster order and nematic cluster order, since the dynamics of  $\tau_{\pi\nu}$  plays no distinct role.

## 1.6 Summary and outlook

In the above section we have combined simulations of the WASP model introduced in chapter II with a new particle cluster decomposition method, the cluster size-order representation; at its basis lies the observation that individual active particles form local clusters with a distinct intrinsic ordering. This intrinsic ordering is crucial to understand the emergence of global order and patterns, and allows to trace self-organization phenomena of the active system on all length scales. Since the WASP model possesses a vast number of parameters, we restricted ourselves to the parameter intervals which was found to be relevant for the paradigmatic actin motility assay.

Here, even for globally disordered systems, our analysis in section 1.3 shows that

there are nontrivial collective effects of the underlying particles: active disorder exhibits giant density fluctuations and an ensemble of locally emerging polar clusters, which are very sensitive to a variation of the control parameters of the system. Hence, analogies of active disorder with equilibrium gasses are ill-suited in this context. In section 1.4, we investigated in depth the formation of global polar order, popularly termed the flocking transition. We found that phase separation of the flocking state is equivalent to the coexistence of an ordered and an unordered cluster population, respectively, that continuously exchange mass. Here, we showed that the essential physics of flocking is governed by the dynamics of particle clusters, with their emergent properties - both cluster size and cluster order - controlling the onset of order. Here, random fluctuations play a crucial role and determine the time scales of nucleation, which is the dominant pathway of order emergence. From this perspective, the Vicsek ordering paradigm (VOP) and its corresponding critical onset of (homogeneous) polar order, which were mentioned in the beginning of this section, appear to be absent in this active system. To identify the relevant mechanisms between clusters of different size and order, we introduced a kinetic model of 2-species cluster assembly which reproduces the same statistics and bifurcation scenario as the active system, even without exhibiting any information of a spatial extension. Both approaches predict a steady-state particle flow of the flocking state, which is unique for non-equilibrium systems and has no analogy to equilibrium phase transitions. This aspect could help to identify the microscopic mechanisms of micro-phase separation in active systems, which is also associated with finite length and time scales. Our analysis shows that understanding the local processes on the particle scale is already sufficient to describe the kinetics of collective motion and polar nucleation, drawing an interesting connection to the physics of population dynamics. Furthermore, our approach provides a simple framework to assess intrinsic mechanisms of active systems on a conceptual level, without relying on coarse-grained field descriptions. From wide parts of this analysis in section 1.4 we have prepared a manuscript that is to be submitted for peer review, and which is also found below in section 1.7. Section 1.5 focusses on the cluster dynamics of emerging nematic order, which we find to be very different from polar flocking: instead of rare nucleation events that are driven by inherently heterogeneous particle clusters, nematic patterns in WASP systems continuously build up from locally polar clusters without delay time. Presumably, this is driven by a gradual alignment of interacting cluster along a global nematic axis, with spontaneous symmetry breaking of cluster orientations at the onset. Our data indicates that this onset is connected with the synchronization of single particle and local cluster orientations, underlining again the conjecture that physical processes on all length and time scales contribute to the collective state of the active system. In principle, the cluster size-order representation is readily applicable to other collective phenomena of active systems. In particular, the emergence of coexisting

polar and nematic order found in the previous chapter (Ref. [127]) implies that the mechanisms found in sections 1.4, 1.5 are simultaneously present here. Although a simplified kinetic picture of the nematic dynamics is still lacking, we hypothesize that there exists an equivalent description of the three-phase coexistence (polar, nematic, and disorder) in terms of an appropriate cluster assembly dynamics, which may describe the evolution of an ensemble of clusters in the presence of different ordering attractors. The correspondence of the WASP system with the physics of self-assembly and population dynamics in section 1.4.2 could also be relevant for biological systems such as aggregating bacterial colonies [27, 114] and migrating cell layers [33, 34], which also frequently exhibit arrested coarsening (that is, micro-phase separation). As a future task, it remains to explicitly derive the kinetic rates between clusters from first principles, or how physical interactions may alter the underlying bifurcation scenario of flocking. For example, additional cues like hydrodynamic interactions may enter the processes of interacting clusters at the intermediate scale. Furthermore, other collective phenomena, like vortex formation [6, 25, 157], may be suitable for a similar approach.

## 1.7 Prepared manuscript

# Cluster assembly kinetics and fluctuations drive polar nucleation of active polymers

by

L. Huber<sup>1</sup>, T. Krüger<sup>1</sup>, and E. Frey<sup>1</sup>

<sup>1</sup>Department of Physics, Arnold Sommerfeld Center for Theoretical Physics and  
Center for NanoScience, Ludwig-Maximilians-Universität München,  
Theresienstraße 37, 80333 München, Germany

reprinted on pages [157–162](#)

Supplemental Material reproduced on pages [163–170](#).



# Cluster assembly kinetics and fluctuations drive polar nucleation of active polymers

Lorenz Huber,<sup>1</sup> Timo Krüger,<sup>1</sup> and Erwin Frey<sup>1,\*</sup>

<sup>1</sup>*Arnold Sommerfeld Center for Theoretical Physics (ASC) and Center for NanoScience (CeNS),  
Department of Physics, Ludwig-Maximilians-Universität München,  
Theresienstrasse 37, D-80333 München, Germany*

The onset of polar flocking in active matter systems resembles a discontinuous gas-liquid phase transition, accompanied by the formation of microphase-separated polar patterns. While these features have been observed in a variety of models and experiments, little is known about the underlying microscopic processes that generate these collective phenomena. Here we show that the onset of polar order is governed by the mesoscale dynamics of two different populations of particle clusters, one with and one without internal polar order. Using agent-based simulations in the experimentally relevant parameter regime, we describe how order emerges spontaneously by nucleation or external excitation, and identify the relevant mechanisms. From these observations we introduce a simple kinetic model of two different cluster species, which agrees well with the agent-based simulations. Both approaches predict that collective order is maintained by a steady cyclic particle turnover from unordered to ordered clusters and back, respectively, promoting microphase separation on the global scale.

The polar flocking transition in active matter marks the onset of collective motion and was observed in many experiments, ranging from biopolymer systems [1–4] to colloids [5, 6] and discs [7–10]. It was recently established that this transition is discontinuous [11–13] in general and exhibits a subcritical parameter region of polar patterns [4, 14–18], as illustrated in [Fig. 1(a)]. While flocking appears to be akin to a gas-liquid transition [17, 19] with long-range polar order, differences to an equilibrium analogue remain. In particular, simulations and experiments show that the dynamics between ordered, dense regions and disordered, dilute regions is dominated by *micro-phase separation*: that is, the coarsening of polar flocks becomes arrested at finite size, resulting in stationary patterns such as polar fronts or clusters [1, 17, 20]. Here, stochastic fluctuations on the particle scale play a decisive role and were observed to affect this coarsening dynamics as well as the overall behavior of the transition [14, 17, 20], and even allow for spontaneous nucleation of clusters below the onset of order [21]. Yet, a description or comprehension of the microscopic mechanisms that underlie these phenomena is lacking, even on a qualitative level.

In this letter, we show that the essential physics of flocking is governed by the dynamics of particle clusters, with their emergent properties - both cluster size and cluster order - controlling the onset. By analyzing the evolution of clusters using agent-based simulations of **w**eakly **a**ligning **s**elf-propelled **p**olymers (WASP's), we find that phase separation of the flocking state is equivalent to the coexistence of an ordered and an unordered cluster population, respectively, that continuously exchange mass. To identify the relevant mechanisms between clusters of different size and order, we introduce a kinetic model of 2-species cluster assembly which reproduces the same statistics and bifurcation scenario as the active system, even without a spatial extension. Here,

both approaches predict a steady-state particle flow of the flocking state. Our analysis shows that understanding the local processes on the particle scale is already sufficient to describe the kinetics of collective motion and polar nucleation. Our approach provides a simple framework to assess intrinsic mechanisms of active systems on a conceptual level, without relying on coarse-grained field descriptions.

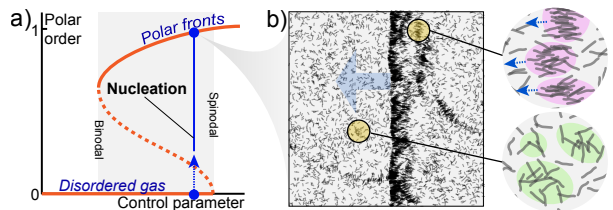


FIG. 1. a) Schematic of the typical bifurcation scenario of global polar order (orange). Control parameters are, for example, particle density or interaction strength. Between the binodal and spinodal lines, flocking is triggered by spontaneous nucleation events (blue line). (b) Illustration of clustering of active polymers in the polar, phase-separated state. Locally, both ordered (pink shading) and disordered (green shading) clusters can be found.

We consider agent-based simulations of systems with  $M$  polymer filaments on a two-dimensional substrate with periodic boundary conditions (see Refs. [22, 23]). Motivated by *in vitro* assays of gliding polymers [1–4, 24–26], each filament of length  $L$  assumed to consist of a head that performs a persistent random walk with persistence length  $L_p$  and velocity  $v$ , and a tail that follows its head, creating a trailing motion without movement perpendicular to the filament contour. Interactions between filaments are weak and dominated by aligning interactions [4, 22]; upon local contact with adjacent filament contours, a polar and a nematic torque are exerted on

a filament head proportional to  $\varphi_p \cos \theta$  and  $\varphi_n \cos(2\theta)$ , respectively ( $\theta$  being the impact angle). These filament systems were shown to reproduce local collision statistics and collective phenomena - polar and nematic patterns - on large scales ( $M \propto \mathcal{O}(10^6)$ ) alike [22], with varying filament density  $\rho$  and relative alignment strength  $\alpha = \varphi_n/\varphi_p$  as experimentally motivated control parameters. Here, we focus on the formation of large polar fronts as illustrated in Fig. 1(b). In the flocking state, one observes that filaments are locally organized into clusters of different sizes and, on closer inspection, different internal ordering [Fig. 1(b)]: filament clusters in a polar front are highly ordered flocks while clusters elsewhere are much less structured.

To investigate the role of clusters with different sizes and order in the evolution of a system of WASP's, we introduce the cluster-size-order representation: a system of filaments  $f^{(i)}$ ,  $i \in \{1, 2, \dots, M\}$ , can be uniquely decomposed into a set of clusters  $\{c\}$ . A filament belongs to a cluster  $c$  if its minimal distance to  $c$  is smaller than a cutoff  $\gamma$  with  $\gamma \ll L$ . Every cluster can be assigned a cluster size  $k$  and a cluster polar order  $p = \frac{1}{k} |\sum_{j=1}^k \exp(i\theta_j)|$ , where the index runs over all cluster filament orientations  $\theta_j$ . From these definitions we can introduce a set of observables that quantify processes on all length scales: first, we can build a global order parameter  $\Omega_p = \sum_{\{c\}} \pi(k)^{(c)} k^{(c)} / M$  by averaging the individual polar cluster orders  $p$  weighted by the respective cluster size  $k$ . Here, the net cluster order  $\pi(k) = p(k) - \Delta_k$  shifts  $p(k)$  by an amount  $\Delta_k = (7 + 1/k)/(8\sqrt{k}) + \mathcal{O}(k^{-5/2})$  [23]. This statistical correction stems from the fact that even random clusters have, on average, a nonzero order  $\Delta_k$  which would contribute to the measured order (this is evident for single filaments). Second, we can record the statistics of  $k$  and  $p$  of the full ensemble of clusters using the corresponding distribution functions, the cluster size distribution  $\psi(k)$  and the cluster-size-order distribution  $\Psi(k, p)$ , normalized such that  $\sum_{k=1}^M k \int_0^1 dp \Psi(k, p) = \sum_{k=1}^M k \psi(k) = 1$ . Third, we can combine  $p$  and  $k$  into an extensive quantity, the cluster polarity  $S = p \cdot k$ , which is equivalent the amount of ordered filaments within a cluster.

Using these definitions, we simulate a system of WASP's using random initial conditions and parameters  $\rho = 1.51/L^2$ ,  $\varphi_p = 0.036$ ,  $\alpha = 2$  which reproduce the collision statistics of the polar actin motility assay slightly above the previously reported onset of flocking [22]. Within a short time  $\nu$ , the system generates a small but nonzero  $\Omega_p$  [Fig. 2(a), Movie 1], which dwells for a long time  $t_d$  (note that time is rescaled in units of the longest single-particle correlation time  $L_p/v$ ). This quasi-stationary, disordered system shows a cluster size distribution  $\psi(k)$  with an exponential tail [Fig. 2(b)], similar to previous studies [27–34]. The cluster size-order distribution  $\Psi(k, p)$  in Fig. 2(c) shows that most of the clusters possess a cluster polar order  $p$  centered around

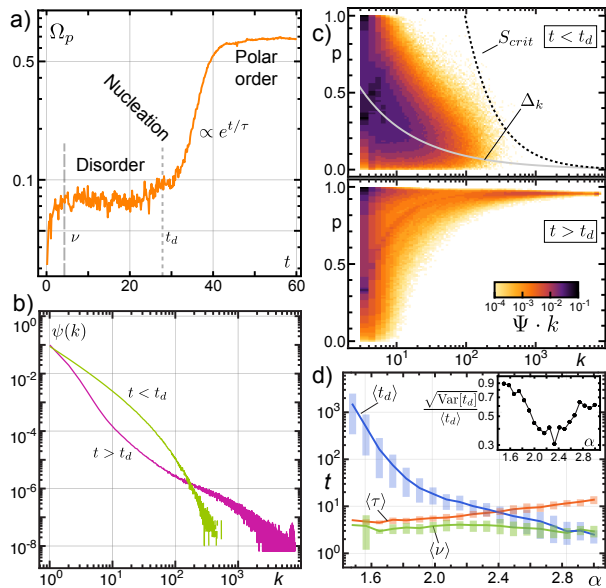


FIG. 2. a) Evolution of the order parameter  $\Omega_p$ . The initial time scale  $\nu$  and the nucleation time  $t_d$  are marked by long-dashed and short-dashed lines, respectively. b) Cluster size distribution  $\psi(k)$  before (green) and after (purple) nucleation. c) Cluster size-order distribution  $\Psi(k, p)$  as a function of  $k$  and  $p$ , before (upper panel) and after (lower panel) nucleation at time  $t_d$ . The black dashed line an estimated nucleation threshold at  $S_{crit} = p_c \cdot k \approx 90$ . d) Time scale analysis of  $t_d$ ,  $\nu$ , and growth times  $\tau$  as a function of  $\alpha$ . Solid lines denote average values, error bars represent the 15th, respective 85th percentiles taken over 100 realizations for every  $\alpha$ . Inset: relative fluctuation of dwell times  $\sqrt{\text{Var}[t_d]}/\langle t_d \rangle$  as a function of  $\alpha$ .

$\Delta_k$ , indicating that the individual clusters are hardly more ordered than randomly assembled clusters. At time  $t_d$ , a sufficiently large and ordered cluster nucleates and rapidly percolates the system, as can be seen by  $\Omega_p$  growing exponentially over an order of magnitude with a growth time  $\tau$  before becoming stationary [Fig. 2(a)]. This final state is now dominated by very ordered and large clusters, as is demonstrated by the altered shape of  $\Psi(k, p)$  and  $\psi(k)$  where large clusters are almost perfectly polar while small clusters remain at small  $p$  [Fig. 2(b,c)]. To investigate how these time scales of nucleation depend on the control parameters, we performed multiple simulations at different values of  $\alpha$  and recorded  $\nu$ ,  $t_d$ ,  $\tau$  by fitting a test function to  $\Omega_p$  [23]. For  $\alpha \in [1.5, 3]$ , nucleation always took place if only waited sufficiently long [Fig. 2(d)], even far below the previously reported onset (at  $\alpha \approx 1.8$  [22]). Here, the average dwell time  $\langle t_d \rangle$  grows very strongly with decreasing  $\alpha$  and the statistics behave like an exponential distribution ( $\sqrt{\text{Var}[t_d]}/\langle t_d \rangle \approx 1$  [Fig. 2(d)]) similar to the decay dynamics of classical nucleation theory. For increasing  $\alpha$ , the average dwell time

$\langle t_d \rangle$  shrinks and eventually becomes comparable to the average values  $\langle \nu \rangle, \langle \tau \rangle$ , meaning that the system effectively nucleates instantly. This can be interpreted as the spinodal point and is accompanied by a change of  $\sqrt{\text{Var}[t_d]}/\langle t_d \rangle$  [Fig. 2(d)].

The formation of polar order presented in [Fig. 2], in

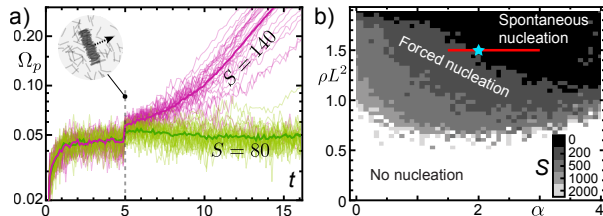


FIG. 3. a) Evolution of  $\Omega_p$  for disordered systems ( $\rho L^2 = 1.51$ ,  $\alpha = 1.25$ ) perturbed by an ordered cluster of polarity  $S$  at time  $t = 5$  (green:  $S = 80$ ; pink:  $S = 140$ ). Thin lines correspond to single trajectories, thick curves to the mean evolution, respectively. b) Phase diagram as a function of  $\alpha$ ,  $\rho$ , and  $\kappa$ . The gray regions denote regimes where the final system is polar ( $\Omega_p > 0.2$ ), the gray scale corresponding to different  $S$ . The red line depicts the parameters of Fig. 2(d), the blue star Fig. 2(a-c), respectively.

particular the shape of  $\Psi(k, p)$ , suggests that the flocking instability - above which nucleating clusters grow inexorably - depends on both sufficiently large size ( $k \gg 1$ ) and sufficiently large order ( $p \approx 1$ ), in contrast to condensation processes of equilibrium liquids. Here it is reasonable that this instability is primarily set by a critical amount of ordered filaments within a cluster  $S_{crit} = p_c k$ : if the polarity of a cluster  $S > S_{crit}$ , it will grow, or decay otherwise. Since the ensemble of clusters is stochastic and described by a distribution function  $\Psi(k, p)$ , the dwell time  $t_d$  resembles a first passage time to the instability  $S_{crit}$ . To probe the instability we performed a "cluster stability analysis" by inserting a single, perfectly ordered cluster of size  $\tilde{k} = S$  (since  $\tilde{p} = 1$ ) into a disordered system sufficiently long after initialization while keeping the overall density of the system constant. As can be seen by [Fig. 3], there is a critical polarity  $S_{crit}$  (and hence a critical line  $p_{crit}(k) \approx S_{crit}/k$  [Fig. 2](c)) above which nucleation can be artificially triggered, up to stochastic fluctuations [23]. Indeed, tracking when a cluster polarity  $S > S_{crit}$  seems to capture the earliest stages of nucleation [Fig. S1(a), Movie 1]. We performed the cluster stability analysis for different filament densities  $\rho$  and relative alignment strengths  $\alpha$ , creating a phase diagram of excitability [Fig. 3(b)]. Notably, the excitable region spans a very large portion of the (previously reported [22]) disordered regime. In most parts of this region, as it was assessed in [Fig. 2(d)], spontaneous nucleation virtually never occurs within the time scales feasible for experiment and simulations. Yet,  $S_{crit}$  appears mostly small ( $\mathcal{O}(10^2)$ ) compared to the overall number of particles.

The above analysis suggests several kinetic mechanisms that govern polar flocking: (i) in the metastable disordered state, mostly unordered clusters emerge. (ii) At  $t_d$ , a nucleating polar cluster is spawned, which behaves inherently different due to its internal ordering and coherence; it incorporates more and more disordered clusters, but eventually splits up due to orientational splay [23], which resembles an effective self-replication of polar clusters and creates the exponential growth of the order parameter  $\Omega_p$ . (iii) At steady state, the growth of polar clusters is balanced by evaporating single particles or small clusters back into the "pool" of unordered clusters [see Fig. 2(c) and [23]], hence resembling a cyclic competition between effectively two cluster species.

To test whether these simple observations of WASP's alone are sufficient to understand the mechanics of flocking, we introduce a kinetic toy model that describes the assembly of two competing cluster species, an unordered type  $a$  and an ordered type  $b$ . Using  $a_k = (\mathbf{a})_k$  and  $b_k = (\mathbf{b})_k$  as the cluster size distributions of the unordered species and the ordered species, respectively, the dynamics of our model is given by a set of coagulation-fragmentation equations [35–37],  $\dot{\mathbf{a}} = \mathbf{F}(\mathbf{a}, \mathbf{b})$  and  $\dot{\mathbf{b}} = \mathbf{G}(\mathbf{a}, \mathbf{b})$ , where  $\mathbf{F}$  and  $\mathbf{G}$  include all species-specific rates (see [23] for the full equations). These equations conserve the number of  $M$  particles,  $\sum_{k=1}^M k(a_k + b_k) \equiv 1$  and  $\sum_{k=1}^M k \partial_t (a_k + b_k) \equiv 0$ . Fig. 4(a) illustrates the corresponding interaction rates: for the unordered species  $a$ , cluster assembly occurs by the coagulation of smaller clusters of sizes  $i$  and  $j$  with a rate  $\alpha_{i,j} := v \sigma_{aa} X_{aa}(i, j)/A$ , where  $v$  is the velocity,  $A$  the area of the system,  $\sigma_{aa}$  the scattering propensity of between unordered clusters, and  $X_{aa}(i, j)$  a term proportional to the scattering cross section. Likewise, for the ordered species  $b$ , there is a coagulation rate  $\eta_{i,j} := v \sigma_{bb} X_{bb}(i, j)/A$ . In addition, ordered clusters of size  $i$  "imbibe" unordered ones of size  $j$  at a rate  $\gamma_{i,j} := v \sigma_{ab} X_{ab}(i, j)/A$ . Cluster disassembly occurs via fragmentation of ordered clusters at a constant rate  $\mu_{i,j} = \mu_0$  and evaporation of single unordered particles from  $a$  and  $b$  clusters at a rate  $\beta_i := \beta_0 Y_a(i)$  and  $\lambda_i := \lambda_0 Y_b(i)$ , respectively. Finally, unordered cluster may spontaneously nucleate into an ordered cluster, at a rate  $\omega_i := \omega_0 Z(i)$ . We further specify the generic size factors  $X_{\bullet,\bullet}$ ,  $Y_\bullet$ ,  $Z$  by observations from WASP simulations (see [23] for expressions). Note that without the presence of ordered clusters  $b$ , these rates would resemble previous works of Peruani et al. [28, 30, 32].

Next, we integrate the evolution using a simple Euler scheme and initial conditions  $a_1(t = 0) = 1$  [38], and concentrate on the influence of the scattering propensities  $\sigma_{ab}, \sigma_{bb}$  of coagulating clusters since they couple  $a_k, b_k$  nonlinearly (note that we fixed  $\sigma_{aa}$  such that  $a_k$ , in the absence of  $b$ , behaves as an exponentially truncated power law [28, 30, 32] that resembles a disordered

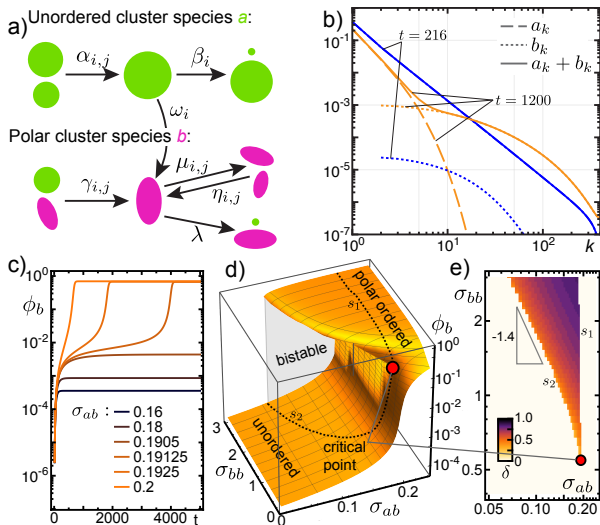


FIG. 4. a) Illustration of the two-species kinetic model with respective rates. b) Evolution of the cluster size distributions of species  $a$  (long-dashed lines) and species  $b$  (short-dashed lines) and the sum of both (solid lines) at two different times (blue at  $t = 216$  and orange at  $t = 1200$ ). c) Evolution of the mass fraction  $\phi_b$ , for different  $\sigma_{ab}$  ( $\sigma_{bb} = 1$ ). d) Bifurcation diagram of stationary mass fractions  $\phi_b$  as a function of  $\sigma_{ab}$  and  $\sigma_{bb}$ . The dashed lines  $s_1$ ,  $s_2$  mark the upper, respectively lower, boundary of the bistable region. e) Top view on the bistable region of d), with the coloring corresponding to the hysteresis value  $\delta = \phi_b^{upper} - \phi_b^{lower}$ .

distribution like in [Fig. 2(b)]). These variables - controlling interactions of polar clusters - play a similar role as the alignment interactions in WASP systems.

For  $\sigma_{ab} = 0.2$ ,  $\sigma_{bb} = 1$ , the total cluster size distribution  $a_k + b_k$  (solid lines in Fig. 4(b)) evolves from the initially exponentially suppressed power law to a heavy-tailed distribution with a kink at small  $k$  similar to [Fig. 2(b)]. This is driven by the rapid growth of the ordered mass fraction  $\phi_b = \sum_k k b_k$  which corresponds to the order parameter  $\Omega_p$  [Fig. 2(a)]. Similarly,  $\phi_b$  grows, after dwelling for some finite time at a small value, exponentially fast towards a distribution with many large and polar clusters [Fig. 4(c)]. Furthermore, we found that this transition towards the  $b$ -dominated state is discontinuous, and analyzed the stable solutions in the  $\sigma_{ab}$ - $\sigma_{bb}$  space [Fig. 4(d,e)] using different initial conditions, yielding a vast bistable parameter regime. While the stability of the disorder-dominated branch (bounded by  $s_1$ ) is virtually unaffected by  $\sigma_{bb}$ , the boundary of the order-dominated branch behaves approximately like a power law  $s_2 = \sigma_{bb}^{(upper)} \propto \sigma_{ab}^{-1.4}$ . Surprisingly, there is a critical point at which the transition becomes continuous, which would correspond to a different bifurcation scenario of the flocking transition. Hence we hypothesize that the stability of polar nucleation and phase separation is, in princi-

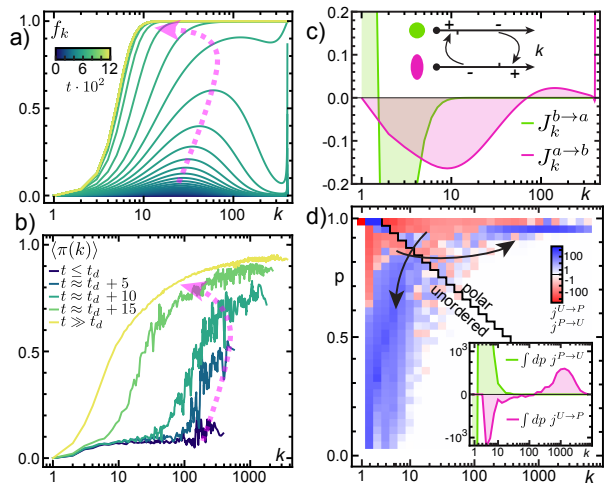


FIG. 5. a) Evolution of the relative fraction  $f_k$ . The color gradient depicts different times. b) Evolution of the mean net cluster order  $\langle \pi(k) \rangle$  during nucleation in WASP simulations. c) Steady-state particle fluxes  $J_k^{(b \rightarrow a)}$ ,  $J_k^{(a \rightarrow b)}$  from both species as a function of  $k$ . Inset: visualization of flux directions. d) Steady-state particle fluxes  $j^{U \rightarrow P}(k, p)$ ,  $j^{P \rightarrow U}(k, p)$  of the polar state in WASP simulations in  $k$ - $p$  space. The black line depicts the chosen division into an unordered (U) and a polar partition (P). Inset:  $j^{U \rightarrow P}(k, p)$ ,  $j^{P \rightarrow U}(k, p)$  integrated over  $p$  for comparison with c).

ple, susceptible to varying interactions on the mesoscopic cluster level. Next, we compare the internal dynamics of the kinetic model with the WASP simulations. For both approaches, ordered clusters are initially formed from intermediate sizes  $k$  and then spread out towards larger and smaller  $k$ , which is quantified by the relative cluster fraction  $f_k = b_k / (a_k + b_k)$  [Fig. 5(a)] and the mean net cluster order  $\langle \pi(k) \rangle_p = \int_0^1 dp \pi(k) \Psi(k, p)$  [Fig. 5(b)], respectively. The rate equations of the kinetic model allow to directly visualize the steady-state fluxes between both cluster species  $J_k^{(b \rightarrow a)}$ ,  $J_k^{(a \rightarrow b)}$  [Fig. 5(c)], which predict that unordered clusters are converted to large ordered clusters over a wide range of  $k$ ; smaller ordered clusters, in turn, evaporate single filaments back into the unordered mass (see [23] for details). Indeed in WASP simulations, by a heuristic subdivision of  $k$ - $p$  cluster space and tracking the particle fluxes  $j^{U \rightarrow P}(k, p)$ ,  $j^{P \rightarrow U}(k, p)$  between the unordered partition (U) and the ordered (P) partition [Fig. 5(d)], we also observe a cyclic steady-state particle flow in the flocking state. Overall, the statistical properties as well as the physical processes of both the kinetic model and WASP simulations compare remarkably well.

To summarize, we found that the formation of local particle clusters controls the flocking onset in active systems. In contrast to phase-separating transitions without broken symmetry, nucleating clusters require both

sufficiently large size and order. Our analysis estimates the relevant time scales of cluster self-organization and how flocking can be artificially excited, which should be readily verifiable in actin and microtubule gliding experiments. We show that polar flocking can be analogously described by a kinetic two-species model, revealing an interesting correspondence of active matter with the physics of self-assembly and population dynamics, and should be relevant for biological systems such as aggregating bacterial colonies [39, 40] and migrating cell layers [41, 42]. Here, the constant turnover of ordered and unordered clusters provides an explanation how the coarsening of polar active matter becomes arrested. As a future task, it remains to explicitly derive the kinetic rates between clusters from first principles to elucidate why a clusters nucleates, or how physical interactions may alter the underlying bifurcation scenario of flocking. Furthermore, other collective phenomena may be eligible for a similar approach, such as nematic laning [43–45], vortex formation [26, 46, 47] or coexisting types of order[22].

This research was supported by the German Excellence Initiative via the program ‘NanoSystems Initiative Munich’ (NIM), and the Deutsche Forschungsgemeinschaft (DFG) via project B02 within the Collaborative Research Center (SFB 863) “Forces in Biomolecular Systems”.

\* [frey@lmu.de](mailto:frey@lmu.de)

- [1] V. Schaller, C. Weber, C. Semmrich, E. Frey, and A. R. Bausch, *Nature* **467**, 73 (2010).
- [2] T. Butt, T. Mufti, A. Humayun, P. B. Rosenthal, S. Khan, S. Khan, and J. E. Molloy, *Journal of Biological Chemistry* **285**, 4964 (2010).
- [3] S. Hussain, J. E. Molloy, and S. M. Khan, *Biophysical Journal* **105**, 1456 (2013).
- [4] R. Suzuki, C. A. Weber, E. Frey, and A. R. Bausch, *Nature Physics* **11**, 839 (2015).
- [5] A. Bricard, J.-B. Caussin, N. Desreumaux, O. Dauchot, and D. Bartolo, *Nature* **503**, 95 (2013).
- [6] A. Kaiser, A. Snezhko, and I. S. Aranson, *Science Advances* **3**, e1601469 (2017).
- [7] J. Deseigne, O. Dauchot, and H. Chaté, *Physical Review Letters* **105** (2010), 10.1103/PhysRevLett.105.098001.
- [8] J. Deseigne, S. Léonard, O. Dauchot, and H. Chaté, *Soft Matter* **8**, 5629 (2012).
- [9] C. A. Weber, T. Hanke, J. Deseigne, S. Léonard, O. Dauchot, E. Frey, and H. Chaté, *Physical Review Letters* **110** (2013), 10.1103/PhysRevLett.110.208001.
- [10] K.-D. N. T. Lam, M. Schindler, and O. Dauchot, *New Journal of Physics* **17**, 113056 (2015).
- [11] G. Grégoire, H. Chaté, and Y. Tu, **181**, 157.
- [12] G. Grégoire and H. Chaté, *Physical Review Letters* **92** (2004), 10.1103/PhysRevLett.92.025702.
- [13] E. Bertin, M. Droz, and G. Grégoire, *Physical Review E* **74** (2006), 10.1103/PhysRevE.74.022101.
- [14] A. P. Solon and J. Tailleur, *Physical Review Letters* **111** (2013), 10.1103/PhysRevLett.111.078101.
- [15] J.-B. Caussin, A. Solon, A. Peshkov, H. Chaté, T. Dauxois, J. Tailleur, V. Vitelli, and D. Bartolo, *Physical Review Letters* **112**, 148102 (2014).
- [16] F. Thüroff, C. A. Weber, and E. Frey, *Physical Review X* **4**, 041030 (2014).
- [17] A. P. Solon, H. Chaté, and J. Tailleur, *Physical Review Letters* **114** (2015), 10.1103/PhysRevLett.114.068101.
- [18] A. Morin and D. Bartolo, **8**, 10.1103/PhysRevX.8.021037.
- [19] A. P. Solon and J. Tailleur, *Physical Review E* **92**, 042119 (2015).
- [20] H. Chaté, F. Ginelli, G. Grégoire, and F. Raynaud, *Physical Review E* **77** (2008), 10.1103/PhysRevE.77.046113.
- [21] C. A. Weber, V. Schaller, A. R. Bausch, and E. Frey, **86**, 10.1103/PhysRevE.86.030901.
- [22] L. Huber, R. Suzuki, T. Krüger, E. Frey, and A. R. Bausch, *Science* **361**, 255 (2018).
- [23] See Supplemental Material.
- [24] M. P. Sheetz, R. Chasan, and J. A. Spudich, *The Journal of Cell Biology* **99**, 1867 (1984).
- [25] T. Sanchez, D. T. N. Chen, S. J. DeCamp, M. Heymann, and Z. Dogic, *Nature* **491**, 431 (2012).
- [26] Y. Sumino, K. H. Nagai, Y. Shitaka, D. Tanaka, K. Yoshikawa, H. Chaté, and K. Oiwa, *Nature* **483**, 448 (2012).
- [27] C. Huepe and M. Aldana, *Physical Review Letters* **92** (2004), 10.1103/PhysRevLett.92.168701.
- [28] F. Peruani, A. Deutsch, and M. Bär, *Physical Review E* **74** (2006), 10.1103/PhysRevE.74.030904.
- [29] H. P. Zhang, A. Be’er, E.-L. Florin, and H. L. Swinney, *Proceedings of the National Academy of Sciences* **107**, 13626 (2010).
- [30] F. Peruani, L. Schimansky-Geier, and M. Bär, *The European Physical Journal Special Topics* **191**, 173 (2010).
- [31] Y. Yang, V. Marceau, and G. Gompper, *Physical Review E* **82** (2010), 10.1103/PhysRevE.82.031904.
- [32] F. Peruani and M. Bär, *New Journal of Physics* **15**, 065009 (2013).
- [33] Y. Fily, S. Henkes, and M. C. Marchetti, *Soft Matter* **10**, 2132 (2014).
- [34] Ö. Duman, R. E. Isele-Holder, J. Elgeti, and G. Gompper, *Soft Matter* **14**, 4483 (2018).
- [35] M. v. Smoluchowski, *Zeitschrift für Physikalische Chemie* **92U** (1918), 10.1515/zpch-1918-9209.
- [36] S. Chandrasekhar, *Reviews of Modern Physics* **15**, 1 (1943).
- [37] P. L. Krapivsky, S. Redner, and E. Ben-Naim, *A Kinetic View of Statistical Physics* (Cambridge University Press, Cambridge; New York, 2010) oCLC: 672330146.
- [38] If not stated otherwise,  $M = 400$ ,  $A = 800$ ,  $v = \beta_0 = \lambda_0 = 1$ ,  $\mu_0 = 0.025$ ,  $\sigma_{aa} = 1.6$ ,  $\omega_0 = 10^{-4}$ .
- [39] F. Peruani, J. Starruß, V. Jakovljevic, L. Søgaard-Andersen, A. Deutsch, and M. Bär, *Physical Review Letters* **108** (2012), 10.1103/PhysRevLett.108.098102.
- [40] D. Nishiguchi, K. H. Nagai, H. Chaté, and M. Sano, *Physical Review E* **95** (2017), 10.1103/PhysRevE.95.020601.
- [41] K. Kawaguchi, R. Kageyama, and M. Sano, *Nature* **545**, 327 (2017).
- [42] T. B. Saw, A. Doostmohammadi, V. Nier, L. Kocgozlu, S. Thampi, Y. Toyama, P. Marcq, C. T. Lim, J. M. Yeomans, and B. Ladoux, *Nature* **544**, 212 (2017).
- [43] F. Ginelli, F. Peruani, M. Bär, and H. Chaté,

- Physical Review Letters **104** (2010), [10.1103/PhysRevLett.104.184502](#).
- [44] A. Peshkov, I. S. Aranson, E. Bertin, H. Chaté, and F. Ginelli, *Physical Review Letters* **109** (2012), [10.1103/PhysRevLett.109.268701](#).
  - [45] S. Ngo, A. Peshkov, I. S. Aranson, E. Bertin, F. Ginelli, and H. Chaté, *Physical Review Letters* **113** (2014), [10.1103/PhysRevLett.113.038302](#).
  - [46] M. Loose and T. J. Mitchison, *Nature Cell Biology* **16**, **38** (2014).
  - [47] J. Denk, L. Huber, E. Reithmann, and E. Frey, *Physical Review Letters* **116**, 178301 (2016).

# Supplemental Material: Cluster assembly kinetics and fluctuations drive polar nucleation of active polymers

Lorenz Huber, Timo Krüger, and Erwin Frey\*

*Arnold Sommerfeld Center for Theoretical Physics (ASC) and Center for NanoScience (CeNS),  
Department of Physics, Ludwig-Maximilians-Universität München, Theresienstrasse 37, 80333 München, Germany*

## WASP SIMULATIONS

In the following, we discuss the details of the implementation of the agent-based simulations of **Weakly-Aligning Self-propelled Polymers** (WASP's). For a rigorous description please also refer to the Supplemental material of Ref. [1].

### Model

We describe a system of  $M$  polymers, where every polymer has a length  $L$  and a width  $d$  and is modeled as a discrete, slender chain of  $N - 1$  cylinders, connected by  $N$  spherical joints. In this way, every point along the contour has a well-defined, smooth surface and tangential direction, reducing artificial friction effects due to the discretization which are present in bead-spring-like representations [2]. Polymers perform a trailing motion, meaning that only its tip is allowed to change direction while its tail may only follow in the direction tangential to the contour line. This resembles the typical situation of experimental motility assays, where filaments are pinned to motor proteins and motion orthogonal to the contour is suppressed [3, 4]. The tip of a polymer performs a persistent random walk due to orientational diffusion, and changes direction due to local alignment interaction upon collision with other polymers. The equations of motion for the tip of a polymer  $n$  read:

$$\frac{\partial}{\partial t} \mathbf{r}_0^{(n)} = v \mathbf{u}_0^{(n)} = v \begin{pmatrix} \cos \theta_0^{(n)} \\ \sin \theta_0^{(n)} \end{pmatrix}, \quad (\text{S1})$$

$$\frac{\partial}{\partial t} \theta_0^{(n)} = -\frac{\delta H_0^{(n)}}{\delta \theta_0^{(n)}} + \sqrt{\frac{2v}{L_p}} \xi^{(n)}, \quad (\text{S2})$$

where  $\mathbf{r}_0^{(n)}$  is the position and  $\mathbf{u}_0^{(n)}$  the director of the tip,  $v$  the (constant) velocity,  $L_p$  the persistence length of the path.  $\xi^{(n)}$  is an angular random white noise with zero mean and unit variance, and  $H_0^{(n)} = \sum_{m,j} U_{m,j}^{(n)}$  is the total sum of all alignment potentials that are present at the tip, running over all filaments  $m$  and respective contours  $j$ . Every potential is a smooth ramp which is only present in the area covered by a polymer, and has

the form:

$$U_{m,j}^{(n)} = C \left( \left| \mathbf{r}_0^{(n)} - \mathbf{r}_j^{(m)} \right|_{shDist} \right) \times [A_p(\theta_0^{(n)} - \theta_j^{(m)}) + A_n(\theta_0^{(n)} - \theta_j^{(m)})] \quad (\text{S3})$$

with the polar and nematic terms

$$A_p(\theta) = -\frac{\varphi_p v}{d} \cos \theta, \quad A_n(\theta) = -\frac{\varphi_n v}{d} \cos 2\theta, \quad (\text{S4})$$

and

$$C(x) = \begin{cases} 0 & \text{for } x > d \\ (d-x)/d & \text{else} \end{cases}, \quad (\text{S5})$$

being a linear ramp that smoothly increases interaction strength. The amplitudes  $\varphi_{p,n}$  are scales of the typical angular displacement upon a single collision. In Eq. (S3)  $|\dots|_{shDist}$  denotes the shortest possible distance between the tip position and the contour of an adjacent polymer. In this way, alignment of filaments strictly takes place only upon point contact, which allows to resolve collisions on the smallest scales without needing some spatial averaging procedure like in Vicsek-type models [5–7]. In contrast to the motion of the tip, tail cylinders only follow their front neighbor, parallel the contour line. This then reads

$$\frac{\partial}{\partial t} \mathbf{r}_i^{(n)} = K_s \frac{\mathbf{u}_{i-1}^{(n)} + \mathbf{u}_i^{(n)}}{2} \left( \left| \mathbf{r}_i^{(n)} - \mathbf{r}_{i-1}^{(n)} \right| - \frac{L}{N-1} \right), \quad (\text{S6})$$

where  $K_s$  is a sufficiently strong spring constant ( $K_s \gg 1$ ) that maintains a constant cylinder length of  $\frac{L}{N-1}$ . The directors of tail cylinders  $\mathbf{u}_i^{(n)}$  are given by the renormalized connecting vector  $\mathbf{r}_{i-1}^{(n)} - \mathbf{r}_i^{(n)}$ . To avoid the accidental and unphysical fixed point when too many filaments overlap at a single point and get trapped by diverging alignment torques, we added a very weak repulsion force  $-s \frac{\partial H_0^{(n)}}{\partial \mathbf{r}_0^{(n)}}$  with a small amplitude  $s \ll 1$  to Eq. (S1) acting only on tips and being proportional to the sum of all linear ramps [Eq. (S5)] which did not change the phenomenology.

Note that primary parameters that tune the interaction are the alignment amplitudes  $\varphi_p$ ,  $\varphi_n$ , which allow for a and independent, continuous variation of the preferences to align in a polar or nematic fashion. As was shown in Ref. [1], this allowed for the large-scale formation of both

polar and nematic patterns. To yield a proper comparison, we also adapted the convention of  $\alpha = \varphi_n / \varphi_p$  being the relative alignment strength, which, for low  $\varphi_n$ , also promotes polar nucleation.

### Implementation and Parameters

Computationally, we integrate the dynamics by a straight-forward Euler algorithm, which was implemented in C++ using a heavily parallelized architecture in OpenMP. Maximal performance of the simulation was provided by employing a cell algorithm and corresponding Verlet lists [8] to exploit the local nature of filament interactions. This implementation allowed for optimal scaling of simulation times with particle number, and we were able to achieve large simulation times for systems of more than  $\mathcal{O}(10^6)$  discretized polymers using a single 32-core CPU. Throughout this work and if not stated otherwise, we fixed many parameters similar to [1]: filament aspect ratio  $L/d = 21$ , discretization  $N = 5$ , persistence length  $L_p = 31.75L$ , and velocity  $v = 1$ . The polar alignment strength remained fixed  $\varphi_p = 0.036 \approx 2.1^\circ$  similar to the scenario of colliding actin filaments [4]. We used a system of  $10^4$  polymers and a periodic simulation box of length  $L_{box} = 81.3L$  with random initial conditions. Note that all simulation times are given in units of the longest single filament correlation time  $L_p/v$ . The cluster cut-off parameter is set to  $\gamma = (L - d)/N$  corresponding to the length of the discretized cylinder within a polymer. For the phase diagram of excitability in Fig. 3(b), the maximal simulation time was fixed to  $t_{max} = 50$ ; systems that nucleated within this time without external cluster insertion were termed as 'spontaneously nucleated'.

### Cluster-Order Representation and Order Parameters

A subsequent simulation times we decomposed the system of polymers into clusters of close-by or overlapping objects. Practically, we calculated all distances between adjacent polymers and assigned them to the same cluster if this distance was  $< L/(N - 1)$ , accepting a small error for the fate of numerical performance (if  $N$  is not too small).

To correctly calculate the net cluster (polar) order  $\pi(k)$  the value of the expected random deviation  $\Delta_k$  needs to be calculated. Given a filament cluster of size  $k$  with uniformly random orientations  $U_j \in [-\pi; \pi]$ , and the shortcut notation  $\delta_m^n = U_m - U_n$ , and  $\sum_{m=1}^k \sum_{n=m+1}^k =$

$$\begin{aligned} & \sum_{(m,n)}, \\ \Delta_k &= \frac{1}{k} \langle |\sum_{j=1}^k e^{iU_j}| \rangle = \frac{1}{k} \langle \sqrt{k + 2 \sum_{(m,n)} \cos \delta_m^n} \rangle \\ &= \frac{1}{k} \langle \sqrt{k} + \frac{1}{\sqrt{k}} \sum_{(m,n)} \cos \delta_m^n - \frac{1}{2k^{3/2}} \sum_{(m,n)} \cos^2 \delta_m^n \\ & \quad + \frac{1}{2k^{5/2}} \sum_{(m,n)} \cos^3 \delta_m^n + \mathcal{O}(k^{-3/2}) \rangle. \end{aligned} \quad (\text{S7})$$

It can be straightforwardly shown that  $\langle \cos^2 \delta_m^n \rangle = \frac{1}{2}$ . Since  $\langle \cos^j \delta_m^n \rangle = 0$  for  $j$  odd, Eq (S7) can be further reduced to

$$\begin{aligned} \Delta_k &= \frac{1}{\sqrt{k}} \left( 1 - \frac{(k-1)}{8k} \right) + \mathcal{O}(k^{-5/2}) \\ &= \frac{1}{\sqrt{k}} \left( \frac{7}{8} + \frac{1}{8k} \right). \end{aligned} \quad (\text{S8})$$

This first-order correction is close to the typical scaling of mean value deviation  $\propto k^{-1/2}$ .

From the individual values of  $\pi(k)$  one can construct the cluster order parameter  $\Omega_p$  and compare it with the standard global polar order parameter  $\mathcal{P} = \langle |e^{i\theta}| \rangle$  which is averaged over all filament orientations irrespective of clusters, which is shown in Fig. S1(a). While both curves correlate to a great extent, there are differences: in the disordered phase  $\Omega_p$  still displays a nonzero value stemming from small average polarity of underlying clusters, which is averaged out by the definition of  $\mathcal{P}$ . In the nucleated phase,  $\Omega_p$  is lower than  $\mathcal{P}$  due to the negligence of individual, ordered filaments (since  $\pi(1) = 0$ ). It should be noted that one can also assign nematic order parameters for both clusters and global values,  $\Omega_n$  and  $\mathcal{N}$ , by just replacing every angle  $\theta$  by  $2\theta$ . Since, however, the nematic order parameter is slaved to the polar order, it is of minor relevance for our analysis.

In Fig. S1(b) we tracked the maximal polarity of the cluster population,  $S_{max} = \max_{\{c\}} S = \max_{\{c\}} p k$ , during nucleation. As can be seen,  $S_{max}$  is relatively good measure for the earliest stages of flocking: large polarity of clusters is suddenly sparked by random fluctuations; when it is not large enough ( $\lesssim S_{crit}$ ), it decays back to a smaller value (see marked events in Fig. S1(b)); when it is sufficiently large, it strongly grows even earlier than  $\Omega_p$ . Hence, whenever one would find that, in a disordered system,  $S_{max} \gg S_{crit}$ , it undergoes polar nucleation. It should be noted that the exact value of  $S_{crit}$  should, here ( $\alpha = 2$ ), be rather takes as a reference line. This is because we estimated  $S_{crit} \approx 90$  from the cluster stability analysis in Fig. S3 at  $\alpha = 1.5$  which is much less likely interfered by spontaneous nucleation. In addition, corrections to the simple transition criterion are expected for different cluster sizes.

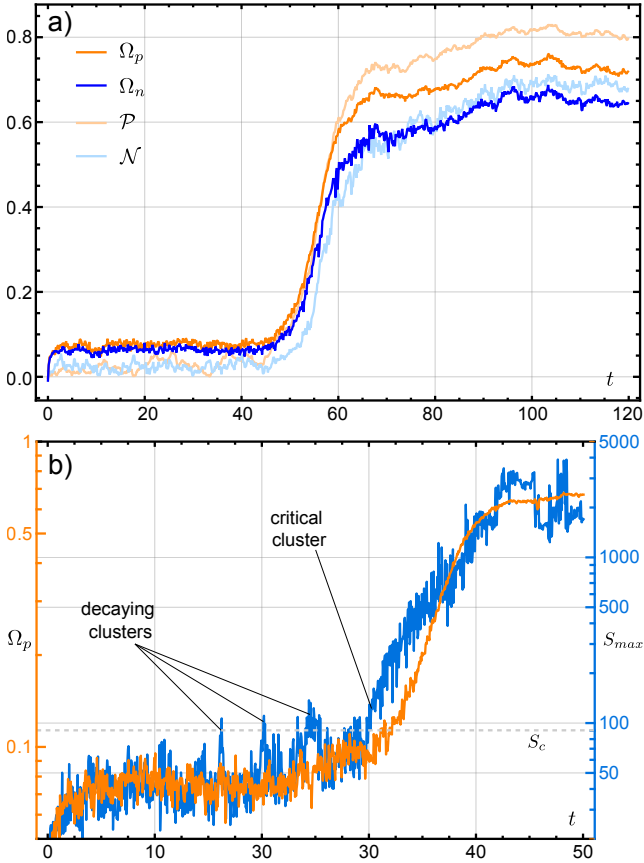


FIG. S1. (a) Evolution of various order parameters for the simulation shown in Fig. 1(b). (b) Comparison of the evolutions of  $\Omega_p$  (orange) and  $S_{max}$  (blue). The dashed gray line indicates  $S_{crit} = 110$ . Parameters for (a,b) are identical to Fig. 2, with different random initial conditions for (a) and (b).

### Time Scale Analysis

As described in the main text, we obtained the initial burn-in time  $\nu$ , the dwell time  $t_d$ , and growth time  $\tau$  by fitting a piecewise function of the form

$$f(t) = \begin{cases} a \frac{t}{t+\nu(1/a-1)} & t < \nu \\ a & \text{for } \nu < t < t_d \\ a \exp[(t-t_d)/\tau] & \text{else} \end{cases} \quad (\text{S9})$$

to the evolution of  $\Omega_p(t)$  until  $\Omega_p(t) > 0.5$ . It should be noted that the functional form for  $t < \nu$  could also be chosen differently, as long as it captures the time scale  $\nu$  upon which  $\Omega_p$  becomes metastable. In addition to Fig. 2(d), we also probed the system size dependence of  $t_d$  in Fig. S2(a) and found that  $\langle t_d \rangle$  scales inversely with the area of the system. This favors the intuitive assumption that critical fluctuations occur independently in adjacent parts of the system, hence in larger systems one has to wait less for nucleation. The constant value of the growth time  $\tau \approx 4.5$  confirms the observation of ex-

ponential cluster growth for a large range of system sizes. Note that this power-law decrease in  $\langle t_d \rangle$  competes with the exponential increase of  $\langle t_d \rangle$  as a function of parameter distance to the purely polar region in Fig. 3(a). The thermodynamic limit is hence peculiar, and depends on the behavior of the parameter regions where nucleation times are far beyond numerically accessible simulation times, i.e. nucleation virtually never occurs. It is possible that  $t_d$  truly diverges here for any finite system size. We also recorded the statistics of nucleation times  $p(t_d)$  at one point in parameter space in Fig. S2(b). Similar to other classical nucleating systems, this exhibits an exponential distribution of times.

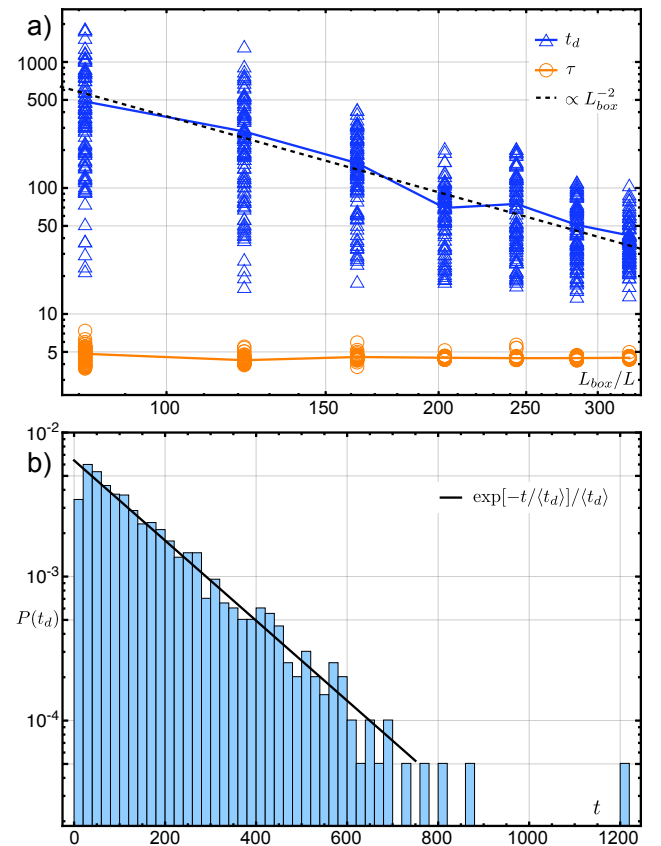


FIG. S2. (a) Time scale analysis of waiting times  $t_d$  and growth times  $\tau$  as a function of the system size  $L_{box}$  in units of the polymer length  $L$ . Solid lines denote average values (taken over 90-100 independent simulations at each point), the black dashed line shows a scaling law proportional to the area of the system. (b) Waiting time probability density  $P(t_d)$  taken over an ensemble of 1000 simulations. The black solid line depicts an exponential approximation. Parameters:  $\rho L^2 = 1.51$ ,  $\alpha = 1.583$  for (a) and  $\alpha = 1.67$ ,  $L_{box} = 81.3L$  for (b).

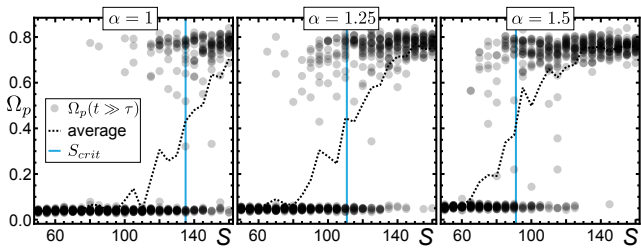


FIG. S3. Cluster stability analysis as a function of the perturbing cluster size  $\tilde{k} = S$  for different values of  $\alpha$ . Gray circles denote the final order  $\Omega_p$  of single trajectories, with the dashed line being the average. Vertical blue lines depict the approximate values for the critical polarity  $S_{crit}$ .  $\rho L^2 = 1.51$ .

### Cluster Stability Analysis

As mentioned in the main text, we probed the stability of the disordered state by inserting perfectly ordered clusters of size  $\tilde{k}$  (and hence polarity  $S = \tilde{k}$ ) into the systems, sufficiently long after initialization at time  $t = 5 > \nu$  and while keeping the overall density constant. This was achieved by randomly extracting  $\tilde{k}$  filaments, redirecting them in the same direction and placing them back into the system, tightly stacked in transversal direction with a distance  $d$ . We then tracked the evolution order parameter  $\Omega_p$  until  $t = 50$ . Fig. S3 shows the statistics of the analysis as a function of  $\tilde{k}$ , for three different values of  $\alpha$ . Note that for these examples, the values of  $S_{crit}$  are small compared to the total number of filaments, despite the corresponding nucleation times  $t_d$  being extremely large  $t \gg 10^3$ . Due to the finite width of the sigmoidal shape in Fig. S3,  $S_{crit}$  is by itself a stochastic variable that does not guarantee nucleation.

### Steady-State Flow of the Flocking State

In order to assess the steady state particle current in cluster space as shown in Fig. 5(c), we have investigated the exchange of filaments between different cluster size-order groups in the WASP simulations. Unlike as in the kinetic model, WASP clusters can have any order  $p$ . Thus, for proper comparison, the size-order space was first divided ad hoc into two regions, a polar and a disordered one, respectively. The heuristic separation line is shown in Fig. 5(d). All clusters above the dividing line are defined as polar for our analysis, all clusters below as unordered. For any point  $(k, p)$  in the polar (unordered) region, we counted all filaments going from this point into the unordered (polar) region of the size-order space, resulting in the particle current  $j^{P \rightarrow U}(k, p)$  ( $j^{U \rightarrow P}(k, p)$ ). For the data in Fig. 5(d) this was done for a system in the steady ordered state, over a time of  $\Delta t = 50$  and by averaging over 30 realizations. Furthermore, we mapped out the remaining dependence on the cluster polar order

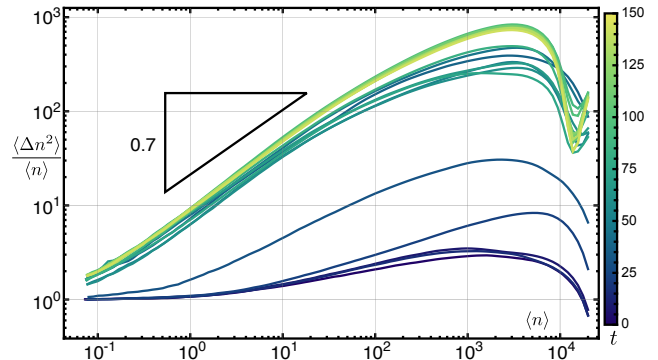


FIG. S4. Evolution of the rescaled number fluctuations  $\langle \Delta n^2 \rangle / \langle n \rangle$  as a function of  $\langle n \rangle$ . Different colors correspond to different simulation times. The black triangle denotes a scaling exponent of 0.7. Parameters and data are identical to Fig. 2(a-c).

$p$  by integrating  $\int j^{P \rightarrow U}(k, p) dp$  over the polar domain, and  $\int j^{U \rightarrow P}(k, p) dp$  over the unordered domain, resulting in an effectively one-dimensional exchange flux (inset of Fig. 5(d)). The curve for the current into the ordered phase agrees well with the results of the kinetic model at a qualitative level. The apparent difference between the currents into the disordered regions stems from the fact that, in contrast to the kinetic model, the smallest clusters in the agent-based simulations can only be classified as either ordered or unordered (e.g. a single filament must be ad hoc defined as ordered or unordered).

### Complementary Observations

#### Number Fluctuations

In addition to the analysis shown in Figs. 2-3, we also investigated different aspects of the evolution and structure formation. We calculated the number fluctuations  $\langle \Delta n^2 \rangle = \langle n^2 \rangle - \langle n \rangle^2$  as a function of the average number of particles within a certain area  $\langle n \rangle$  during the evolution towards a fully nucleated state [Fig. S4]. As can be seen, even in the initially disordered domain giant number fluctuations, scaling faster than  $\langle n \rangle$ , are present at mesoscopic scales. Although intrinsic mechanisms can hardly be deduced from  $\langle \Delta n^2 \rangle$ , one can see that during nucleation giant fluctuations conquer all length scales successively, leaving an anomalous scaling behavior with an exponent of roughly 1.7, similar to other flocking active matter systems [9].

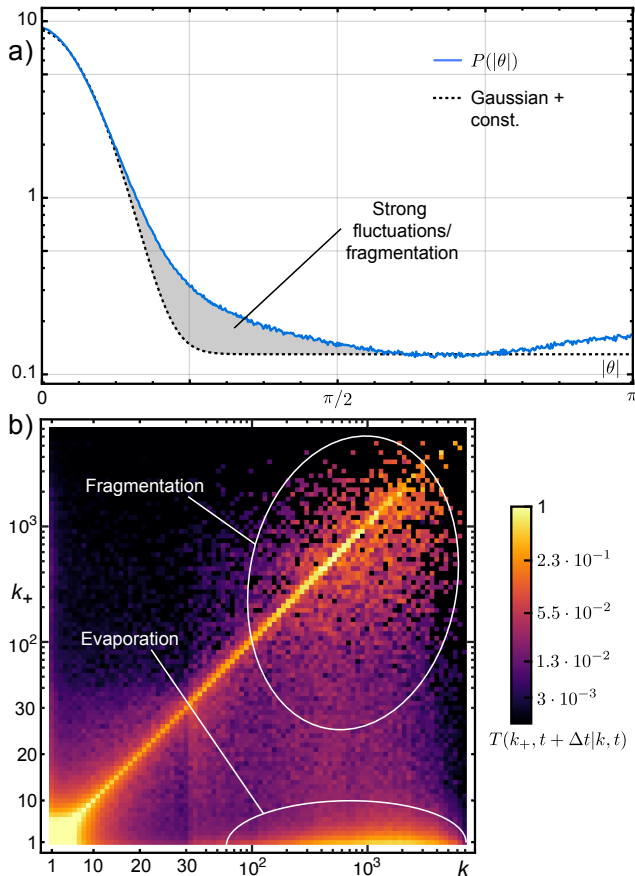


FIG. S5. (a) Probability density  $P(|\theta|)$  of angular orientations  $\theta$  relative to the dominant direction in the stationary nucleated phase. The dashed curve corresponds to a simple Gaussian approximation of polar orientations, embedded by uniform random orientations from the disordered regions. The gray region marks the deviation from this approximation. Parameters and data are identical to Fig. 2. (b) Transition matrix  $T(k_+, t + \Delta t | k, t)$  with  $\Delta t = 0.0125$ . As a guide to the eye, regions with dominant fragmentation or evaporation are encircled in white. Parameters:  $\rho L^2 = 1.51$ ,  $\alpha = 1.67$ .

#### Particle scattering between clusters

As it was argued in the main text and Fig. 2(a), once a nucleating cluster has emerged the polar phase grows exponentially fast until the majority of filaments remain within extremely ordered clusters. This coarsening dynamics is not similar to classical nucleation processes of slow domains where one would rather expect some kind of power law, since growth of one phase can only occur via a domain interface and is limited by a finite mass transport capacity. For our active system, we argue following process: a single cluster accumulates mass very fast and quickly forms a spreading polar front. This front is not compact and stable, but will quickly split up with fragments traveling into different directions. Due to this 'splay' in motion, the fragments can by themselves again

quickly accumulate filament mass. In this way, a self-replication is realized and exponential growth will prevail until a large fraction of space is occupied with polar clusters. In the data this can be seen in the stationary distribution of orientation angles in the polar phase, showing large fluctuations in its tails which correspond to individual clusters trying to split up from the global front direction [Fig. S5(a)]. Furthermore, one can track the scattering of individual particles from clusters of different size at stationarity. The transition probability  $T(k_+, t + \Delta t | k, t)$  quantifies which fraction of filaments of a cluster  $k$  at time  $t$  scatter into a cluster of size  $k_+$  at time  $t + \Delta t$ , and it is normalized such that  $\sum_{k_+} T(k_+, t + \Delta t | k, t) = k \cdot c(k)$ . For  $\Delta t \rightarrow 0$ , this transition probability will just be a diagonal  $T(k_+, t | k, t) = \delta_{k_+, k} k c(k)$  while for  $\Delta t \rightarrow \infty$ , the distribution in  $k_+$  will be independent in to first cluster size  $k$ , i.e.  $T(k_+, \infty | k, t) = k_+ c(k_+) k c(k)$ . Hence we recorded  $T(k_+, t + \Delta t | k, t)$  for sufficiently small  $\Delta t = 0.0125$  in Fig. S5(b) to observe short-time processes. It can be seen that, while most clusters remain stable during this time (signal along diagonal), especially large polar clusters either frequently fragment or coalesce into similarly sized clusters (bright off-diagonal events in the upper right of Fig. S5(b)), or evaporate very small clusters or single filaments (bottom right signal in Fig. S5(b)). This supports the implementation of corresponding transition rates in the kinetic model Eqs. (S12, S13).

## KINETIC NUCLEATION MODEL

### Equations

The evolution of the distributions for the unordered species  $a$  and the ordered species  $b$  is given by:

$$\dot{\mathbf{a}} = \mathbf{F}(\mathbf{a}, \mathbf{b}) \quad (\text{S10})$$

$$\dot{\mathbf{b}} = \mathbf{G}(\mathbf{a}, \mathbf{b}) \quad (\text{S11})$$

where the current vectors  $\mathbf{F} = (F_1, F_2, \dots, F_M)^T$  and  $\mathbf{G} = (G_1, G_2, \dots, G_M)^T$  incorporate all possible reaction channels:

$$\begin{aligned} F_1 &= 2\beta_2 a_2 + \sum_{i=3}^M \beta_i a_i - \sum_{i=1}^{M-1} \alpha_{i,1} a_i a_1 \\ &\quad + \lambda(2b_2 + \sum_{i=3}^M b_i) - \sum_{i=2}^{M-1} \gamma_{i,1} b_i a_1, \\ F_k &= \beta_{k+1} a_{k+1} - \beta_k a_k + \frac{1}{2} \sum_{i=1}^{k-1} \alpha_{i,k-i} a_i a_{k-i} \\ &\quad - \sum_{i=1}^{M-k} \alpha_{i,k} a_i a_k - \sum_{i=2}^{M-k} \gamma_{i,k} b_i a_k - \omega_k a_k, \end{aligned} \quad (\text{S12})$$

and

$$\begin{aligned}
G_1 &= 0, \\
G_k &= \lambda(b_{k+1} - b_k) - \sum_{i=2}^{M-k} \eta_{i,k} b_i b_k \\
&+ \frac{1}{2} \sum_{i=2}^{k-2} \eta_{i,k-i} b_i b_{k-i} + \mu \left( \sum_{i=2}^{M-k} b_{i+k} - \frac{1}{2} \sum_{i=2}^{k-2} b_k \right) \\
&+ \sum_{i=2}^{k-1} \gamma_{i,k-i} b_i a_{k-i} - \sum_{i=1}^{M-k} \gamma_{k,i} b_k a_i + \omega_k a_k, \quad (\text{S13})
\end{aligned}$$

with  $k \in \{2, \dots, M\}$ . Note that by convention, summation over non-positive indices gives zero contribution. It can be straightforwardly checked that these currents conserve particle mass  $\sum_{k=1}^M k(F_k + G_k) \equiv 0$ .

In the main text, we introduced generic size factors for the coagulation rates:  $\alpha_{i,j} := v\sigma_{aa}X_{aa}(i,j)/A$ ,  $\eta_{i,j} := v\sigma_{bb}X_{bb}(i,j)/A$ ,  $\gamma_{i,j} := v\sigma_{ab}X_{ab}(i,j)/A$ ; the fragmentation rate:  $\mu_{i,j} = \mu_0$ ; the evaporation rates:  $\beta_i := \beta_0 Y_a(i)$ ,  $\lambda_j := \lambda_0 Y_b(i)$ ; and the nucleation rate:  $\omega_j := \omega_0 Z(i)$ . From observations of WASP simulations we introduced simple, heuristic assumptions on the size factors  $X_{\bullet,\bullet}$ ,  $Y_{\bullet}$ ,  $Z$ : a disordered cluster of size  $i$  has approximately spherical shape with a diameter and circumference  $\propto \sqrt{i}$  leading to  $X_{a,a}(i,j) = \sqrt{i} + \sqrt{j}$  and  $Y_a(i) = \sqrt{i}$ , respectively; ordered clusters, however, are more line-shaped with a diameter of  $\propto i$ , hence  $X_{b,b}(i,j) = i + j$ . They evaporate particles mainly via its edges, i.e. there is no size dependence, resulting to  $Y_b(i) = 1$ . Furthermore, when colliding with unordered clusters, we assume that scattering is mainly dominated by the ordered cluster and its size  $i$ , i.e.  $X_{a,b}(i,j) = i$ . Since nucleation was observed to take only place for larger cluster sizes,  $Z(i) := 1/(1 - e^{-(i-m_c)/v_c})$  is assumed to be of sigmoidal shape with a characteristic size  $m_c = 100$  and a width  $v_c = 10$ , which we fixed, for simplicity, throughout the analysis. Note that a variation of  $m_c$  or  $v_c$  resulted only in a shifted onset of the order transition, without a qualitative difference in the ordered state.

### Implementation

We integrated Eqs. (S12, S13) using a straightforward Euler scheme in C++, which, for system sizes  $M \lesssim 1000$ , we found to be numerically faster than an adaptive time-step 4th-order Runge-Kutta algorithm and much simpler than implicit integration schemes, which we expect to be more stable for larger  $M$ .

To complement Eqs. (S12, S13), please note that the boundary terms of species  $a$  and  $b$  are constrained by the domains of existence for the rates, that is, all rates are equal to zero when the indices for species  $a$  are less than 1 and larger than  $M$ , or less than 2 and larger than  $M$  for the indices of species  $b$ . Note that we have assumed that

clusters of size 1 are always disordered, i.e.  $b_1 = \dot{b}_1 = 0$ . As mentioned in the main text, we fixed the model parameters to  $M = 400$ ,  $A = 800$ ,  $v = b_0 = \lambda = 1$ ,  $\mu = 0.025$ ,  $\sigma_{aa} = 1.6$ ,  $\omega_0 = 10^{-4}$ , if not stated otherwise.

### Dynamical and Steady-State Properties

Fig. S6 shows the evolution of individual distributions  $a_k$ ,  $b_k$  over time, for the parameters and data shown in Fig. 4 ( $\sigma_{ab} = 0.2$  and  $\sigma_{bb} = 1$ ). It can be seen that there is little change at intermediate times, and that the dynamics only speeds up drastically when there is a significant fraction of  $b$  clusters.

To estimate the degree of system size dependence, we

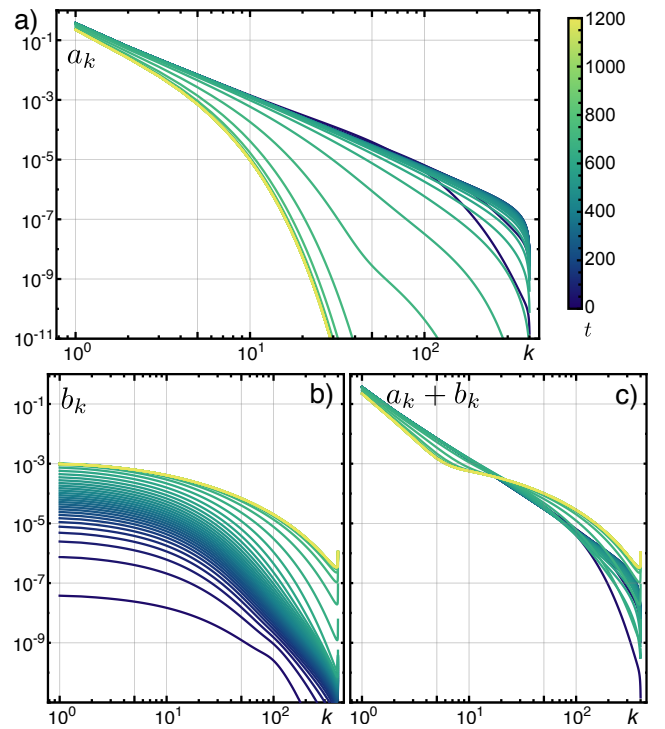


FIG. S6. Evolution of cluster species distributions: (a) disordered species  $a_k$ , (b) ordered species  $b_k$ , and (c) sum of both  $a_k + b_k$ .

varied  $M$  and  $A$  simultaneously while  $\rho = M/A = 0.5$ . As can be seen in Fig. S7, there is little change in the mass fractions and distributions (apart from some artefacts at the maximal cluster boundary) which become quickly stationary.

The inter-species fluxes of the mass,  $J_k^{(b \rightarrow a)}$  and  $J_k^{(a \rightarrow b)}$ ,

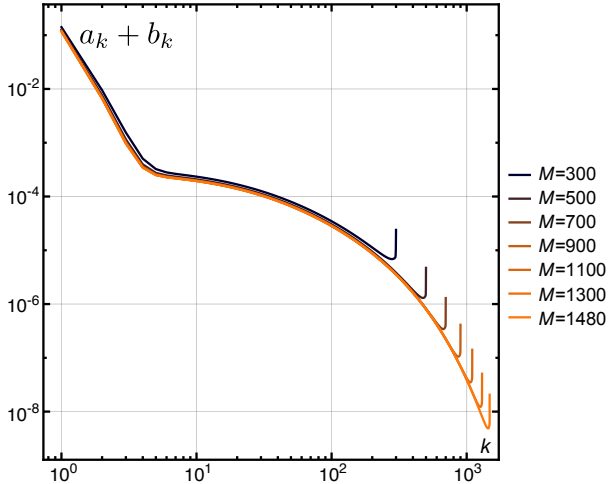


FIG. S7. Stationary total cluster distribution  $a_k + b_k$  as a function of the system size  $M$ . Parameters:  $\sigma_{aa} = 1.4$ ,  $\sigma_{ab} = 0.2$ ,  $\sigma_{bb} = 0.8$ ,  $q_0 = 0.01$ .

as depicted in Fig. 5(c), are given by:

$$J_1^{(b \rightarrow a)} = \lambda(2b_2 + \sum_{i=3}^M b_i) - \sum_{i=2}^{M-1} \gamma_{i,1} b_i a_i,$$

$$J_k^{(b \rightarrow a)} \stackrel{k \geq 1}{=} k \cdot \left( - \sum_{i=2}^{M-k} \gamma_{i,k} b_i a_k - \omega_k a_k \right), \quad (\text{S14})$$

and

$$J_k^{(a \rightarrow b)} \stackrel{k \geq 1}{=} k \cdot \left( \lambda(b_{k+1} - b_k) + \sum_{i=2}^{k-1} \gamma_{i,k-i} b_i a_{k-i} - \sum_{i=1}^{M-k} \gamma_{k,i} b_k a_i + \omega_k a_k \right), \quad (\text{S15})$$

which is analogous to the rates  $\dot{a}_k$ ,  $\dot{b}_k$  with all species-internal rates set to zero. To complement Fig. 5(c), Fig. S8 shows the individual contributions proportional to  $\lambda$ ,  $\gamma_{i,k}$ , and  $\omega_k$ , respectively. From Eq. (S14) it is obvious that species  $a$  only gains by evaporation of ordered clusters into single, disordered filaments. In contrast, species  $b$  gains cluster mass by coalescence of smaller ordered and unordered clusters, transferring it to large cluster sizes, which is only balanced by filament evaporation.

### Parameter Space and Hysteresis

The stability diagram Fig. 4(d,e) was obtained by starting with initial conditions  $a_k(t=0) = \delta_{1,k}$ ,  $b_k(t=0) = 0$  for the lower branch [Fig. S9(a)] and a set of stationary,  $b$ -dominated distributions  $a_k(t=0)$ ,  $b_k(t=0)$  for the upper branch [Fig. S9(b)]. The corresponding hysteresis in Fig. 4(e) was obtained by subtracting these

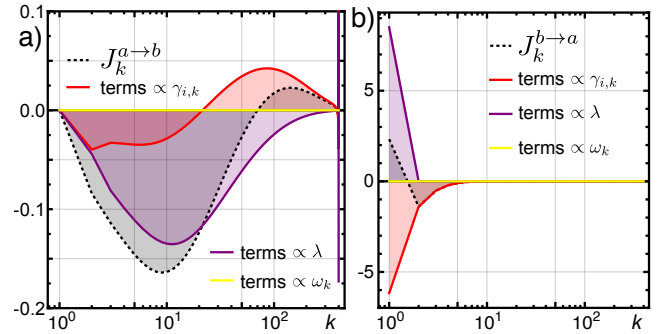


FIG. S8. Stationary inter-species particle fluxes  $J_k^{(a \rightarrow b)}$  (a) and  $J_k^{(b \rightarrow a)}$  (b) and individual rate contributions as a function of cluster size  $k$ . Parameters and data identical to Fig. 4.

stationary masses. In addition to the phase space of varying  $\sigma_{ab}$  and  $\sigma_{bb}$ , we also performed this procedure for varying  $\rho = M/A$  and  $\sigma_{bb}$  in Fig. S10, since particle density another relevant control parameter of active matter systems like in the WASP simulations. Again, a discontinuity and hysteresis is observed for varying density. Similar to Fig. 4(d,e), the appearance of a bifurcation point seems to be primarily determined by the scattering amplitude  $\sigma_{bb}$ .

To visualize how of mass flux  $J_k^{(a \rightarrow b)}$  are affected by

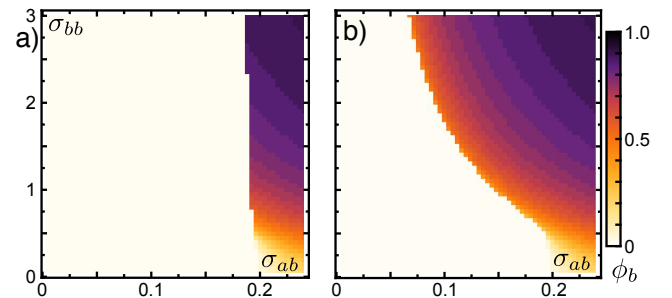


FIG. S9. Density plot of the stationary mass fraction  $\phi_b$  as a function of  $\sigma_{ab}$  and  $\sigma_{bb}$  with different initial conditions: (a) dominated by  $a$  clusters, and (b) dominated by  $b$  clusters. Parameters and data identical to Fig. 5(d,e).

different parameters and the presence of the instability, we recorded them while varying the parameters in Figs. S11. The amplitude of  $J_k^{(a \rightarrow b)}$  is minimal in the disordered,  $a$ -dominated phase, become strong in the ordered,  $b$ -dominated phase, and is maximal close to the transition. As expected, below the bifurcation point the fluxes vary quickly, but continuously, while they become discontinuous above.

It should be noted that we also varied different parameters like  $\lambda$ ,  $\mu$ ,  $\sigma_{aa}$ , and  $\omega_0$ , and found no qualitatively different behavior. As elaborated by the authors of Refs [10],  $\sigma_{aa}$ ,  $\beta_0$  and their ratio determine the shape of the distribution  $a_k$  in the absence of species  $b$  and ex-

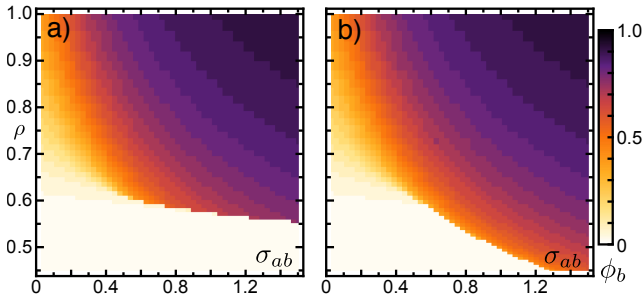


FIG. S10. Density plot of the stationary mass fraction  $\phi_b$  as a function of  $\sigma_{bb}$  and the density  $\rho$  with different initial conditions: (a) dominated by  $a$  clusters, and (b) dominated by  $b$  clusters. Parameters:  $\sigma_{aa} = 1.8$ ,  $\sigma_{ab} = 0.15$ ,  $\omega_0 = 10^{-3}$ .

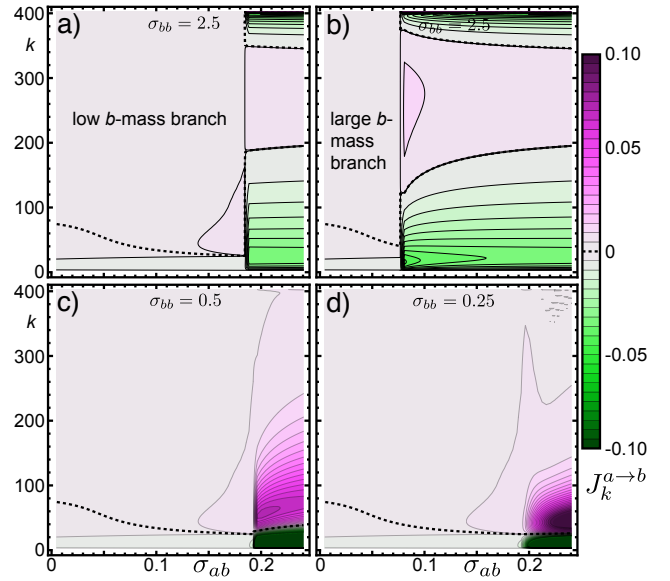


FIG. S11. Contour maps of the flux  $J_k^{(a \rightarrow b)}$  as a function of  $k$  and  $\sigma_{ab}$  at different points in parameter space,  $\sigma_{bb} = 2.5$  (a,b),  $\sigma_{bb} = 0.5$  (c), and  $\sigma_{bb} = 0.25$  (d). Above the bifurcation point at  $\sigma_{bb} \approx 0.5$ , two branches are present (a,b). Parameters and data identical to Fig. 5(d,e).

hibits a critical transition from a unimodal to a bimodal distribution. For our system, we took parameter such that they are always below this point to avoid structure formation in this domain.

\* [frey@lmu.de](mailto:frey@lmu.de)

- [1] L. Huber, R. Suzuki, T. Krüger, E. Frey, and A. R. Bausch, *Science* **361**, 255 (2018).
- [2] M. Abkenar, K. Marx, T. Auth, and G. Gompper, *Physical Review E* **88**, 062314 (2013).
- [3] V. Schaller, C. Weber, C. Semmrich, E. Frey, and A. R. Bausch, *Nature* **467**, 73 (2010).
- [4] R. Suzuki, C. A. Weber, E. Frey, and A. R. Bausch, *Nature Physics* **11**, 839 (2015).
- [5] T. Vicsek, A. Czirók, E. Ben-Jacob, I. Cohen, and O. Shochet, *Physical Review Letters* **75**, 1226 (1995).
- [6] S. Ngo, F. Ginelli, and H. Chaté, *Physical Review E* **86** (2012), 10.1103/PhysRevE.86.050101.
- [7] K. H. Nagai, Y. Sumino, R. Montagne, I. S. Aranson, and H. Chaté, *Physical Review Letters* **114** (2015), 10.1103/PhysRevLett.114.168001.
- [8] D.-B. Wang, F.-B. Hsiao, C.-H. Chuang, and Y.-C. Lee, *Computer Physics Communications* **177**, 551 (2007).
- [9] J. Deseigne, O. Dauchot, and H. Chaté, *Physical Review Letters* **105** (2010), 10.1103/PhysRevLett.105.098001.
- [10] F. Peruani and M. Bär, *New Journal of Physics* **15**, 065009 (2013).

## MOVIE DESCRIPTIONS

**movie1.mov:** Time evolution from an initially disordered system to a nucleated state.

## 2 Robustness of the Vicsek ordering paradigm

### 2.1 Background

In this section we aim to address the basic issue whether the phenomenology of the original Vicsek model is sufficient to qualitatively understand more versatile microscopic active models with polar alignment. In particular, these questions are:

1. Is the phase transition from disorder to polar order universal?
2. How generic is the Vicsek ordering paradigm (VOP)<sup>3</sup>?
3. Can we identify generic criteria to classify (polar order) transitions?

Concerning point 1, within the last years several authors have proclaimed the existence of a (polar) 'Vicsek universality class' [18, 19, 53, 57, 86], and suggested that most agent-based models and experiments with polar pattern formation would actually belong to this class, rendering all quantitative differences of the microscopic alignment interactions as irrelevant on macroscopic scales. However, recent studies of a model of vibrating discs by Lam et al. [38, 56] challenge this conjecture (see also below in section 2.3), posing the question exactly how generic the Vicsek behavior is for arbitrary polar alignment models.

In the following, we will first review the properties of the Vicsek ordering paradigm using the kinetic theory introduced by Bertin et al. [42, 52, 54], which constitutes a continuous mean-field version of the Vicsek model. This will in many parts repeat the analysis of section 1.3, chapter II. Then, we will sketch how to approach models with more detailed alignment interactions than the simple Vicsek collision rule, and how to continuously vary them towards physically realistic representations of microscopic models. Subsequently, we will perform a detailed bifurcation analysis of the stationary states and show that there is a whole plethora of different dynamical phenomena. In these models, Vicsek universality and the VOP *break down* as one imposes more physically reasonable alignment rules. Using a modified Vicsek model, we also show that the critical behavior is altered in agent-based simulations.

### 2.2 Revisiting the kinetic approach for the Vicsek model

As in section 1.3, chapter II, we consider a dilute system of point-like particles, which are self-propelled with a velocity  $v_0$  and subject to orientational diffusion as well

---

<sup>3</sup> Note that the VOP predicts a transition from a homogeneous, disordered phase via polar pattern formation towards a homogeneous polar phase upon changing the control parameters, as it was introduced in chapter I and the beginning of this chapter (see Fig. III.1(a,b)).

as binary collisions. We further neglect particle chirality (corresponding to  $\kappa_0 = 0$  in section 1.3, chapter II) and any higher-order collisions or correlations. Then the kinetic Boltzmann equation [42, 52, 54, 55, 78, 117, 118] for the one-particle distribution function  $f(\mathbf{r}, \theta, t)$  reads

$$\partial_t f + v_0 \mathbf{e}_\theta \cdot \partial_{\mathbf{r}} f = \mathcal{I}_d[f] + \mathcal{I}_c[f, f], \quad (\text{III.11})$$

which describes the evolution of  $f(\mathbf{r}, \theta, t)$  within a phase-space element  $d\mathbf{r} d\theta$  (see also Eq. (II.10)). Note that  $\mathbf{e}_\theta$  is the unit vector in direction  $\theta$ . As before, we can rescale the Boltzmann equation by setting the particle quantities  $d = \lambda = v_0 = 1$  without loss of generality. In Eq. (III.11) particles are subject to orientational diffusion and binary particle collisions, as given by the terms  $\mathcal{I}_d[f]$  and  $\mathcal{I}_c[f, f]$ , respectively:

$$\mathcal{I}_d[f] = \left\langle \int_{-\pi}^{\pi} d\phi f(\phi) [\delta(\theta - \phi - \eta) - \delta(\theta - \phi)] \right\rangle_{\eta}, \quad (\text{III.12})$$

$$\begin{aligned} \mathcal{I}_c[f, f] &= \left\langle \int_{-\pi}^{\pi} d\phi_1 \int_{-\pi}^{\pi} d\phi_2 \mathcal{S}(|\phi_1 - \phi_2|) f(\phi_1) f(\phi_2) \right. \\ &\quad \left. \times [\delta(\theta - \frac{1}{2}(\phi_1 + \phi_2) - \zeta) - \delta(\theta - \phi_1)] \right\rangle_{\zeta}, \end{aligned} \quad (\text{III.13})$$

where  $\mathcal{S}(\psi) = 4|\sin(\frac{\psi}{2})|$  is the scattering cross section for spherical particles in two dimensions. For the diffusion integral  $\mathcal{I}_d[f]$ , it is assumed that the angular noise  $\eta$  is Gaussian distributed with amplitude  $\sqrt{\text{Var}[\eta]} = \sigma_d$ . The specificities of the Vicsek collision rule are reflected in Eq. (III.13): the structure of the collision kernel  $[\delta(\theta - \frac{1}{2}(\phi_1 + \phi_2) - \zeta) - \delta(\theta - \phi_1)]$  is such that the two colliding particles align along their mean direction  $\frac{\phi_1 + \phi_2}{2}$ , irrespective of their relative orientation prior to collision,  $\phi_1 - \phi_2$ . In addition to alignment, a constant Gaussian collision noise  $\zeta$  with variance  $\sigma_c^2$  is added. For simplicity, and for the lack of any other motivation, this noise amplitude is set equal to the diffusion noise in the original description of the Vicsek model, i.e.  $\sigma_c = \sigma_d = \sigma$  [42, 52, 54]. Then, the only remaining free parameters are the noise amplitude  $\sigma$  and the mean particle density  $\bar{\rho} = A^{-1} \int_A d\mathbf{r} \int_{-\pi}^{\pi} d\theta f(\mathbf{r}, \theta, t)$ . Further progress in analyzing the Boltzmann equation (III.11) is provided by a Fourier expansion of the distribution  $f(\mathbf{r}, \theta, t)$  into its angular momenta via  $f_k(\mathbf{r}, t) = \int_{-\pi}^{\pi} d\theta e^{i\theta k} f(\mathbf{r}, \theta, t)$ , which yields

$$\partial_t f_k + \frac{1}{2} \left[ \partial_x (f_{k+1} + f_{k-1}) - i \partial_y (f_{k+1} - f_{k-1}) \right] = -(1 - \hat{P}_k(\sigma)) f_k + \sum_{n=-\infty}^{\infty} \mathcal{I}_{n,k} f_n f_{k-n}, \quad (\text{III.14})$$

with  $\hat{P}_k(\sigma) = e^{-(k\sigma)^2/2}$  and the collision integrals  $\mathcal{I}_{n,k}(\sigma)$  are given by

$$\mathcal{I}_{n,k}(\sigma) = \int_{-\pi}^{\pi} \frac{d\Delta}{2\pi} \mathcal{S}(|\Delta|) \left[ \hat{P}_k(\sigma) \cos(\Delta(n - k/2)) - \cos(\Delta n) \right], \quad (\text{III.15})$$

where the integration runs over all incoming angles  $\Delta := |\phi_1 - \phi_2|$ . For Vicsek alignment in the binary limit, Eq. (III.15) can be exactly solved:

$$\mathcal{I}_{n,k}(\sigma) = \frac{8}{\pi} \left( \hat{P}_k(\sigma) \frac{(k - 2n) \sin[(k - 2n)\pi/2] - 1}{(k - 2n)^2 - 1} + \frac{1 - 2n \sin[n\pi]}{4n^2 - 1} \right) \quad (\text{III.16})$$

In general, Eq. (III.14) constitutes an infinite hierarchy of nonlinear equations that couples all Fourier modes  $f_k$ . For  $k=0$ , Eq. (III.15) yields the continuity equation  $\partial_t \rho = -\nabla \cdot \mathbf{j}$  for the local density  $\rho(\mathbf{r}, t) := f_0(\mathbf{r}, t)$  with the particle current given by  $\mathbf{j}(\mathbf{r}, t) = v_0 (\text{Re } f_1, \text{Im } f_1)^T$ . Note that  $f_1$  is a measure of the local polarization or polar order parameter  $|f_1| = \bar{\rho} \mathcal{P}$ , and likewise is  $|f_2| = \bar{\rho} \mathcal{N}$  (recall that  $\bar{\rho}$  is the homogeneous density). The real and imaginary parts of  $f_k$  represent the contributions in x- and y-direction, respectively. Since  $\mathcal{I}_{n,0}=0$  for all  $n$ , there exists a homogeneous disordered state with  $f_0 = \bar{\rho}$  and all other  $f_k = 0$  which solves Eq. III.14 for all parameters  $\bar{\rho}$  and  $\sigma$ . To linear order, the dynamics of small perturbations  $\delta f_k$  with respect to this isotropic state is given by

$$\partial_t \delta f_k = \mu_k(\bar{\rho}, \sigma) \delta f_k \quad \text{where} \quad \mu_k(\bar{\rho}, \sigma) = (\mathcal{I}_{0,k} + \mathcal{I}_{k,k}) \bar{\rho} - (1 - \hat{P}_k(\sigma)) \quad (\text{III.17})$$

quantify the local linear stability of this state. For the Vicsek collision rule, only  $\mathcal{I}_{0,1} + \mathcal{I}_{1,1}$  and hence  $\mu_1$  can become positive for small  $\sigma$  (since  $1 - \hat{P}_k(\sigma) > 0$ ), defining a critical density at  $\mu_1(\rho_c, \sigma) = 0$ :  $\rho_1(\sigma) = \frac{\pi}{4} \lambda (1 - e^{-\sigma^2/2}) / (2e^{-\sigma^2/2} - 4/3)$  which behaves  $\propto \sigma^2$  for small  $\sigma$  and diverges for  $\sigma \rightarrow (-2 \log \frac{2}{3})^{1/2} \approx 0.9$  (Fig. III.17(a,d)).  $\rho_1(\sigma)$  can also be inverted, yielding the critical noise  $\sigma_1(\bar{\rho})$ .

Further progress to elucidate the character of this transition can be achieved by truncating the hierarchy Eq. (III.14) to only include the slow variables of the dynamics. Following Ref. [52], we assume small currents  $f_1 \ll 1$  in the vicinity of the transition and argue that  $\rho - \bar{\rho} \sim f_1$ ,  $\partial_{x/y} \sim f_1$ ,  $\partial_t \sim f_1$ ,  $f_2 \sim f_1^2$ . From this, we retain only terms up to cubic order in  $f_1$  in Eq. (III.14). After some algebra one can obtain a closed set of hydrodynamic equations for  $f_0$  and  $f_1$ , please refer to section 1.4.3, chapter II for details. First, we will focus on the solutions of the hydrodynamic equations at the homogeneous level, which read as

$$\partial_t f_1 = (\mu_1 - \xi_1 |f_1|^2) f_1 \quad (\text{III.18})$$

when spatial gradients are neglected. The coefficient of the cubic term is given by

$$\xi_1 = -\frac{\mathcal{I}_{1,2}(\mathcal{I}_{-1,1} + \mathcal{I}_{2,1})}{\mu_2}. \quad (\text{III.19})$$

The nonlinear Eq. (III.18) yields the homogeneously ordered solution

$$f_1 = \sqrt{\frac{\mu_1}{\xi_1}}, \quad (\text{III.20})$$

which is only stable above threshold  $\mu_1 > 0$  when  $\xi_1 > 0$ . As can be seen from Fig. III.17(e), indeed  $\xi_1 > 0$  everywhere along the region where also  $\mu_1 > 0$ , rendering the ordering onset to be a *supercritical* transition with a *critical exponent*  $\frac{1}{2}$ . Here, we refer to  $\mu_1$  as a *local* stability criterion since we have so far neglected the spatial gradients of Eq. (III.14). A posteriori, this justifies the assumption that polar order is small in the vicinity of the onset. It is important to emphasize that Toner and Tu postulated equations with the same cubic behavior for the slow modes of the Vicsek model, but using only symmetry arguments on the macroscopic level [50, 69].

To go beyond the vicinity of the onset, it is no longer justified to neglect the influence of higher-order modes by using weakly nonlinear assumptions (Eq. (III.18)). Therefore we have numerically solved for the homogeneous solutions  $F_k(\sigma, \vec{\rho})$  of Eq. (III.14) for large modes  $K \geq k \geq 1$  ( $K \gg 1$ ), setting all terms involving  $f_{m>K}$  to zero. See also section 1.3.3, chapter II for further details on this adaptive mode solving scheme. Here, the stationary modes  $F_k(\sigma, \vec{\rho})$  exhibit an exponential decrease as a function of  $k$  (Fig. III.17(f)), showing that the relative error of the remaining truncation scheme shrinks adiabatically for large  $K$ . However, the amplitudes of higher-order  $F_k$  also grow very strongly with the distance to the onset, which hence requires to include ever higher orders. Fig. III.17(b) shows the corresponding values of the polar order  $\mathcal{P}(\sigma, \vec{\rho}) = F_1(\sigma, \vec{\rho})/\bar{\rho}$  for different values of  $\vec{\rho}$  in comparison to the solution of Eq. (III.18). To complete the above analysis of the critical behavior for the hydrodynamic equations on more general grounds, we found that, within a reasonable range above the onset, all solutions obey the same scaling relation

$$f_1(\sigma, \vec{\rho}) \propto \bar{\rho} \cdot \Lambda\left(\frac{\sigma_1 - \sigma}{\bar{\rho}^a}\right) \quad (\text{III.21})$$

where the scaling function is given by  $\Lambda(x) = x^b$ , with the critical exponent of the Vicsek class being  $b = \frac{1}{2}$  and similarly  $a = \frac{1}{2}$  due to  $\sigma_1 \propto \sqrt{\bar{\rho}}$  for small  $\bar{\rho}$  (Fig. III.17(a)). Hence, rescaling the solutions like  $f_1(\sigma_1 - \hat{\sigma}\sqrt{\bar{\rho}}, \vec{\rho})/\bar{\rho}$  collapses all data onto a single master curve  $\Lambda(\hat{\sigma})$ , as can be seen in Fig. III.17(c).

This critical transition from disorder to polar order is the central aspect of collective

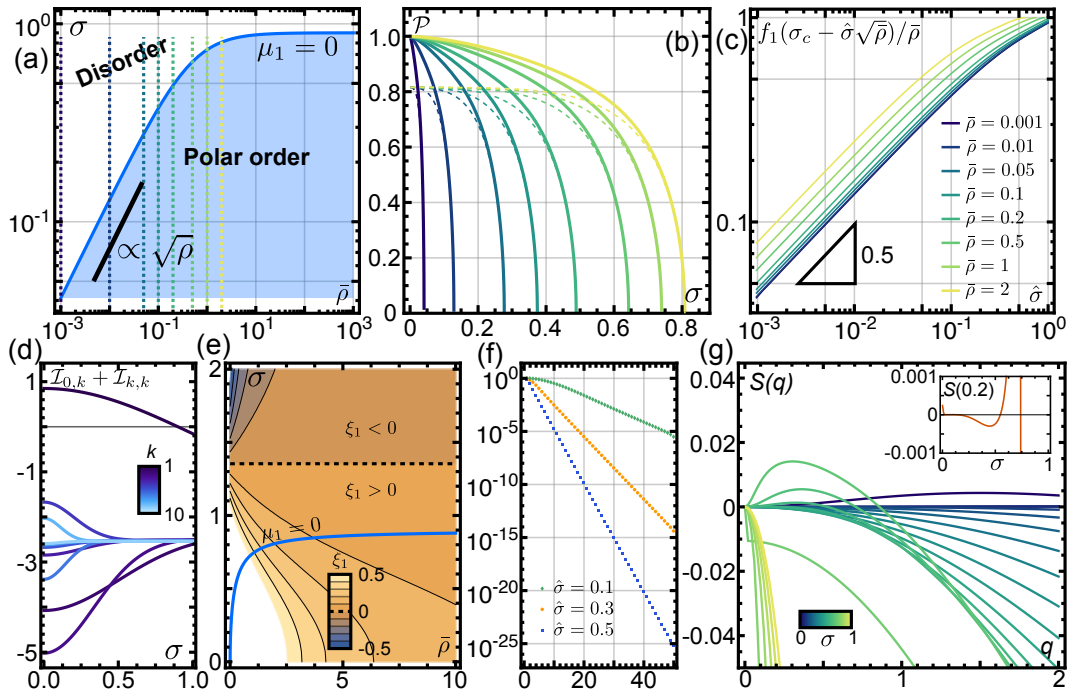


**Figure III.17** (a) Critical line  $\rho_1$  at which the disordered state becomes unstable. The dashed lines denote the density slices of (b,c). (b) Polar order  $\mathcal{P}$  of homogeneous solutions  $F_k(\sigma, \bar{\rho})$  (solid lines) and of  $f_1 = \sqrt{\frac{\mu_1}{\xi_1}}$  (dashed lines) at different densities. (c) Corresponding scaling function  $\Lambda(\hat{\sigma})$  shows the critical behavior of the Vicsek class, with a scaling exponent of  $\hat{\sigma}^{0.5}$ . (d) Behavior of  $\mathcal{I}_{0,k} + \mathcal{I}_{k,k}$  as function of  $\sigma$ , which is an upper bound of  $\mu_k$ , shows that only mode  $k = 1$  can become unstable. (e) Behavior of  $\xi_1$  as a function of  $\bar{\rho}$ ,  $\sigma$ . Note that for the transition at  $\mu_1 = 0$ ,  $\xi_1$  is always positive. (f) Amplitude of numerical solutions  $F_k$  at different  $\hat{\sigma}$  for  $\bar{\rho} = 2$ . While  $F_k$  decreases exponentially with  $k$ , they also exponentially grow with  $\hat{\sigma}$ . (g) Growth rates  $S(q)$  of inhomogeneous perturbations of  $F_k$  as a function of wavenumbers  $q$ , for different  $\sigma$  at  $\bar{\rho} = 1$ . At intermediate  $\sigma$ ,  $S(q > 0) < 0$  and hence  $F_k$  is stable. Inset: growth rate at  $q = 0.5$  shows the stability of  $\sigma$ -regions. Note that for small  $\sigma$ , the homogeneous state becomes again unstable (see also Fig. II.10, chapter II for the re-entrant stability).

order in the kinetic theory, and early studies of the Vicsek model suggested that this was the only relevant instability [49, 66, 67]. Yet, the corresponding homogeneously ordered solutions, which are locally stable, are in fact laterally unstable in the vicinity of the onset, which renders the transition to be ultimately discontinuous and gives rise to stationary polar patterns, in agreement with numerical studies [55] and agent-based simulations [41, 45]. Please refer to section 1.3.3 (in particular, see Eqs. (II.16, II.17, II.18)), chapter II for further details on the (lateral) stability analysis of the Vicsek model for a system of  $K$  modes and how to obtain the growth rates  $S(q)$ . Here, the corresponding dispersion relation of inhomogeneous perturbations is such that there exists a finite band of unstable wavenumbers  $q \in [0, q_c]$  which destabilize the ordered state (see Fig. III.17(g)). Adapting the terminology of Greenside and Cross [158] for the classification of linear dispersion relations, this corresponds to an instability of type  $II_s$ . As one goes deeper into the ordered phase by further increasing  $\bar{\rho}$  or decreasing  $\sigma$ , the homogeneous state eventually becomes stable [54, 157]. This marks the second phase transition line  $(\rho_2, \sigma_2)$  of the polar active system. Hence, the kinetic Boltzmann approach fully recovers the Vicsek ordering paradigm (VOP) that was initially established in simulations of the Vicsek model.

## 2.3 Kinetic Boltzmann ansatz for generic alignment models

While the above derivation has already been established previously [42, 52, 54], let us make some critical remarks about the underlying assumptions that enter the kinetic theory. In particular, we highlighted that the observed behavior depends crucially on the collision integral  $\mathcal{I}_c[f, f]$  of Eq. (III.13) and its corresponding Fourier components  $\mathcal{I}_{n,k}$  of Eq. (III.15).  $\mathcal{I}_{n,k}$ , in turn, depends specifically on the Vicsek alignment rule, which impose perfect half-angle alignment of binary collisions, plus an angle-independent, constant Gaussian noise. Let us compare this with a typical situation of alternative alignment processes of colliding objects, which are gradual and continuous in time and have a finite correlation time/length, and are frequently encountered in experiments or agent-based simulations [20, 25–27, 36, 37]:

- For large incoming angles  $\Delta := |\phi_1 - \phi_2| \gg 0$  one would expect only a small increase of alignment, or even anti-alignment for the case of active rods, due to the large relative velocity of the objects and the resulting short duration of the collision.
- For small incoming angles  $\Delta \ll \pi$ , the collision duration increases drastically resulting in a further alignment that saturates when the active objects are perfectly parallel and touching.

- Furthermore for extended objects, the collision may strongly depend and many more microscopic degrees of freedom than just the relative angle  $\Delta$ , like the impact parameter, which results to a complicated scattering spectrum of the outgoing angles. Here, the collision noise  $\zeta$  of the kinetic theory plays the role of emulating this complicated, possibly chaotic influence on average, which enters the analysis via its standard deviation  $\sigma_c$ . Likely, the variance of scattering is minimal for  $\Delta \ll \pi$  and maximal for  $\Delta = |\phi_1 - \phi_2| \gg 0$  due to the differences in the relative velocities.

In simple words, this would imply that polar order in gradually-aligning model systems is predominantly driven by acute collision angles, and disalignment by obtuse angles. Indeed, this diagnosis also describes interactions in the experimental actin motility assay and the WASP simulations (see also sections 2, chapter II and 1). On the other hand, the Vicsek collision rule is almost diametrically opposed to this situation: the degree of alignment is strongest for large incoming angles  $\Delta \approx \pi$  and minimal for  $\Delta \approx 0$ ; since the collision noise is independent on  $\Delta$  and also contributes for  $\Delta = 0$ , there is even an effective *misalignment* at small  $\Delta$  (Fig. III.18(a)). This assessment of alignment is similar to the analysis of Lam et al. [38, 56], who found a discontinuous transition to polar order on the basis of their specific model of aligning discs, which they attribute to these differences in the effective alignment: that is, obtuse-angle-alignment favors a supercritical transition as opposed to acute-angle-alignment, which drives a discontinuous transition. Naturally, this poses the question to which extent the above results for the Vicsek model are at least qualitatively applicable to more general alignment models, or in plain words: how 'large' is the Vicsek universality class in the space of all possible models (Fig. III.18(b))? Can we find different criteria to classify the (polar) ordering phenomena in active systems?

To this end, we will draw three different case studies of polar alignment models, which are parametrized such that they depart continuously from the Vicsek model. In general, let  $\Phi(\Delta)$  be the alignment kernel and  $\tilde{P}_k(\Delta)$  the Fourier component of a collision noise  $\zeta$  with distribution  $P(\zeta, \Delta)$  of a model such that binary collisions with an incoming angle  $\Delta$  yield an outgoing angle  $\Phi(\Delta) + \zeta$ , then the collision integrals read

$$I_{n,k} = \frac{1}{\pi} \int_0^{\pi-\psi} d\Delta S(|\Delta|) \left( \tilde{P}_k(\Delta) \cos[\Delta(n-k/2)] \cos[k\Phi(\Delta)/2] - \cos[n\Delta] \right). \quad (\text{III.22})$$

In this way, we can quantify arbitrary alignment assumption by imposing the specific functions  $\Phi(\Delta)$  and  $\tilde{P}_k(\Delta)$ , where collision and diffusion noise,  $\sigma_c$ ,  $\sigma_d$ , can be independent. Note that we have also introduced a cut-off parameter  $\psi$ , which is equivalent of setting  $\Phi(\Delta > \pi - \psi) = \Delta$  in the Boltzmann equation (i.e. no

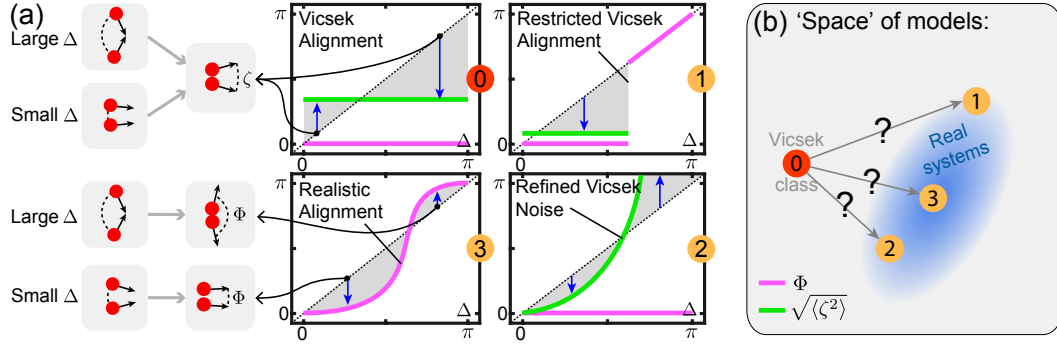


**Figure III.18** Schematic of different alignment models, illustrated by different binary collision curves. (a) Comparison of Vicsek alignment (upper-left part) with gradual alignment of mixed nematic and polar symmetry (lower-left part), similar to alignment in the WASP model. In the 4 cases depicted, the alignment kernel  $\Phi$  and the standard deviation of collision noise  $\sqrt{\langle \zeta^2 \rangle}$  are sketched. Blue arrows in the binary statistics depict the ordering tendency (upwards: anti- or misalignment, downwards: alignment). (b) Illustration of the 'space' of alignment models. 'Realistic' systems only constitute a small subspace, which do not necessarily coincide with the domain of the Vicsek class.

alignment for  $\Delta > \pi - \psi$ ). Here the Vicsek model is recovered for  $\Phi(\Delta) = 0$  and  $\tilde{P}_k(\Delta) = P_k = e^{-(k\sigma)^2/2}$  (where  $\sigma = \sigma_d$  and  $\psi = 0$ ). The three cases considered below are illustrated in Fig. III.18(b) and given by:

1. **Restricted Vicsek alignment**, parametrized by  $\psi$  and  $\sigma_c$ :  $\Phi(\Delta) = 0$  for  $\Delta < \pi - \psi$ ,  $\Phi(\Delta) = \Delta$  otherwise, and  $\tilde{P}_k(\Delta) = e^{-(k\sigma_c)^2/2}$ .
2. **Refined Vicsek noise**, parametrized by  $a$  and  $b$ :  $\Phi(\Delta) = 0$  and  $\tilde{P}_k(\Delta) = e^{-(k\sigma_c(\Delta))^2/2}$  with  $\sigma_c(\Delta) = a\sigma^b$ .
3. **Realistic alignment**, parametrized by  $c$  and  $d$ :  $\Phi(\Delta) = G(\Delta, c, d)$  (with  $G$  having both polar and nematic symmetry terms, see section 2.3.3) and  $\tilde{P}_k(\Delta) = 1$  for simplicity.

Using these examples we will repeat the above analysis of section 2.2 and identify the behavior of the phase diagram using a detailed bifurcation analysis: first, we will focus on the homogeneous states and their corresponding transition properties in terms of local stability. Then in section 2.5, we will specify their stability for spatially extended systems, which leads to pattern formation.

### 2.3.1 Restricted Vicsek alignment

In this first example, we consider a alignment kernel and collision noise assumption as the following:

$$\begin{aligned}\Phi(\Delta) &= \begin{cases} 0 & \text{for } \Delta \leq \pi - \psi \\ \Delta & \text{for } \Delta > \pi - \psi \end{cases}, \\ \tilde{P}_k(\Delta) &= e^{-(k\sigma_c)^2/2}.\end{aligned}\quad (\text{III.23})$$

This is motivated by the assumption that alignment is predominantly located at acute collision angles  $\Delta$  and that diffusion and collision noise are independent variables. Here, polar alignment is perfect only within a collision cone of angle  $\psi$  and zero otherwise (Fig. III.19(a)). The collision noise is a Gaussian fluctuation constant in  $\Delta$ , independent of the diffusion noise  $\sigma_d$ . With these definition one can still exactly solve Eq. (III.22) which yields

$$\begin{aligned}\mathcal{I}_{n,k}(\sigma) &= \frac{1}{\pi} \int_0^{\pi-\psi} d\Delta S(|\Delta|) \left( \tilde{P}_k(\Delta) \cos[\Delta(n-k/2)] - \cos[n\Delta] \right) \\ &= \frac{8}{\pi} \left( \frac{1 - 2n \cos[\psi/2] \sin[n(\pi - \psi)] - \sin[\psi/2] \cos[n(\pi - \psi)]}{4n^2 - 1} + \hat{P}_k(\sigma_c) \times \right. \\ &\quad \left. \frac{(k - 2n) \sin[(\pi - \psi)/2] \sin[(k - 2n)\pi/2] + \cos[(\pi - \psi)/2] \cos[(k - 2n)\pi/2] - 1}{(k - 2n)^2 - 1} \right)\end{aligned}\quad (\text{III.24})$$

where one recovers Eq. (III.16) for  $\psi \rightarrow 0$  and  $\sigma_c \rightarrow \sigma_d$ . From this we can readily calculate the linear coefficients of the disordered stationary state  $f_k = 0$  ( $k \neq 1$ ) as a function of the cut-off angle  $\psi$ . Interestingly, not only the first coefficient  $\mu_1$  can become positive but also higher orders, in particular  $\mu_2$ : this can be seen when plotting  $\mathcal{I}_{0,k} + \mathcal{I}_{k,k}$  (Figs. III.19(c,f,g)) which, in the limiting case for  $\bar{\rho} \gg 1$  and  $\sigma \rightarrow 0$ , are proportional to the linear coefficients  $\mu_k \rightarrow \mu_k^{\max} = \bar{\rho}(\mathcal{I}_{0,k} + \mathcal{I}_{k,k})$ . Hence, not only homogeneous polar order may emerge, but also nematic order beyond a certain value of  $\psi$  (Fig. III.19(g)). Fig. III.19(b) shows the corresponding onset lines  $\mu_1 = 0$  and  $\mu_2 = 0$  for varying density and diffusion noise. Note that for nematic order to be dominant,  $\mu_2 > 0$  needs to be the only unstable mode, which holds true only in a small region in parameter space at larger densities  $\bar{\rho}$ . Furthermore, the limiting behavior of the transition curves is different from the ordinary Vicsek model with the critical noise  $\sigma_{d,1} \rightarrow \infty$ , because of the decoupling of diffusion and collision noise. This means that there is a finite density, at which ordering due to collisions (which is a nonlinear effect) cannot be suppressed by any finite diffusion. Hence, we will concentrate on rather low  $\bar{\rho}$ ,  $\sigma_d$  where the typical square-root scaling of the transition is still present and where we can focus on the

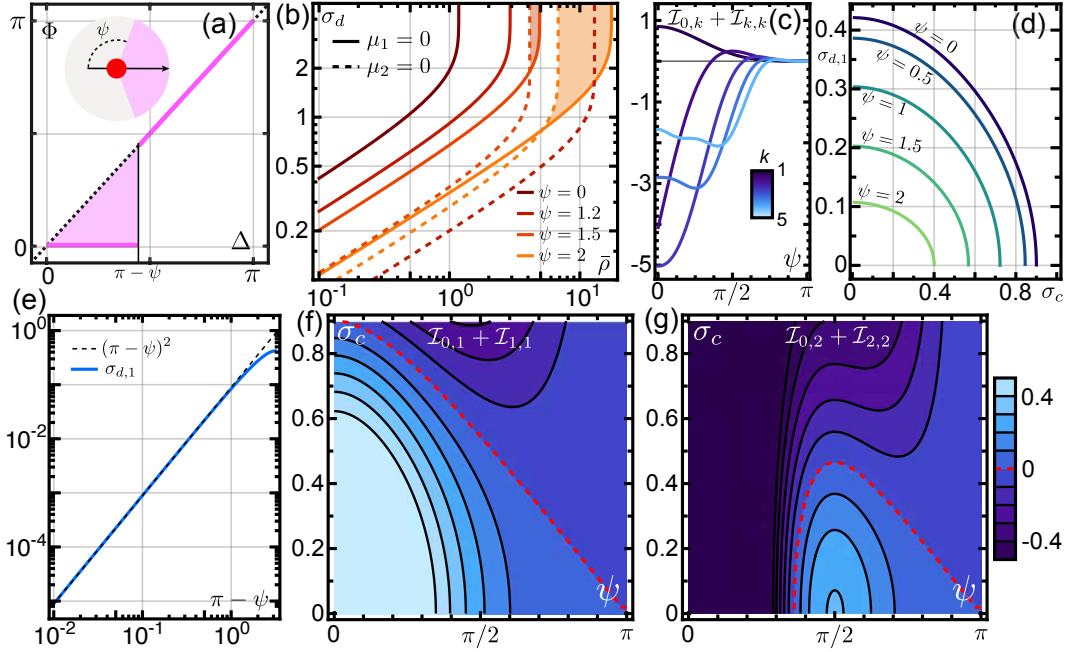


**Figure III.19** (a) Illustration of the alignment kernel  $\Phi(\Delta)$  for the restricted Vicsek model. Alignment only takes place for  $\Delta$  in the interval  $[0, \pi - \psi]$  (pink-shaded region). (b) Onset of polar order ( $\mu_1 = 0$ , solid lines) and nematic order ( $\mu_2 = 0$ , dashed lines) as a function of  $\bar{\rho}$  and  $\sigma_d$  for different cut-off angles  $\psi$ . Note that for large densities and  $\psi$ , the onset of nematic order dominates (shaded regions). (c)  $\mathcal{I}_{0,k} + \mathcal{I}_{k,k}$  for different  $k$  and  $\psi$ . (d) Critical noise  $\sigma_{d,1}$  for different  $\sigma_c$ ,  $\psi$ . (e) Scaling of  $\sigma_{d,1}$  for  $\pi - \psi$ . Contour maps of (f)  $\mathcal{I}_{0,1} + \mathcal{I}_{1,1}$  and (g)  $\mathcal{I}_{0,2} + \mathcal{I}_{2,2}$  for different  $\psi$ ,  $\sigma_c$ . For (b,c,e):  $\sigma_c = 0$ ; for (d,e):  $\bar{\rho} = 0.1$ .

formation of homogeneous polar order rather than nematic order. Note that the collision noise  $\sigma_c$  has a similar influence on the transition curve as diffusion noise  $\sigma_d$  (Fig. III.19(d)), by lowering the threshold value. As can be seen in Fig. III.19(e), introducing  $\psi$  also strongly suppresses the (polar) critical noise  $\sigma_{d,1}$ , and one can easily check that it exhibits power law scaling with  $(\pi - \psi)^2$  around maximal cut-off  $\psi \rightarrow \pi$ :

$$\begin{aligned} \sigma_{d,1} &= \sqrt{-2 \log[1 - (\mathcal{I}_{0,1} + \mathcal{I}_{1,1})\bar{\rho}]} \\ &\approx \frac{\sqrt{\bar{\rho}}(\pi - \psi)^2}{2\sqrt{\pi}} + \mathcal{O}((\pi - \psi)^2) \end{aligned} \quad (\text{III.25})$$

While the value  $\mu_1$  determines only the onset of linear instability and hence polar order, we are left to calculate the ordered solutions and their stability. In the vicinity of the transition, it was argued that the ordered state is, to lowest order, described by the solution of the cubic Eq. (III.18),  $f_1 = \sqrt{\mu_1/\xi_1}$ , where the sign of

the cubic coefficient  $\xi_1$  determines whether Eq. (III.18) is super- or subcritical, with  $f_1$  either stable or unstable. Remarkably, for the restricted Vicsek model,  $\xi_1$  may become negative for sufficiently large cut-off angle  $\psi$ . From the functional form of Eq. (III.19), we can trace back the sign change to the term  $\mathcal{I}_{2,1} + \mathcal{I}_{-1,1}$ . Here we have excluded  $\mu_2 = 0$ , since this corresponds to the nematic onset at which the polar order is no longer dominant, and the remaining term  $\mathcal{I}_{1,2}$  stays positive (Figs. III.20(a-c)). As a result, the onset of polar order undergoes a bifurcation from a supercritical to a subcritical transition in terms of local stability, with a critical point  $\psi_c \approx 1.83064$  (at  $\sigma_c = 0$ ). The corresponding lowest-order solutions Eq. (III.20) are hence unbound and become unphysical as they diverge (Fig. III.20(d)). This peculiar breakdown of the hydrodynamic description is analogous the active system of Refs. [38, 56] and apparently refutes a classification into the Vicsek universality class, despite only minor modifications of the original Vicsek model. Figs. III.20(c) show the parameter regions in which the onset is super-or subcritical, respectively, as a function of  $\psi$  and  $\sigma_c$ . Since  $\psi \leq \psi_c$  corresponds to alignment cones that are smaller than  $\pi/2$ , collisions can only compensate a moderate amount of collision noise  $\sigma_c$  (see Fig. III.20(b)) which further decreases acute angle alignment in the remaining alignment cone.

In the subcritical regime, we can no longer resort to low-order approximations to specify the stationary solutions and are required to calculate the full solutions  $F_k$  ( $k \leq K$ ) for large  $K$  using the adaptive mode solving scheme introduced in detail in section 1.3.3, chapter II. Once we have found a solution, we used a pseudo-arclength continuation method to continuously track the solutions towards different parameter values. This has the advantage that one can continuously quantify all connected branches of the subcritical onset. Figs. III.20(d-f) show the polar order  $\mathcal{P}$  obtained from the higher-mode solution corresponding to the subcritical bifurcation. Here, the upper and the lower branch are locally stable, separated by an unstable branch which is approximated by the solution  $\sqrt{\mu_1/\xi_1}$ . Consequently, there exists a subcritical region where both the ordered and the disordered state are locally stable. At the onset  $\mu_1 = 0$ , a disordered system would hence locally jump discontinuously from  $\mathcal{P} = 0$  to the upper branch at  $\Delta\mathcal{P}^+$ , which represents a very different bifurcation scenario than in the original Vicsek case (section 2.2). In Figs. III.20(e,f) we have quantified the bistable region as a function of  $\bar{\rho}$  and  $\psi$  for different values of  $\sigma_d$  (for simplicity we set  $\sigma_c = 0$ ). While the size of this region is rather small compared to the total size of the ordered domain, Fig. III.20(g) shows that the 'jump size'  $\Delta\mathcal{P}^+$  at onset increases as  $\sigma_d$  decreases. Thus at the onset and in the absence of spatial perturbations, the corresponding systems would jump from complete disorder to almost perfect polar order.

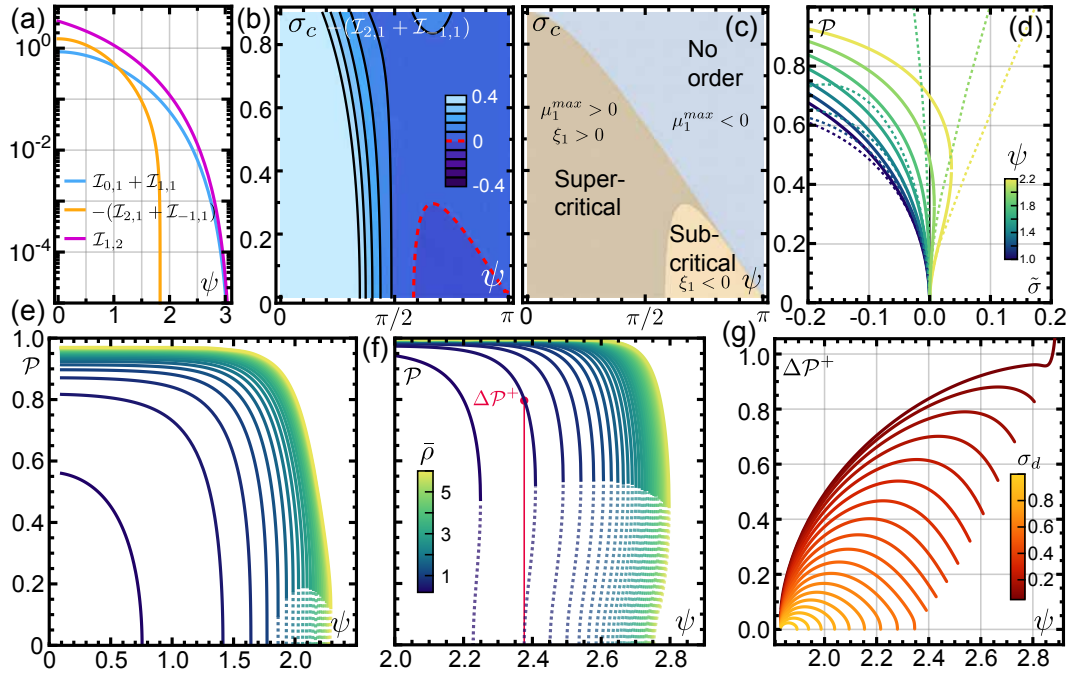


**Figure III.20** (a) Dependence of different collision integral modes in the cut-off angle  $\psi$ . While  $\mathcal{I}_{1,2} > 0$ , the other factor of the nonlinear coefficient  $\xi_1$ ,  $\mathcal{I}_{2,1} + \mathcal{I}_{-1,1}$ , changes sign at  $\psi = \psi_c$ . (b) Dependence of the sign change  $\mathcal{I}_{2,1} + \mathcal{I}_{-1,1}$  on  $\psi$  and  $\sigma_c$ . (c) Phase diagram of systems exhibiting either a supercritical, Vicsek-like transition to order (dark-beige shading), a subcritical one (light-beige shading), or no onset (gray shading) for different  $\psi$  and  $\sigma_c$ . This was obtained by superimposing  $-(\mathcal{I}_{2,1} + \mathcal{I}_{-1,1}) > 0$  of (b) and  $\mathcal{I}_{0,1} + \mathcal{I}_{1,1} > 0$  of Fig. III.19(f) (with  $\mu_1^{max} := \bar{\rho}(\mathcal{I}_{0,1} + \mathcal{I}_{1,1})$ ). (d) Polar order at the onset as a function of  $\tilde{\sigma} := \sigma_d / \sigma_{d,1} - 1$ , obtained from lowest order Eq. (III.20) (dashed lines) and from  $F_k$  of the adaptive mode truncation scheme with  $K = 50$  (solid lines) for  $\bar{\rho} = 0.1$ . For  $\psi > \psi_c$  the bifurcation becomes subcritical. (e,f) Bifurcation scenarios for different  $\psi$ ,  $\bar{\rho}$ , for  $\sigma_d = 0.5$  (e), and for  $\sigma_d = 0.1$  (f). A red line exemplarily depicts the jump size  $\Delta\mathcal{P}^+$ . (g) Dependence of  $\Delta\mathcal{P}^+$  as a function of  $\psi$  for different  $\sigma_d$ . For (a, d-g),  $\sigma_c = 0$ .

### 2.3.2 Refined Vicsek collision noise

In our second example, we consider the standard Vicsek alignment kernel, but with a differential collision noise assumption parametrized as the following:

$$\begin{aligned} \Phi(\Delta) &= 0, \\ \tilde{P}_k(\Delta) &= \exp[-(k\sigma_d \mathcal{V}(\Delta))^2/2] \quad \text{with} \quad \mathcal{V}(\Delta) = a\Delta^b. \end{aligned} \quad (\text{III.26})$$

which is motivated by the assumption that the collision outcome hardly varies for small incoming angles  $\Delta$ , but strongly for large  $\Delta$  which is true for  $b > 0$ . Note that collision noise is now coupled with diffusion noise, and that the standard Vicsek case is recovered for  $a = 1$  and  $b = 0$ . Hence we are left to analyze the behavior of the model for different  $a, b$ . We consider two examples with  $a = 0.5, b = 2$  and  $a = 0.3, b = 3$  to distinguish the influence of the different parametrizations (see cases 1, 2 in Fig. III.21(a), respectively). For both cases, there exist critical points at which the nonlinear coefficients of the hydrodynamic equations,  $\xi_1$ , changes sign within the range of the polar onset, defined by  $\mu_1^{\max} = \bar{\rho}(\mathcal{I}_{0,1} + \mathcal{I}_{1,1}) > 0$  (Fig. III.21(b)). This indicates a local bifurcation scenario from a super- to a subcritical transition to polar order, as for the previous model in section 2.3.1. Figs. III.21(d,e) show the transition curves of both examples, including the critical point. Here, we have calculated the homogeneous steady states  $F_k$  and quantified the domain of the subcritical branches using the adaptive mode solving method for  $K = 40$ ; the corresponding solutions of the polar order  $\mathcal{P}$  for different densities  $\bar{\rho}$  are given in Figs. III.21(f,g). For large densities, the discontinuity is extremely strong with the jump size  $\Delta\mathcal{P}^+$  approaching unity. Furthermore, this demonstrates that there is, in fact, a vast bistable parameter region which covers a good fraction of the ordered regime (compared to the onset value  $\sigma_{d,1}$ ). Interestingly, this regime continues to grow with  $\bar{\rho}$  beyond the range of densities that were numerically feasible. From the model definitions Eq. (III.26) it is clear that the parameter  $a$  in the collision noise is defined collinear to  $\sigma_d$ , such that for the values of the collision integrals  $\mathcal{I}_{n,k}(\sigma_d \cdot a, b)$  a relative change of  $a$  can be always compensated by an inverse change in  $\sigma_d$ . Since the criticality of the onset at infinite densities  $\bar{\rho} \rightarrow \infty$  depends only on the sign of the collision integrals  $\mathcal{I}_{2,1} + \mathcal{I}_{-1,1}$  when  $\mu_1^{\max} = \bar{\rho}(\mathcal{I}_{0,1} + \mathcal{I}_{1,1}) > 0$ , we can, without loss of generality, subdivide the domain of parameters into a supercritical and a subcritical regime, respectively, by changing  $b$  and  $a \cdot \sigma_d$ . Fig. III.21(c) shows that beyond a threshold exponent  $b^* \approx 1.05$ , the phase portraits always exhibit a subcritical bifurcation point at the onset, as in Figs. III.21(d,e). Below  $b^*$ , the transition to homogeneous order is always supercritical. Above  $b^*$ , the discontinuous character of the transition and the domain size of the subcritical region grows successively with  $b$ , as can be seen by the comparison of cases 1 and 2 in Fig. III.21. In total, this analysis shows that an

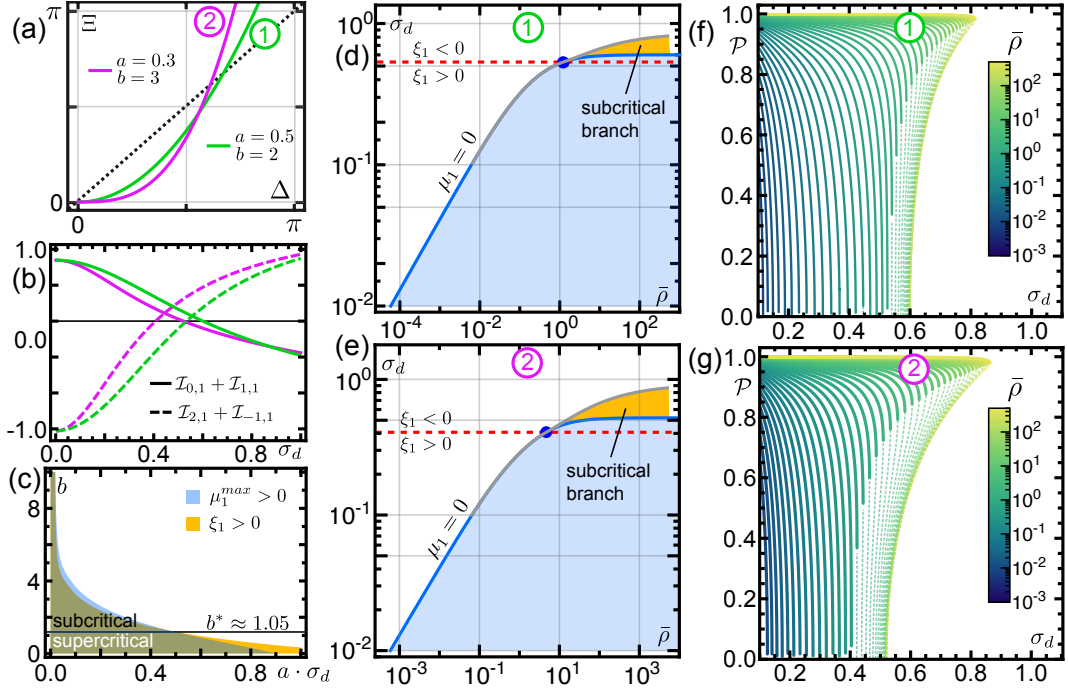


**Figure III.21** (a) Differential collision noise  $\mathcal{V}(\Delta)$  for two different cases:  $a = 0.5$ ,  $b = 2$  (green line, (1));  $a = 0.3$ ,  $b = 3$  (pink line, (2)). (b) Critical behavior of cases 1 (green lines), 2 (pink lines) as illustrated by the sign of collision integrals  $\mathcal{I}_{0,1} + \mathcal{I}_{1,1}$  (solid lines) and  $\mathcal{I}_{2,1} + \mathcal{I}_{-1,1}$  (dashed lines): the bifurcation point occurs when  $\mathcal{I}_{2,1} + \mathcal{I}_{-1,1} = 0$  while  $\mathcal{I}_{0,1} + \mathcal{I}_{1,1} > 0$ . (d,e) Phase portraits for varying  $\bar{\rho}$  and  $\sigma_d$ , corresponding to the parameters depicted in (a). The blue lines depict the onset noise  $\sigma_{d,1}$ , red-dashed lines show  $\xi_1 = \mathcal{I}_{2,1} + \mathcal{I}_{-1,1} = 0$ , the blue circle the subcritical bifurcation point. The gray lines depict the domain boundaries of homogeneous solutions  $F_k$  obtained by adaptive mode solving (see (f,g)), which mark the border of the subcritical branch (orange). (f,g) Polar order  $\mathcal{P} = F_1/\bar{\rho}$  as a function of  $\sigma_d$  for various  $\bar{\rho}$ , corresponding to the parameters depicted in (a). The unstable branches are depicted by light dashed lines.

angle dependence of the collision noise is capable of changing the local bifurcation scenario of the active system. For a subcritical transition, a certain 'imbalance' between acute and obtuse scattering is required, as indicated by the finite value of  $b^*$ .

### 2.3.3 Variable alignment rules

In our third example, we choose a parametrization of the collision kernel which resembles the gradual alignment that is often encountered in experiments or agent-based simulations [20, 25–27, 36, 37], including the motility assay or the WASP simulations of the previous sections. For simplicity, we set the collision noise to

zero in order to fully concentrate on the effect of the collision kernel alone. The assumptions then read:

$$\begin{aligned}\Phi(\Delta; e, f) &= \pi \frac{\arctan[f(\Delta - \pi/2 - e)] + \arctan[f(\pi/2 + e)]}{\arctan[f(\pi/2 - e)] + \arctan[f(\pi/2 + e)]}, \\ \tilde{P}_k(\Delta) &= 0.\end{aligned}\tag{III.27}$$

While the particular functional form could also have been chosen differently, Eq. (III.27) has interesting features: as can be seen in Fig. III.22(a,b), varying the parameter  $e$  changes the alignment symmetry from a perfectly nematic alignment at  $e = 0$  to a polar alignment at  $e = \pi/2$ , and changing  $f$  changes the 'strength' of the alignment, with no alignment at  $f = 0$  and full alignment at  $f \rightarrow \infty$  (which recovers the Vicsek case for  $e = \pi/2$ ). Hence, it is clear that there will be an influence of emerging nematic states for small  $e$  when alignment interactions possess mixed polar and nematic symmetries. However here, we will rather focus on the local stability of the homogeneous polar solution. Since there are no direct analytical expression for the collision integrals  $\mathcal{I}_{n,k}$ , we calculate them numerically for different values of  $e$  and  $f$ . Figs. III.22(c-f) show contour maps of the collision intergral moments as a function of  $e$  and  $f$ , which are crucial for the onsets of polar or nematic order, respectively, or whether there is a super- or subcritical transition: in Fig. III.22(c) it can be seen that there is a sign change in  $\mathcal{I}_{0,1} + \mathcal{I}_{1,1} = \mu_1^{max}/\bar{\rho}$  indicating that there is no polar onset below the neutral line. Likewise for the precursor of nematic order  $\mathcal{I}_{0,2} + \mathcal{I}_{2,2} = \mu_2^{max}/\bar{\rho}$  (Fig. III.22(d)), no nematic onset is found above the line  $\mu_2^{max} = 0$ . Concerning the criticality of the polar onset, we find that there is a sign flip in  $\xi_1$  which predominantly depends on  $e$ , as can be seen by  $\mathcal{I}_{-1,1} + \mathcal{I}_{2,1} \sim -\xi_1$  in Fig. III.22(e). From this, we can draw a phase diagram of the possible states as a function of  $e$  and  $f$  in Fig. III.22(f), illustrating that for any collision 'strength'  $f$  there is always a finite interval where both types of homogeneous ordered states, polar and nematic, coexist. Interestingly, the criticality line where  $\xi_1 = 0$  is always located inside this interval. For all collision integrals, a change in  $f$  seems to change the situation only quantitatively. To visualize a specific scenario of the onset of order, we therefore fixed  $f = 100 \gg 1$  such that  $\Phi(\Delta)$  is almost fully aligning and  $\sigma_d = 0.4$ , without loss of generality. Fig. III.22(g) then depicts the phase diagram for different  $e$  and  $\bar{\rho}$ , where the domains of polar or nematic order are shaded red, respectively blue. Using the adaptive mode solving method, we have explored the polar order  $\mathcal{P}$  of the stationary states for  $K = 40$  modes in the polar domain (Fig. III.22(h)). It can be seen that again, there exists a subcritical parameter region where polar order prevails below the onset  $\mu_1 = 0$  and below  $\xi = 0$ , as it was already found in the previous sections 2.3.1, 2.3.2. Interestingly, as the subcritical branch enters the domain of nematic order  $\mu_2 > 0$ , a critical transition is again recovered here since

$\xi_1 \sim \mu_2$  experiences another sign flip. Why this critical branch still extends far beyond the domain of  $\mu_1 > 0$ , or how the homogeneous polar state is interacting with the nematic state, is however beyond the focus of this analysis.

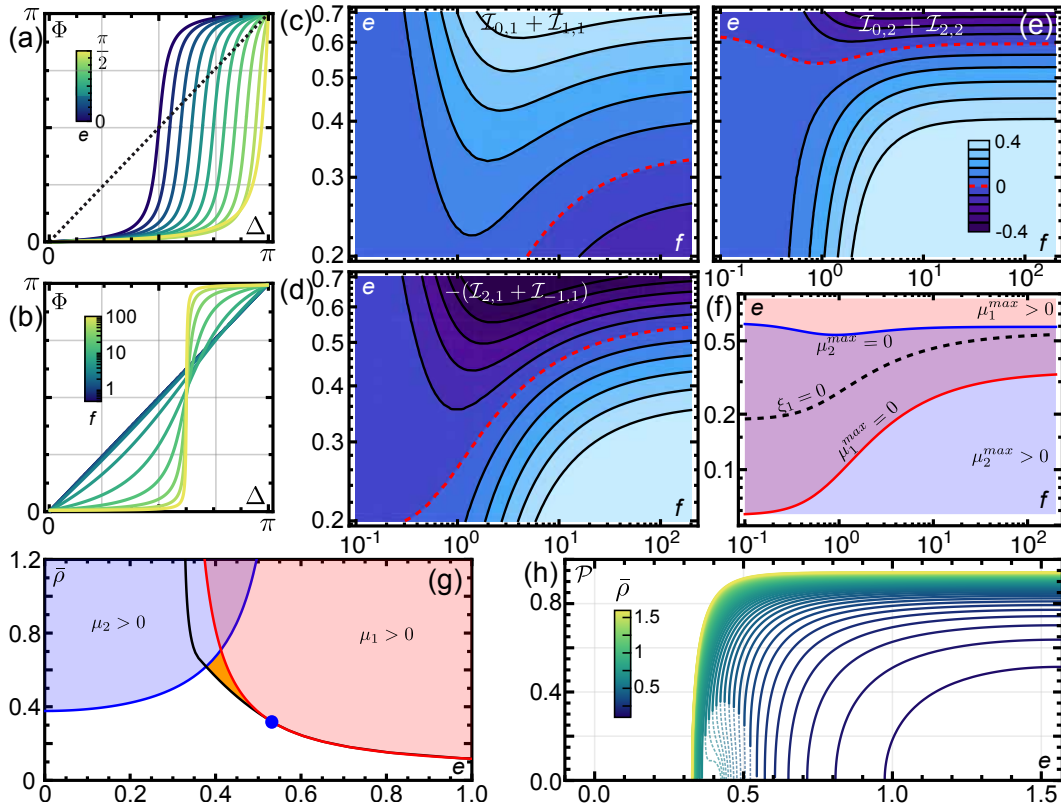


**Figure III.22** (a,b) Parametrization of the collision kernel  $\Phi(\Delta; e, f)$  for varying  $e$  (a) and  $f$  (b). (c-e) Contour maps of collision integrals as a function of  $e$  and  $f$ . Red dashed lines show where the values are zero. (f) Phase diagram for different  $e$  and  $f$  given by the zero lines of (c-e). (g) Phase diagram for different  $e$  and  $\bar{\rho}$ . Red and blue shading denote the polar, respectively nematic regimes. The bifurcation point where  $\xi_1 = 0$  is marked by a blue dot. The domain boundary of the states depicted in (h) is marked by a black line, with the subcritical 'pocket' marked by orange shading. (h) Polar order  $\mathcal{P}$  obtained from adaptive mode solving for  $K = 40$  as a function of  $e$ , for different  $\bar{\rho}$ . Locally stable branches are marked by solid lines, unstable ones by dashed lines. For (g,h):  $\sigma_d = 0.4$ .

## 2.4 Criticality of collective order

The three case studies presented in the previous section provide evidence that, quite generally, there is a bifurcation that changes the criticality of the ordering transition from super- to subcritical. In the latter scenario, a homogeneously disordered state above the onset jumps discontinuously from disorder to strong polar order. These

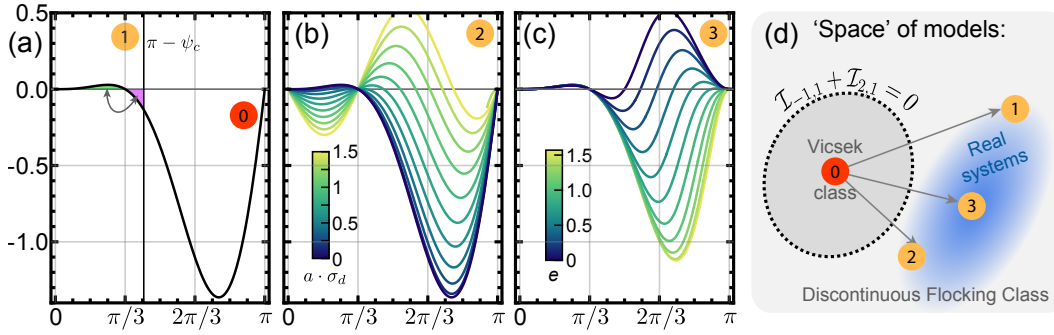


**Figure III.23** (a,b,c) Integrands  $C_{1,2}$  of Vicsek alignment (full black line in (a)), restricted Vicsek alignment (black line until  $\Delta = \pi - \psi_c$  in (a)), refined collision noise (b) with  $b = 2$ , and gradual alignment (c) with  $f = 2$ . For  $\psi = \psi_c$  in (a), positive (green shading) and negative (pink shading) contributions are balanced. The color gradients depict the variation of respective parametrizations. (d) Illustration of the 'space' of models: the criterion  $\mathcal{I}_{-1,1} + \mathcal{I}_{2,1} = 0$  represents a demarcation line that separates the Vicsek class from a different, discontinuous flocking class.

ordered states are locally stable against homogeneous perturbations and may exist even far below the onset where the disordered state becomes locally unstable, as it was shown in Figs. III.20, III.21, III.22. Let us emphasize again that so far, this statement holds only when gradient terms of the full Boltzmann equations Eq. (III.14) are negligible, that is, when we consider homogeneous solutions or the local stability of a spatially extended system. We will consider the presence of spatial gradients in section 2.5. As for the criticality of the homogeneous solutions, it was found that it is associated with the necessary criterion  $\xi_1 = 0$  or, in the absence of nematic solutions,  $\mathcal{I}_{-1,1} + \mathcal{I}_{2,1} = 0$ . Coming back to the original expression for the collision integrals, this criterion is equivalent to the integral expression:

$$\mathcal{I}_{-1,1} + \mathcal{I}_{2,1} \sim \int_0^\pi d\Delta C_{1,2}(\Delta) = 0, \quad (III.28)$$

$$C_{1,2}(\Delta) = \sin \Delta (2 \cos \Delta - 1) \left( \tilde{P}_1 \cos \frac{\Phi}{2} - \cos \frac{\Delta}{2} \right),$$

where  $\tilde{P}_1$  and  $\Phi$  are the Fourier-transformed collision noise distribution and the alignment kernel of an arbitrary parametrization. The meaning of this condition can be graphically explained: for the simple case of  $\tilde{P}_1 = 1$  and  $\Phi = 0$  (i.e. Vicsek case with  $\sigma_c = 0$ ), the curve  $C_{1,2}(\Delta)$  has a small positive contribution at acute angles  $\Delta$  and a large negative contribution at obtuse angles  $\Delta$  (Fig. III.23(a)); with the integral over  $\Delta$  being overall negative, resulting in a supercritical transition. For the case of a restricted Vicsek alignment rule, where alignment only occurs within a cone of angle  $\psi$  (section 2.3.1), the sign change is triggered when the

truncated negative contribution in the integral  $\int C_{1,2}$  balances the positive part for  $\psi = \psi_c$  (Fig. III.23(a)). Likewise, for the models with differential collision noise (section 2.3.2) and gradual alignment with mixed symmetry (section 2.3.3), the corresponding parametrizations may subsequently deform the negative contribution of  $C_{1,2}$  until the total integral vanishes (Fig. III.23(b,c)). Note that due to the functional form of  $C_{1,2}$ , this effect stems from (i) the fact that non-aligning terms at large angles  $\Delta$  always reduce the negative contribution, without discriminating randomization by collision noise or anti-aligning effects; and (ii) unperturbed alignment at small  $\Delta$  which would otherwise diminish the positive contribution of  $C_{1,2}$ . As a result, this shows that the criticality of the polar ordering transition can be changed by exactly the same assumptions that we imposed in the beginning of this section, and which we claim to refine active matter models towards more realistic physics of particle alignment: that is, strong alignment and little angular variation for acute scattering, and little alignment or strong variation for obtuse scattering. Consequently, we argue that quite generically, more 'realistic' active matter models should possess a different onset dynamics (driven by a subcritical bifurcation) than the Vicsek class (supercritical transition) – and should hence belong to a different class (Fig. III.23(d)).

## 2.5 Lateral stability of collective order

Until now, we have analyzed the different alignment models strictly assuming the absence of any spatial perturbation. The results concerning the change of the onset criticality are hence only valid for sufficiently small systems where gradients are small, or temporarily at laterally isolated points of an extended system. This section is therefore devoted to specify the (linear) stability of the homogeneous steady states that we found in section 2.3 in the presence of spatial perturbations. Before we study the stability of stationary states close to the onset of order, in particular when the local bifurcation scenario changes from super- to subcritical, let us first revisit the second phase transition from polar patterns to homogeneous polar order, which is, for the original Vicsek case, located deep in the ordered domain.

### 2.5.1 Homogeneous polar order revisited

As a first step, let us try to reconcile the full phase diagram behavior of the presented alignment models with the Vicsek case in section 2.2, that is, to find the second phase transition beyond which the homogeneous ordered state becomes stable again [54, 55, 157]. To this end, we need to specify the stability of the homogeneously ordered states far above the onset,  $\mu_1 \gg 0$ . Please refer to section 1.3.3, chapter II for a more detailed description of the linear stability analysis. In essence, we linearize Eqs. (III.14) for small spatial variations of the homogeneous states

$f_k(t, \mathbf{r}) \rightarrow (F_k + \delta f_k(t, \mathbf{r}))$  and calculate the eigenvalues  $S_k$  of the system using a Fourier transform to replace the gradient terms like  $\partial_x \rightarrow iq_x$  and  $\partial_y \rightarrow iq_y$ . Then, the maximal eigenvalue  $S(q) = \max_k S_k$  with  $q = |\mathbf{q}|$  determines if the homogeneous state is stable ( $S(q) \leq 0$ ) or unstable  $S(q) > 0$ . To begin with, we consider alignment model 1 (section 2.3.1) with restricted Vicsek alignment and independent collision noise. For the simplest case, when  $\psi = 0$  and  $\sigma_c = 0$ , we recover the Vicsek model without collision noise (but still finite diffusion noise  $\sigma_d$ ). With these assumptions, the dispersion relation  $S(q)$  shows a long-wavelength band of unstable modes (Fig. III.24(a)), corresponding to a type-II<sub>s</sub> instability, throughout the ordered phase, which possesses a maximal growth rate  $S_{max} = \max_q S(q)$  at a wave number  $q_{max}$ . This resembles, as expected, the onset dynamics for original Vicsek alignment, see Fig. III.17(g).

However surprisingly, we find *no* stabilization of the homogeneous states deeper in in the phase space for larger  $\bar{\rho}$  or lower  $\sigma_d$  (Fig. III.24(d)). Thus, there is always a finite band of unstable modes for  $\sigma_c = 0$ , which produce patterns. Further away from the onset, we found that the properties of  $S_{max}$  and  $q_{max}$  exhibit a behavior that is well approximated by a power law scaling  $S_{max} \sim \sigma_d^{1/2}$  and  $q_{max} \sim \sigma_d^{-3/4}$  (Fig. III.24(b,c)). Up to these scaling relations, the dispersion relations look qualitatively similar, which suggests that the corresponding emergent patterns should be, to linear order, comparable and only gradually different. This is of course only a precursor of the true nonlinear patterns at best, which are unknown at this point. A stable homogeneous state can be recovered by a finite collision noise  $\sigma_c$ . Figs. III.24(e,f) illustrate the stability diagram<sup>4</sup> for a fixed density  $\bar{\rho} = 0.1$  and varying  $\sigma_d, \sigma_c$ . As it was seen in Fig. III.19(d), the first transition at  $\sigma_{d,1}$  steadily decreases and vanishes at  $\sigma_c \rightarrow \sigma_\infty = \sqrt{\log(9/4)} \approx 0.9$ . In contrast, as  $\sigma_c$  is increased, a stable domain of homogeneous, polar order emerges at low  $\sigma_d < \sigma_{d,2}$  with  $\sigma_{d,2}$  being the second transition threshold of the active system. Here, also  $\sigma_{d,2}$  behaves like a power law in  $\sigma_c$  with a first regime  $\sigma_{d,2} \sim \sigma_c^{3/2}$  at low  $\sigma_c$ , followed by  $\sigma_{d,2} \sim \sigma_c^{2/3}$  at intermediate  $\sigma_c$  and finally  $\sigma_{d,2}$  asymptotically approaches  $\sigma_{d,1} \sim (\sigma_\infty - \sigma_c)^{1/2}$  at large  $\sigma_c$ . This intriguing behavior is not specific for any density, but also appears similarly at different values of  $\bar{\rho}$  (Figs. III.24(g,h)). We note that the original Vicsek alignment assumption, as used in section 1.3, chapter II and in Refs. [42, 52, 54], is represented by diagonal slices with  $\sigma_c = \sigma_d = \sigma$  in Figs. III.24(e-h). Hence, the superlinear scaling law  $\sigma_{d,2} \sim \sigma_c^{3/2}$  explains the re-entrant, lobe-like shape of the unstable, pattern-forming parameter region at small  $\sigma$  in the original phase diagram as it was found in Fig. II.10(b), chapter II.

<sup>4</sup> Note that due to the shape of the dispersion, it fully suffices to numerically calculate only one value  $S(\Delta q)$  with  $\Delta q \leq q_{max}$  and determine its sign, as shown in Fig. III.24(f-h).

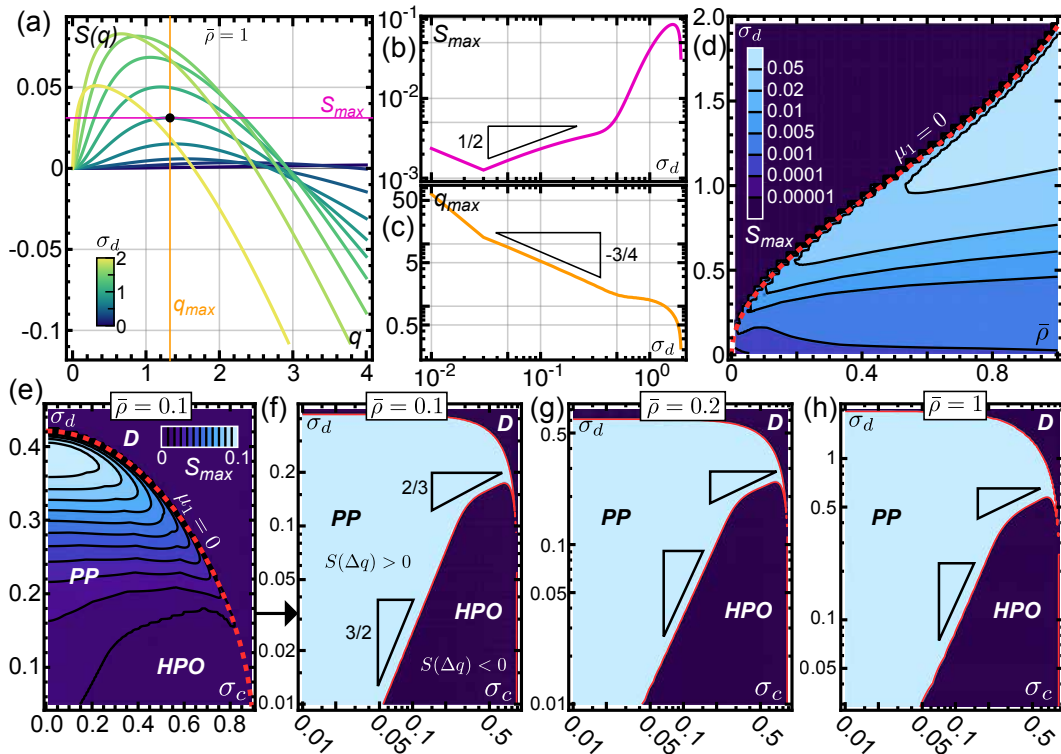


**Figure III.24** (a) Dispersion relation  $S(q)$  for Vicsek alignment in model 1 ( $\psi = 0$ ) and  $\sigma_c = 0$ ,  $\bar{\rho}$ , and for different  $\sigma_d$ . All curves show a band  $q \in [0, q_c]$  of unstable modes. As an example, one curve illustrates the values  $S_{max}$  and  $q_{max}$ . (b,c) Maximal growth rates  $S_{max}$  (b) and wave numbers  $q_{max}$  (c) corresponding to (a). Black triangles depict power law exponents of  $1/2$  and  $-3/4$ , respectively. (d) Phase diagram for alignment model 1 with  $\psi = 0$  and  $\sigma_c = 0$ , as a function of  $\bar{\rho}$  and  $\sigma_d$ . The color map indicates  $S_{max}$  at each point, which is positive for all ordered states. (e-h) Corresponding phase diagrams for varying  $\sigma_d$  and  $\sigma_c$ , for  $\bar{\rho} = 0.1$  (e,f),  $\bar{\rho} = 0.2$  (g), and  $\bar{\rho} = 1$ . (h). In (e-h) the shading is given by  $S(\Delta q) < 0$  (dark blue) and  $S(\Delta q) > 0$  (light blue) for  $\Delta q = 2$ . Here, we discriminate the corresponding states as disorder (**D**), polar patterns (**PP**), or homogeneous polar order (**HPO**). Black triangles depict power law exponents of  $3/2$  and  $2/3$ , respectively.

### 2.5.2 Onset of polar patterns

Next, we examine the behavior of our alignment models near the onset of order, and in the presence of a subcritical bifurcation of the homogeneous disordered state. In particular, we focus on the question whether the latter has a qualitative impact on the corresponding dispersion relation  $S(q)$  and the corresponding stability of homogeneous states. For alignment model 1 with a finite restriction angle  $\psi > 0$  of the alignment cone, we found that beyond a critical value  $\psi > \psi_c = 1.83064$  (for  $\sigma_c = 0$ ) when the transition becomes discontinuous, the branch of ordered solutions extends into a subcritical parameter region. Fig. III.25 compares the dispersion relations of supercritical and subcritical branches, when either  $\psi < \psi_c$  or  $\psi > \psi_c$ , respectively. It can be seen that both cases are qualitatively very similar, resembling a type-II<sub>s</sub> instability, and there is no drastic change that would indicate any kind of bifurcation on the level of patterns. Hence it would be tempting to conclude that at the onset  $\mu_1 = 0$ , irrespective of its criticality, spatial patterns emerge in a similar fashion. However, this statement would be premature and only hold to linear order, and the full nonlinearities of the system, which are particularly prominent on the subcritical branch, may yield qualitatively different patterns in the spatially extended system.

Compared to the supercritical case, there remain substantial differences. For

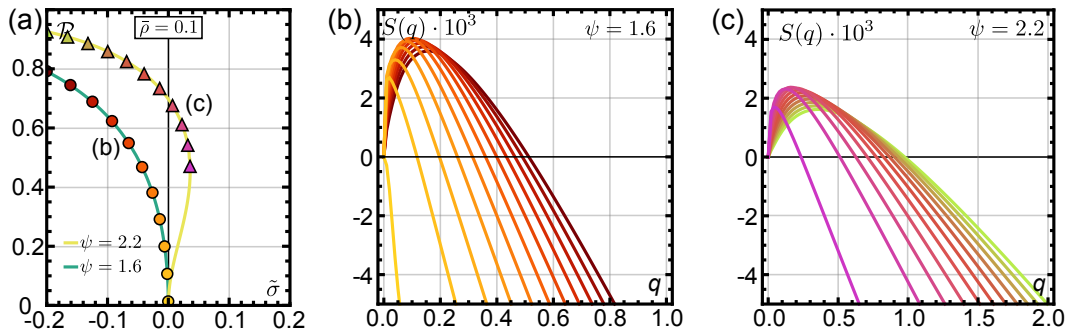


**Figure III.25** (a) Polar order at the onset as a function of  $\tilde{\sigma} := \sigma_d/\sigma_{d,1} - 1$  as already depicted in Fig. III.20(d) with  $\bar{\rho} = 0.1$ , for a supercritical ( $\psi = 1.6 < \psi_c$ , green line) and a subcritical ( $\psi = 2.2 > \psi_c$ , yellow line) case, respectively. The colored markers depict the locations of individual dispersions from (b,c). (b,c) Dispersions  $S(q)$  for  $\psi = 1.6$  (b),  $\psi = 2.2$  (c), and  $\bar{\rho} = 0.1$  for different relative noise values  $\tilde{\sigma}$ .

instance, the dynamics from an initially disordered state to the emergence of polar patterns depends foremost on the local bifurcation structure and then subsequently from the build-up of gradients due to unstable modes in the dispersion  $S(q)$ . Furthermore, the existence of large subcritical polar domains that coexist with a stable disordered state may, in the presence of local fluctuations, render the transition to order to be dominated by spontaneous nucleation events even far

from the onset line (which corresponds to a spinodal of the phase transition). On more general grounds, this description already shares several features that were similarly found in the previous section 1.4, where we examined the transition to polar order in simulations of the WASP model. Here, we found that polar order is easily excitable in a large fraction of the disordered region below the onset. Last but not least, we emphasize that the sophistication of local alignment assumptions enables us to 'engineer' the local and lateral bifurcation structure of the active system: as it was seen above in section 2.5.1, only the presence of collision noise  $\sigma_c$  seems to stabilize homogeneous polar states and thus facilitates the second phase transition  $\sigma_{d,2}$ , which, for large  $\sigma_c$ , confines the region where patterns emerge to a narrow band in parameter space. Hence we hypothesize that, as one additionally promotes a subcritical homogeneous transition to polar order, this narrow band of patterns may be 'folded' even below the onset  $\sigma_{d,1}$ , that is,  $\sigma_{d,2} > \sigma_{d,1}$  (see sketch in Fig. III.26). This would result in an exotic parameter domain where, at the onset  $\sigma_{d,1}$ , the system would discontinuously jump from a disordered state to a homogeneously ordered state, by undercutting the region of instability. Below  $\sigma_{d,1}$ , both states would coexist in juxtaposition with each other.

The question remains under which circumstances this situation can be constructed.

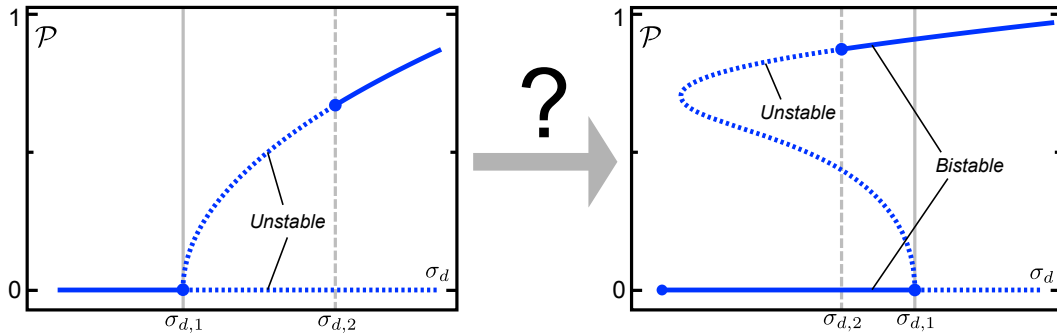


Figure III.26 Sketch of speculative bifurcation as a function of  $\sigma_d$ .

As one can see from Fig. III.20(d-f), the subcritical regions of the restricted Vicsek alignment are not particularly large, relative to the respective parameter values of the onset  $\mu_1 = 0$ . Hence, this would require a very narrow band of instabilities or patterns which could be achieved by a large collision noise  $\sigma_c$ . However, as we have assessed in Fig. III.19(c), too large  $\sigma_c$  diminishes the subcriticality. To circumvent this dilemma, we concentrate on the second model (section 2.3.2) where we assume standard Vicsek alignment but a differential collision noise (Eq. (III.26))  $\sigma_c(\Delta) \rightarrow \sigma_d \mathcal{T}(\Delta)$  with  $\mathcal{T}(\Delta) = a\Delta^b$ . This model exhibits large subcritical branches (Figs. III.21(d-g)), which even grow as (collision) noise is increased. First, let us examine the dispersions of spatial perturbations as one enters the subcritical polar branches (for fixed  $a = 0.5$ ,  $b = 2$ ), which appear beyond a bifurcation

point at  $(\bar{\rho}^*, \sigma_d^*)$  in Fig. III.27(a): for a fixed density  $\bar{\rho} \gtrsim \bar{\rho}^*$  slightly above the bifurcation, the dispersion  $S(q)$  appears similar to the previous cases for varying  $\sigma_d$ , with a long-wavelength band of unstable modes (Fig. III.27(b)). As one goes further away from  $(\bar{\rho}^*, \sigma_d^*)$ , the situation is however qualitatively different as it is illustrated in Fig. III.27(c). Initially, on the outer regions of the subcritical polar branch,  $S(q)$  exhibits again an instability of type II<sub>s</sub>; by subsequently decreasing  $\sigma_d$  however, the long-wavelength band of unstable modes vanishes, and a new unstable, short-wavelength band appears (corresponding to a *type-I<sub>s</sub>* instability [158]). Note that this behavior occurs already in the subcritical domain with  $\sigma_d > \sigma_{d,1}$ . When further decreasing  $\sigma_d$ , the unstable long-wavelength band appears again such that there are now two instabilities present (type I<sub>s</sub> and II<sub>s</sub>). By consecutive variation of  $\bar{\rho}$  and  $\sigma_d$ , we have calculated the corresponding phase diagram in Fig. III.27(e) based on dispersion relation  $S(q)$ . This shows that there is indeed a parameter region where the type-II<sub>s</sub> instability vanishes, and which extends onto the subcritical branch.

As for the new short-wavelength instability, we found that it is very sensitive to additional cues of the noise parametrization  $\Upsilon(\Delta)$ : for instance, when adding a very small constant term  $\Upsilon(\Delta) \rightarrow \Upsilon(\Delta) + \epsilon$  with  $\epsilon \ll \sigma_d$  the instability can be easily suppressed (Fig. III.27(d)), without significantly distorting the remaining structure of the phase diagram. This suggests that collision noise for very acute scattering angles  $\Delta \rightarrow 0$  plays a major role, as already a small nonzero value can suppress the lateral instability. As a result, a parameter region of a stable homogeneous state appears, and importantly, it spreads far over the onset  $\mu_1 = 0$  as it is seen in Fig. III.27(f) for  $a = 0.3$ ,  $b = 3$ ,  $\epsilon = 0.2$ . In this parameter region, both homogeneous states, the disordered and the ordered one, are linearly stable (see regions  $D+H$  in Fig. III.27(f)), hence confirming the above conjecture. We emphasize that for active systems with such collision noise assumptions, the onset and formation of polar order and patterns is drastically different than for the original Vicsek model, despite sharing the same alignment rule.

Let us remark here that this analysis does not allow for a characterization of the full inhomogeneous solutions, which could potentially be many as elaborated by Refs. [43, 44, 46, 47]. These may exist in addition to the homogeneous solutions presented here, and it not clear to which extent they would contribute to the actual dynamics of the full system. Here, direct simulations of the full Boltzmann equation (III.11) would be needed to elucidate these aspects.

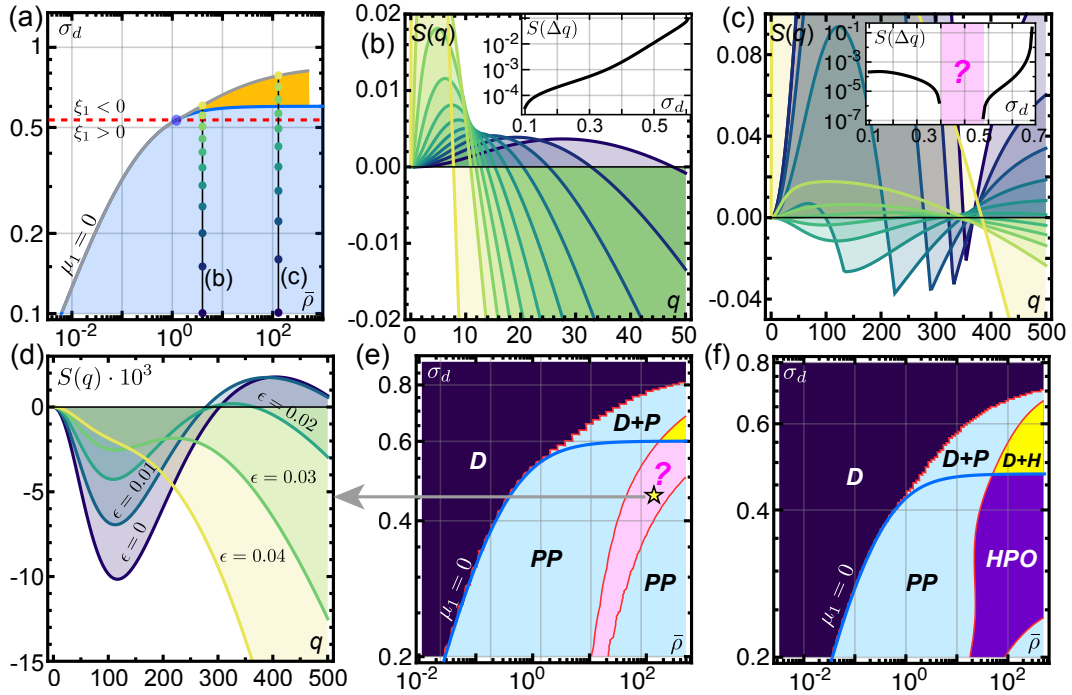


**Figure III.27** (a) Phase portrait for varying  $\bar{\rho}$  and  $\sigma_d$  as already shown in Fig. III.21(d) with  $a = 0.5$ ,  $b = 2$ . The blue line depicts the onset noise  $\sigma_{d,1}$ , the red-dashed line  $\xi_1 = \mathcal{I}_{2,1} + \mathcal{I}_{-1,1} = 0$ , the blue circle the subcritical bifurcation point  $(\bar{\rho}^*, \sigma_d^*)$ , and the gray line the outer boundary of the subcritical polar region (orange shaded). The two lines with colored markers denote the dispersion slices as shown in (b,c). (b,c) Dispersion relations  $S(q)$  for different  $\sigma_d$  (see corresponding colored markers in (a)), with  $\bar{\rho} = 4$  (b) and  $\bar{\rho} = 131$  (c). Respective insets:  $S(\Delta q)$  with  $\Delta q = 2$  for different  $\sigma_d$ . The pink shading denotes the region where a type  $I_s$  instability occurs. (d) Sensitivity of the type  $I_s$  instability with respect to small constant noise amplitudes  $\epsilon$ , as indicated by  $S(q)$ . Here,  $\bar{\rho} = 131$  and  $\sigma_d = 0.45$ . (e,f) Phase portraits for  $a = 0.5$ ,  $b = 2$ ,  $\epsilon = 0$  (e) and  $a = 0.3$ ,  $b = 3$ ,  $\epsilon = 0.2$  (f). The color code marks different stability domains: stable disorder (dark blue,  $D$ ), polar patterns (light blue,  $PP$ ), stable homogeneous polar order (purple,  $HPO$ ), type- $I_s$  patterns (pink,  $?$ ), stable disorder and polar patterns (light blue,  $D+P$ ), stable disorder and stable homogeneous polar order (yellow,  $D+H$ ).

## 2.6 Agent-based simulations

In the analytical investigation as presented above we showed that, despite several simplifying assumptions of the kinetic Boltzmann ansatz such as molecular chaos (point-like interactions with zero correlation length) or diluteness (only binary collisions), small modifications of the underlying alignment rules already lead to a variety of new and unexpected results. Hence, we would expect that the full dynamics of agent-based simulations would also yield a diversity of novel results. Therefore, we also addressed the question of refined alignment assumptions using a direct agent-based approach with simulations of a Vicsek-like model. Since it is difficult to assess the ambiguous correspondence of noise on the particle level in the (microscopic) Vicsek model to either the diffusion or the collision noises  $\sigma_d$ ,  $\sigma_c$  on the field level of the kinetic theory, we resorted to a direct modification of the alignment rules which is very analogous to the mean-field analysis of restricted polar alignment (see section 2.3.1), and hence allows for an unambiguous comparison. In particular, we imposed a collision rule which aligns the orientation of a particle  $i \in \{1, 2, 3, \dots, M\}$  ( $M$  being the total number of particles) with adjacent particles only if their orientations reside within an interaction cone with a relative angle  $\phi$ . For the simulations, the corresponding update rules for particle  $i$  read as

$$\begin{aligned} \mathbf{r}_i^{t+1} &= \Delta r \begin{pmatrix} \cos[\theta_i^{t+1}] \\ \sin[\theta_i^{t+1}] \end{pmatrix} + \mathbf{r}_i^t + \Lambda_i^{t+1}, \\ \theta_i^{t+1} &= \arg \left[ \sum_{j \in \mathcal{N}_i} \exp(i\theta_j^t) \right] + \delta\xi_i^t, \end{aligned} \quad (\text{III.29})$$

where  $\mathbf{r}_i^t$  denotes the position of particle  $i$ ,  $\theta_i^t$  its orientation,  $\Delta r$  the amount of displacement,  $\mathcal{N}_i$  the averaging 'neighborhood' which is defined by spatial and angular proximity,  $\arg$  the argument of a complex number, and  $\delta\xi_i^t \in [-s\pi, s\pi]$  the (uniform) angular noise with an amplitude  $s$ . The superscript  $t$  marks the time dependence. Note that we have also introduced a randomization term

$$\Lambda_i^t = \begin{pmatrix} \Lambda_x \\ \Lambda_y \end{pmatrix} \cdot \begin{cases} 1 & \text{with probability } \gamma \\ 0 & \text{with probability } 1 - \gamma \end{cases}, \quad (\text{III.30})$$

with  $\Lambda_x, \Lambda_y \in [0, L]$  being uniformly distributed positions in the system of size  $L$ . This additional term resembles an effective mixing of the system, with each particle being randomly redistributed. By setting  $\gamma = 1$ , the system is 'well-mixed' and we can explicitly exclude the influence of spatial gradients to resolve the influence of local instabilities. The interaction neighborhood  $\mathcal{N}_i$  is defined as

$$\mathcal{N}_i = \{j \mid |\mathbf{r}_i - \mathbf{r}_j| \leq a \cap |\theta_i - \theta_j| \leq \phi\}, \quad (\text{III.31})$$

where all  $j$  are the corresponding particle indices,  $a$  is the neighborhood radius, and  $\phi$  the alignment cut-off. With these definitions at hand and setting  $\Delta r = 0.5$ ,  $a = 1$ , and  $L = 128$ , we have simulated various systems of Vicsek-like particles and concentrated on the effect of varying the noise  $s$ , the density  $\rho := M/L^2$ , and the cut-off angle  $\phi$ . Specifically, we have compared the two opposing limits of  $\gamma = 1$  (full re-shuffling at every step, no spatial gradients) and  $\gamma = 0$  (no re-shuffling). For the ordinary Vicsek model with  $\gamma = 0$  and  $\phi = \pi$  one recovers the Vicsek ordering paradigm where the onset of polar order  $(\rho_1, s_1)$  is accompanied by travelling polar fronts, and, for larger particle densities  $\rho$  or smaller noise strengths  $s$ , a homogeneous polar state emerges [45], with a global polar order parameter  $\mathcal{P}$ . For the limit  $\gamma = 1$ , no patterns in space can emerge since spatiotemporal correlations are suppressed. In Fig. III.28(a), we have plotted the hysteresis  $\Delta\mathcal{P} = \mathcal{P}^+ - \mathcal{P}^-$  to quantify the degree of discontinuity for different noise strength  $s$  and varying cut-off  $\phi$  for a fixed density of  $\rho = 2$ , where  $\mathcal{P}^+$  denotes the stationary polar order with perfectly ordered initial conditions and  $\mathcal{P}^-$  the corresponding polar order for random initial conditions. As expected for the supercritical behavior of the Vicsek class, no hysteresis is found for large  $\phi^* < \phi \lesssim \pi$  (Fig. III.28(a-b)), indicating a continuous transition on the level of homogeneous solutions. Upon decreasing  $\phi$ , the onset of order is subsequently shifted to smaller values of  $s_1$  or equivalently, larger  $\rho_1$ . Remarkably, for  $\phi$  below a certain threshold  $\phi^* \approx 0.75$  (corresponding to a value  $\bar{\psi} \cong \pi - \phi^* \approx 2.4$  for the kinetic model with restricted alignment in section 2.3.1, where we found  $\psi^* \approx 1.83$ ), a hysteresis loop develops, showing that the underlying transition is subcritical and discontinuous even in the absence of patterns. When  $\phi$  is further decreased, the hysteretic, bistable parameter region further grows. Despite all differences of the agent-based simulations with the kinetic mean-field analysis, this compares very well with the theoretical bifurcation scenario presented in section 2.3.1. In addition, the Vicsek simulations allow for a direct comparison of the homogeneous states (Fig. III.28(c)) with the full, spatially extended system when setting  $\gamma = 0$  as it is given for different values of  $\rho$  and  $s$  in Fig. III.28(d). Interestingly, in the vicinity of the onset in Fig. III.28(d), the spatially extended system exhibits bistability or subcritical behavior of the disordered state and polar patterns (which are analogous to Fig. III.28(g)), as it was already suggested in the linear stability analysis in Fig. III.25(c). However, this domain does not coincide with the corresponding bistable region of the reshuffled system ( $\gamma = 1$ , Fig. III.28(c)), but is shifted towards larger noise  $s$  above  $s_+$ . Furthermore, while the discontinuity of spatial patterns and the corresponding appearance of hysteresis is well-known for the Vicsek model [45, 46], the hysteretic region seems to be larger here. Deeper in the ordered phase, the hysteresis amplitude  $\Delta\mathcal{P}$  apparently grows again for both extended and well-mixed systems. Upon closer inspection, this turns out to stem from the formation of large, irregular clusters instead of polar fronts (Fig. III.28(f)); due to their prolonged coherence and the narrow interaction

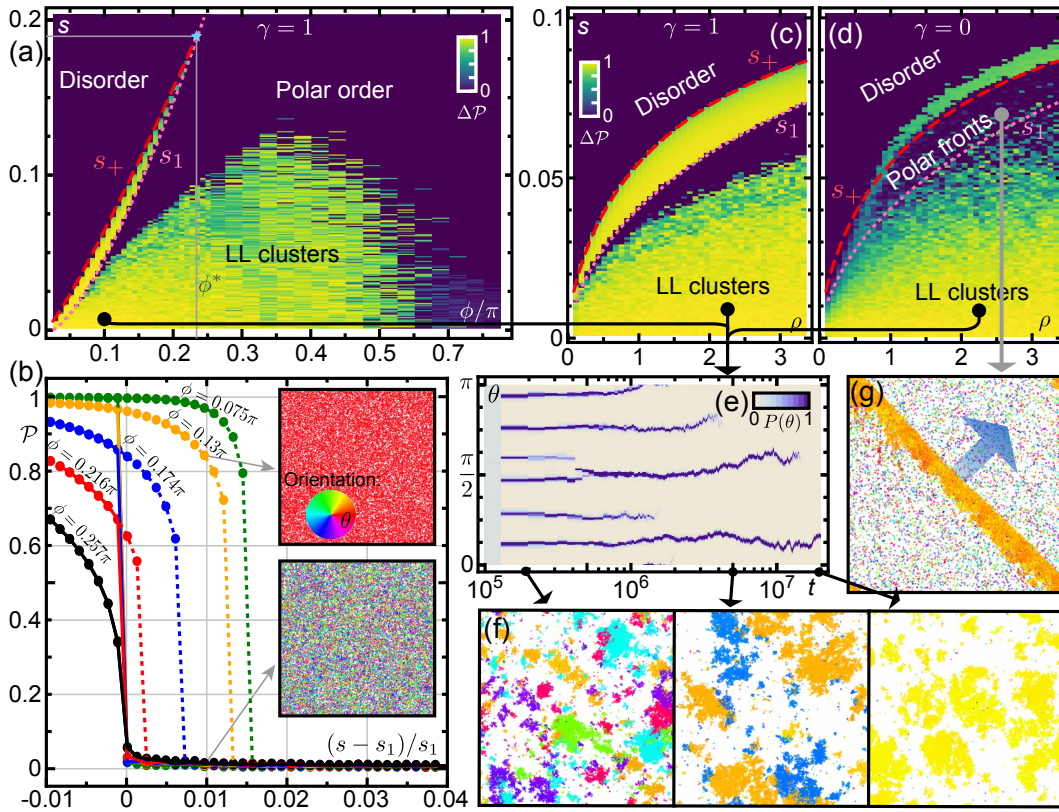


**Figure III.28** (a) Hysteresis map  $\Delta P$  as a function of  $\phi$  and  $s$  for the well-mixed system with  $\gamma = 1$ ,  $\rho = 2$ . The onset noise, below which polar order emerges, is denoted with  $s_1$  (short-dashed, rose line). The subcritical branch is bounded by  $s_+$  as shown by the long-dashed, red line. The critical point  $\phi^*$  is marked by a blue star. The large hysteretic region at low noise correspond to long-lived clusters (LL clusters), see also in (c,d) and the analysis in (e,f). (b) One dimensional slices through (a) in  $s$ -direction for different  $\phi$  (in units  $\pi$ ) illustrate the respective hysteresis loops. Insets: Snapshots of the system for different final states. (c) Hysteresis map as a function of  $\rho$  and  $s$ , for  $\gamma = 1$  and  $\phi = 0.1\pi$ . As in (a) we marked the domain boundaries of the subcritical branch with  $s_+$  and  $s_1$ , respectively. (d) Analogous plot to (c) of the spatially extended system with  $\gamma = 0$ .  $s_+$  and  $s_1$  are identical to (c) for reference. (e) Kymograph of the orientational distribution  $P(\theta)$  of the 'clustered' phase at  $\rho = 2.25$ ,  $s = 0.009$ ,  $\phi = 0.1\pi$ , and  $\gamma = 0$ . (f) Panels show corresponding snapshots at different times. (g) Snapshot of stationary polar pattern for  $\rho = 2.56$ ,  $s = 0.075$ ,  $\phi = 0.1$ , and  $\gamma = 0$ . Except for (e), we recorded the (nearly) stationary values of  $\mathcal{P}$  at a time  $t = 5 \cdot 10^4$ .

cone  $\phi \ll \pi$ , these structures are extremely long-lived and show only very slow coarsening. For the well-mixed system, these clusters exist too, but only in angular space.

Taken together, the modified Vicsek simulations experience a similar local bifurcation structure as predicted by the kinetic theory. For the spatially extended system, some differences arise to the standard Vicsek model, such as a prolonged subcritical region of wave-like polar patterns, or the formation of irregular clusters, which only exhibit extremely slow coarsening towards global order. To reveal further features beyond VOP such as the transitions predicted in Fig. III.27, one would need to further refine the update rules of the simulations, in particular concerning an angle dependence of the collision noise. Then, we would expect new types of patterns and phase transitions to emerge, similar to the prediction of section 2.5.2.

## 2.7 Summary and outlook

To conclude, in this section we have introduced a theoretical analysis of a variety of different interaction assumptions for active particles, by employing a kinetic Boltzmann approach on the mesoscopic level of fields and by direct agent-based simulations of a Vicsek-like model. In particular, the aim of this investigation was to provide a systematic comparison of the corresponding phase transitions and bifurcation scenarios with the original Vicsek model, and to identify more general organization principles of collective order formation. Let us briefly revisit and assess the questions that we have asked in the beginning:

1. *Is the phase transition from disorder to order universal?* Our study suggests that there is no such thing as a universal transition to polar order that describes all active systems, at least not in the sense of a (Vicsek) universality class. While for a particular set of alignment rules we indeed recover a supercritical bifurcation of the homogeneous polar state, accompanied by a square root dependence of the amplitude on the control parameter, a vast variety of other alignment rules exhibit a discontinuous transition to polar order, even on the homogeneous level. As a result, hydrodynamic equations of the slow modes, which have been central to analyze the emergence of order and patterns in the Vicsek model [42–44, 46, 47, 52, 54], break down and become non-physical. In this case, the ordered state depends on the full dynamics of a large number of contributing field modes. Importantly, this change of behavior is not exotic and can be triggered by only mild alterations of the most simple Vicsek alignment assumptions. Nevertheless, we still found that the onset of polar order is (mostly) accompanied by a long-wavelength (type II<sub>s</sub>) instability of the homogeneous states. It remains to be shown to which extent the subcriticality – and its associated nonlinearities – affect the formation of patterns, such as travelling fronts or flocks.

2. *How generic is the Vicsek ordering paradigm?* We found that the ordering 'paradigm' is model-specific, and depends crucially on the microscopic alignment assumptions. Foremost, we emphasize that the stability of the ubiquitously-mentioned homogeneous polar phase [19, 45, 50, 53–55] depends, in the kinetic theory, on the existence of a collision noise. Here the domain size of the uniformly-ordered phase exhibits a non-monotonous, power-law behavior as a function of the collision noise. Furthermore, while we found that there is always a 'band' of polar patterns in phase space, which separates the homogeneous states of the active system (that is, the disordered and the uniformly-ordered state), this region can be completely shifted or 'folded' onto the subcritical branch of the ordered states, and that makes a direct, discontinuous transition between the two homogeneous states possible.
3. *Can we identify generic criteria to classify (polar order) transitions?* In our kinetic approach, we indeed found a sufficient, analytical criterion for the bifurcation between a super- and a subcritical transition to polar order. In the language of Fourier-transformed collision integrals Eq. (III.15) this is given by the moments  $\mathcal{I}_{2,1} + \mathcal{I}_{-1,1} = 0$  and depends on the functional form of the alignment kernel  $\Phi(\Delta)$  and the collision noise  $\tilde{P}_k(\Delta)$  for different collision angles  $\Delta$ . Roughly speaking, the bifurcation can be triggered when alignment is dominated by acute scattering (small  $\Delta$ ), and misalignment by obtuse scattering (large  $\Delta$ ); note that misalignment can be achieved in various ways, by the absence of alignment, by anti-alignment, or by enhanced collision noise. Intriguingly, a typical, realistic situation of microscopic alignment interactions in agent-based or experimental active systems fulfils the requirements for a subcritical ordering transition, as it was already noted by Refs. [38, 56]. Consequently, we would expect that our findings are of utmost importance for those systems.

On more general grounds, our results demonstrate that, on the basis of a versatile parametrization of microscopic alignment assumptions, a variety of different bifurcation scenarios can be constructed. For instance, we found that there are always homogeneous ordered solutions which are unstable with respect to spatial perturbations, irrespective of them being rooting in either a supercritical or a subcritical bifurcation branch. Hence for some parameters, the steady state properties such as the full nonlinear patterns, may not be substantially different. Thus here, the local bifurcation structure (that is, without gradients) would only serve as a scaffold for patterns, similarly to reaction-diffusion systems [159, 160]. On the other hand, differences of the local criticality may become manifest in, for instance, affecting the time scales and dynamics of pattern formation from an initially disordered system. Furthermore, we found that subcriticality also allows for a direct transition from the disordered and a stable uniformly ordered state, which

would represent a new type of active matter phase transition.

As next steps, successive agent-based simulations are needed to access the stationary patterns in systems with generic alignment. This could be achieved, for instance, by probing the stationary states in systems with other Vicsek-like models with variable, angle-dependent collision noise, or with gradual alignment kernels, or by employing simulations with local and continuous spatio-temporal dynamics: in particular, the WASP simulations developed in chapter II can be readily employed to test polar order formation for arbitrary interaction dynamics of particles with various shapes, such as polymers, rods, or disks. Furthermore, one would need to extend the analytical investigation towards finding the inhomogeneous solutions of the systems, and to assess their stability. From this, one could rigorously test all nonlinear phenomena of the active system, similar to Refs. [43, 44, 46, 47]. However, this is a difficult task to achieve since lowest-order hydrodynamic equations break down. Here, direct numerical calculations of the full Boltzmann equation [55] and further agent-based simulations are needed to elucidate the dynamics of the active systems.

*What I cannot create, I do not understand.*

— Richard Feynman

## IV Conclusion

### 1 Discussion

To summarize this thesis, let us briefly revisit the main results of the previous chapters. In the presented projects, we addressed a fundamental question of nonequilibrium physics: how is self-organization in active systems affected by microscopic details? What is the influence of broken or competing particle symmetries on the emergent properties of a system? To which extent do active matter phase transitions depend on local processes and interactions?

First, in chapter II, we examined the influence of different types of symmetries on pattern formation and the emergence of order on the collective scale. In section 1, we have presented a theoretical investigation [157] of a recently-found experimental system with chiral active particles [6]; here, the bacterial cell division protein FtsZ forms curved polymers, which are attached to a flat membrane by anchor proteins in a reconstituted *in vitro* system, and effectively move along clockwise trajectories by a treadmilling assembly-disassembly mechanism. In this experiment, ring-like structures of FtsZ polymers are formed which closely resemble the Z-ring, a key component of the bacterial cell division machinery. Here, we performed both direct agent-based simulations of FtsZ polymers and a kinetic mean-field approach to study the underlying collective phenomena. Our analysis shows that even in the absence of cohesive forces, dynamic ring-like structures emerge spontaneously by the interplay of self-propulsion, curvature and steric repulsion alone. In this context, the patterns can be controlled by changing only the total density of filaments on the membrane. These predictions have subsequently been confirmed experimentally in a study by Ramirez et al. [7], who rigorously tested different anchoring mechanisms of FtsZ and filament densities. Furthermore, our study suggests that the active dynamics of FtsZ may also be essential for the cell division mechanism of bacteria. Despite still lacking understanding of the full process, recent studies have indeed found that active treadmilling is vital for the division of the bacterial cell [8–10]. On more general grounds, several authors have extended our investigation towards hydrodynamic effects of chiral active systems [11–14], or towards studying particle flocking in chiral, Vicsek-like models [15–17].

An interesting conjecture from this study is that altering the particle symmetries – albeit only slightly – has a crucial impact on the emergent properties of a reconstit-

uted biological system. Hence, this implies that such active systems may also be drastically affected by changing other constituent symmetries than particle motion. To this end, in section 2, we studied how collective order and its corresponding symmetry (nematic or polar) depends on the details of microscopic interactions between active particles, using the actin motility assay [21, 22, 124]. Based on experimental observations showing that the symmetry of alignment interactions between propelled actin filaments can be tuned by the presence of a depletion agent (section 2.1.2), we introduced a multiscale computational model of **Weakly-Aligning Self-propelled Polymers** (WASP's) which allows to simultaneously resolve physical processes on the scale of individual filaments and on collective scales of millions of objects (section 2.2.1). In our work (published in Ref. [127]), we combined both theory and experiment to rigorously analyze how polar and nematic order emerge as a function of alignment symmetry. Here, we showed that active matter systems are able to produce steady states that have no equilibrium analogue: the dynamic coexistence of patterns with polar and nematic symmetry for a broad range of control parameters (section 2.2.6). From a physical point of view, this shows that the famous Gibbs phase rule [28] and the universality principle [29, 30] do not hold for nonequilibrium systems. This disproves the prevailing paradigm of active matter, where order, symmetry, and phase transitions in active matter were thought to be robust [11, 19, 52, 62, 86, 161] – that is, to not depend on subtle details – and even share similarities to equilibrium systems [86, 162–167]. From a biological point of view, these striking results imply that the emergence of order in living systems is not necessarily constrained by underlying constituent symmetry, but is flexible enough to produce different types of order from identical building blocks and conditions. Hence, active and living matter are 'unchained' from the limitations of universality and the Gibbs phase rule.

These findings, which have revealed that emergent states of active matter refute an equilibrium-like description, call for a detailed assessment of the dynamics towards these ordered states. Therefore, chapter III is devoted to characterize the phase transitions of active matter, in particular for polar active systems, in the context of the microscopic details of local physical processes. In section 1 we employed the WASP model introduced in chapter II to study how individual active particles self-organize into different collective structures. This was achieved by a cluster decomposition method (section 1.2) which casts the system into clusters of different size, polar order, and nematic order. Here we showed that collective order already arises on the level of local particle clusters (section 1.3), and that the transition to global polar order is controlled by the constant turnover of clusters with different order (section 1.4). In essence, this transition and the ordered state can be described by the steady-state dynamics of two competing populations of particle clusters. Our analysis demonstrates that the essential dynamics of the

flocking state is represented by a cyclic steady-state flow in the 'phase space' of the cluster size - cluster order ensemble, analogous to stationary polar patterns encountered in mean-field theories which can be represented by closed orbits of a nonlinear system [43, 44, 46, 47]. This shows that the time scales associated with a cycling cluster flow are vital to understand the full dynamics of the emerging state. Furthermore, the cluster representation was also used to examine nematic pattern formation (section 1.5), which indicated that the onset of nematic order is associated with a synchronization of different time scales of filament cluster correlations.

Finally, in section 2 of chapter III we studied the robustness of the Vicsek ordering paradigm and its associated bifurcation structure when the microscopic alignment rules depart from the simplified assumptions of Vicsek. Specifically, using a kinetic mean-field approach for mesoscopic length scales we found that the local stability of the order-disorder onset changes – from an originally supercritical bifurcation – to a subcritical ordering transition. This changed scenario appears to be generic for realistic alignment assumptions, where alignment is dominated by acute scattering events and misalignment is promoted by obtuse scattering (section 2.4). By assessing the lateral stability of homogeneous solutions, we found that the stability of a homogeneous polar state crucially depends on the existence of collision noise, also for the original Vicsek case as studied by Bertin and coworkers [42, 52, 54] (section 2.5.1). In total, versatile alignment models exhibit previously unseen bifurcation structure, like a stable coexistence of the disordered and the uniformly polar state (section 2.5.2). We also performed agent-based simulations of a Vicsek-like model which confirmed a subcritical transition of the homogeneous states (section 2.2). Taken together, our investigation shows that the Vicsek ordering paradigm and its associated Vicsek class is rather the exception than the rule, and in general, there exists a whole zoo of different states, patterns, and corresponding transitions.

In conclusion, we found that the microscopic details of active matter systems have a decisive impact on the collective properties and self-organization – to such an extent, that a reduction of the full active system onto a few relevant parameters or length scales is often not possible. In this context, a variety of unique phenomena arise, like the generic three-phase coexistence of ordered states or the malleable bifurcation structure of ordering transitions, which, in general, defy a description analogous to equilibrium physics. This calls for multi-scale research approaches to assess the physical properties on all necessary length scales of an active system. An exciting consequence of this is that especially in experimental systems with a complex micro-structure, new and unexpected emergent features may appear.

## 2 Outlook

From the results presented in this thesis, a couple of outstanding research questions arise. For the pattern formation in the FtsZ system (section 1, chapter II), it would be exciting to successively approach the full complexity of the bacterial cell division. As a first step, one would need to study how patterns emerge within a cylindrical cell geometry and to which extent the interaction of substrate and filament curvature affects self-organization. Here, additional spatial cues might be relevant; for instance, it was found that FtsZ filaments not only form curved, but also intrinsically twisted filaments [168–171] which could give rise to helical trajectories of treadmilling in a cylindrical geometry such as the bacterial cell membrane. Furthermore, it remains to be examined how a stable treadmilling process of FtsZ filaments can be maintained by complex interactions with anchoring [6, 7, 98] or inhibitory proteins [172, 173].

In the experiments with the actin motility assay in section 2.3, chapter II, a

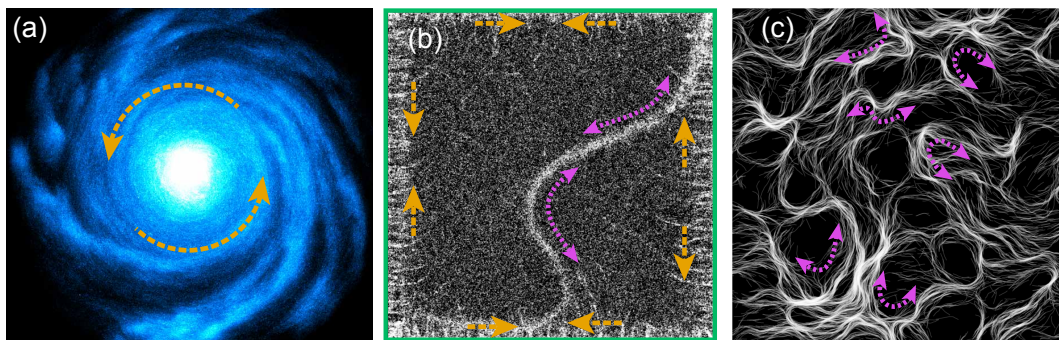


**Figure IV.1** (a) Rotating actin swirl, with a diameter of  $\sim 0.5\text{mm}$ . (b) Large-scale WASP simulations with hard boundaries (green box) and coexisting patterns (parameters like in Fig. II.24). Polar fronts are concentrated in the vicinity of the wall, nematic trails in the middle. (c) High-density WASP simulations ( $\rho_0 L^2 = 30$ ). Orange arrows illustrate polar motion, pink arrows nematic motion, respectively.

variety of interesting phenomena were found, but a systematic examination is still lacking. For instance, we saw stable, rotating actin swirls (Fig. IV.1(a)), or the emergence of an almost regular array of nematic vortices for very large PEG concentrations (Fig. II.33(e)); in this regime we also observed the formation of previously unreported, active actin bundles (Fig. II.33(d)). In addition, we noticed that the processivity of actin filaments – and their corresponding collective patterns – can also be tuned without crowding agents such as PEG, for instance by changing the assay buffer dilution. For all of these observations, a theoretical comprehension has yet to be developed. As for the coexistence of polar and nematic order, which was also confirmed by agent-based simulations, a deeper insight into the underlying

mechanisms from a kinetic point of view would be desirable. In this context, the strong sensitivity of the emergent patterns on the local alignment interactions could be exploited to create an 'adaptive' active system: slight spatial heterogeneities of local alignment would hence lead to large gradients of the emergent properties, and would even allow to tune them from the outside. Furthermore, we would expect similar types 'anomalous' coexistence of mutually exclusive, emergent states also in different active systems. Since the coexistence of polar and nematic order requires a mixed type of underlying alignment symmetry, the presence of competing 'target states' (or *attractors*) seems to be essential and could also play a role for other collective phenomena.

These and more question can be readily addressed from a theoretical point by employing simulations of the WASP model (section 2.2). Specifically, it remains to be analyzed how spatial boundaries allow to locate and control the emergent properties of the active system. Preliminary results show that already simple domain boundaries suffice to segregate different types of collective order (Fig. IV.1(b)). Furthermore, up to now only a small parameter region of the WASP model has been explored, and a systematic investigation beyond this regime could likely reveal many more unexpected phenomena. For example, individual simulations in the high-density or long-filament limit  $\rho_0 L^2 \gg 1$  show an intriguing steady state (Fig. IV.1(c)), which is composed of dynamic streams, and the creation and annihilation of topological defects, similarly to related systems such as active nematics [33, 61, 62, 161].

On more general grounds, the WASP model also allows to rigorously test the influence of polydisperse active particle ensembles; by assigning every entity different local properties instead of identical ones, such as different filament lengths, velocities, persistence lengths, or interaction parameters. This is highly important for a broad range of experimental systems such as animal swarms [174–178], where the constituent particles are inherently polydisperse, and agent-based simulations of the WASP model could readily address the relevance of leadership self-organization or demixing of different collectives.

### 3 Future perspectives

To conclude my thesis, I would like to express my opinion on the general course and the latest developments of active matter research and personally review its current state of affairs. Since the advent of the field in 1995 when Vicsek published his seminal work [49], a true plethora of new phenomena and model systems have been found and explored. While there are a multitude of different types of research directions and methodologies in literature (please resort to reviews [19, 53, 57, 86] for a complete list), theoreticians have particularly focused on approaching

collective phenomena using methods of statistical physics and its corresponding terminology (e.g. 'phase transition', 'equation of state', 'universality', etc.). So far, this scheme has been quite successful and researchers were able to show how active matter systems, which are inherently out of equilibrium, depart from equilibrium counterparts [179]. Examples of this would be the violation of the Mermin-Wagner theorem by the long-range order of polar flocking [50], or phase coexistence without common Maxwell construction [167], or broken universality [127]. As a result, it seems to me that many such properties of statistical mechanics are tacitly assumed to also hold for active systems until someone proves otherwise. While it is certainly important to reveal and highlight these anomalous properties, this route towards a 'grand theory' of nonequilibrium statistical mechanics could turn out to be inherently flawed – and the suspicion arises that this is nothing more than a successive stripping of the hallmarks of equilibrium statistics. Since building a rigorous theory of active matter systems from first principles might be very difficult or even impossible, adapting adequate methods and terminology from different research disciplines could be very beneficial. Specifically, active systems might in general be better described by the theory of nonlinear systems of spatially extended systems, instead of thermodynamics; by specifying *attractors* and *bifurcations* rather than *phases* and *phase transitions*. Ultimately, it remains to be seen whether it is possible to generalize active matter into a unifying framework, or whether it stays a vast collection of different case studies.

From a different point of view, as already outlined in the introduction of this thesis, the declared objective of active matter is to understand the physics of living systems, as it is also highlighted in this popular article [180]. In my opinion, it would be very fruitful if research would focus more on the role, functions, and behavior of active systems that are embedded in a more complex system, e.g. within a living organism or within a community of agents with various social interactions and different objectives; rather than the study of individual, isolated systems that rely on simplistic assumptions. Just like active matter was initially designed to understand *how* birds flock, one should start to address the more complex question *why* birds flock. After all, self-organization in living systems is hardly understood, and research in this area has only just begun. Exciting fields are emerging here which promise new insights, for example the connection of active matter system with the (evolutionary) dynamics of populations [176]: here little is known about active motion – or migration of the collective – as an additional 'strategy' in the sense of game theory. In a similar fashion, many macroscopic active systems, from microbial communities to large animal groups or socio-economic scenarios, consist of complex entities, which are able to memorize and learn from their environment, and ultimately adapt their behavior or motility. Here, further research is necessary to quantitatively assess the interplay of learning and activity, which was previously only described in a phenomenological fashion [177]. Overall, it is important to bear

in mind that living active systems are often only functional units of a larger complex system, and it is widely unexplored how active systems are affected by a dynamical feedback with a surrounding environment. As knowledge about this functionality progresses (e.g. polar motion  $\cong$  uni-directional transport vs. nematic motion  $\cong$  bi-directional transport), active systems could potentially serve as artificial, self-organized machines: very simple examples of such active machines that exploit spontaneous motion would be bacteria-propelled micro-rotors [181, 182], driven obstacles [183] or even logical gates [184]. Taken together, I believe that active matter physics has the potential to change the comprehension of living systems, with many fascinating results beyond the well-trodden paths of equilibrium physics still to come.



## Bibliography

- [1] P. W. Anderson. More Is Different. *Science* **177**(4047), 393–396, 1972. DOI: [10.1126/science.177.4047.393](https://doi.org/10.1126/science.177.4047.393). (Cit. on p. ix).
- [2] P. J. Buske, A. Mittal, R. V. Pappu and P. A. Levin. An intrinsically disordered linker plays a critical role in bacterial cell division. *Seminars in Cell & Developmental Biology*, 2014. DOI: [10.1016/j.semcdb.2014.09.017](https://doi.org/10.1016/j.semcdb.2014.09.017). (Cit. on pp. x, 12).
- [3] E. L. Meier and E. D. Goley. Form and function of the bacterial cytokinetic ring. *Curr. Opin. Cell Biol.* **26**, 19–27, 2014. DOI: [10.1016/j.ceb.2013.08.006](https://doi.org/10.1016/j.ceb.2013.08.006). (Cit. on pp. x, 12).
- [4] M. A. Oliva, S. C. Cordell and J. Löwe. Structural insights into FtsZ protofilament formation. *Nat. Struct. Mol. Biol.* **11**(12), 1243–1250, 2004. DOI: [10.1038/nsmb855](https://doi.org/10.1038/nsmb855). (Cit. on pp. x, 12).
- [5] M. Osawa, D. E. Anderson and H. P. Erickson. Curved FtsZ protofilaments generate bending forces on liposome membranes. *EMBO J.* **28**(22), 3476–3484, 2009. DOI: [10.1038/emboj.2009.277](https://doi.org/10.1038/emboj.2009.277). (Cit. on pp. x, 12).
- [6] M. Loose and T. J. Mitchison. The bacterial cell division proteins FtsA and FtsZ self-organize into dynamic cytoskeletal patterns. *Nat. Cell Biol.* **16**(1), 38–46, 2013. DOI: [10.1038/ncb2885](https://doi.org/10.1038/ncb2885). (Cit. on pp. x, xi, 6, 12, 13, 17, 19, 31, 154, 201, 204).
- [7] D. A. Ramirez-Diaz, D. A. García-Soriano, A. Raso, J. Mücksch, M. Feingold, G. Rivas and P. Schwill. Treadmilling analysis reveals new insights into dynamic FtsZ ring architecture. *PLOS Biology* **16**(5), e2004845, 2018. DOI: [10.1371/journal.pbio.2004845](https://doi.org/10.1371/journal.pbio.2004845). (Cit. on pp. x, 13, 30, 201, 204).
- [8] A. W. Bisson-Filho, Y.-P. Hsu, G. R. Squyres, E. Kuru, F. Wu, C. Jukes, Y. Sun, C. Dekker, S. Holden, M. S. VanNieuwenhze *et al.* Treadmilling by FtsZ filaments drives peptidoglycan synthesis and bacterial cell division. *Science* **355**(6326), 739–743, 2017. (Cit. on pp. x, 30, 201).
- [9] X. Yang, Z. Lyu, A. Miguel, R. McQuillen, K. C. Huang and J. Xiao. GTPase activity-coupled treadmilling of the bacterial tubulin FtsZ organizes septal cell wall synthesis. *Science* **355**(6326), 744–747, 2017. (Cit. on pp. x, 30, 201).

- [10] K. M. Schoenemann and W. Margolin. Bacterial Division: FtsZ treadmills to build a beautiful wall. *Current Biology* **27**(8), R301–R303, 2017. (Cit. on pp. [x](#), [30](#), [201](#)).
- [11] B. C. van Zuiden, J. Paulose, W. T. Irvine, D. Bartolo and V. Vitelli. Spatiotemporal order and emergent edge currents in active spinner materials. *Proceedings of the National Academy of Sciences* **113**(46), 12919–12924, 2016. (Cit. on pp. [x](#), [201](#), [202](#)).
- [12] W. Liu, W. Yu, C. Yang, M. Liu, Y. Zhang and M. Lei. Analytic solutions for the generalized complex Ginzburg–Landau equation in fiber lasers. *Nonlinear Dynamics* **89**(4), 2933–2939, 2017. (Cit. on pp. [x](#), [201](#)).
- [13] D. Banerjee, A. Souslov, A. G. Abanov and V. Vitelli. Odd viscosity in chiral active fluids. *Nature Communications* **8**(1), 1573, 2017. (Cit. on pp. [x](#), [201](#)).
- [14] T. Banerjee and A. Basu. Active hydrodynamics of synchronization and ordering in moving oscillators. *Physical Review E* **96**(2), 022201, 2017. (Cit. on pp. [x](#), [201](#)).
- [15] B. Liebchen and D. Levis. Collective behavior of chiral active matter: pattern formation and enhanced flocking. *Physical review letters* **119**(5), 058002, 2017. (Cit. on pp. [x](#), [201](#)).
- [16] D. Levis and B. Liebchen. Micro-flock patterns and macro-clusters in chiral active Brownian disks. *Journal of Physics: Condensed Matter* **30**(8), 084001, 2018. (Cit. on pp. [x](#), [201](#)).
- [17] G.-J. Liao and S. H. Klapp. Clustering and phase separation of circle swimmers dispersed in a monolayer. *Soft matter* **14**(38), 7873–7882, 2018. (Cit. on pp. [x](#), [201](#)).
- [18] T. Vicsek and A. Zafeiris. Collective motion. *Physics Reports* **517**(3), 71–140, 2012. DOI: <http://arxiv.org/abs/1207.2929>. (Cit. on pp. [xi](#), [1](#), [2](#), [5](#), [68](#), [84](#), [171](#)).
- [19] M. C. Marchetti, J. F. Joanny, S. Ramaswamy, T. B. Liverpool, J. Prost, M. Rao and R. A. Simha. Hydrodynamics of soft active matter. *Rev. Mod. Phys.* **85**, 1143–1189, 2013. DOI: [10.1103/RevModPhys.85.1143](https://doi.org/10.1103/RevModPhys.85.1143). (Cit. on pp. [xi](#), [xiii](#), [1](#), [5](#), [18](#), [121](#), [126](#), [171](#), [199](#), [202](#), [205](#)).
- [20] J. Deseigne, O. Dauchot and H. Chaté. Collective Motion of Vibrated Polar Disks. *Physical Review Letters* **105**(9), 2010. DOI: [10.1103/PhysRevLett.105.098001](https://doi.org/10.1103/PhysRevLett.105.098001). (Cit. on pp. [xi](#), [xii](#), [2](#), [136](#), [176](#), [184](#)).
- [21] V. Schaller, C. A. Weber, C. Semmrich, E. Frey and A. R. Bausch. Polar patterns of driven filaments. *Nature* **467**(7311), 73–7, 2010. DOI: [10.1038/nature09312](https://doi.org/10.1038/nature09312). (Cit. on pp. [xi](#), [xii](#), [2](#), [4](#), [6](#), [49](#), [77](#), [78](#), [202](#)).

- [22] T. Butt, T. Mufti, A. Humayun, P. B. Rosenthal, S. Khan, S. Khan and J. E. Molloy. Myosin Motors Drive Long Range Alignment of Actin Filaments. *Journal of Biological Chemistry* **285**(7), 4964–4974, 2010. DOI: [10.1074/jbc.M109.044792](https://doi.org/10.1074/jbc.M109.044792). (Cit. on pp. xi, xii, 2, 49, 78, 202).
- [23] A. Bricard, J.-B. Caussin, N. Desreumaux, O. Dauchot and D. Bartolo. Emergence of macroscopic directed motion in populations of motile colloids. *Nature* **503**(7474), 95–98, 2013. DOI: [10.1038/nature12673](https://doi.org/10.1038/nature12673). (Cit. on pp. xi, xii, 2, 4).
- [24] D. Inoue, B. Mahmot, A. M. R. Kabir, T. I. Farhana, K. Tokuraku, K. Sada, A. Konagaya and A. Kakugo. Depletion force induced collective motion of microtubules driven by kinesin. *Nanoscale* **7**(43), 18054–18061, 2015. DOI: [10.1039/C5NR02213D](https://doi.org/10.1039/C5NR02213D). (Cit. on pp. xi, 4, 47, 83).
- [25] Y. Sumino, K. H. Nagai, Y. Shitaka, D. Tanaka, K. Yoshikawa, H. Chaté and K. Oiwa. Large-scale vortex lattice emerging from collectively moving microtubules. *Nature* **483**(7390), 448–452, 2012. DOI: [10.1038/nature10874](https://doi.org/10.1038/nature10874). (Cit. on pp. xi, 2, 4, 6, 19, 47, 83, 154, 176, 184).
- [26] R. Suzuki, C. A. Weber, E. Frey and A. R. Bausch. Polar pattern formation in driven filament systems requires non-binary particle collisions. *Nat Phys* **11**(10), 839–843, 2015. DOI: [10.1038/nphys3423](https://doi.org/10.1038/nphys3423). (Cit. on pp. xi, xii, 49–51, 53, 61, 76, 77, 121, 176, 184).
- [27] D. Nishiguchi, K. H. Nagai, H. Chaté and M. Sano. Long-Range Nematic Order and Anomalous Fluctuations in Suspensions of Swimming Filamentous Bacteria. *Physical Review E* **95**(2), 2017. DOI: [10.1103/PhysRevE.95.020601](https://doi.org/10.1103/PhysRevE.95.020601). (Cit. on pp. xi, 154, 176, 184).
- [28] J. W. Gibbs. *The scientific papers of JW Gibbs, vol. 1*. 1961 (cit. on pp. xi, 83, 202).
- [29] L. P. Kadanoff. Scaling laws for Ising models near T c. *Physics Physique Fizika* **2**(6), 263, 1966. (Cit. on pp. xi, 4, 83, 202).
- [30] K. G. Wilson. The renormalization group: Critical phenomena and the Kondo problem. *Reviews of modern physics* **47**(4), 773, 1975. (Cit. on pp. xi, 4, 83, 202).
- [31] D. A. Fletcher and P. L. Geissler. Active Biological Materials. *Annual Review of Physical Chemistry* **60**(1), 469–486, 2009. DOI: [10.1146/annurev.physchem.040808.090304](https://doi.org/10.1146/annurev.physchem.040808.090304). (Cit. on pp. xi, 5, 84).
- [32] L. Blanchoin, R. Boujemaa-Paterski, C. Sykes and J. Plastino. Actin Dynamics, Architecture, and Mechanics in Cell Motility. *Physiological Reviews* **94**(1), 235–263, 2014. DOI: [10.1152/physrev.00018.2013](https://doi.org/10.1152/physrev.00018.2013). (Cit. on pp. xi, 2, 5, 84).

- [33] K. Kawaguchi, R. Kageyama and M. Sano. Topological defects control collective dynamics in neural progenitor cell cultures. *Nature*, 2017. DOI: [10.1038/nature22321](https://doi.org/10.1038/nature22321). (Cit. on pp. xi, 5, 84, 154, 205).
- [34] T. B. Saw, A. Doostmohammadi, V. Nier, L. Kocgozlu, S. Thampi, Y. Toyama, P. Marcq, C. T. Lim, J. M. Yeomans and B. Ladoux. Topological defects in epithelia govern cell death and extrusion. *Nature* **544**(7649), 212–216, 2017. DOI: [10.1038/nature21718](https://doi.org/10.1038/nature21718). (Cit. on pp. xi, 5, 84, 154).
- [35] J. Deseigne, S. Léonard, O. Dauchot and H. Chaté. Vibrated Polar Disks: Spontaneous Motion, Binary Collisions, and Collective Dynamics. *Soft Matter* **8**(20), 5629, 2012. DOI: [10.1039/c2sm25186h](https://doi.org/10.1039/c2sm25186h). (Cit. on p. xii).
- [36] C. A. Weber, T. Hanke, J. Deseigne, S. Léonard, O. Dauchot, E. Frey and H. Chaté. Long-Range Ordering of Vibrated Polar Disks. *Physical Review Letters* **110**(20), 2013. DOI: [10.1103/PhysRevLett.110.208001](https://doi.org/10.1103/PhysRevLett.110.208001). (Cit. on pp. xii, 4, 6, 176, 184).
- [37] S. Hussain, J. E. Molloy and S. M. Khan. Spatiotemporal Dynamics of Actomyosin Networks. *Biophysical Journal* **105**(6), 1456–1465, 2013. DOI: [10.1016/j.bpj.2013.08.001](https://doi.org/10.1016/j.bpj.2013.08.001). (Cit. on pp. xii, 49, 176, 184).
- [38] K.-D. N. T. Lam, M. Schindler and O. Dauchot. Self-propelled hard disks: implicit alignment and transition to collective motion. *New Journal of Physics* **17**(11), 113056, 2015. DOI: [10.1088/1367-2630/17/11/113056](https://doi.org/10.1088/1367-2630/17/11/113056). (Cit. on pp. xii, xiii, 122, 125, 171, 177, 181, 199).
- [39] A. Kaiser, A. Snezhko and I. S. Aranson. Flocking Ferromagnetic Colloids. *Science Advances* **3**(2), e1601469, 2017. (Cit. on p. xii).
- [40] G. Grégoire, H. Chaté and Y. Tu. Moving and staying together without a leader. *Physica D: Nonlinear Phenomena* **181**(3), 157–170, 2003. DOI: [10.1016/S0167-2789\(03\)00102-7](https://doi.org/10.1016/S0167-2789(03)00102-7). (Cit. on pp. xii, xiii, 6, 63).
- [41] G. Grégoire and H. Chaté. Onset of Collective and Cohesive Motion. *Physical Review Letters* **92**(2), 2004. DOI: [10.1103/PhysRevLett.92.025702](https://doi.org/10.1103/PhysRevLett.92.025702). (Cit. on pp. xii, 3, 176).
- [42] E. Bertin, M. Droz and G. Grégoire. Boltzmann and Hydrodynamic Description for Self-Propelled Particles. *Physical Review E* **74**(2), 2006. DOI: [10.1103/PhysRevE.74.022101](https://doi.org/10.1103/PhysRevE.74.022101). (Cit. on pp. xii, xiii, 3, 6, 19, 20, 51, 63, 84, 121, 171, 172, 176, 189, 198, 203).
- [43] A. P. Solon and J. Tailleur. Revisiting the Flocking Transition Using Active Spins. *Physical Review Letters* **111**(7), 2013. DOI: [10.1103/PhysRevLett.111.078101](https://doi.org/10.1103/PhysRevLett.111.078101). (Cit. on pp. xii, 63, 121, 122, 127, 149, 193, 198, 200, 203).

- [44] A. P. Solon and J. Tailleur. Flocking with Discrete Symmetry: The Two-Dimensional Active Ising Model. *Physical Review E* **92**(4), 042119, 2015. DOI: [10.1103/PhysRevE.92.042119](https://doi.org/10.1103/PhysRevE.92.042119). (Cit. on pp. [xii](#), [4](#), [121](#), [122](#), [127](#), [149](#), [193](#), [198](#), [200](#), [203](#)).
- [45] H. Chaté, F. Ginelli, G. Grégoire and F. Raynaud. Collective Motion of Self-Propelled Particles Interacting without Cohesion. *Physical Review E* **77**(4), 2008. DOI: [10.1103/PhysRevE.77.046113](https://doi.org/10.1103/PhysRevE.77.046113). (Cit. on pp. [xii](#), [xiii](#), [3](#), [6](#), [18](#), [26](#), [30](#), [63](#), [84](#), [121](#), [122](#), [126](#), [127](#), [176](#), [196](#), [199](#)).
- [46] A. P. Solon, H. Chaté and J. Tailleur. From Phase to Microphase Separation in Flocking Models: The Essential Role of Nonequilibrium Fluctuations. *Physical Review Letters* **114**(6), 2015. DOI: [10.1103/PhysRevLett.114.068101](https://doi.org/10.1103/PhysRevLett.114.068101). (Cit. on pp. [xii](#), [121](#), [122](#), [127](#), [149](#), [193](#), [196](#), [198](#), [200](#), [203](#)).
- [47] J.-B. Caussin, A. Solon, A. Peshkov, H. Chaté, T. Dauxois, J. Tailleur, V. Vitelli and D. Bartolo. Emergent Spatial Structures in Flocking Models: A Dynamical System Insight. *Physical Review Letters* **112**(14), 148102, 2014. DOI: [10.1103/PhysRevLett.112.148102](https://doi.org/10.1103/PhysRevLett.112.148102). (Cit. on pp. [xii](#), [63](#), [121](#), [122](#), [149](#), [193](#), [198](#), [200](#), [203](#)).
- [48] R. P. Sear. Nucleation: theory and applications to protein solutions and colloidal suspensions. *Journal of Physics: Condensed Matter* **19**(3), 033101, 2007. (Cit. on pp. [xii](#), [138](#)).
- [49] T. Vicsek, A. Czirók, E. Ben-Jacob, I. Cohen and O. Shochet. Novel Type of Phase Transition in a System of Self-Driven Particles. *Phys. Rev. Lett.* **75**(6), 1226–1229, 1995. DOI: [10.1103/PhysRevLett.75.1226](https://doi.org/10.1103/PhysRevLett.75.1226). (Cit. on pp. [xiii](#), [2](#), [3](#), [6](#), [10](#), [18](#), [55](#), [176](#), [205](#)).
- [50] J. Toner and Y. Tu. Long-range order in a two-dimensional dynamical XY model: how birds fly together. *Phys. Rev. Lett.* **75**(23), 4326, 1995. DOI: [10.1103/PhysRevLett.75.4326](https://doi.org/10.1103/PhysRevLett.75.4326). (Cit. on pp. [xiii](#), [3](#), [4](#), [21](#), [84](#), [121](#), [174](#), [199](#), [206](#)).
- [51] S. Mishra, A. Baskaran and M. C. Marchetti. Fluctuations and pattern formation in self-propelled particles. *Phys. Rev. E* **81**, 061916, 2010. DOI: [10.1103/PhysRevE.81.061916](https://doi.org/10.1103/PhysRevE.81.061916). (Cit. on pp. [xiii](#), [4](#), [21](#), [63](#)).
- [52] A. Peshkov, E. Bertin, F. Ginelli and H. Chaté. Boltzmann-Ginzburg-Landau approach for continuous descriptions of generic Vicsek-like models. *Eur. Phys. J.-Spec. Top.* **223**(7), 1315–1344, 2014. DOI: [10.1140/epjst/e2014-02193-y](https://doi.org/10.1140/epjst/e2014-02193-y). (Cit. on pp. [xiii](#), [3](#), [4](#), [7](#), [19](#), [20](#), [27](#), [28](#), [64](#), [68](#), [84](#), [121](#), [171–173](#), [176](#), [189](#), [198](#), [202](#), [203](#)).

- [53] J. Toner, Y. Tu and S. Ramaswamy. Hydrodynamics and phases of flocks. *Annals of Physics* **318**(1), 170–244, 2005. DOI: [10.1016/j.aop.2005.04.011](https://doi.org/10.1016/j.aop.2005.04.011). (Cit. on pp. [xiii](#), [5](#), [121](#), [126](#), [171](#), [199](#), [205](#)).
- [54] E. Bertin, M. Droz and G. Grégoire. Hydrodynamic equations for self-propelled particles: microscopic derivation and stability analysis. *J. Phys. A-Math. Theor.* **42**(44), 445001, 2009. (Cit. on pp. [xiii](#), [3](#), [4](#), [18–21](#), [23](#), [24](#), [27](#), [51](#), [121](#), [171](#), [172](#), [176](#), [188](#), [189](#), [198](#), [199](#), [203](#)).
- [55] F. Thüroff, C. A. Weber and E. Frey. Numerical Treatment of the Boltzmann Equation for Self-Propelled Particle Systems. *Phys. Rev. X* **4**, 041030, 2014. DOI: [10.1103/PhysRevX.4.041030](https://doi.org/10.1103/PhysRevX.4.041030). (Cit. on pp. [xiii](#), [4](#), [19](#), [20](#), [25](#), [26](#), [121](#), [172](#), [176](#), [188](#), [199](#), [200](#)).
- [56] K.-D. N. T. Lam, M. Schindler and O. Dauchot. Polar active liquids: a universal classification rooted in nonconservation of momentum. *Journal of Statistical Mechanics: Theory and Experiment* **2015**(10), P10017, 2015. DOI: [10.1088/1742-5468/2015/10/P10017](https://doi.org/10.1088/1742-5468/2015/10/P10017). (Cit. on pp. [xiii](#), [6](#), [122](#), [125](#), [171](#), [177](#), [181](#), [199](#)).
- [57] S. Ramaswamy. The Mechanics and Statistics of Active Matter. *Annual Review of Condensed Matter Physics* **1**(1), 323–345, 2010. DOI: [10.1146/annurev-conmatphys-070909-104101](https://doi.org/10.1146/annurev-conmatphys-070909-104101). (Cit. on pp. [1](#), [5](#), [68](#), [171](#), [205](#)).
- [58] D. Helbing. Traffic and related self-driven many-particle systems. *Reviews of modern physics* **73**(4), 1067, 2001. (Cit. on p. [2](#)).
- [59] J. L. Silverberg, M. Bierbaum, J. P. Sethna and I. Cohen. Collective motion of humans in mosh and circle pits at heavy metal concerts. *Physical review letters* **110**(22), 228701, 2013. (Cit. on p. [2](#)).
- [60] M. J. Shelley. The Dynamics of Microtubule/Motor-Protein Assemblies in Biology and Physics. *Annual Review of Fluid Mechanics* **48**(1), 487–506, 2016. DOI: [10.1146/annurev-fluid-010814-013639](https://doi.org/10.1146/annurev-fluid-010814-013639). (Cit. on p. [2](#)).
- [61] T. Sanchez, D. T. N. Chen, S. J. DeCamp, M. Heymann and Z. Dogic. Spontaneous motion in hierarchically assembled active matter. *Nature* **491**(7424), 431–434, 2012. DOI: [10.1038/nature11591](https://doi.org/10.1038/nature11591). (Cit. on pp. [2](#), [205](#)).
- [62] F. C. Keber, E. Loiseau, T. Sanchez, S. J. DeCamp, L. Giomi, M. J. Bowick, M. C. Marchetti, Z. Dogic and A. R. Bausch. Topology and dynamics of active nematic vesicles. *Science* **345**(6201), 1135–1139, 2014. (Cit. on pp. [2](#), [202](#), [205](#)).
- [63] H.-R. Jiang, N. Yoshinaga and M. Sano. Active motion of a Janus particle by self-thermophoresis in a defocused laser beam. *Physical review letters* **105**(26), 268302, 2010. (Cit. on p. [2](#)).

- [64] A. Kudrolli, G. Lumay, D. Volfson and L. Tsimring. Swarming and Swirling in Self-Propelled Polar Granular Rods. *Phys. Rev. Lett.* **100**(5), 058001, 2008. DOI: [10.1103/PhysRevLett.100.058001](https://doi.org/10.1103/PhysRevLett.100.058001). (Cit. on pp. 2, 6).
- [65] A. E. Turgut, H. Çelikkanat, F. Gökçe and E. Şahin. Self-organized flocking in mobile robot swarms. *Swarm Intelligence* **2**(2-4), 97–120, 2008. (Cit. on p. 2).
- [66] M. Aldana, V. Dossetti, C. Huepe, V. Kenkre and H. Larralde. Phase transitions in systems of self-propelled agents and related network models. *Physical review letters* **98**(9), 095702, 2007. (Cit. on pp. 3, 6, 176).
- [67] B. Gönci, M. Nagy and T. Vicsek. Phase transition in the scalar noise model of collective motion in three dimensions. *The European Physical Journal Special Topics* **157**(1), 53–59, 2008. (Cit. on pp. 3, 6, 176).
- [68] N. D. Mermin and H. Wagner. Absence of Ferromagnetism or Antiferromagnetism in One- or Two-Dimensional Isotropic Heisenberg Models. *Physical Review Letters* **17**(22), 1133–1136, 1966. DOI: [10.1103/PhysRevLett.17.1133](https://doi.org/10.1103/PhysRevLett.17.1133). (Cit. on p. 3).
- [69] J. Toner and Y. Tu. Flocks, herds, and schools: A quantitative theory of flocking. *Physical Review E* **58**(4), 4828–4858, 1998. DOI: [10.1103/PhysRevE.58.4828](https://doi.org/10.1103/PhysRevE.58.4828). (Cit. on pp. 3, 4, 174).
- [70] T. B. Liverpool and M. C. Marchetti. Instabilities of Isotropic Solutions of Active Polar Filaments. *Physical Review Letters* **90**(13), 2003. DOI: [10.1103/PhysRevLett.90.138102](https://doi.org/10.1103/PhysRevLett.90.138102). (Cit. on pp. 4, 6).
- [71] L. Giomi, M. C. Marchetti and T. B. Liverpool. Complex Spontaneous Flows and Concentration Banding in Active Polar Films. *Physical Review Letters* **101**(19), 2008. DOI: [10.1103/PhysRevLett.101.198101](https://doi.org/10.1103/PhysRevLett.101.198101). (Cit. on p. 4).
- [72] A. Baskaran and M. C. Marchetti. Hydrodynamics of self-propelled hard rods. *Phys. Rev. E* **77**(1), 011920, 2008. DOI: [10.1103/PhysRevE.77.011920](https://doi.org/10.1103/PhysRevE.77.011920). (Cit. on pp. 4, 21).
- [73] E. Bertin, A. Baskaran, H. Chaté and M. C. Marchetti. Comparison between Smoluchowski and Boltzmann approaches for self-propelled rods. *Physical Review E* **92**(4), 2015. DOI: [10.1103/PhysRevE.92.042141](https://doi.org/10.1103/PhysRevE.92.042141). (Cit. on p. 4).
- [74] H. Chaté, F. Ginelli and R. Montagne. Simple Model for Active Nematics: Quasi-Long-Range Order and Giant Fluctuations. *Phys. Rev. Lett.* **96**(18), 180602, 2006. DOI: [10.1103/PhysRevLett.96.180602](https://doi.org/10.1103/PhysRevLett.96.180602). (Cit. on p. 4).
- [75] H. Chaté, F. Ginelli, G. Grégoire, F. Peruani and F. Raynaud. Modeling collective motion: variations on the Vicsek model. *Eur. Phys. J. B* **64**(3-4), 451–456, 2008. DOI: [10.1140/epjb/e2008-00275-9](https://doi.org/10.1140/epjb/e2008-00275-9). (Cit. on pp. 4, 26, 30).

- [76] F. Ginelli, F. Peruani, M. Bär and H. Chaté. Large-Scale Collective Properties of Self-Propelled Rods. *Phys. Rev. Lett.* **104**(18), 184502, 2010. DOI: [10.1103/PhysRevLett.104.184502](https://doi.org/10.1103/PhysRevLett.104.184502). (Cit. on pp. 4, 18, 64, 84).
- [77] F. Peruani, F. Ginelli, M. Bär and H. Chaté. Polar vs. apolar alignment in systems of polar self-propelled particles. *Journal of Physics: Conference Series* **297**, 012014, 2011. DOI: [10.1088/1742-6596/297/1/012014](https://doi.org/10.1088/1742-6596/297/1/012014). (Cit. on pp. 4, 10, 84, 121).
- [78] A. Peshkov, I. S. Aranson, E. Bertin, H. Chaté and F. Ginelli. Nonlinear Field Equations for Aligning Self-Propelled Rods. *Phys. Rev. Lett.* **109**, 268701, 2012. DOI: [10.1103/PhysRevLett.109.268701](https://doi.org/10.1103/PhysRevLett.109.268701). (Cit. on pp. 4, 6, 19, 20, 64, 84, 151, 172).
- [79] R. Großmann, F. Peruani and M. Bär. Mesoscale pattern formation of self-propelled rods with velocity reversal. *Physical Review E* **94**(5), 2016. DOI: [10.1103/PhysRevE.94.050602](https://doi.org/10.1103/PhysRevE.94.050602). (Cit. on pp. 4, 151).
- [80] F. Peruani, A. Deutsch and M. Bär. Nonequilibrium clustering of self-propelled rods. *Phys. Rev. E* **74**(3), 030904, 2006. DOI: [10.1103/PhysRevE.74.030904](https://doi.org/10.1103/PhysRevE.74.030904). (Cit. on p. 4).
- [81] D. Grossman, I. S. Aranson and E. Ben Jacob. Emergence of agent swarm migration and vortex formation through inelastic collisions. *New Journal of Physics* **10**(2), 023036, 2008. DOI: [10.1088/1367-2630/10/2/023036](https://doi.org/10.1088/1367-2630/10/2/023036). (Cit. on p. 4).
- [82] G. Baglietto and E. V. Albano. Finite-size scaling analysis and dynamic study of the critical behavior of a model for the collective displacement of self-driven individuals. *Physical Review E* **78**(2), 2008. DOI: [10.1103/PhysRevE.78.021125](https://doi.org/10.1103/PhysRevE.78.021125). (Cit. on p. 4).
- [83] C. A. Weber, V. Schaller, A. R. Bausch and E. Frey. Nucleation-induced transition to collective motion in active systems. *Physical Review E* **86**(3), 2012. DOI: [10.1103/PhysRevE.86.030901](https://doi.org/10.1103/PhysRevE.86.030901). (Cit. on pp. 4, 71).
- [84] A. M. Menzel and H. Löwen. Traveling and Resting Crystals in Active Systems. *Physical Review Letters* **110**(5), 2013. DOI: [10.1103/PhysRevLett.110.055702](https://doi.org/10.1103/PhysRevLett.110.055702). (Cit. on p. 4).
- [85] C. A. Weber, C. Bock and E. Frey. Defect-Mediated Phase Transitions in Active Soft Matter. *Physical Review Letters* **112**(16), 2014. DOI: [10.1103/PhysRevLett.112.168301](https://doi.org/10.1103/PhysRevLett.112.168301). (Cit. on p. 4).
- [86] A. M. Menzel. Tuned, driven, and active soft matter. *Physics reports* **554**, 1–45, 2015. (Cit. on pp. 5, 171, 202, 205).

- [87] G. Gonnella, D. Marenduzzo, A. Suma and A. Tiribocchi. Motility-induced phase separation and coarsening in active matter. *Comptes Rendus Physique* **16**(3), 316–331, 2015. DOI: [10.1016/j.crhy.2015.05.001](https://doi.org/10.1016/j.crhy.2015.05.001). (Cit. on p. 5).
- [88] M. E. Cates and J. Tailleur. Motility-Induced Phase Separation. *Annual Review of Condensed Matter Physics* **6**(1), 219–244, 2015. DOI: [10.1146/annurev-conmatphys-031214-014710](https://doi.org/10.1146/annurev-conmatphys-031214-014710). arXiv: [1406.3533](https://arxiv.org/abs/1406.3533). (Cit. on p. 5).
- [89] I. D. Couzin and N. R. Franks. Self-organized lane formation and optimized traffic flow in army ants. *Proceedings of the Royal Society B: Biological Sciences* **270**(1511), 139–146, 2003. DOI: [10.1098/rspb.2002.2210](https://doi.org/10.1098/rspb.2002.2210). (Cit. on p. 5).
- [90] A. John, A. Schadschneider, D. Chowdhury and K. Nishinari. Collective effects in traffic on bi-directional ant trails. *Journal of theoretical biology* **231**(2), 279–285, 2004. (Cit. on p. 5).
- [91] K. H. Nagai, Y. Sumino, R. Montagne, I. S. Aranson and H. Chaté. Collective Motion of Self-Propelled Particles with Memory. *Phys. Rev. Lett.* **114**, 168001, 2015. DOI: [10.1103/PhysRevLett.114.168001](https://doi.org/10.1103/PhysRevLett.114.168001). (Cit. on pp. 6, 55).
- [92] A. Kaiser and H. Löwen. Vortex arrays as emergent collective phenomena for circle swimmers. *Phys. Rev. E* **87**(3), 032712, 2013. DOI: [10.1103/PhysRevE.87.032712](https://doi.org/10.1103/PhysRevE.87.032712). (Cit. on pp. 6, 19).
- [93] H. H. Wensink, V. Kantsler, R. E. Goldstein and J. Dunkel. Controlling active self-assembly through broken particle-shape symmetry. *Phys. Rev. E* **89**(1), 010302, 2014. DOI: [10.1103/PhysRevE.89.010302](https://doi.org/10.1103/PhysRevE.89.010302). (Cit. on p. 6).
- [94] H. H. Wensink and H. Löwen. Aggregation of self-propelled colloidal rods near confining walls. *Physical Review E* **78**(3), 031409, 2008. DOI: [10.1103/PhysRevE.78.031409](https://doi.org/10.1103/PhysRevE.78.031409). (Cit. on p. 6).
- [95] N. Nikola, A. P. Solon, Y. Kafri, M. Kardar, J. Tailleur and R. Voituriez. Active Particles with Soft and Curved Walls: Equation of State, Ratchets, and Instabilities. *Physical Review Letters* **117**(9), 2016. DOI: [10.1103/PhysRevLett.117.098001](https://doi.org/10.1103/PhysRevLett.117.098001). (Cit. on p. 6).
- [96] P. M. Chaikin, T. C. Lubensky and T. A. Witten. *Principles of condensed matter physics*. Vol. 1. Cambridge university press Cambridge, 1995. (Cit. on p. 10).
- [97] M. Ingerson-Mahar and Z. Gitai. A growing family: the expanding universe of the bacterial cytoskeleton. *FEMS Microbiol. Rev.* **36**(1), 256–66, 2012. DOI: [10.1111/j.1574-6976.2011.00316.x](https://doi.org/10.1111/j.1574-6976.2011.00316.x). (Cit. on p. 12).
- [98] S. Pichoff and J. Lutkenhaus. Unique and overlapping roles for ZipA and FtsA in septal ring assembly in *Escherichia coli*. *EMBO J.* **21**(4), 685–693, 2002. (Cit. on pp. 12, 204).

- [99] Z. Li, M. J. Trimble, Y. V. Brun and G. J. Jensen. The structure of FtsZ filaments in vivo suggests a force-generating role in cell division. *EMBO J.* **26**(22), 4694–4708, 2007. (Cit. on p. 12).
- [100] S. J. Holden, T. Pengo, K. L. Meibom, C. F. Fernandez, J. Collier and S. Manley. High throughput 3D super-resolution microscopy reveals *Caulobacter crescentus* in vivo Z-ring organization. *PNAS*, 201313368, 2014. DOI: [10.1073/pnas.1313368111](https://doi.org/10.1073/pnas.1313368111). (Cit. on p. 12).
- [101] V. García-Morales and K. Krischer. The complex Ginzburg–Landau equation: an introduction. *Contemp. Phys.* **53**(2), 79–95, 2012. DOI: [10.1080/00107514.2011.642554](https://doi.org/10.1080/00107514.2011.642554). (Cit. on pp. 13, 28, 31).
- [102] O. Kratky and G. Porod. Röntgenuntersuchung gelöster Fadenmoleküle. *Recl. Trav. Chim. Pays-B.* **68**(12), 1106–1122, 1949. DOI: [10.1002/recl.19490681203](https://doi.org/10.1002/recl.19490681203). (Cit. on p. 14).
- [103] N. Saitô, K. Takahashi and Y. Yunoki. The Statistical Mechanical Theory of Stiff Chains. *J. Phys. Soc. Jpn.* **22**(1), 219–226, 1967. DOI: [10.1143/JPSJ.22.219](https://doi.org/10.1143/JPSJ.22.219). (Cit. on p. 14).
- [104] G. Chirico and J. Langowski. Kinetics of DNA supercoiling studied by Brownian dynamics simulation. *Biopolymers* **34**(3), 415–433, 1994. (Cit. on pp. 14, 16).
- [105] H. Wada and R. R. Netz. Stretching helical nano-springs at finite temperature. *Europhys. Lett.* **77**(6), 68001, 2007. DOI: [10.1209/0295-5075/77/68001](https://doi.org/10.1209/0295-5075/77/68001). (Cit. on pp. 14, 16).
- [106] R. E. Goldstein and S. A. Langer. Nonlinear dynamics of stiff polymers. *Phys. Rev. Lett.* **75**(6), 1094, 1995. (Cit. on p. 16).
- [107] M. Hinczewski, X. Schlagberger, M. Rubinstein, O. Krichevsky and R. R. Netz. End-Monomer Dynamics in Semiflexible Polymers. *Macromol.* **42**(3), 860–875, 2009. DOI: [10.1021/ma802017g](https://doi.org/10.1021/ma802017g). (Cit. on p. 16).
- [108] C. Bennemann, J. Baschnagel, W. Paul and K. Binder. Molecular-dynamics simulation of a glassy polymer melt: Rouse model and cage effect. *Comput. Theor. Polym. Sci.* **9**(3), 217–226, 1999. (Cit. on p. 16).
- [109] P. Kloeden and E. Platen. *Numerical Solution of Stochastic Differential Equations*. Springer, Berlin, 1992. (Cit. on p. 16).
- [110] J. K. G. Dhont. *An Introduction to Dynamics of Colloids*. Elsevier, Amsterdam, May 1996. (Cit. on p. 17).
- [111] X. Lu and Y. Hu. *Molecular Thermodynamics of Complex Systems*. Springer, Heidelberg, Nov. 2008. (Cit. on p. 17).

- [112] I. H. Riedel, K. Kruse and J. Howard. A self-organized vortex array of hydrodynamically entrained sperm cells. *Science* **309**(5732), 300–3, 2005. DOI: [10.1126/science.1110329](https://doi.org/10.1126/science.1110329). (Cit. on p. 18).
- [113] T. Ihle. Kinetic theory of flocking: Derivation of hydrodynamic equations. *Phys. Rev. E* **83**(3), 030901, 2011. DOI: [10.1103/PhysRevE.83.030901](https://doi.org/10.1103/PhysRevE.83.030901). (Cit. on p. 18).
- [114] F. Peruani, J. Starruß, V. Jakovljevic, L. Sjøgaard-Andersen, A. Deutsch and M. Bär. Collective Motion and Nonequilibrium Cluster Formation in Colonies of Gliding Bacteria. *Phys. Rev. Lett.* **108**(9), 098102, 2012. (Cit. on pp. 18, 126, 127, 154).
- [115] V. Schaller, C. A. Weber, B. Hammerich, E. Frey and A. R. Bausch. Frozen steady states in active systems. *Proc. Natl. Acad. Sci. U.S.A.* **108**(48), 19183–19188, 2011. (Cit. on p. 19).
- [116] Y. Yang, F. Qiu and G. Gompper. Self-organized vortices of circling self-propelled particles and curved active flagella. *Phys. Rev. E* **89**(1), 012720, 2014. DOI: [10.1103/PhysRevE.89.012720](https://doi.org/10.1103/PhysRevE.89.012720). (Cit. on p. 19).
- [117] C. A. Weber, F. Thüroff and E. Frey. Role of particle conservation in self-propelled particle systems. *New J. Phys.* **15**(4), 045014, 2013. (Cit. on pp. 19, 20, 172).
- [118] F. Thüroff, C. A. Weber and E. Frey. Critical Assessment of the Boltzmann Approach to Active Systems. *Phys. Rev. Lett.* **111**, 190601, 2013. DOI: [10.1103/PhysRevLett.111.190601](https://doi.org/10.1103/PhysRevLett.111.190601). (Cit. on pp. 19, 20, 49, 172).
- [119] A. Peshkov, S. Ngo, E. Bertin, H. Chaté and F. Ginelli. Continuous Theory of Active Matter Systems with Metric-Free Interactions. *Phys. Rev. Lett.* **109**, 098101, 2012. DOI: [10.1103/PhysRevLett.109.098101](https://doi.org/10.1103/PhysRevLett.109.098101). (Cit. on p. 20).
- [120] I. S. Aranson and L. Kramer. The world of the complex Ginzburg-Landau equation. *Rev. Mod. Phys.* **74**, 99–143, 2002. DOI: [10.1103/RevModPhys.74.99](https://doi.org/10.1103/RevModPhys.74.99). (Cit. on pp. 28, 31).
- [121] G. R. Dennis, J. J. Hope and M. T. Johnsson. XMDS2: Fast, scalable simulation of coupled stochastic partial differential equations. *Computer Physics Communications* **184**(1), 201–208, 2013. DOI: <https://doi.org/10.1016/j.cpc.2012.08.016>. (Cit. on p. 29).
- [122] S. Fürthauer, M. Stempel, S. W. Grill and F. Jülicher. Active chiral fluids. *Eur. Phys. J. E* **35**(9), 89, 2012. (Cit. on p. 30).
- [123] S. Fürthauer, M. Stempel, S. W. Grill and F. Jülicher. Active Chiral Processes in Thin Films. *Phys. Rev. Lett.* **110**, 048103, 2013. DOI: [10.1103/PhysRevLett.110.048103](https://doi.org/10.1103/PhysRevLett.110.048103). (Cit. on p. 30).

- [124] M. P. Sheetz and J. A. Spudich. Movement of myosin-coated fluorescent beads on actin cables in vitro. *Nature* **303**, 31, 1983. (Cit. on pp. 47, 202).
- [125] P. Guillamat, J. Ignés-Mullol and F. Sagués. Control of active liquid crystals with a magnetic field. *Proceedings of the National Academy of Sciences* **113**(20), 5498–5502, 2016. DOI: [10.1073/pnas.1600339113](https://doi.org/10.1073/pnas.1600339113). (Cit. on p. 47).
- [126] C. A. Weber, R. Suzuki, V. Schaller, I. S. Aranson, A. R. Bausch and E. Frey. Random bursts determine dynamics of active filaments. *Proceedings of the National Academy of Sciences* **112**(34), 10703–10707, 2015. DOI: [10.1073/pnas.1421322112](https://doi.org/10.1073/pnas.1421322112). (Cit. on p. 48).
- [127] L. Huber, R. Suzuki, T. Krüger, E. Frey and A. R. Bausch. Emergence of coexisting ordered states in active matter systems. *Science* **361**(6399), 255–258, 2018. DOI: [10.1126/science.aao5434](https://doi.org/10.1126/science.aao5434). (Cit. on pp. 50, 68, 70, 72, 73, 77–82, 125, 138, 139, 149, 154, 202, 206).
- [128] M. Abkenar, K. Marx, T. Auth and G. Gompper. Collective behavior of penetrable self-propelled rods in two dimensions. *Physical Review E* **88**(6), 062314, 2013. DOI: [10.1103/PhysRevE.88.062314](https://doi.org/10.1103/PhysRevE.88.062314). (Cit. on p. 52).
- [129] R. Suzuki and A. R. Bausch. The emergence and transient behaviour of collective motion in active filament systems. *Nature Communications* **8**(1), 2017. DOI: [10.1038/s41467-017-00035-3](https://doi.org/10.1038/s41467-017-00035-3). (Cit. on pp. 52, 61, 125).
- [130] S. Ngo, F. Ginelli and H. Chaté. Competing Ferromagnetic and Nematic Alignment in Self-Propelled Polar Particles. *Physical Review E* **86**(5), 2012. DOI: [10.1103/PhysRevE.86.050101](https://doi.org/10.1103/PhysRevE.86.050101). (Cit. on pp. 55, 67, 68, 71, 84).
- [131] D.-B. Wang, F.-B. Hsiao, C.-H. Chuang and Y.-C. Lee. Algorithm Optimization in Molecular Dynamics Simulation. *Computer Physics Communications* **177**(7), 551–559, 2007. DOI: [10.1016/j.cpc.2007.05.009](https://doi.org/10.1016/j.cpc.2007.05.009). (Cit. on p. 57).
- [132] L. Isserlis. On certain probable errors and correlation coefficients of multiple frequency distributions with skew regression. *Biometrika* **11**(3), 185–190, 1916. (Cit. on p. 61).
- [133] S. MacLean-Fletcher and T. D. Pollard. Identification of a factor in conventional muscle actin preparations which inhibits actin filament self-association. *Biochemical and Biophysical Research Communications* **96**(1), 18–27, 1980. DOI: [10.1016/0006-291X\(80\)91175-4](https://doi.org/10.1016/0006-291X(80)91175-4). (Cit. on p. 74).
- [134] J. A. Spudich and S. Watt. The regulation of rabbit skeletal muscle contraction I. Biochemical studies of the interaction of the tropomyosin-troponin complex with actin and the proteolytic fragments of myosin. *Journal of Biological Chemistry* **246**(15), 4866–4871, 1971. (Cit. on p. 74).

- [135] S. J. Kron, Y. Y. Toyoshima, T. Q. Uyeda and J. A. Spudich. [33] Assays for actin sliding movement over myosin-coated surfaces. *Methods in enzymology*. Vol. 196. Elsevier, 1991, pp. 399–416. (Cit. on p. 74).
- [136] B. Mahault, X.-c. Jiang, E. Bertin, Y.-q. Ma, A. Patelli, X.-q. Shi and H. Chaté. Self-Propelled Particles with Velocity Reversals and Ferromagnetic Alignment: Active Matter Class with Second-Order Transition to Quasi-Long-Range Polar Order. *Physical Review Letters* **120**(25), 2018. DOI: [10.1103/PhysRevLett.120.258002](https://doi.org/10.1103/PhysRevLett.120.258002). (Cit. on p. 84).
- [137] P. Gross and S. Grill. Ordnung aus Unordnung. *Physik-Journal* **10**, 22–23, 2018. (Cit. on p. 84).
- [138] A. Morin and D. Bartolo. Flowing Active Liquids in a Pipe: Hysteretic Response of Polar Flocks to External Fields. *Physical Review X* **8**(2), 2018. DOI: [10.1103/PhysRevX.8.021037](https://doi.org/10.1103/PhysRevX.8.021037). (Cit. on p. 121).
- [139] A. Chepizhko and V. Kulinskii. The kinetic regime of the Vicsek model. *AIP Conference Proceedings*. Vol. 1198. 1. AIP. 2009, pp. 25–33. (Cit. on p. 122).
- [140] V. Narayan, S. Ramaswamy and N. Menon. Long-Lived Giant Number Fluctuations in a Swarming Granular Nematic. *Science* **317**(5834), 105–108, 2007. DOI: [10.1126/science.1140414](https://doi.org/10.1126/science.1140414). (Cit. on p. 126).
- [141] J. Palacci, S. Sacanna, A. P. Steinberg, D. J. Pine and P. M. Chaikin. Living Crystals of Light-Activated Colloidal Surfers. *Science* **339**(6122), 936–940, 2013. DOI: [10.1126/science.1230020](https://doi.org/10.1126/science.1230020). (Cit. on p. 126).
- [142] J. Tailleur and M. E. Cates. Statistical Mechanics of Interacting Run-and-Tumble Bacteria. *Phys. Rev. Lett.* **100**, 218103, 2008. DOI: [10.1103/PhysRevLett.100.218103](https://doi.org/10.1103/PhysRevLett.100.218103). (Cit. on pp. 126, 130).
- [143] Y. Fily and M. C. Marchetti. Athermal Phase Separation of Self-Propelled Particles with No Alignment. *Physical Review Letters* **108**(23), 2012. DOI: [10.1103/PhysRevLett.108.235702](https://doi.org/10.1103/PhysRevLett.108.235702). (Cit. on pp. 126, 130).
- [144] F. Peruani, L. Schimansky-Geier and M. Bär. Cluster dynamics and cluster size distributions in systems of self-propelled particles. *The European Physical Journal Special Topics* **191**(1), 173–185, 2010. DOI: [10.1140/epjst/e2010-01349-1](https://doi.org/10.1140/epjst/e2010-01349-1). (Cit. on pp. 126, 127, 134, 143, 145).
- [145] F. Peruani and M. Bär. A kinetic model and scaling properties of non-equilibrium clustering of self-propelled particles. *New Journal of Physics* **15**(6), 065009, 2013. DOI: [10.1088/1367-2630/15/6/065009](https://doi.org/10.1088/1367-2630/15/6/065009). (Cit. on pp. 126, 127, 134, 143, 145).

- [146] C. Huepe and M. Aldana. Intermittency and Clustering in a System of Self-Driven Particles. *Phys. Rev. Lett.* **92**, 168701, 2004. DOI: [10.1103/PhysRevLett.92.168701](https://doi.org/10.1103/PhysRevLett.92.168701). (Cit. on pp. [126](#), [134](#)).
- [147] Y. Fily, S. Henkes and M. C. Marchetti. Freezing and phase separation of self-propelled disks. *Soft Matter* **10**(13), 2132–2140, 2014. DOI: [10.1039/C3SM52469H](https://doi.org/10.1039/C3SM52469H). (Cit. on pp. [126](#), [134](#)).
- [148] Ö. Duman, R. E. Isele-Holder, J. Elgeti and G. Gompper. Collective dynamics of self-propelled semiflexible filaments. *Soft Matter* **14**(22), 4483–4494, 2018. DOI: [10.1039/C8SM00282G](https://doi.org/10.1039/C8SM00282G). (Cit. on pp. [126](#), [134](#)).
- [149] F. Peruani, A. Deutsch and M. Bär. Nonequilibrium clustering of self-propelled rods. *Phys. Rev. E* **74**(3), 2006. DOI: [10.1103/PhysRevE.74.030904](https://doi.org/10.1103/PhysRevE.74.030904). (Cit. on pp. [126](#), [127](#), [134](#), [143](#), [145](#)).
- [150] H. P. Zhang, A. Be'er, E.-L. Florin and H. L. Swinney. Collective Motion and Density Fluctuations in Bacterial Colonies. *Proceedings of the National Academy of Sciences* **107**(31), 13626–13630, 2010. DOI: [10.1073/pnas.1001651107](https://doi.org/10.1073/pnas.1001651107). (Cit. on p. [134](#)).
- [151] Y. Yang, V. Marceau and G. Gompper. Swarm Behavior of Self-Propelled Rods and Swimming Flagella. *Physical Review E* **82**(3), 2010. DOI: [10.1103/PhysRevE.82.031904](https://doi.org/10.1103/PhysRevE.82.031904). (Cit. on p. [134](#)).
- [152] V. I. Kalikmanov. Classical nucleation theory. *Nucleation theory*. Springer, 2013, pp. 17–41. (Cit. on p. [138](#)).
- [153] M. v. Smoluchowski. Versuch Einer Mathematischen Theorie Der Koagulationskinetik Kolloider Lösungen. *Zeitschrift für Physikalische Chemie* **92U**(1), 1918. DOI: [10.1515/zpch-1918-9209](https://doi.org/10.1515/zpch-1918-9209). (Cit. on p. [141](#)).
- [154] S. Chandrasekhar. Stochastic Problems in Physics and Astronomy. *Reviews of Modern Physics* **15**(1), 1–89, 1943. DOI: [10.1103/RevModPhys.15.1](https://doi.org/10.1103/RevModPhys.15.1). (Cit. on p. [141](#)).
- [155] P. L. Krapivsky, S. Redner and E. Ben-Naim. *A Kinetic View of Statistical Physics*. OCLC: 672330146. Cambridge University Press, Cambridge; New York, 2010. (Cit. on p. [141](#)).
- [156] E. Bertin, H. Chaté, F. Ginelli, S. Mishra, A. Peshkov and S. Ramaswamy. Mesoscopic Theory for Fluctuating Active Nematics. *New Journal of Physics* **15**(8), 085032, 2013. DOI: [10.1088/1367-2630/15/8/085032](https://doi.org/10.1088/1367-2630/15/8/085032). (Cit. on p. [151](#)).
- [157] J. Denk, L. Huber, E. Reithmann and E. Frey. Active Curved Polymers Form Vortex Patterns on Membranes. *Physical Review Letters* **116**(17), 178301, 2016. DOI: [10.1103/PhysRevLett.116.178301](https://doi.org/10.1103/PhysRevLett.116.178301). (Cit. on pp. [154](#), [176](#), [188](#), [201](#)).

- [158] M. C. Cross and H. Greenside. *Pattern Formation and Dynamics in Nonequilibrium Systems*. Cambridge University Press, 2009. (Cit. on pp. 176, 193).
- [159] J. Halatek and E. Frey. Rethinking pattern formation in reaction–diffusion systems. *Nature Physics* **14**(5), 507, 2018. (Cit. on p. 199).
- [160] F. Brauns, J. Halatek and E. Frey. Phase-space geometry of reaction–diffusion dynamics. *arXiv preprint arXiv:1812.08684*, 2018. (Cit. on p. 199).
- [161] L. Giomi. Geometry and topology of turbulence in active nematics. *Physical Review X* **5**(3), 031003, 2015. (Cit. on pp. 202, 205).
- [162] D. Loi, S. Mossa and L. F. Cugliandolo. Effective temperature of active matter. *Physical Review E* **77**(5), 051111, 2008. (Cit. on p. 202).
- [163] D. Loi, S. Mossa and L. F. Cugliandolo. Effective temperature of active complex matter. *Soft Matter* **7**(8), 3726–3729, 2011. (Cit. on p. 202).
- [164] G. S. Redner, M. F. Hagan and A. Baskaran. Structure and dynamics of a phase-separating active colloidal fluid. *Physical review letters* **110**(5), 055701, 2013. (Cit. on p. 202).
- [165] T. Speck, J. Bialké, A. M. Menzel and H. Löwen. Effective Cahn-Hilliard equation for the phase separation of active Brownian particles. *Physical Review Letters* **112**(21), 218304, 2014. (Cit. on p. 202).
- [166] G. Gonnella, D. Marenduzzo, A. Suma and A. Tiribocchi. Motility-induced phase separation and coarsening in active matter. *Comptes Rendus Physique* **16**(3), 316–331, 2015. (Cit. on p. 202).
- [167] A. P. Solon, J. Stenhammar, R. Wittkowski, M. Kardar, Y. Kafri, M. E. Cates and J. Tailleur. Pressure and phase equilibria in interacting active Brownian spheres. *Physical review letters* **114**(19), 198301, 2015. (Cit. on pp. 202, 206).
- [168] S. S. Andrews and A. P. Arkin. A Mechanical Explanation for Cytoskeletal Rings and Helices in Bacteria. *Biophysical Journal* **93**(6), 1872–1884, 2007. DOI: [10.1529/biophysj.106.102343](https://doi.org/10.1529/biophysj.106.102343). (Cit. on p. 204).
- [169] S. Arumugam, G. Chwastek, E. Fischer-Friedrich, C. Ehrig, I. Mönch and P. Schwille. Surface Topology Engineering of Membranes for the Mechanical Investigation of the Tubulin Homologue FtsZ. *Angewandte Chemie International Edition* **51**(47), 11858–11862, 2012. DOI: [10.1002/anie.201204332](https://doi.org/10.1002/anie.201204332). (Cit. on p. 204).
- [170] E. Ramírez-Aportela, J. R. López-Blanco, J. M. Andreu and P. Chacón. Understanding Nucleotide-Regulated FtsZ Filament Dynamics and the Monomer Assembly Switch with Large-Scale Atomistic Simulations. *Biophysical Journal* **107**(9), 2164–2176, 2014. DOI: [10.1016/j.bpj.2014.09.033](https://doi.org/10.1016/j.bpj.2014.09.033). (Cit. on p. 204).

- [171] P. G. d. P. Salas, I. Hörger, F. Martín-García, J. Mendieta, Á. Alonso, M. Encinar, P. Gómez-Puertas, M. Vélez and P. Tarazona. Torsion and curvature of FtsZ filaments. *Soft Matter* **10**(12), 1977–1986, 2014. DOI: [10.1039/C3SM52516C](https://doi.org/10.1039/C3SM52516C). (Cit. on p. 204).
- [172] J. Lutkenhaus. Assembly dynamics of the bacterial MinCDE system and spatial regulation of the Z ring. *Annu. Rev. Biochem.* **76**, 539–562, 2007. (Cit. on p. 204).
- [173] S. Arumugam, Z. Petra ek and P. Schwille. MinCDE exploits the dynamic nature of FtsZ filaments for its spatial regulation. *Proceedings of the National Academy of Sciences* **111**(13), E1192–E1200, 2014. DOI: [10.1073/pnas.1317764111](https://doi.org/10.1073/pnas.1317764111). (Cit. on p. 204).
- [174] I. D. Couzin, J. Krause, N. R. Franks and S. A. Levin. Effective leadership and decision-making in animal groups on the move. *Nature* **433**(7025), 513, 2005. (Cit. on p. 205).
- [175] G. Ariel, O. Rimer and E. Ben-Jacob. Order–Disorder Phase Transition in Heterogeneous Populations of Self-propelled Particles. *Journal of Statistical Physics* **158**(3), 579–588, 2015. DOI: [10.1007/s10955-014-1095-7](https://doi.org/10.1007/s10955-014-1095-7). (Cit. on p. 205).
- [176] A. M. Berdahl, A. B. Kao, A. Flack, P. A. H. Westley, E. A. Codling, I. D. Couzin, A. I. Dell and D. Biro. Collective animal navigation and migratory culture: from theoretical models to empirical evidence. *Philosophical Transactions of the Royal Society B: Biological Sciences* **373**(1746), 20170009, 2018. DOI: [10.1098/rstb.2017.0009](https://doi.org/10.1098/rstb.2017.0009). (Cit. on pp. 205, 206).
- [177] M. Nagy, I. D. Couzin, W. Fiedler, M. Wikelski and A. Flack. Synchronization, coordination and collective sensing during thermalling flight of freely migrating white storks. *Philosophical Transactions of the Royal Society B: Biological Sciences* **373**(1746), 20170011, 2018. DOI: [10.1098/rstb.2017.0011](https://doi.org/10.1098/rstb.2017.0011). (Cit. on pp. 205, 206).
- [178] C. J. Torney, J. G. C. Hopcraft, T. A. Morrison, I. D. Couzin and S. A. Levin. From single steps to mass migration: the problem of scale in the movement ecology of the Serengeti wildebeest. *Philosophical Transactions of the Royal Society B: Biological Sciences* **373**(1746), 20170012, 2018. DOI: [10.1098/rstb.2017.0012](https://doi.org/10.1098/rstb.2017.0012). (Cit. on p. 205).
- [179] É. Fodor, C. Nardini, M. E. Cates, J. Tailleur, P. Visco and F. van Wijland. How Far from Equilibrium Is Active Matter? *Physical Review Letters* **117**(3), 2016. DOI: [10.1103/PhysRevLett.117.038103](https://doi.org/10.1103/PhysRevLett.117.038103). (Cit. on p. 206).
- [180] G. Popkin. The physics of life. *Nature* **529**(7584), 16–18, 2016. DOI: [10.1038/529016a](https://doi.org/10.1038/529016a). (Cit. on p. 206).

- [181] Y. Hiratsuka, M. Miyata, T. Tada and T. Q. P. Uyeda. A microrotary motor powered by bacteria. *Proceedings of the National Academy of Sciences* **103**(37), 13618–13623, 2006. DOI: [10.1073/pnas.0604122103](https://doi.org/10.1073/pnas.0604122103). (Cit. on p. 207).
- [182] G. Vizsnyiczai, G. Frangipane, C. Maggi, F. Saglimbeni, S. Bianchi and R. Di Leonardo. Light controlled 3D micromotors powered by bacteria. *Nature Communications* **8**, 15974, 2017. DOI: [10.1038/ncomms15974](https://doi.org/10.1038/ncomms15974). (Cit. on p. 207).
- [183] A. Kaiser, A. Peshkov, A. Sokolov, B. ten Hagen, H. Löwen and I. S. Aranson. Transport Powered by Bacterial Turbulence. *Physical Review Letters* **112**(15), 158101, 2014. DOI: [10.1103/PhysRevLett.112.158101](https://doi.org/10.1103/PhysRevLett.112.158101). (Cit. on p. 207).
- [184] F. G. Woodhouse and J. Dunkel. Active matter logic for autonomous microfluidics. *Nature Communications* **8**, 15169, 2017. DOI: [10.1038/ncomms15169](https://doi.org/10.1038/ncomms15169). (Cit. on p. 207).



# Acknowledgements

Zuallererst gilt mein Dank meinem Doktorvater Erwin Frey für seine führende Hand über viele Jahre hinweg, von der ersten Hilfe bei Problemen aus meiner Zeit als Sportstudent, über meine Masterarbeit bis hin zum heutigen Tag. Erwin, erst durch Deine vielen inspirierenden Worte aus meinen Vorlesungstagen fand ich einen spannenden Zugang zur Theorie der Biophysik. Ohne Deine vielen kreativen Ideen oder den Freiraum, vielen verschiedenen Forschungsthemen nachzugehen und dort in die Tiefe zu tauchen, wären viele meiner Ergebnisse nie zustande gekommen. Und ohne so manche Hartnäckigkeit Deinerseits und intensive Diskussionen wären viele Resultate nur halb so klar gewesen, und es hätte auch nur halb so viel Spaß gemacht. Du hast es geschafft, eine menschlich wie fachlich tolle Forschungsgruppe um Dich zu scharen und ich hoffe das bleibt Dir noch lange erhalten.

Ein besonderer Dank gilt an dieser Stelle auch Andreas Bausch, an dessen Labor ich mit offenen Armen empfangen wurde und einige Monate intensiv forschen, experimentieren und diskutieren konnte. Und vor allem *lernen*, was sich ein Theoretiker vielleicht nicht immer gerne eingestehen möchte! Ohne Deine Begeisterungsfähigkeit und Hilfsbereitschaft wäre alles bei weitem nicht so gut gewesen.

Des weiteren möchte ich besonders die Kollegen (und mittlerweile gute Freunde) hervorheben, mit denen ich einen großen Teil dieser aufregenden Zeit intensiv zusammen forschen durfte: Jonas, mit dem ich viel zusammen gearbeitet habe, einige Masterstudenten betreute und schon mit dem Rollkoffer durch den Central Park spaziert bin; Emanuel, mit dem ich zahllose Kaffee- und andere Getränke einnehmen konnte, schon viele niveauvolle Gespräche führen durfte und auch abseits der Wissenschaft abenteuerliche Erlebnisse hatte; Timo, mit dem ich viele spannende und vor allem sehr anspruchsvolle physikalische, numerische und experimentelle Probleme sowohl diskutieren, durchleben und meistern durfte; Fridjof, der mir mit seiner Hilfsbereitschaft schon bei manchem nichtlinearen und stilistischen Problem helfen konnte. Des weiteren danke ich meinen Masterstudenten Federico, Raphael, Daniel, Peter, Johanna und Michi, die mich über die Jahre begleitet haben.

Vielen lieben Dank an die ganze Arbeitsgruppe, die großartige Atmosphäre in jeglicher Hinsicht hat mein Doktorstudium zu einer einzigartigen Zeit in meinem Leben gemacht. Da wären die alten 'Hasen' aus meiner Vorgänger-Generation, der enthusiastische und stets hilfsbereite Louis, mein langjähriger Zimmergenosse Karl, der ewige Jacob, mein alter Betreuer Philipp, der allwissende Cornelius, der smarte Hannes, der bescheidene Markus, die fröhliche Marianne und die doppelten Matthiasse. Und natürlich alle aus meiner oder der jüngeren Generation wie Silke,

Raphaela, Flo, Felix, Isabella, Patrick, Philipp, und – last but not least – vielen Dank auch an Chase Broedersz für so manches hilfreiche Kaffeegespräch. Danke an dieser Stelle auch an Emanuel, Timo, Jonas, Fridtjof und Isabella für das Korrekturlesen dieser Arbeit.

Nicht wegzudenken aus meinem Arbeits-Alltag am Lehrstuhl waren auch die ehrgeizige Bouldertruppe, die zwar oft Fluktuationen unterlag aber stets ein hohes Niveau hatte; oder die Mittagsgruppe zusammen mit Bene aus dem 4. Stock und früher noch mit Jun, ohne die ich wahrscheinlich verhungert wäre. Ganz besonders danke ich der Hochzeitsconnection, die mir das wohl mit Abstand schwerste Rätsel meines Lebens bescherten.

Abseits vom akademischen Leben möchte ich meinen Freunden Felix, Ferdi, Mathias, Caj, Maksim, Marco und Lukas danken, die mich auch jederzeit im Alltag unterstützten. Hierbei auch danke an das Segelbundesliga-Team des CYC, im Speziellen Poldo, Moritz, Simon, Flo und Niko, welche stets interessiert an meiner Forschung waren und mich auch manchmal zum Nachdenken gebracht und inspiriert haben.

Zu guter Letzt, mein größter Dank gilt meiner Familie, der jahrelangen Unterstützung meiner Eltern Gila und Manfred, und natürlich meiner Frau Lisa und meiner Tochter Josefine. Ohne euch, eure helfenden Hände und richtigen Worte wäre das alles nicht möglich gewesen.